Università di Pavia

Università degli Studi di Pavia
Dipartimento di Fisica

INFN Sez. di Pavia

DOTTORATO DI RICERCA IN FISICA – XXIX CICLO

Development and performance of Micropattern Gaseous Detectors for the CMS muon system upgrade

Ilaria Vai

Submitted to the Graduate School of Physics in partial fulfillment of the requirements for the degree of

DOTTORE DI RICERCA IN FISICA

DOCTOR OF PHILOSOPHY IN PHYSICS

at the

University of Pavia

Supervisor: Prof. Cristina Riccardi

Ai miei genitori, Andrea
ed Andrea

Contents

List of Figures

List of Tables

Introduction

This PhD work is involved in the framework of the upgrade of the muon system of the Compact Muon Solenoid (CMS) experiment. The CMS muon system during the first period of operation (Run 1) of the Large Hadron Collider (LHC) was instrumented with three different kinds of gaseous detectors: Drift Tubes (DT) in the barrel, Cathode Strip Chambers (CSC) in the endcaps and Resistive Plate Chambers (RPC) as complementary technology in both regions. This configuration obtained excellent results during Run 1, but it needs to be improved in order to keep them also in the next LHC phases, during which a huge increase of the LHC luminosity is foreseen, up to 5×10^{34} cm^{-2}s^{-1}. These conditions will deeply affect the performance of the detectors as they will induce a remarkable growth of the pileup and a huge worsening of the background conditions. In order to face these challenges, the CMS Collaboration is performing a general upgrade of all the subsystems, involving also the muon system which will undergo deep changes. Beyond a general improvement of the installed detectors, including interventions both on the chambers themselves and their electronics, the muon system upgrade foresees also the installation of new muon stations in the high η region of the muon system, region fundamental for many physics channels, like for example $H \rightarrow ZZ^* \rightarrow 4\mu$. This region was suffering from lack of redundancy, as the technologies available at that time were not considered able to cope with the high rates and high background characteristic of those regions. The proposed new stations are in total five: the first three, called GE1/1, GE2/1 and ME0, foresee the implementation of Micropattern Gaseous Detectors (MPGD), while for the last two, RE3/1 and RE4/1, improved versions of RPC are being considered.

This work was involved in the activities for the implementation of the MPGD stations, in particular GE1/1 and ME0.

The GE1/1 station, the only MPGD station already approved by the CMS Collaboration, will be instrumented with Triple-GEM detectors and will be inserted during the Long Shutdown 2 (LS2). The installation of few detectors is foreseen already for the End of Year Technical stop 2016-2017 in order to gain operation experience with the new system. My activity for the GE1/1 station was initially focused on the performance of Triple-GEM detectors in the background environment of the muon system, in particular the neutron component. My contribution then moved to the development of the Detector Control System (DCS) to be used for the control of the GE1/1 chambers once installed in CMS.

The experience obtained with GE1/1 then allowed me to focus on the R&D for the very forward ME0 station. Its inclusion, as well as GE2/1, has not been approved yet by the CMS Collaboration, but is proposed for LS3. For this new station, the Collaboration is considering two different technologies: as baseline, again Triple-GEM detectors with a configuration similar to GE1/1. The optional solution instead is a new MPGD, the Fast Timing Micropattern (FTM) detector, intended to exploit the timing information for the pileup and neutron background rejection. Starting from my second PhD year, I was involved in the R&D of this new technology and I became responsible of the test to be performed on the new prototypes.

The framework in which this thesis was developed is described in the first Chapter, which is focused on the upgrade of the CMS experiment and in particular of its muon system, analyzing in detail the motivation adduced for the installation of the new stations.

The technologies to be implemented in these new stations, will be discussed in Chapter 2. In particular classic gaseous detectors and their limitations will be analyzed and then compared with the new MPGD solutions. Great attention will be given to the GEM technology selected for the GE1/1 station.

Chapter 3 will be dedicated to the GE1/1 station: the geometry of the chambers and the performance obtained will be discussed in detail. Great attention will be given to the behavior of Triple-GEM in a huge radiation environment.

The Slice Test and the DCS system of the GE1/1 station will be presented in Chapter 4.

Chapter 5 instead will be focused on the two stations GE2/1 and ME0: after a brief introduction to both the stations, with the analysis of the considered

technological solutions, we will move to description of the prototypes developed for the ME0 station, analyzing in detail the performance obtained.

Finally Chapter 6 will be dedicated to the conclusion and the plans for the future.

Chapter 1

The upgrade of the CMS experiment

The Compact Muon Solenoid (CMS) experiment [1] is one of the experiments installed at the Large Hadron Collider (LHC) [3]. Exactly as its complementary experiment ATLAS [2], CMS is a *general purpose experiment*, aimed at answering fundamental questions in particle physics, like the origin of elementary particle masses and the nature of the dark matter.

The CMS experiment achieved important results during the first LHC Run and now entered a complex upgrade phase. The general structure of the detector will be greatly improved and, in particular, the muon system, in which context this thesis is developed, will undergo major changes.

1.1 Physics at the CMS experiment

During the first physics run in 2011-2012, the LHC collider reached a peak luminosity of 7.7×10^{33} $\mathrm{cm}^{-2}\mathrm{s}^{-1}$ and delivered an integrated luminosity of $\sim$25 fb^{-1} to the CMS experiment. Among the countless remarkable results obtained from these data, a fundamental goal has been reached with the observation in 2012 of a new particle of mass $\sim$125 GeV by the ATLAS and CMS collaborations [4, 5], identified as a Higgs Boson. In Fig.1.1 we can see the signals from CMS that contributed to establishing the existence of this new particle. The CMS experiment, as well at the ATLAS experiment, was also able to start a detailed study of the properties of this new particle, in order to confirm its nature. For example the decays of the new boson to the gauge

bosons of the Standard Model (SM), the W, Z, and the photon, were verified, each with more than 5 standard deviation significance.

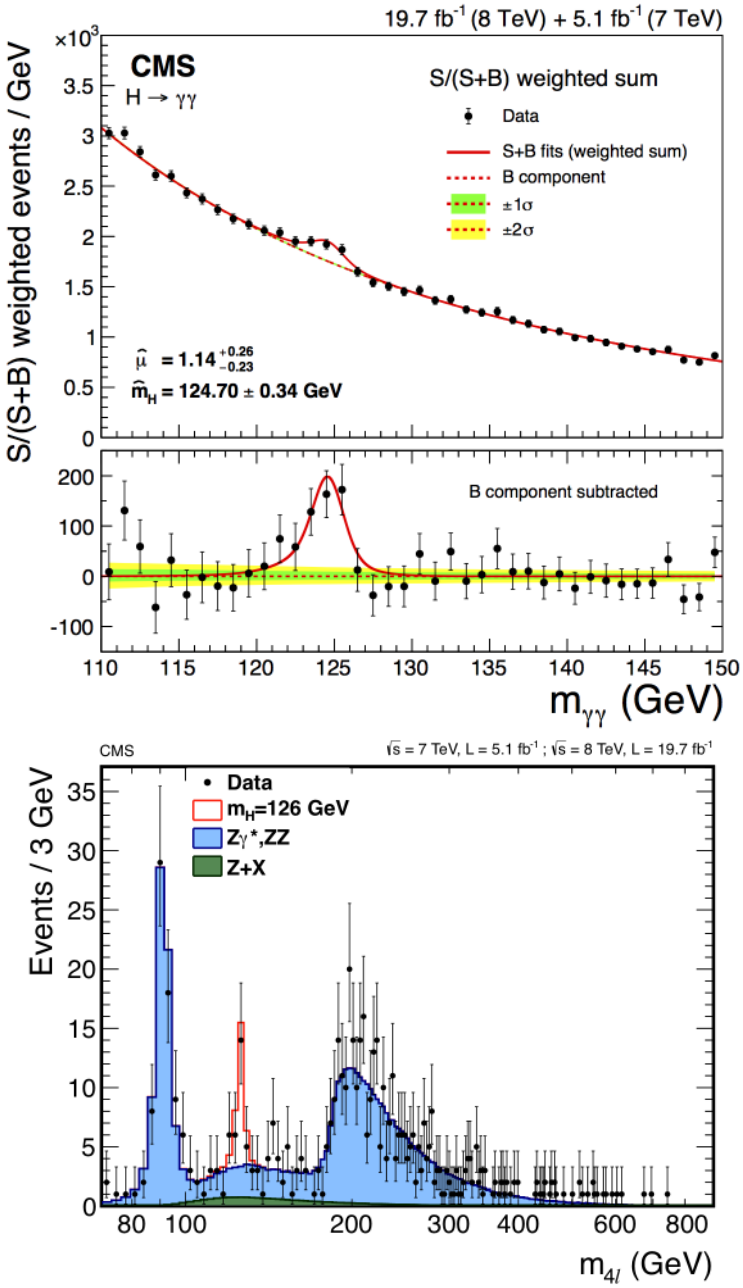

Figure 1.1: Top: the upper side plot shows the $\gamma\gamma$ mass spectrum with a peak near 125 GeV. The bottom plot shows this distribution with the background subtracted. Bottom: mass spectrum of four leptons. The three peaks are, in order of increasing mass, the decay of the Z boson, the Higgs bosons decaying into $Z(l^+l^-)Z^*(l'^+l'^-)$ and di-boson production of two $Z(l^+l^-)$, where l and l' are either a muon or electron [6].

However, the Higgs boson study has not yet been completed and will be an extensive part of the CMS program in the next years. The analysis will include precise measurements of the Higgs boson couplings, probing of its tensor structure, and the search for rare SM and Beyond SM (BSM) decays. The gigantic dataset that will be produced will give access to all the p-p production processes and decays of the Higgs boson. In Fig.1.2 we can compare the CMS results at 8 TeV center-of-mas-energy (left) and a projection for the measurement of Higgs boson couplings in a dataset of 3000 fb^{-1} at 14 TeV center-of-mass energy (right) as a function of the boson or fermion masses [12]: percent-level precision can be reached for most coupling measurements. In addition, the coupling to the second-generation fermions could be analyzed for the first time through the measurement of the Higgs boson decay to two muons. Finally, the Higgs boson self-coupling could be studied thanks to the measurements of di-Higgs production with a cross section of about 40 fb.

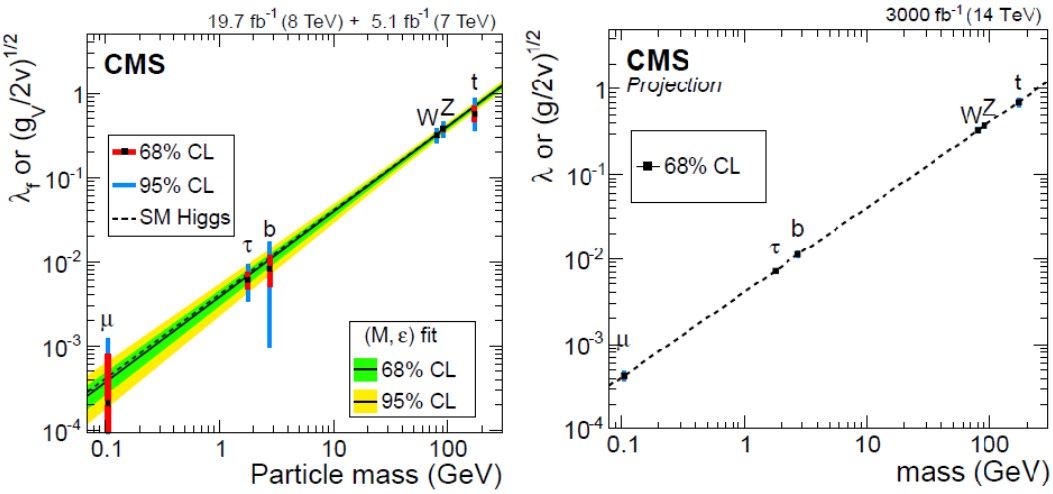

Figure 1.2: Observed and projected precision on Higgs boson couplings as a function of boson or fermion masses [6].

The predicted mass distribution for $H \to ZZ^* \to 4l$ in a dataset of 3000 fb^{-1} with the upgraded CMS detector is shown in Fig.1.3. This is a crucial measurement: the coupling to electrons is too small to be measured, but the coupling to τ-leptons will be well-measured and the couplings to the muons will become accessible. Studies of the vector boson scattering processes will allow a test of the role of the Higgs boson in the electroweak symmetry breaking. These measurements could also be sensitive to new physics through the triple-gauge couplings (TGCs) and quartic-gauge couplings (QGCs), through the

fundamental exploitation of forward-jet tagging.

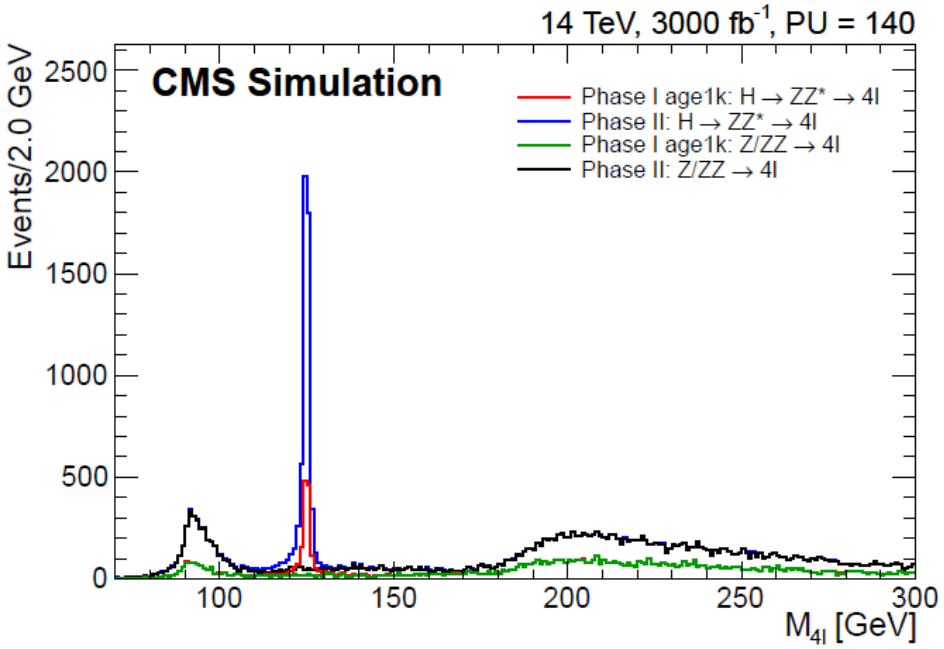

Figure 1.3: Four lepton mass distributions for a luminosity 3000 fb^{-1} for the signal, $H \rightarrow ZZ \rightarrow 4l$, and for the irreducible $ZZ \rightarrow 4l$ background. Both processes have been simulated with the aged phase-I detector with pileup of 140 and the phase-II detector with pileup of 140. [6].

Moreover, the SM does not provide answers to other questions, for which new physics is required. Radiative corrections to the Higgs should cause its mass to increase to very high values. New physics is expected at masses not too far from 1 TeV to cancel this growth. The theory known as supersymmetry (SUSY) contains a partner for every SM particle but with spin that is less by 1/2 unit. These particles, in the assumption that the lightest ones are not too much heavier than 1 TeV, can cancel the growth of the Higgs mass from radiative corrections and can also provide a dark matter candidate.

Fig.1.4 shows the cross sections for many kinds of supersymmetric particles from Minimal Superymmetric Standard Model (MSSM) [7] as a function of their masses. Up to now, SUSY has not yet been observed at the LHC. In simplified models of supersymmetry, the SUSY partners of the gluons, the *gluinos*, and quarks, the *squarks*, with masses below about 1 TeV are excluded, while scenarios with 3rd generation squarks, the sbottoms and the stops, with masses below 1 TeV are still compatible with the data, as shown in Fig.1.5.

The possible explanations of this fact are two: these particles exist at

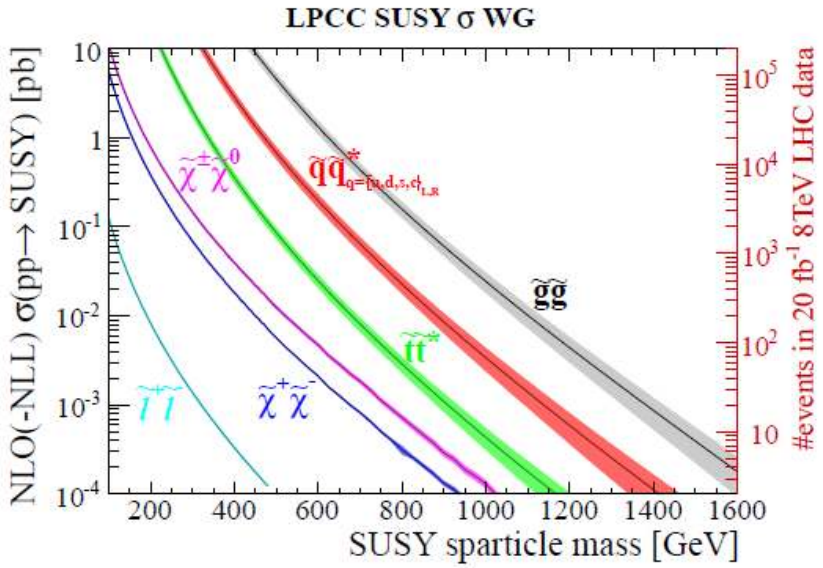

Figure 1.4: Cross section for SUSY particles as a function of their masses [6].

masses above the current level of sensitivity or they could be present at lower masses but their cross sections are lower than expected or their experimental signatures are more difficult to observe. In both cases, sensitivity for searches of new particles grows with increased luminosity.

One of the next priorities for the physics program at the LHC will therefore be the hunt for dark matter, that is not included in the present standard model formulation. Several specific searches for dark matter have been developed in recent years using for example mono-object (jet, photon, vector boson, top, etc.) signatures. These searches turn out to be competitive with the direct search experiments, and projections indicate that the high luminosity upgrade of the LHC can drive this search below the neutrino coherent scattering limit, which will be a concern for the direct experiments [23].

The approach of observing new physics through the study of rare decays will also benefits from the increased statistics. For example, the decay $B_s \to \mu^+\mu^-$ will become a precision measurement while the decay $B_d \to \mu^+\mu^-$ will be established and will be measured with reasonable accuracy, with a significance improved from 2.2 σ at 300 fb^{-1} to 6.8 σ at 3000 fb^{-1}.

The Higgs boson could be used as a search tool for dark matter at the LHC: if the dark matter particle is relatively light, the search for dark matter in the decay of Higgs particles, via the so called *invisible decay* channel will be important. Another channel proposed to search for dark matter is mono-Higgs

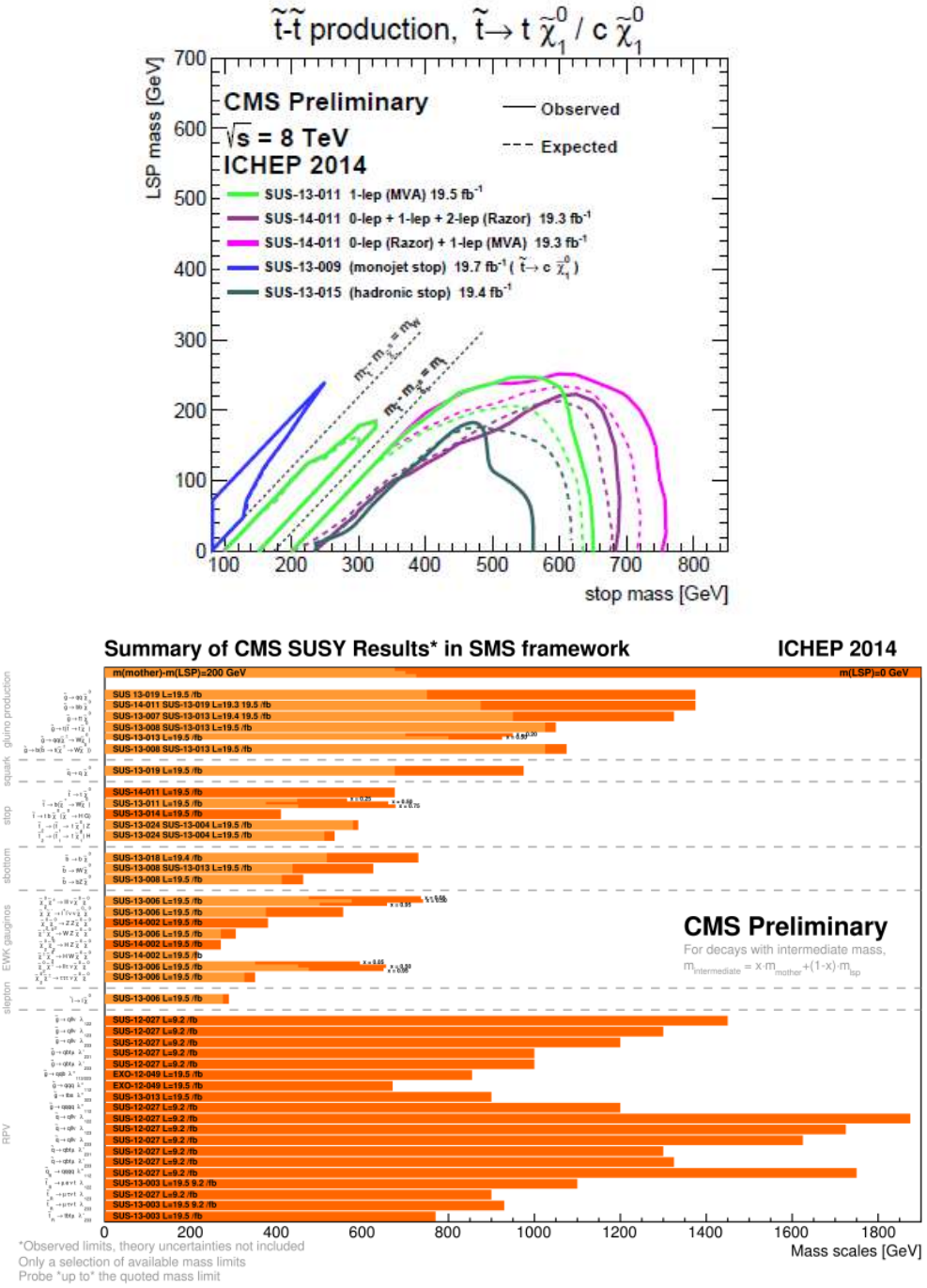

Figure 1.5: The top plot shows the mass limits for *stop*, the supersymmetric partner of the top quark. The bottom plot shows the SUSY mass limits from the full dataset of the 2011 and 2012 runs [6].

production [24].

In addition and in support of these discovery topics, many measurements of

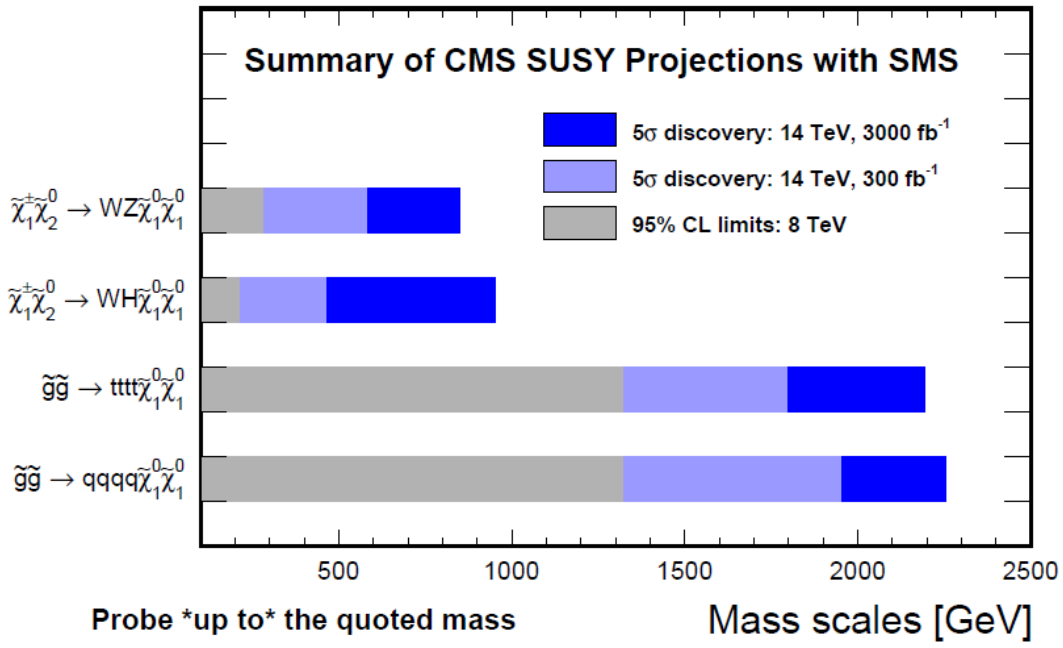

Figure 1.6: Mass reach of SUSY searches from selected 8 TeV results (masses excluded at 95% CL) and from projections for 14 TeV running at high luminosities (highest masses for 5σ observation). Simplified models are used for the interpretations in each case [6].

SM phenomena will be made also to help defining SM backgrounds that must be known and well-modeled to carry out the discovery portion of the program [6].

No evidence of new physics has been collected so far at the LHC, but the results obtained have deeply changed the landscape for these searches, as some theories and models have been largely eliminated and others have had their parameters sharply limited. The sensitivity of CMS for SUSY and many other new physics signals observation improves with increasing luminosity. Moreover, precision Higgs studies request higher luminosity.

For these reasons, the LHC machine group now has developed a plan to increase the peak luminosity and reach a higher integrated luminosity, well above those for which CMS was designed, that will be described in Section 1.2.

In order to deal with these new conditions and preserve the efficiency, resolution, and background rejection obtained so far, the CMS detector is going to take on a series of major upgrades [6], that will be discussed in detail in the rest of the chapter.

1.2 The next LHC phases

The Large Hadron Collider (LHC) is a two-ring superconducting proton accelerator and collider installed in the 27 km long tunnel, previously used by the LEP collider [8].

In the LHC collisions, a number of events per second equal to

$$R_{event} = L\sigma_{event} \tag{1.1}$$

are generated, where σ_{event} is the cross section for the event under study and L the machine luminosity. L depends only on the beam parameters and can be written as

$$L = \frac{N_b^2 n_b f_{rev} \gamma_r}{4\pi\epsilon_n \beta^*} F \tag{1.2}$$

where N_b is the number of particles per bunch, n_b the number of bunches per beam, f_{rev} the revolution frequency, γ_r the relativistic gamma factor, ϵ_n the normalized transverse beam emittance, β^* the beta function at the collision point[1] and F the geometric luminosity reduction factor due to the crossing angle at interaction point (IP)

$$F = 1/\sqrt{1 + \left(\frac{\theta_c \sigma_z}{2\sigma^*}\right)^2} \tag{1.3}$$

where θ_c is the full crossing angle at the IP, σ_z the RMS bunch length and σ^* the transverse RMS beam size at the IP [3].

LHC was designed to accelerate protons up to an energy of 7 TeV per beam and a luminosity of 10^{34} cm^{-2}s^{-1}: in order to reach these characteristics the beams of protons are inserted into the LHC ring after different acceleration stages in the LHC injection chain, that is shown in Fig.1.7.

Fig.1.8 displays a projection of the LHC performance through 2035: the LHC schedule foresees a series of long periods of data-taking, referred to as Run-I, Run-II, etc. interleaved with long shutdowns, called LS1, LS2, LS3, etc.

[1]The beta function in accelerator physics is a function related to the transverse size of the particle beam at the location s along the nominal beam direction: $\sigma(s) = \sqrt{\epsilon\beta(s)}$, where the beam is assumed to have a gaussian shape in the transverse direction, s is the location along the nominal beam trajectory, $\sigma(s)$ is the width of the gaussian and ϵ is the beam emittance [9]

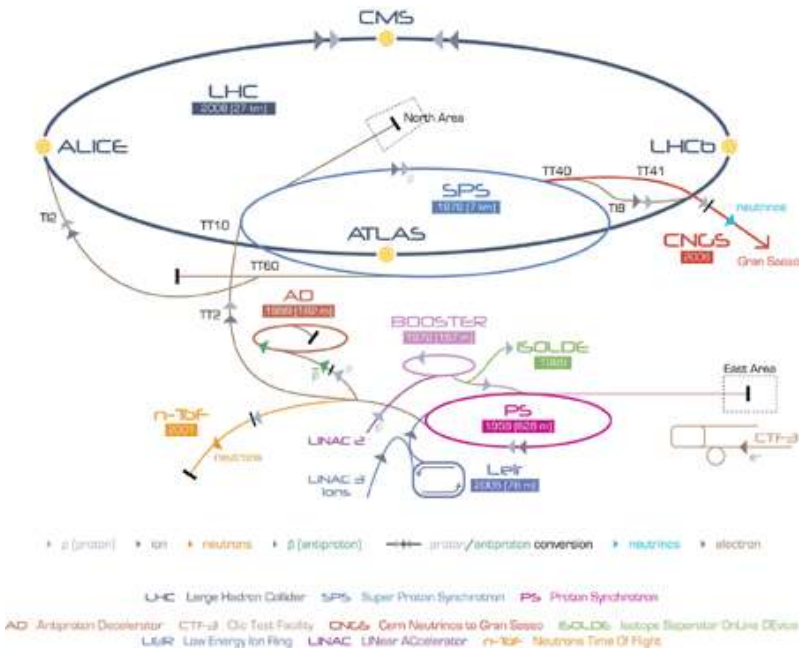

Figure 1.7: Layout of the LHC and its injectors chain.

Run-I for example is the name given to the data-taking period in 2011 and 2012. LS1, started in 2013 and ended at the beginning of 2015, allowed modifications to the LHC to enable it to run at the center-of-mass energy of 13 TeV and then to raise it closer to the design energy of 14 TeV over time. Run-II has begun in 2015, with the expectation of reducing the bunch spacing from 50 ns to 25 ns and reach the original performance goal for the LHC (instantaneous luminosity of 1×10^{34} cm^{-2}s^{-1} with 25 ns bunch spacing) soon after the startup. These are the operating conditions for which the CMS experiment was designed.

Before the LS2 planned for 2018-2019, a new scheme to form the bunch trains in the Proton Synchrotron (PS) will allow the luminosity to exceed the original design. A further improvement to the injection chain in LS2 will allow the delivery of very bright bunches, with the possibility to reach a peak luminosity of 2×10^{34} cm^{-2}s^{-1}. At this point, the LHC program foresees that the machine would deliver a total integrated luminosity of over 300 fb^{-1} by 2023.

The CMS detector will undergo a series of upgrades in the period from LS1 through LS2, called CMS Phase-I Upgrade and well described in [11] to maintain the good performance achieved in Run 1 also after these first LHC improvements.

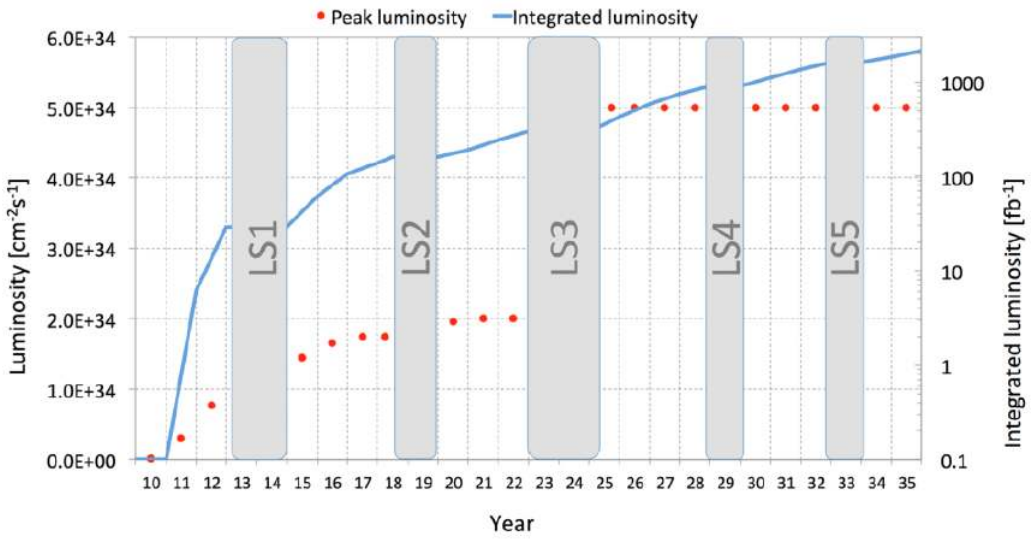

Figure 1.8: Projected LHC performance through 2035, showing preliminary dates for long shutdowns of LHC and projected luminosities [6].

The quadrupoles that focus the beams at the ATLAS and CMS collision regions are expected to be close to the end of their lives due to radiation damage by 2023, so there will be another long shutdown, LS3, to replace them with new low-β quadrupole triplets [10]. Moreover, crab cavities [10] will be added in order to optimize the bunch overlap at the interaction region. The result of these interventions will be a significant improvement of the LHC luminosity, up to a peak luminosity of 5-7 $\times$ 10^{34} cm^{-2}s^{-1} in 2025, with a planned delivery of 250 fb^{-1} of integrated luminosity per year for a further 10 years of operation, for a total of up to 3000 fb^{-1}. The high luminosity period that follows LS3 with the upgraded LHC is referred to here as High Luminosity-LHC (HL-LHC) or Phase-II [6].

1.2.1 Challenges in the next LHC phases

The upgrade of the LHC machine will pose great challenges to the experiments. The main ones will be the radiation damage to the detector from the high integrated luminosity of the HL-LHC and the very high *pileup* that comes from the high instantaneous luminosity [6].

Radiation damage The main source of radiation is from the particles produced in the proton-proton collisions. The charged particles, mainly pions, ionize in the detectors, but also undergo nuclear interactions, with the conse-

quent production of cascades of particles.

Photons, mainly produced from π^0 decays, interact in the material of the beam pipe or tracking systems and form e^+e^- pairs or reach the calorimeters where they produce electromagnetic cascades. Particles are also backscattered from the calorimeters or escape from cascades within them.

Neutrons may travel long distances, slowing down and scattering many times in the detector, producing also photons and electrons. This results in a mixed field of neutrons, photons, and electrons that have lost any correlation with the bunch structure of the original collisions and form a relatively uniform background in space and time within the detector volume.

Simulations with Monte Carlo transport codes MARS'109 [25] and FLUKA [26] are used to predict the magnitude and composition of radiation as a function of luminosity.

Fig.1.9 shows the absorbed dose after an integrated luminosity of 3000 fb^{-1} in different region of the CMS detector.

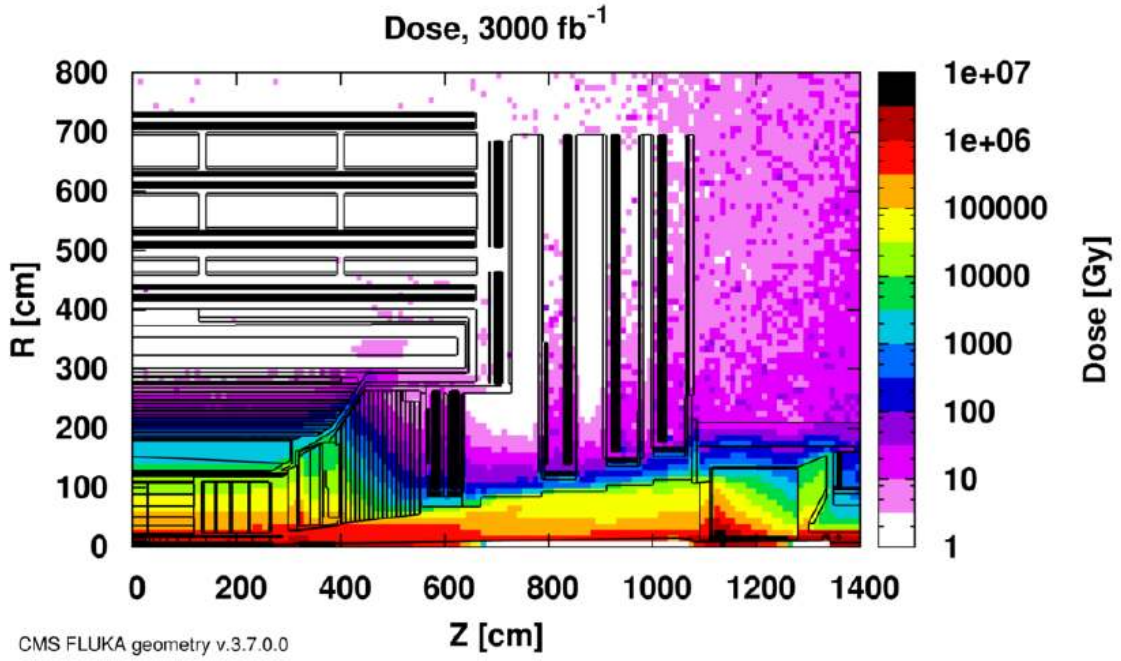

Figure 1.9: Absorbed dose in the CMS cavern after an integrated luminosity of 3000 fb^{-1}. R is the transverse distance from the beamline and Z is the distance along the beamline from the Interaction Point at Z=0 [6].

The damage produced in the detectors by this radiation varies from subdetector to subdetector. For example, in silicon detectors, radiation produces defects in the silicon lattice that change the bulk electrical properties of the

silicon, with consequent increase in the leakage currents and reduction in the Charge Collection Efficiency. For calorimeters, which in CMS are mainly scintillating $PbWO_4$ crystals or plastic scintillating tiles with wavelength-shifting fibers embedded in them, the main problem is the loss of transmission of the media through which the scintillation light must pass. This results in a reduction in the signal that can be quite large, in some cases more than 90% with a corresponding reduction in the resolution [6]. Moreover also the on-detector electronics could be damaged, generally through two fundamental mechanisms, the *lattice displacement* and the *ionization effects*. The lattice displacements, which could be induced by neutrons, heavy charge particles as well as high energetic photons, change the arrangement of the atoms in the crystal lattice, worsening the properties of the semiconductor junctions. Ionization effects instead, caused by charged particles, are usually transient, causing glitches, soft errors and sometimes also effects that can lead to the destruction of the device itself [13].

High pileup Each of the colliding beams at the LHC consists of many intense bunches of protons. Each bunch has a length with RMS of ∼5 cm, transverse dimensions of about 10 μm, and contains a few $\times 10^{11}$ protons. Bunches will be separated in time by 25 ns, corresponding to a spatial separation of approximately 750 cm. There are ∼2800 filled bunches in each beam and this number cannot be substantially increased. The collision of two bunches is called a *bunch crossing* or *BX* and these occur at a rate of 40 MHz. At the nominal luminosity of the HL-LHC, the average number of interactions in a single crossing will be approximately 140 [6].

Most of these interactions are *soft* collisions that do not contribute to the search for new physics. A relatively small fraction of all collisions are *hard* collisions that contain high transverse momentum particles that may come from new high mass objects. However, the presence of some tracks and energy from an average of 140 extra collisions can confuse or degrade the triggers and the offline reconstruction of the hard scattering.

The pileups are divided in three categories, depending on the time at which energy is deposited in the tracking detectors to form hits and in the calorimeters to form showers:

- In-time pileup (IT) refers to hits or energy deposits from the extra p-p collisions in the current bunch crossing, i.e. the collisions other than the

one containing the hard scattering of interest.

- Early Out-Of-time pileup, which refers to energy left in calorimeters from previous BXs in the crossing of interest
- Late Out-Of-time pileup, which refers to energy from later BXs that is integrated along with the trailing portion of the pulse from the BX of interest.

Luminosity increases at the LHC result in higher pileup. One of the main problems related to the increase in pileup is the mis measurement or misidentification of tracks due to the presence of many more hits in the tracking detectors. The other is the addition of extra energy to the calorimeter measurements, such as jet energies, associated with the collision that contained a hard scattering. Pileup confuses the trigger and also the offline reconstruction and interpretation of events. It also increases the amount of data that has to be read out in each BX that contains a hard scattering.

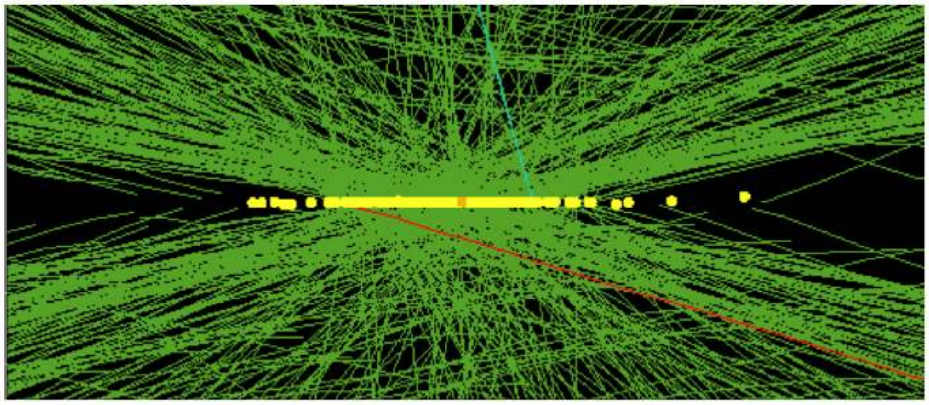

Figure 1.10: High pileup event with 78 reconstructed vertices took in 2012 [6].

In-time pileup can be observed in a single bunch-crossing by the many collision vertices that are reconstructed by the tracking system. For example Fig.1.10 shows the high-pileup crossing that was produced in a special data run in 2012, where there are 78 reconstructed vertices [6].

1.3 The CMS experiment and its upgrade

In order to better understand the CMS structure, first of all it is useful to introduce the coordinate system selected by the Collaboration. The CMS experiment opted for a coordinate system which has the origin centered at the

nominal collision point inside the experiment, the y-axis pointing vertically upward, and the x-axis pointing radially inward toward the center of the LHC. Thus, the z-axis points along the beam direction toward the Jura mountains from LHC Point 5. The azimuthal angle ϕ is measured from the x-axis in the x-y plane and the radial coordinate in this plane is denoted by r. The polar angle θ is measured from the z axis. Pseudorapidity is defined as $\eta = -\ln\tan(\theta/2)$. Thus, the momentum and energy transverse to the beam direction, denoted by p_T and E_T, respectively, are computed from the x and y components. The imbalance of energy measured in the transverse plane is denoted by E_T^{miss} [1].

The layout of the CMS experiment is shown in Fig.1.11. It is driven by the choice of the magnetic field configuration, as large bending power is needed to measure precisely the momentum of high-energy charged particles.

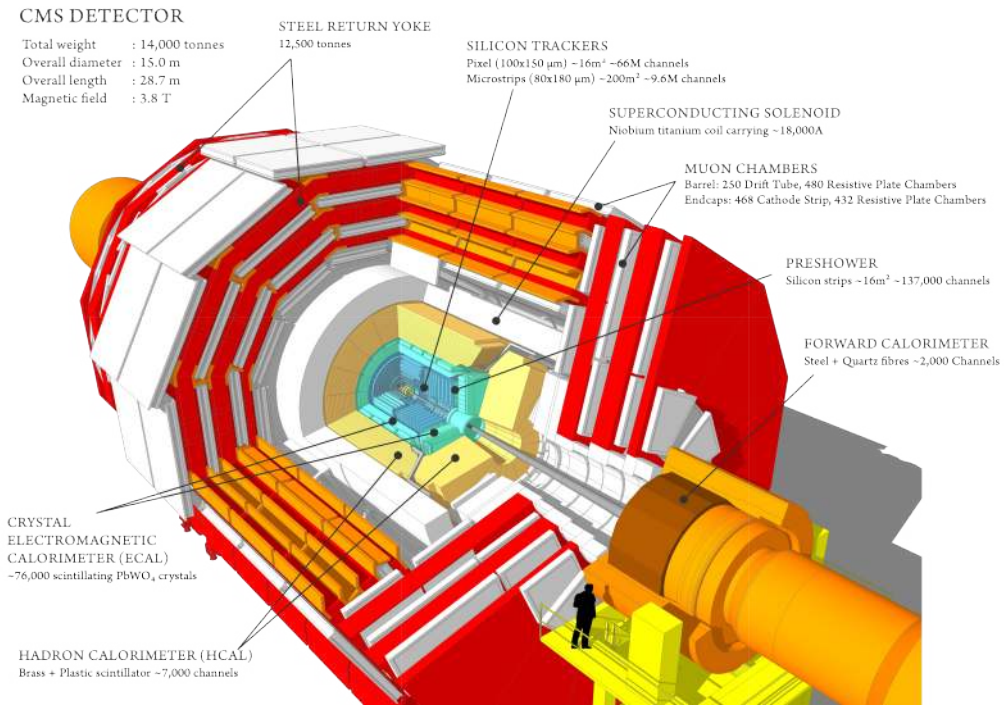

Figure 1.11: Layout of the CMS experiment with its subsystems.

The main element of the CMS experiment is indeed a 13-m-long, 6-m-inner-diameter, 4-T superconducting solenoid. The return field is large enough to saturate 1.5 m of iron, allowing 4 muon stations to be integrated to ensure robustness and full geometric coverage. The muon system, that will be described in more details in Section 1.3.1, is instrumented with gaseous detectors, in particular several layers of aluminium drift tubes (DT) in the barrel region and

cathode strip chambers (CSC) in the endcap region, complemented by resistive plate chambers (RPC).

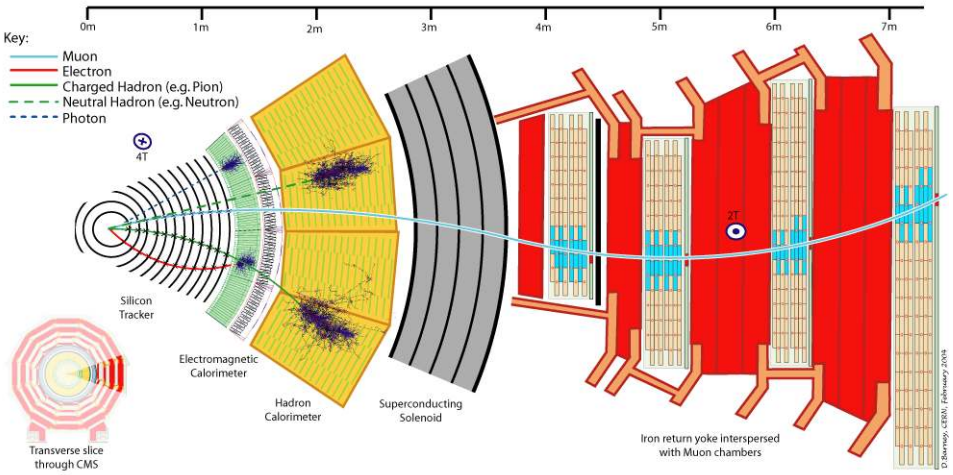

Figure 1.12: Transversal view of the CMS experiment: the interaction of the different kinds of particles with the subsytems is shown.

From Fig.1.12 which shows a slice of the CMS experiment, we can see that the core of the magnet coil is large enough to accommodate the inner tracker and the calorimetry. The tracking volume is given by a cylinder of 5.8-m length and 2.6-m diameter. The high track multiplicities is managed by 10 layers of silicon microstrip detectors, providing the required granularity and precision. The tracking system is completed by 3 layers of silicon pixel detectors, installed close to the interaction region to improve the measurement of the impact parameter, as well as the position of secondary vertices. Outside the tracker, the electromagnetic calorimeter (ECAL) is composed by lead tungstate ($PbWO_4$) crystals with coverage in pseudorapidity up to $\mid \eta \mid < 3.0$. The produced scintillation light is then detected by silicon avalanche photodiodes (APDs) in the barrel region and vacuum phototriodes (VPTs) in the endcap region. The π_0 rejection is performed by the preshower system, installed in front of the endcap ECAL. ECAL is surrounded by a brass/scintillator sampling hadron calorimeter (HCAL) with coverage up to $\mid \eta \mid < 3.0$. Wavelength-shifting (WLS) fibres embedded in the scintillator tiles convert the scintillation light that is then channeled to photodetectors via fibres. These photodetectors (hybrid photodiodes, or HPDs) can provide gain and operate in high axial magnetic fields. A tail-catcher completes the calorimetry system in the barrel region (HO) ensuring that hadronic showers are sampled with nearly 11 hadronic interaction

lengths. Coverage up to a pseudorapidity of 5.0 is provided by an iron/quartz-fibre calorimeter, whose Cerenkov light is detected by photomultipliers.

In total, the CMS detector is 21.6-m long and has a diameter of 14.6 m. It has a total weight of 12500 t.

1.3.1 The CMS muon system

The detection of muons is of fundamental importance to CMS. The muon system has 3 functions: muon identification, momentum measurement and triggering. Good muon momentum resolution and trigger capability are permitted by the high field produced by the solenoidal magnet and its flux-return yoke. The yoke also carries out the function of hadron absorber for the identification of muons. The CMS muon system is designed to have the capability of reconstructing the momentum and charge of muons over the the entire kinematic range of the LHC. In order to reach this aim, CMS uses 3 types of gaseous detectors for muon identification [1].

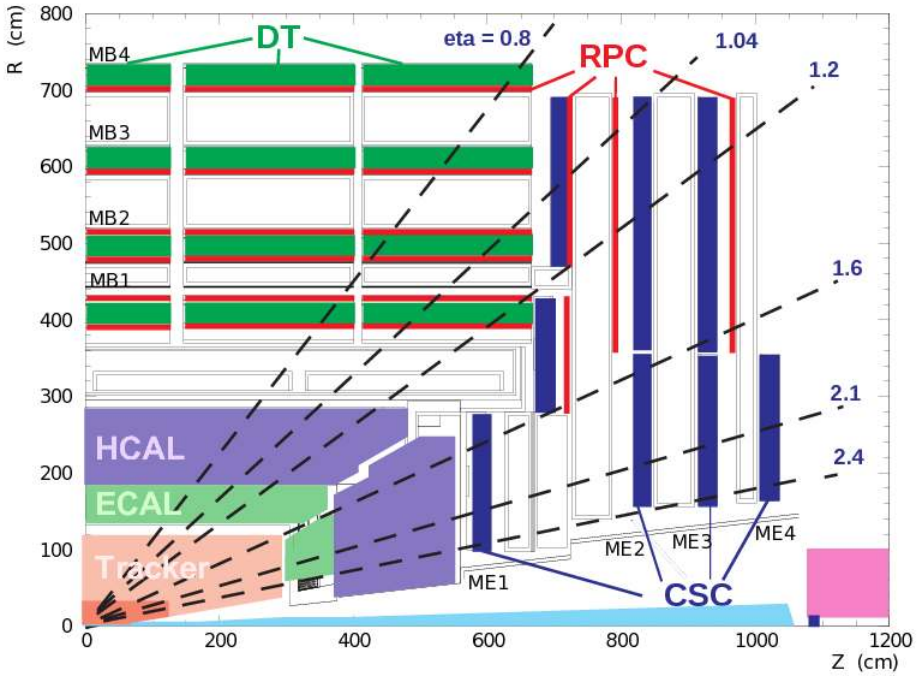

Figure 1.13: Transversal view of the CMS muon system as it was during LHC Run 1.

Due to the cylindrical shape of the CMS detector, the muon system can be divided into two regions, called *Barrel* and *Endcaps*. A transversal view of the muon system, as it was instrumented during the first LHC run, is shown in

Fig.1.13. The *Barrel* is the lateral surface of the cylinder and is instrumented with *Drift Tube* chambers; the *Endcaps* are the two bases of the cylinder and are filled with *Cathode Strip Chambers*. In both the regions, *Resistive Plate Chambers* complete the system.

Drift Tubes ·

The barrel region is characterized by a small neutron-induced background, a low muon rate, and a uniform 4-T magnetic field, mostly contained in the steel yoke. It is divided in 5 wheels, called YB0, YB±1, YB±2; each wheel contains twelve sectors, each covering an azimuthal region of 30 degrees. There are four layers of chambers (*stations*), named MB1-MB4 from the inner to the outer one, in every sector. Each station finally is made of one Drift Tubes (DT) chamber per sector.

Each chamber is composed by twelve layers of contiguous drift tube cells grouped in three superlayers (SL): the innermost and outermost SL, called SL1 and SL3 in Fig.1.14 top, measure the coordinate in the CMS bending plane (r, ϕ), while SL2 measures hit along the beam axis, in the (r, z) plane. The MB4 station, which is located outside the steel return yoke of the CMS magnet, only measures the hit position in the (r, ϕ) plane.

Fig.1.14 bottom gives a schematic representation of the single DT cell: the anode wires of two consecutive cells are separated by 4.2 cm, while the cells themselves are separated by 1 mm thick aluminum I-beams glued between 2.5 mm thick aluminum plates separating consecutive layers. The aluminum strips, called *electrodes* in the picture, are placed above and below the anode wire of the cell and are needed to shape the electric field lines, in order to guarantee a good linearity of the cell behavior over the entire drift volume. The gas mixture used is Ar/CO_2 85%/15%, which allows to reach a drift velocity of 54 μm/ns at the typical voltages applied [14].

Cathode Strip Chambers The two endcap regions of CMS are characterized by high muon rates and background levels; the magnetic field is large and non-uniform. Cathode Strip Chambers (CSC) are here installed, as, with their fast response time, fine segmentation, and radiation resistance, are able to identify muons between $0.9 < \mid \eta \mid < 2.4$. The original CMS plan foresaw 4 stations of CSCs in each endcap, with chambers positioned perpendicular to the beam line and installed between the flux return plates. In reality, only

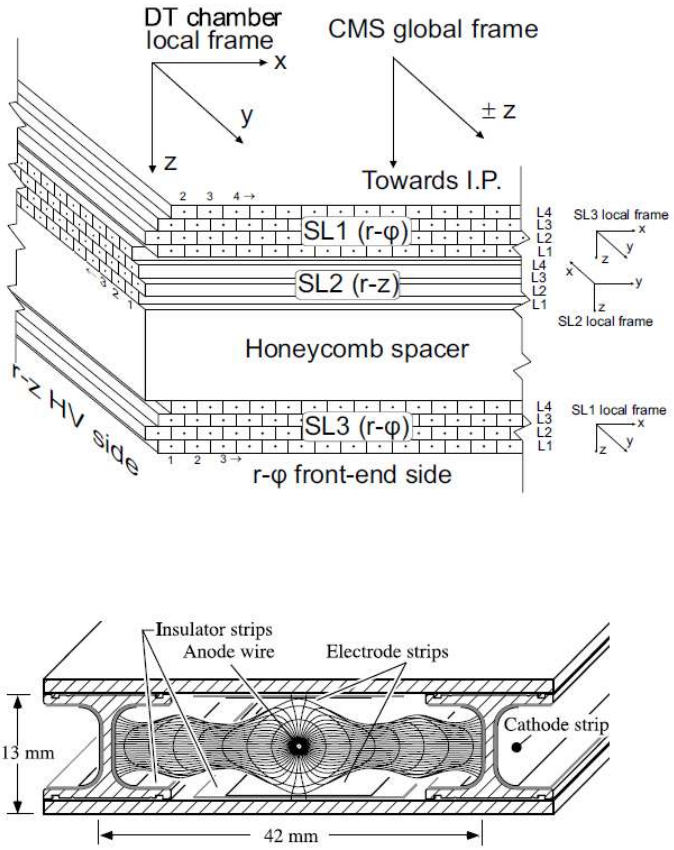

Figure 1.14: Top: schematic layout of a DT chamber. Bottom: layout of a DT cell.[14]

part of the 4th layer of CSC was built for Run 1, the rest of the station has been considered for the upgrade as it will be described in Section 1.4.

In total there are 468 CSC chambers, containing 6 detection layers each, composed of an anode wire plane streched between two planar copper cathodes, one continuous, the other segmented in strips to provide position measurement. While the wires are read out in groups, the strips are read individually and are staggered in alternating layers, except in ME±1/1, where they are cut along a line parallel to the short side of the chamber in order to reduce the rate on the single strip. The strips closer to the beam line constitute ME±1/1a, while the others ME±1/1b [15].

As shown in Fig.1.15 the cathode strips of each chamber run radially outward and provide a precision measurement in the (r,ϕ) bending plane. The anode wires run approximately perpendicular to the strips and are also read out in order to provide measurements of η and the beam-crossing time of a

muon. Each CSC layer provides pattern recognition for rejection of non-muon backgrounds and efficient matching of hits to those in other stations and to the CMS inner tracker.

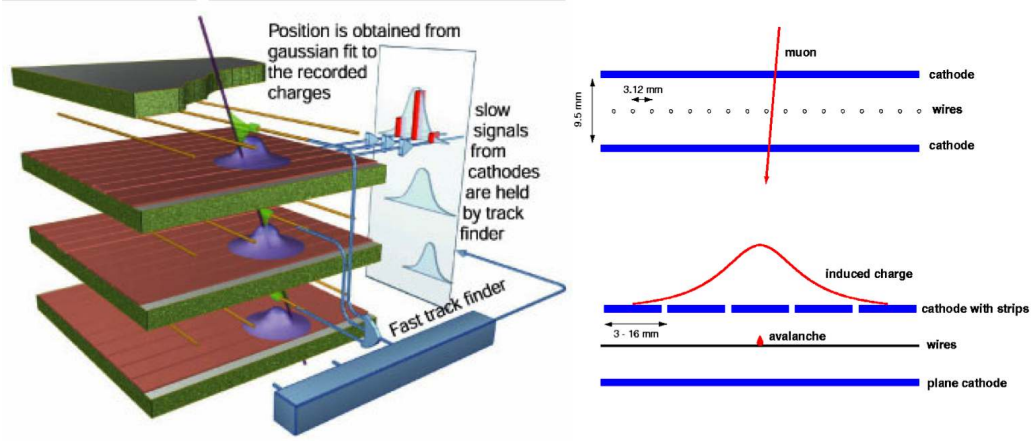

Figure 1.15: Layout of a CMS Cathode Strip Chamber.

A fundamental characteristic of the DT and CSC subsystems is that they can each trigger on the p_T of muons with good efficiency and high background rejection, independent from the rest of the detector [1].

Resistive Plate Chambers A dedicated trigger system consisting of resistive plate chambers (RPC) was added in both the barrel and endcap regions in order to deal with the uncertainty in the background rates and in the ability of the muon system to measure the correct beam-crossing time when the LHC reaches full luminosity. The RPCs provide a fast, independent, and highly-segmented trigger with a sharp p_T threshold over a large portion of the rapidity range ($\mid \eta \mid < 1.6$) of the muon system. The CMS RPCs are double-gap chambers (Fig.1.16 shows a sketch of a single-gap chamber), producing a fast response, with good time resolution but coarser position resolution than the DTs or CSCs.

A RPC consists of two parallel plates, made out of *bakelite*, or phenolic resin, with a bulk resistivity of 10^{10} - 10^{11} Ωcm, separated by a gas gap of a few millimeters. The whole structure is made gas tight. On the outer surfaces of the resistive material, conductive graphite layers are deposited to form the HV and ground electrodes. The read out is performed through aluminum strips separated from the graphite coating by an insulating PET film. While in the past RPCs were operated in streamer mode, i.e. the electric field inside

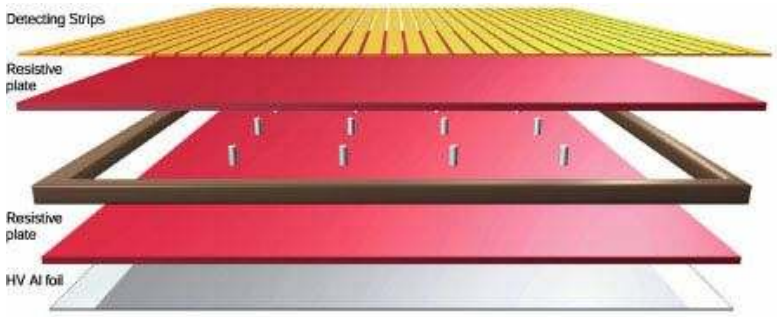

Figure 1.16: Layout of a CMS Resistive Plate Chamber.

the gap is so intense to generate limited discharges localized near the crossing point, CMS decided to operate the detector in avalanche mode. This allowed a significant improvement of the rate capability (from $\sim$ 100 Hz/cm^2 to $\sim$ 1 kHz/cm^2), as the reduction of the electric field applied involved a reduction of the charge produced in the gap, with a consequent decrease of the dead time. The related loss of signal amplitude was compensated by a greater gain at the level of the front end electronics [17].

In the barrel muon system, a total of 6 layers of RPCs are installed, two in each of the first two stations, and one in each of the last two stations. The redundancy in the first two muon stations allows the trigger algorithm to work even for low-p_T tracks that may stop before reaching the outer two stations. In the endcap region, there is a plane of RPCs in each of the first three stations in order to allow the trigger to use the coincidences between stations to reduce background, to improve the time resolution for bunch crossing identification, and to achieve a good p_T resolution [1].

Despite the original CMS plan of installing four endcap stations for both the CSC and the RPC systems, only three RPC stations were completed for the Run 1, due to insufficient funding availability [11]. Moreover, the installation of RPC detectors was not foreseen in the so-called *high-η region* ($\mid \eta \mid > 1.6$) due mainly to two problems: one one side, the RPC technology developed at the moment of the installation was not able to handle the high particle rates expected in those regions. On the other side, those regions are characterized by huge background, mainly composed by neutrons and photons, that was expected to deeply affect the performance of detectors installed there.

1.3.2 General upgrade project

The main goal of the whole upgrade of the CMS experiment is to maintain the excellent performance of the Phase-I detector under the new challenging conditions proposed by the LHC upgrades. As already outlined in Section 1.2, the CMS upgrade program is divided in two parts, called *Phase-I upgrade* and *Phase-II upgrade*. The so-called Phase-I upgrade is ongoing since the end of LHC Run 1 and will last till the end of LS2, including improvements for all the CMS subdetectors in order to deal with the luminosity growth up to 2×10^{34} cm^{-2}s^{-1}. The Phase-II upgrade instead foresees more deep interventions, aimed at preparing the CMS experiment at the operation at 5×10^{34} cm^{-2}s^{-1} up to 3000 fb^{-1}.

Tracker The Phase 1 upgrade of the tracker is focused on the replacement of the present pixel detector, planned for the end of year technical stop of 2016/2017. Due to data losses in the present readout chip, the actual pixel system will not be able to reach the necessary performance with luminosities up to 2×10^{34} cm^{-2} s^{-1} and PU up to 50.

For Phase II, the entire tracker will suffer important radiation damage by LS3 and must be completely replaced. The granularity of both the outer tracker and the pixel systems will be increased by roughly a factor 4, in order to maintain adequate track reconstruction performance at the much higher PU levels of the HL-LHC. A number of design improvements will lead to a much lighter Outer Tracker providing significantly improved p_T resolution and a lower rate of γ-conversions compared to the present detector. The module design will be capable of providing track-stub information to the L1 trigger at 40 MHz for tracks with $p_T \geq 2$ GeV, in order to ensure powerful background rejection at the earliest stage of the event selection. The pixel system will implement smaller pixels and thinner sensors for improved impact parameter resolution and better two-track separation. This will improve b-tagging as well as τ-hadronic decay and track reconstruction efficiencies within boosted jets. With up to 10 additional pixel disks in each of the forward regions the system coverage will be extended to close to $\mid \eta \mid = 4$, to better match the coverage range of the calorimetry [6].

Calorimeters The Phase-I upgrade foresees modifications of the hadronic calorimeter, in particular the HCAL Barrel (HB), the HCAL Endcap (HE)

and the HCAL Forward (HF). Concerning the HF, anomalous signals were identified since the beginning of the operation and reconnected to single muons or particle showers passing through the phototubes that collect the light from the quartz fibers. In order to reduce the rate of these signals, it was decided to exchange the phototubes installed with multi-anode tubes, with the related electronics [19]. For the HE and HB instead, the main problem is related to the operation of Hybrid Photodiode in magnetic field environment, whose main evident effect is the appearance of electrical discharges in the device when high voltage is applied. So far the effect was limited reducing significantly the voltage applied, but it remains however an important source of high-amplitude noise and a risk for the longevity of the HPDs themselves. For this reason the Collaboration decided to substitute them, together with their electronics, with Silicon Photomultiplier (SiPM) [19].

Concerning the Phase-II instead, both the electromagnetic and hadronic endcap calorimeters will suffer significant radiation damage by LS3, and so must be replaced. The replacement is called *High Granularity Calorimeter* (HGCal) and has electromagnetic and hadronic sections with excellent transverse and longitudinal segmentation. It will provide detailed three dimensional images of showers. The electromagnetic section consists of $\sim$30 tungsten and copper plates interleaved with silicon sensors as the active material. The sensors have pads of variable sizes of less than $\sim$1.0 cm^2. The electromagnetic section has 25 X_0 and one interaction length (λ). The hadronic part has a front section of 12 brass and copper plates interleaved with silicon sensors for a depth of 3.5λ. This covers the hadronic shower maximum measurement. It is followed by a *backing hadron calorimeter* of similar design to the current HE detector, brass plates interleaved with plastic scintillating tiles read out with a wavelength shifting fiber, to provide an overall depth of $\sim$10λ for the full calorimeter [6].

Beam radiation protection and luminosity measurement All the presently installed Phase-I beam monitoring devices which are located in high radiation environments, i.e. close to the beam pipe, will have to be replaced due to radiation damage, in order to ensure reliable luminosity and beam background monitoring for HL-LHC.

In particular, the protection systems will be upgraded with new polycrystalline diamond sensors. Moreover, the Machine Induced Background

(MIB) and Luminosity measuring systems in the Pixel volume must also be replaced [6].

Trigger The Phase-I Level-1 trigger upgrade foresees the improvement of the electronics for the calorimeter trigger, muon trigger and global trigger, in order to increase the flexibility of the system. It will be achieved using high bandwidth optical links for most of the data communication between trigger cards, and by using modern, large FPGAs and large memory resources for the trigger logic. The use of optical links allows the architecture to be readily changed, while large FPGAs allow algorithms to evolve as needed [20].

For Phase-II operation instead, the latency of the present L1 trigger, limited to 3.4 μs by the tracker readout, will be increased to 12.5 μs to provide sufficient time for the hardware track reconstruction and matching of tracks to muons and calorimeter information. This change will require upgrades of the readout electronics in some of the existing sub-detectors. Based on the expected performance of the trigger with track information, the proposed L1-trigger acceptance rate is 500 kHz for beam conditions yielding 140 PU. This will allow CMS to maintain thresholds comparable to those that will be used in a typical Phase-I trigger menu. To retain comparable performance in beam conditions that result in 200 PU, the L1 rate must increase to 750 kHz, and so all detectors will have readout capabilities compatible with this possibility. Studies are underway to optimize scenarios for the trigger menu and to determine if a higher acceptance rate would further improve the exploitation of the higher luminosity for key physics signals. Moreover specific sub-detector should be upgraded for CMS to meet these trigger requirements, in particular the front-end electronics of the barrel calorimeter, the Muon readout electronics in the CSCs of the inner rings in stations 2 to 4 and the DT readout [6].

Data acquisition and trigger control The Data Acquisition (DAQ) system will be upgraded to implement the increase of bandwidth and computing power that will be required to accommodate the larger event size and L1-trigger rate, and the greater complexity of the reconstruction at high PU. Assuming an online event selection of 1/100 event at the HLT, as is the case in the current system, the subsequent rate of recorded data will increase at PU of 140(200) to 5(7.5) kHz from LHC Run-I levels of roughly a few hundred Hz [6].

Software and computing The offline software and computing areas would be lacking by a factor of 4(12) of the resources needed for the challenging conditions expected in Phase-II at 140(200) pileup. A significant R&D program has started as part of the upgrade effort to improve the algorithms and approaches used for data reconstruction, analysis, storage and access, and to adapt the CMS software and computing model to new technologies and resources, in order to minimize the computing needs, both at the online and offline levels [6].

1.4 The muon system upgrade project

The main goal of the muon system in the next LHC phases is to preserve the present muon triggering and reconstruction capabilities. In order to reach these aims, it will be necessary to mitigate the efficiency loss due to the aging of the existing detectors and to improve the offline reconstruction resolution.

In HL-LHC moreover, a new *Track Trigger*, which would match candidate tracks with p_T in the inner tracker to muons at L1, will require ultra-high purity muon triggering with low thresholds for a very low fake rate.

A new muon tagger will be necessary, in order to increase the acceptance to new signals and reduce background from *lost leptons* from W, Z, top decays.

Benefits for these items would come from

- Keep high efficiency in the existing muon system
- Use a new trigger and readout electronics, in order to fulfill the bandwidth and latency requirements
- Add new detectors to preserve and improve muon identification in a high background environment and reduce the trigger rate in the forward region
- Use fast timing technologies [27]

1.4.1 Upgrade of the existing stations

The first phase of the muon system upgrade foresees an optimization and improvement of the detectors already installed, to be performed by LS2.

Cathode Strip Chambers For the CSC system, a key point has been the completion of the 4th layer performed during LS1. Together with the detector, also the associated readout electronics, triggering electronics and services have

been improved, in order to reduce the accidental trigger rate and to preserve a low p_T threshold for the Level 1 muon trigger at higher instantaneous luminosity. Another improvement comes for the upgrade of the first layer (ME1/1) electronics with a new CSC Digital Front End Board, that will allow every strip to be read independently. Last item, is the deployment of new muon trigger electronics to deliver the additional muon track segments, which will be produced at high luminosity and by the additional planes, to the upgraded CSC Trigger Track-Finder [11].

Drift Tubes In the DT electronics system the signal amplified and discriminated by the front end electronics is then digitized in the electronics contained in the so-called *minicrates*, in the detector wheels. The trigger and readout information here generated are then sent to the second level of the electronic chain, the Sector Collector (SC) [16]. During the first run, the SC boards were located in racks on the sides of the CMS detector inside the Underground Experimental Cavern (UXC), where they were exposed to radiation and high magnetic fields, and the cooling was marginal. In order to increase their reliability and improving their performance the Phase I DT upgrade was then focused in moving them to the Underground Control Room where the environment is more congenial [11].

The Phase II upgrade instead foresees the refurbishment of the minicrates, due to an unexpected high mortality of the electronics boards dedicated at the track reconstruction. This intervention will also allow the electronics to cope with the rate expected during the Phase-II.

Resistive Plate Chambers Considering the RPC system instead, during LS1 the fourth endcap station has been instrumented with chambers up to $| \eta | = 1.6$. This upgrade has been essentially driven by the impact of the instantaneous peak luminosity on the trigger system, as in the endcaps, the RPC system provides excellent timing with a worse momentum resolution compared to the CSC system. The muon trigger must achieve good enough resolution to identify high-p_T tracks, but the RPC trigger requires segments in at least three stations. The addition of the fourth layer was so necessary in order to achieve the requested redundancy to control the trigger rate at the increased luminosity while preserving high trigger efficiency. The difference in the RPC Level-1 Trigger performance is simulated between the Run 1 system with three

stations and the four station situation after the LS1 in Fig.1.17 [21].

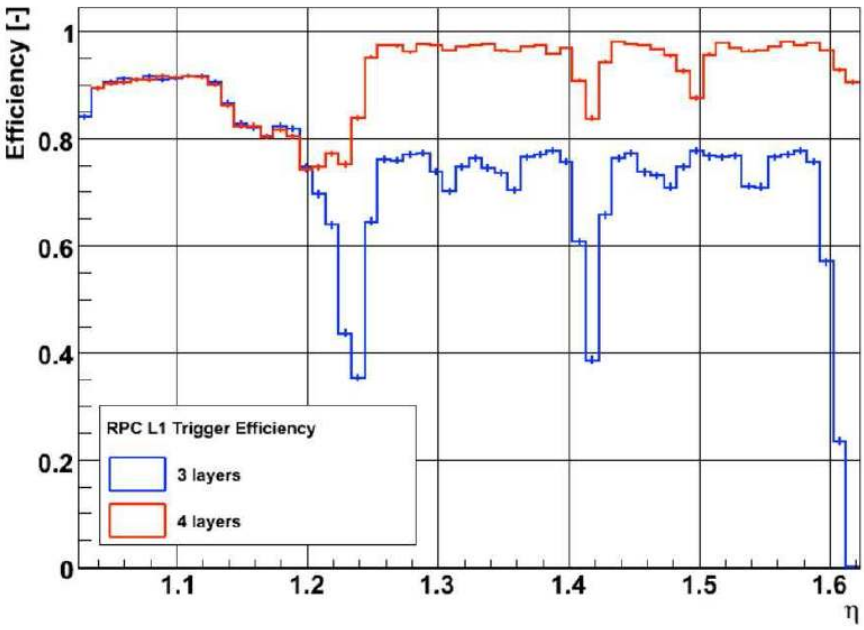

Figure 1.17: Simulated RPC Level-1 trigger efficiency for the Run 1 system with three endcap layers compared to the upgraded situation with four endcap layers [21].

The RPC upgrade foresees also the installation of new stations in the high-η regions RE3/1 and RE4/1, that will be discussed with more details in Section 1.4.2.4.

1.4.2 New stations in the forward muon region

The forward region of the muon system ($|\ \eta\ | > 1.6$) is a very challenging environment, due to the following reasons:

- *Redundancy*: in this region, where we get the highest rates of the entire system, we have also the fewer detector layers, compared for example to the barrel region. Many possible issues could require to restore the redundancy, for example the detector longevity. Indeed, the CSC system would accumulate a charge of the order of $\sim$ C/cm after many years of LHC operation, that could deeply affect their performance.
- *Rate*: it is increasing towards higher η. A worse momentum resolution would degrade the trigger performance in the forward region.

In order to deal with these challenges the CMS Collaboration has already approved the installation of a new station, called GE1/1, in the region shown

in Fig.1.18. The aim of this station, that will be installed in LS2, will be the improvement of trigger and reconstruction in the region $1.55 < | \eta | < 2.1$.

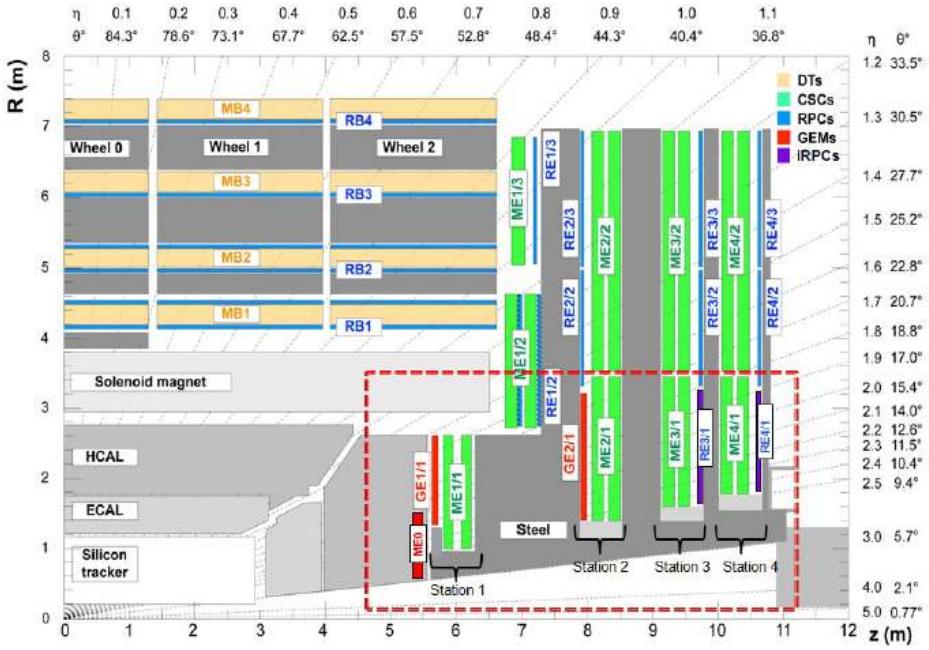

Figure 1.18: A quadrant of the muon system, showing DT chambers (yellow), RPC (light blue), and CSC (green). The locations of new forward muon detectors for phase-II are contained within the dashed box and indicated in red for GEM stations (ME0, GE1/1 and GE2/1) and dark blue for improved RPC stations (RE3/1 and RE4/1). [6].

Still under discussion is the possibility to install other two stations: the GE2/1 station would be inserted in the same η region of GE1/1 and with the same targets. The last one is the ME0 station, to be installed in the very forward η region up to ~ 3, to be used as a muon tagger and for muon trigger and reconstruction at highest η (see Fig.1.18) [27]. For all these three stations, the CMS Collaboration has selected or is considering to use Micropattern Gaseous Detectors (MPGD) [50, 52, 53], technology that will be described in Chapter 2.

Also for the high-η region of the 3rd and 4th station the Collaboration is evaluating the possibility to install new stations, in order to increase also here the redundancy and improve the neutron-induced background rejection. For these regions new generations of improved RPC detectors are considered and an important R&D is ongoing for their development.

1.4.2.1 GE1/1

The aim of the GE1/1 muon station is to improve the L1 muon trigger before the installation of a new silicon tracker and its associated track trigger [28] in LS3. The bending of muons within the CMS solenoid is largest at the position of the first muon station and is much less at the following muon stations because of the magnetic field lines, that bend around in the endcap flux return.

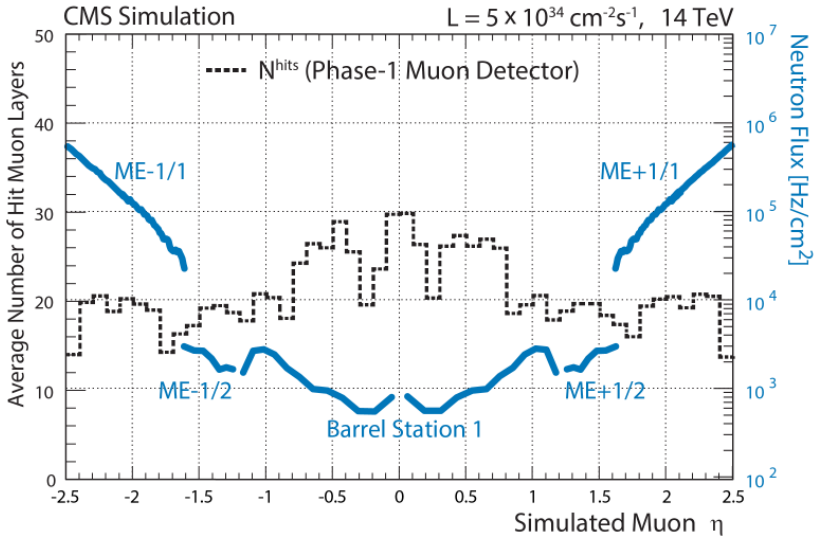

Figure 1.19: The dashed line shows the average number of muon layers with reconstructed hits for a simulated muon as a function of η. It is compared to the flux of neutrons in Hz/cm^2 shown as colored curves, which are the dominant cause of background hits, for the muon station first crossed by a muon with a given η. Forward region is exposed to the highest rates in the system, yet has the fewest muon layers needed for offline and trigger reconstruction and momentum measurement. Depending on the detector type the conversion factor can vary somewhat, but typically the hit rate is of the order of 0.2% of the neutron flux [29].

Despite being operated in the harshest environment, the forward part of the muon detector currently has the least redundancy in the entire muon system. Indeed, while in the range $|\eta| < 1.6$ muon hits are reconstructed by at least two muon detector systems (either DT+RPC, or CSC+RPC), the region of $|\eta| > 1.6$ relies on the CSC system alone. Fig.1.19 illustrates these observations by showing the average number of muon layers with hits for a typical muon as a function of muon η, superimposed with the flux of background particles.

The GE1/1 chambers together with the existing CSC station ME1/1 effectively multiply by a factor of 2.4 - 3.5 the path length traversed by muons

within the first muon station over that of the 6 layers of the ME1/1 CSC chambers alone: the challenge for triggering in the forward region, with $|\eta| > 1.6$ arises from decreasing capabilities to discriminate low momentum muons from the high momentum ones.

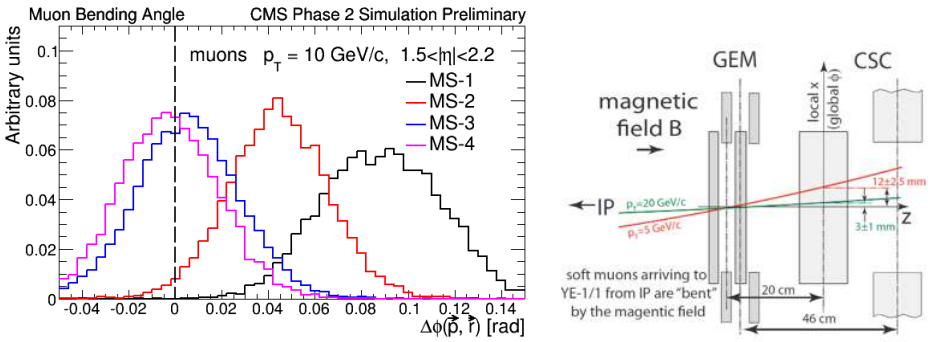

Figure 1.20: Left: Azimuthal bending angle of a simulated 10 GeV muon with respect to a normal vector to a CSC chamber, comparing the distributions for the four stations. Right: Sketch of a measurement of the bending angle with a pair of a CSC and a GEM chamber, illustrating discrimination between lower and higher momentum muons.

The trigger rate is indeed driven by muon momentum mis-measurements associated with the tails in the p_T resolution of the muon trigger. The CSC trigger measures muon p_T using the positions of stubs reconstructed in muon stations that the track crosses: if a soft muon undergoes a substantial scattering in the material of the absorber, it can sometimes be reconstructed as a high-p_T candidate. Of the four muon stations in the CSC system, the first one (ME1/1) is of special importance for triggering. Indeed, the main observable used by the CSC track finder for measuring the muon momentum, i.e. the muon track's lateral displacement (along the direction of a change of the azimuthal angle), is larger in the first station. As a result, presence of a reconstructed segment in the first station plays a key role in the precision of the CSC track finder momentum measurement. Inversely, any inefficiency in reconstructing segments in station ME1/1 reduces momentum resolution. The turning angle from the magnetic field also reaches the maximum in the first station ME1/1, as shown in Fig.1.20 (left). However, muon direction measurement cannot be utilized in the trigger because of low accuracy of a measurement within the ME1/1, limited by the thickness of the CSC chambers of only about 11 cm with a consequent too small lever arm. The achievable improvement in the trigger performance with the addition of GE1/1 is so significant. First, it cre-

ates a large enough lever arm between GE1/1 and ME1/1 chambers to enable a good measurement of the muon direction (the *bending angle*) within the first station, as illustrated in Fig.1.20 (right). Second, the added redundancy allows reducing the fraction of muons with unreconstructed segments in the first station, which in turn reduces the fraction of poorly measured muon candidates. The consequence is an improvement of the L1 stand-alone muon trigger momentum resolution and a drastically reduction of its large contribution to the overall L1 muon trigger rate. The single muon trigger rate curves before and after the GE1/1 upgrade for the region $1.6 < | \eta | < 2.2$ are shown in Fig.1.21. The L1 muon trigger thresholds can be maintained at low p_T values, so that the efficiency for capturing interesting physics processes featuring soft leptons can be kept high [29].

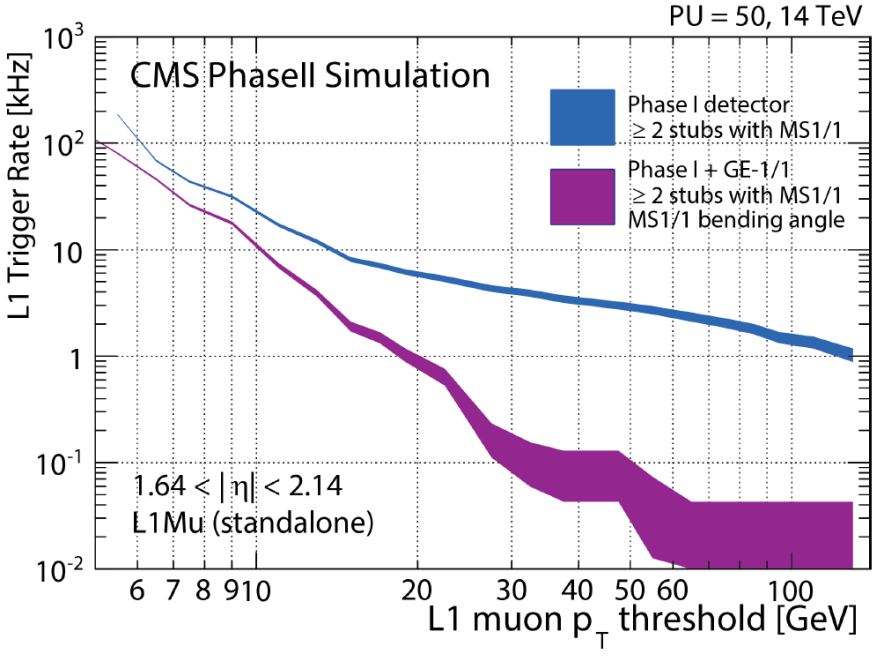

Figure 1.21: Level 1 muon trigger rates before and after the GE1/1 upgrade at a luminosity of 2×10^{34} cm^{-2} s^{-1}, for constant efficiency of 94%. MS1/1 denotes the first endcap muon station Level 1 trigger in both cases, i.e. with CSC-only or with the combination CSC and GEM trigger information. With the addition of GE1/1, the bending angle between the two stations can be used and the trigger rate is greatly reduced. [29].

Maintaining low muon trigger p_T thresholds is important for a broad spectrum of physics studies ranging from new physics searches to the measurements in the Higgs sector. For example studies of the Higgs coupling to the third generation leptons via $H \rightarrow \tau\tau$ and searches for extended Higgs sectors ap-

pearing in various new physics scenarios [30] and which could hold the key to the electroweak baryogenesis [31]. In addition to the inclusive muon trigger, all other trigger paths that rely on muon selections at L1 will benefit from lower thresholds.

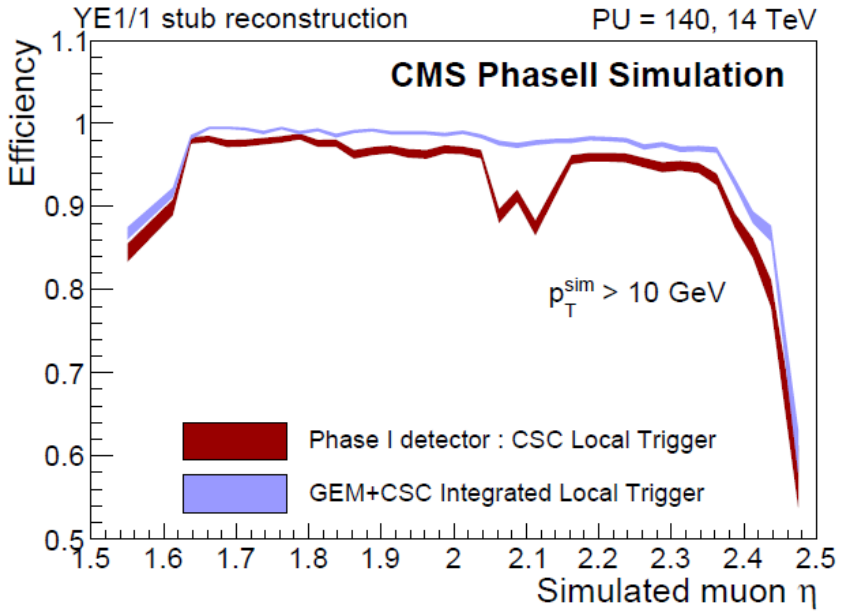

Figure 1.22: Muon track segment (LCT) reconstruction efficiency of the integrated GEM CSC trigger as a function of the simulated muon $|\eta|$, compared to the same for the Phase-I CSC-only algorithm. The upgrade allows for a large reduction in the number of muon candidates without a reconstructed segment in the first station, which have a reduced momentum resolution and make a disproportionally large contribution to the Level-1 trigger rate.

Another aspect to be considered is the efficiency to reconstruct a Muon Track Segment (LCT). In Fig.1.22 a comparison between the integrated CSC-GEM trigger and the reconstruction based on the CSC chamber data alone is shown. Additional redundancy provided by GE1/1 results in an increase in efficiency in the entire η range of the chamber. Moreover, a large drop in efficiency in the ME1/1a-ME1/1b transition region is recovered with help from GEM information.

In LS3 the new silicon tracker and the track trigger for CMS will be commissioned and will be used in coincidence with the L1 muon trigger to form a combined muon trigger, where the momentum resolution for most muons from the primary event vertex will be set by the very high resolution achieved by the track trigger. The aim of the GE1/1 and other planned new muon stations

will be therefore to maintain excellent position matching with the track trigger. The stand-alone muon trigger will run in parallel with the combined muon trigger, but at a higher p_T threshold, providing high efficiency for displaced muons and exotic particles as well as a backup for the combined muon trigger to maintain highest overall muon trigger efficiency.

In summary, the GE1/1 upgrade aims at the following improvements:

- Measuring the bending angle at trigger level through the combined CSC-GEM operation, thus strongly reducing the rate of mis-measured muons driving the trigger rate.
- Improving tracking performance in the high-rate environment.
- Establishing sufficient redundancy in the difficult region $1.6 < \mid \eta \mid < 2.2$, by adding detector planes using the space originally foreseen for RPC detectors [29].

1.4.2.2 GE2/1

The main targets of the GE2/1 station are:

- Sustaining triggering at current trigger thresholds
- Increasing offline muon identification coverage
- Maintaining existing envelope by mitigating aging effects

The installation of GE1/1 will not be sufficient to maintain a highly efficient and low rate general purpose muon trigger, with the foreseen increase in instantaneous luminosity in Phase-II. The GE2/1 station could be capable of producing a reduction of the rate using the bending angle together with ME2/1, in a way similar to what the GE1/1-ME1/1 pair does. However, due to to the lower muon bending in the second station and the lower resolution of ME2/1, the GE2/1 reduction will be two times smaller that the GE1/1 one. On the other hand, GE2/1 is extending triggering to the original CMS muon trigger envelope of 2.4-2.5, while GE1/1 only extends to η=2.15. Trigger rate in this region can be suppressed using bending angle measured between GE2/1 and ME2/1.

In addition to the expected increase in the trigger rate from higher frequency of collisions, there will be a degradation in stub reconstruction in stations 2, 3 and 4 that will increase the fraction of muon candidates with a low number of reconstructed stubs. The plots in Fig. 1.23 shows that at 140 PU, even for a perfectly working existing CSC system (red curves), the typical stub reconstruction efficiency drops below 90% with significant drops due to

the high-voltage spacers inside the CSCs. The consequence is an increase of the frequency of muon p_T mismeasurements, which augments the trigger rate and flattens the rate curve. Fig.1.23 shows also that the installation of stations GE2/1 (RE2/1) restores the local-reconstruction efficiency [6].

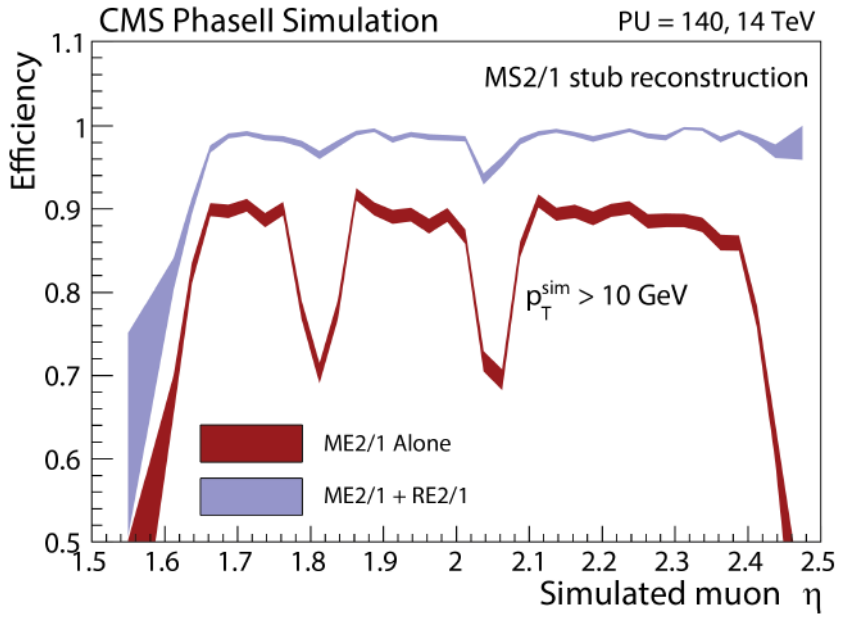

Figure 1.23: The local-trigger primitive (*stub*) reconstruction efficiency in station 2 as a function of eta for the present Phase-I detector (red curve) and with the addition of GE2/1 (blue curve) [6].

The stub alignment algorithm, which discriminates the prompt muons from the displaced muons, actually combines direction- with position-based measurements. In the endcap, the position based measurements suffer from the weaker magnetic field, with a particular deterioration in the region $1.6 < |\eta| < 2.4$. The direction-based measurement instead depends on the magnetic field and on the lever arm: in the low η region, the combination between position-based and direction-based measurement should be sufficient, but not in the higher η region. The GE1/1 and GE2/1 station could be useful as they can increase the lever arm and, using GEM and CSC measurement we could have, for a given station

$$\phi_{dir} = \phi_{GEM} - \arctan \frac{R_{CSC} \sin(\phi_{CSC} - \phi_{GEM})}{R_{GEM} - R_{CSC} \cos(\phi_{CSC} - \phi_{GEM})} \tag{1.4}$$

defining $X = \frac{\tan\theta}{R_{ME11}}$, where $\tan\theta$ and R_{ME11} are obtained from the full muon trajectory to ensure high precision

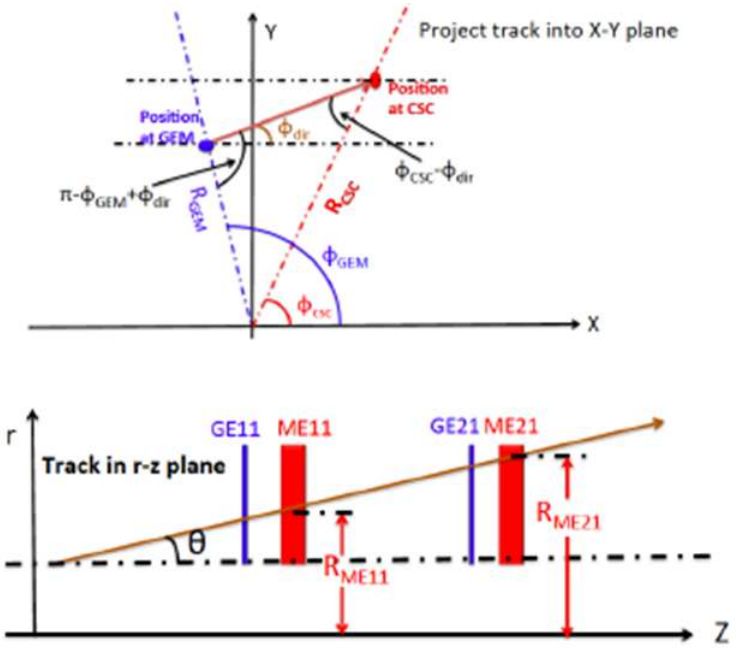

Figure 1.24: Geometry of the stub alignment algorithm in the endcap [33].

$$\phi_{dir}^{st1} = \phi_{GE11} - \arctan \frac{\sin(\phi_{ME11} - \phi_{GE11})}{1 - \cos(\phi_{ME11} - \phi_{GE11}) - D_{GE11,ME11}X} \tag{1.5}$$

$$\phi_{dir}^{st2} = \phi_{GE21} - \arctan \frac{\sin(\phi_{ME21} - \phi_{GE21})}{1 - \cos(\phi_{ME21} - \phi_{GE21}) - \frac{D_{GE21,ME21}X}{D_{ME11,ME21}X+1}} \tag{1.6}$$

and so

$$p_T^{L1} \propto \frac{1}{\phi_{dir}^{st1} - \phi_{dir}^{st2}} \tag{1.7}$$

allowing the identification of both prompt and displaced muons, which are interesting for many physics channels, in particular for some searches of new physics, usually signature driven [33]. For example several models of physics beyond the SM predict neutral particles that decay into final states consisting of collimated jets of light leptons and hadrons (LJ) [34], like those shown in Fig.1.25. These particles which can also be long-lived, will have a strong displaced lepton signature.

In CMS, the excellent momentum resolution of muons is mainly the result

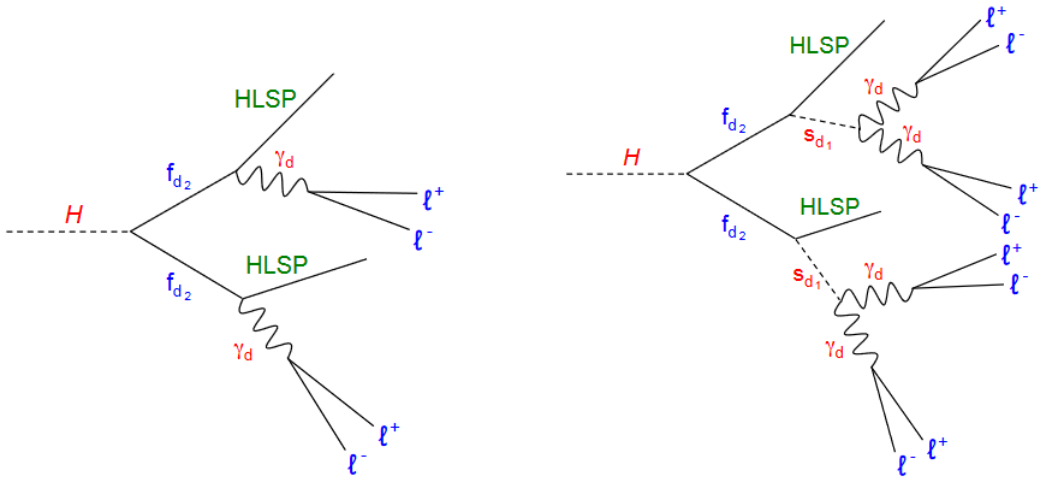

Figure 1.25: Diagram of the two LJ models considered in the analysis [34].

of the precise resolution of the tracker system. For high-momentum muons, though, the muon system contributes substantially to the overall momentum measurement [32], since curvature resolution scales as the square of the lever arm and the muon system provides a much larger lever arm than the tracker alone. As already introduced, there is a poorer resolution in the forward region compared to the barrel, caused by magnetic field inhomogeneity, by showering effects at high momenta and by the lower number of measured points with respect to the rest of the CMS muon system. Additional detectors in the muon system, with good spatial resolution, will improve the limited p_T resolution in the endcap region and provide higher efficiency in a high-background environment. The spatial resolution lower limit, set by the multiple scattering experienced by muons in traversing the CMS material, has been estimated from simulation, assuming the current geometry scenario. The results are displayed in Fig. 1.26, which shows the RMS displacements caused by multiple scattering as a function of p_T in the different endcap stations at a fixed η and ϕ ((| η |, ϕ) = (2.0, 0.0)). The RMS displacement for p_T = 200 GeV is about 500 μm at the surface of GE1/1, about 1 mm at GE2/1, and reaches 3-4 mm at the fourth station (RE4/1) [6].

1.4.2.3 ME0

A new muon detector, ME0, should be located in a space that will become available when the endcap calorimetry will be replaced in LS3, covering the range 2.0 < | η | < 2.8. ME0 chambers should consist of a six-layers detector

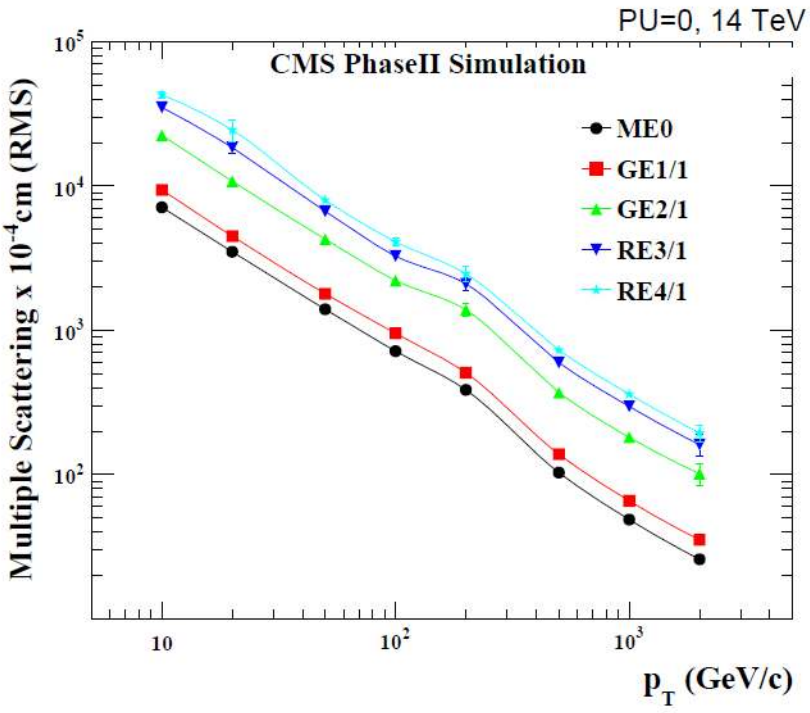

Figure 1.26: The RMS of the multiple scattering displacement as a function of muon p_T for the different forward muon stations. All of the electromagnetic processes such as bremsstrahlung and magnetic field effect are included in the simulation.

and would built segments by fitting groups of three or more hits falling in box of $\Delta\eta \times \Delta\phi = 0.02 \times 0.05$ rad.

The strongest motivation for the insertion of the ME0 station is the increase in the CMS acceptance for physics with muons. In particular this short section of muon detector ($\sim$ 40 cm) could increase the muon acceptance by 10-20%. Two physics cases are generally considered relevant and analyzed in order to understand the improvements obtained: $H \to ZZ^* \to 4\mu$ and $\tau \to 3\mu$.

Starting from $H \to ZZ^* \to 4\mu$, already in 2013 a first study of the sensitivity of the CMS upgraded detector to this channel was performed [35]. The analysis aimed at underlining the improvement of performance that could be achieved with an increase of the detector acceptance, so for this reason two scenario were considered: the first one with upgraded tracker and forward electromagnetic calorimeters but actually the same angular acceptance of Run 1 (called *Conf-3* in the plots), while the second one (called *Conf-4*) with tracking, calorimeters and muon system all increased in acceptance up to $\mid \eta \mid = 4.0$.

First of all, as evident from Fig.1.27, with the extended acceptance con-

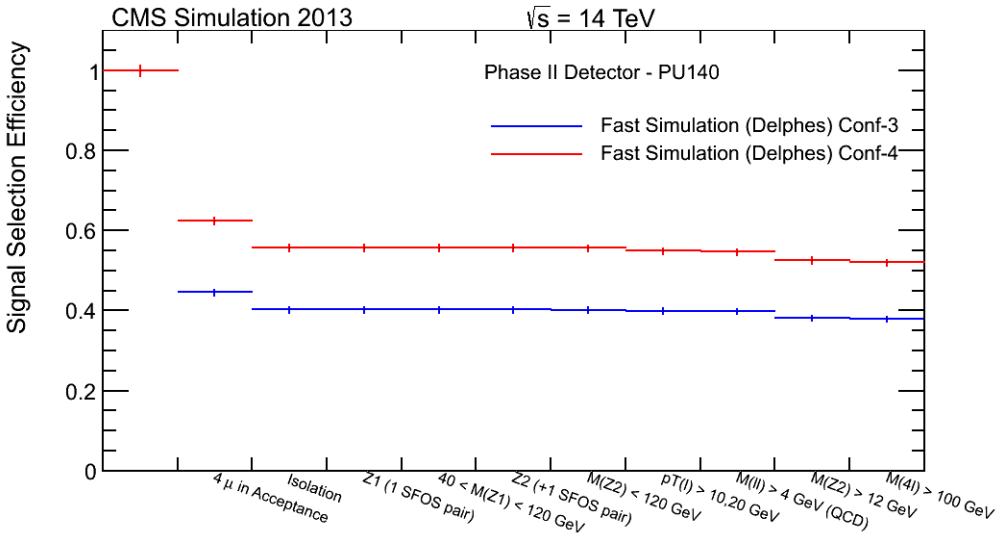

Figure 1.27: Cut flow table for the full analysis chain for the signal sample $H \to ZZ^* \to 4\mu$, for the configuration 3 detector in blue and the configuration 4 in red [35].

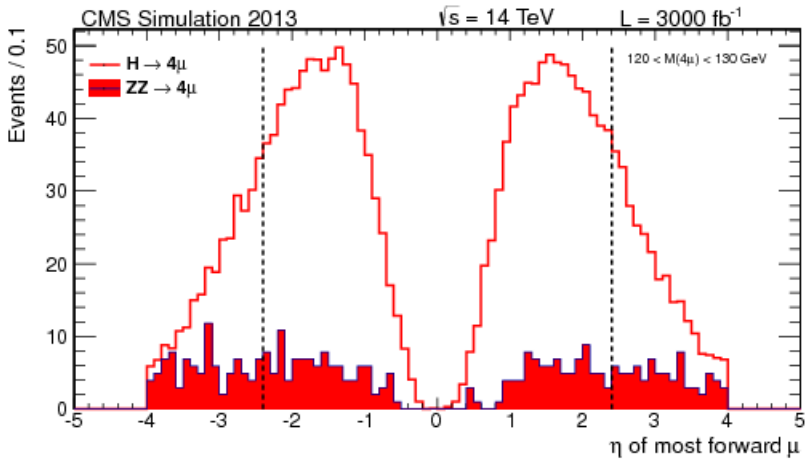

Figure 1.28: η distributions of the most forward among the four μ, after event selection with the configuration 4 detector, for signal $H \to ZZ^* \to 4\mu$ events (empty red) and for irreducible background $ZZ \to 4\mu$ (solid red) The dashed line correspond to the acceptance of the configuration 3 detector [35].

figuration there is a significant improvement in the event selection efficiency with respect to the configuration 3, that has an efficiency similar to the one obtained in Run 1. In Fig.1.28 is clear that a relevant part of the most forward muons in the decay fall in an η region outside the Run 1 acceptance, indicated by the dashed line.

The consequence of the extension of the acceptance is a larger number of

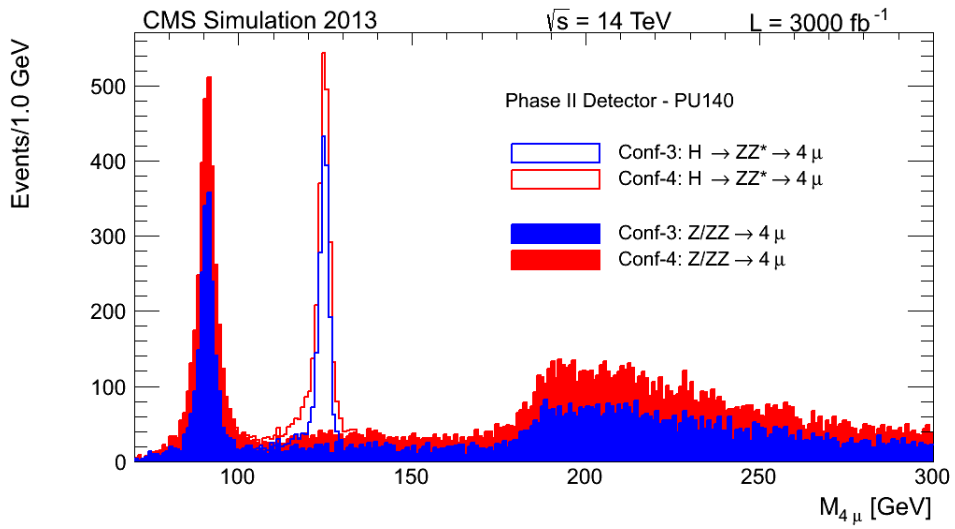

Figure 1.29: Four muons mass distribution obtained with 3000 fb^{-1} for the signal sample, $H \to ZZ^* \to 4\mu$ (solid lines), and for the irreducible background $ZZ \to 4\mu$ (filled histogram)[35].

events expected for the same luminosity, as shown in Fig.1.29.

More recent studies, focused on the ME0 acceptance region considered right now, showed that up to 15% of signal muons is in the ME0 acceptance, in particular up to 8% in the region $2.4 < \mid \eta \mid < 2.8$. Moreover the signal muons are characterized by a soft p_T spectrum, so that it is challenging to separate the signal from pileup without loosing efficiency on signal.

Moving to the second process considered, the $\tau \to 3\mu$ decay, in the SM it has a too small branching ratio (BR = 10^{-40}) to be considered interesting, but becomes accessible to some EXO models, with BR up to 10^{-9}. The more recent results on this decay come from the Belle and LHCb Collaborations, which actually set a limit of 2.1×10^{-8} [36] and 4.6×10^{-8} [37] respectively. This decay is characterized by three muons coming from the same vertex, quite collimated and one of them is very soft, but must be identified very tightly, requiring the selection to be more efficienct in signal event and more background-discriminant. Moreover, most of the produced τ that should be considered for the analysis are produced in the very forward region: recent studies performed show that increasing the muon detection up to $\eta \sim 3$ would make the signal acceptance gain a factor 2.9.

Another important aspect on which the ME0 contribution could be fundamental is pileup and neutron background rejection. Backgrounds from neutrons can be efficiently eliminated requiring hits in a minimum of three layers

to define a segment. ME0 Muon objects are formed by matching TrackerTracks to ME0 segments in local x and y position, as well as in global direction in the bending plane, ϕ: we have a Tight ME0 Muon if a charged track matches a muon segment within $\Delta\phi = 0.15$ rad. If a charged track matches within $\Delta\phi = 0.5$ rad, then we have a Loose ME0 Muon.

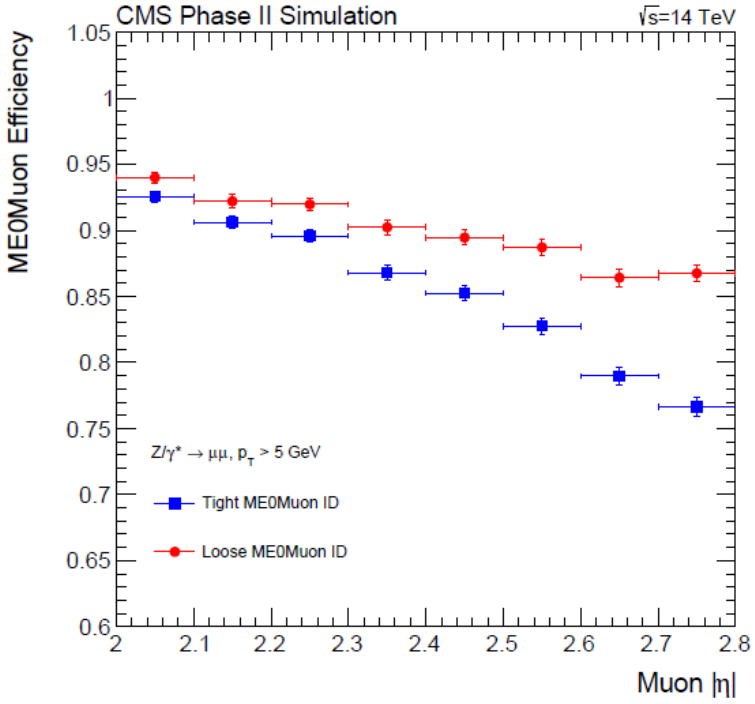

Figure 1.30: Efficiency for ME0 muons as a function of $|\eta|$ [6]

The reconstruction efficiency of ME0 Muons is shown as a function of $|\eta|$ in Fig.1.30. The new ME0 detector will provide efficient muon identification with reasonably low backgrounds, adding an additional measurement for muons up to $|\eta| < 2.4$ and will extend the CMS muon coverage up to $|\eta| = 2.8$ [6].

In the Fig.1.30, the ME0Muon efficiency is decreasing with increasing η. Indeed ME0 segments were reconstructed from rechits spatially close by, but clearly separated in time. Close Out-Of-Time PU hits were clustered into the signal segment, leading to a wrong time estimation of the signal muon and potentially also altering the direction of the segment. This also lead to ME0 segments being matched to a lower p_T track, which turns into an inefficiency. Introducing a window for time clustering, which for fast detectors can be very tight, removes this effect. In Fig.1.31 we can observe the difference between the efficiency without the time window, as shown in the Technical Proposal

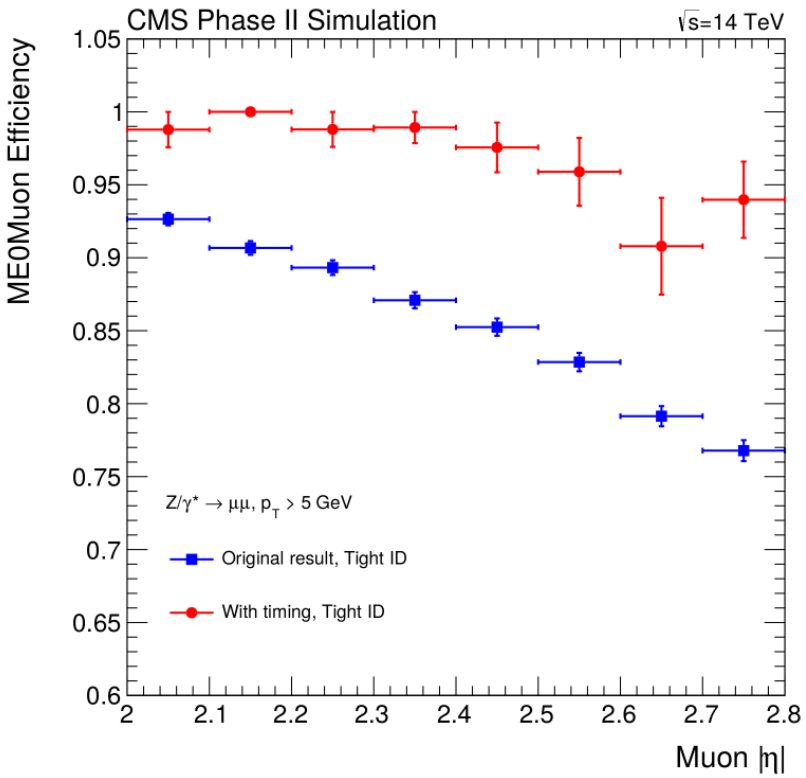

Figure 1.31: Tight ME0Muon Efficiency as reported in the Technical Proposal (blue), where no use was made of the ME0 RecHit time, and the ME0 RecHit time, and the improved efficiency when ME0rechits are clustered in a time interval of 1.5ns (red), for a detector time resolution of 100 ps.

[6], and the efficiency as obtained by time clustering in a 1.5 ns window, for a detector with a time resolution of 100 ps.

Two studies have been performed in order to understand the role of timing information for the ME0 station in pileup rejection, considering:

- the Out Of Time (OOT) pileup, due to events coming from BX preceding or following the one we are considering (the ME0 station is able to see (-5, +3) BX around the BX=0). In these OOT events there can be slower or faster tracks that can be erroneously included in the BX=0.
- the In Time (IT) pileup, due to events coming from the BX=0, as the signal.

Starting from the OOT, in order to study the improvement by using the detectors with high time resolution, different samples (Drell-Yan (DY) $\rightarrow \mu\mu$) with detector time resolution = 100 ps, 1 ns, 5 ns, 7.5 ns, 10 ns, 15 ns and 25 ns were produced with 140 pile-up.

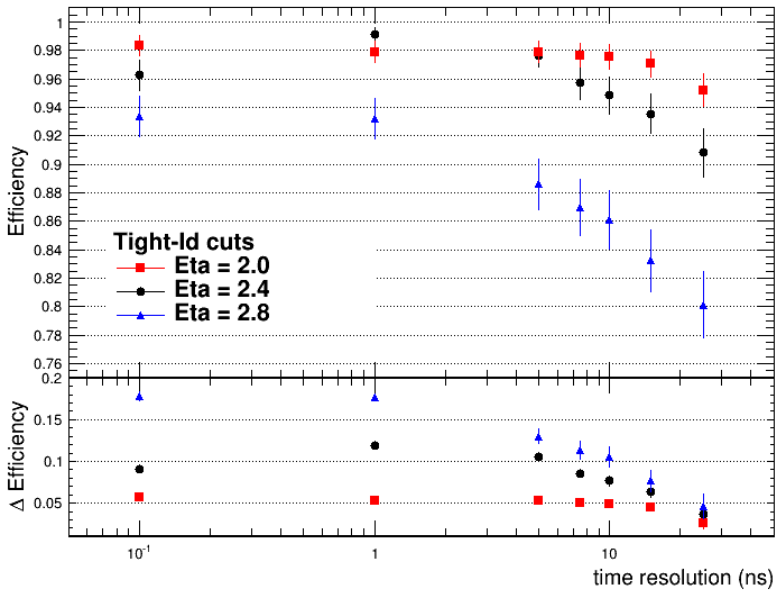

Figure 1.32: Tight ME0Muon efficiencies with respect to the different time resolutions measured in the lower (red squares), middle (black dots) and high (blue triangles) η points for ME0 using DY sample with PU = 140 for tight-Id cuts. The lower plot is for the difference in efficiencies calculated with respect to a standard sample without any time resolution.

Fig.1.32 shows the contribution of the detector time resolution to the muon efficiency for Tight ME0 muons at different values of η. For lower η values the contribution of the time resolution does not seem to be relevant, at least for time resolutions lower than ~ 12 ns. With increasing η, the contribution of the detector time resolution is more relevant. Similar results have been obtained also for Loose ME0 muons.

The same study has been performed, in Fig.1.33, in presence of neutrons background: looking at the $\eta = 2.8$ data, the most affected one, it seems that a detector with a time resolution of the order of 1 ns or below, would be useful to reject the neutron background and keep high the efficiency for Tight ME0 muons.

To summarize, the OOT and the neutron background produce hits that could be associated per error to a real signal segment, changing its real direction. The result is that it is not possible anymore to make the matching between the ME0Segment and the TrackerTrack, the ME0Muons is not reconstructed and the ME0Muon efficiency results to be lower. In this study a time window has been introduced in order to clusterize the segment's hits: if t is the hit time, t is accepted only if falls in the window $[< t > -3\sigma_t - 0.8, < t >$

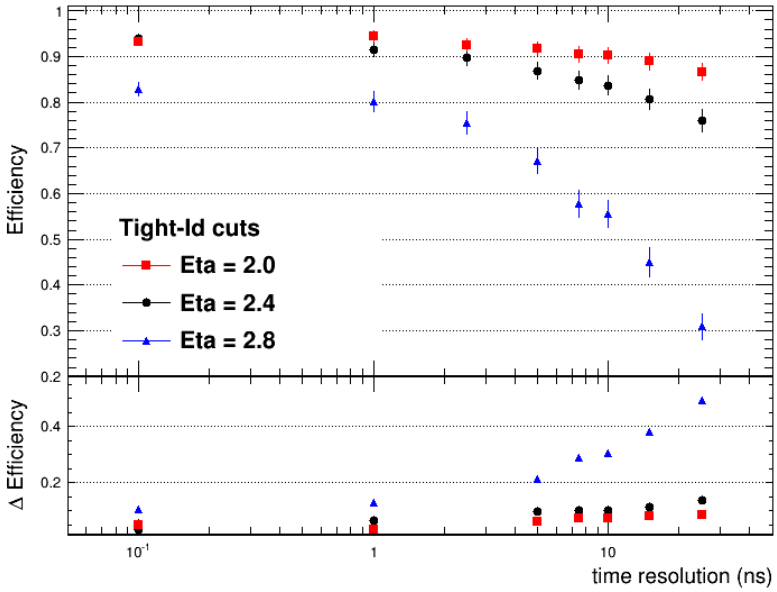

Figure 1.33: Tight ME0Muon efficiencies in presence of neutron background with respect to the different time resolutions measured in the lower (red squares), middle (black dots) and high (blue triangles) η points for ME0 using DY sample with PU = 140 for tight-Id cuts. The lower plot is for the difference in efficiencies calculated with respect to a standard sample without neutron background.

$+3\sigma_t+0.8]$, otherwise it doesn't contribute to the segment reconstruction. The time window, which depends from the time resolution of the detector, allows to eliminate the OOT from the segment, the direction reconstruction is more precise and as a consequence also the matching ME0Segment-TrackerTrack and the efficiency increases. In order to do this, a detector time resolution of 1 ns is enough, because the OOT hits are slower with respect to the signal hits.

The second study instead is focused on the elimination of the IT pileup component, which is much faster and in time with the signal. This kind of pileup creates real tracks, not spurious hits as the OOT, which can be confused with the signal tracks. The study considers a real track signal, always coming from the $H \rightarrow ZZ^* \rightarrow 4\mu$ decay, for example the one with higher p_T and computes the difference between the time of arrival of the track itself, taken as a reference, and other signal tracks or IT pileup muons.

From Fig.1.34, it is clear that, in order to have a net separation between the two distributions, a time resolution lower that 100 ps is needed. We could then affirm that the timing information could be used also to provide an extra cut on the analysis, alternative to the p_T: its efficiency, shown in Fig.1.35, computed

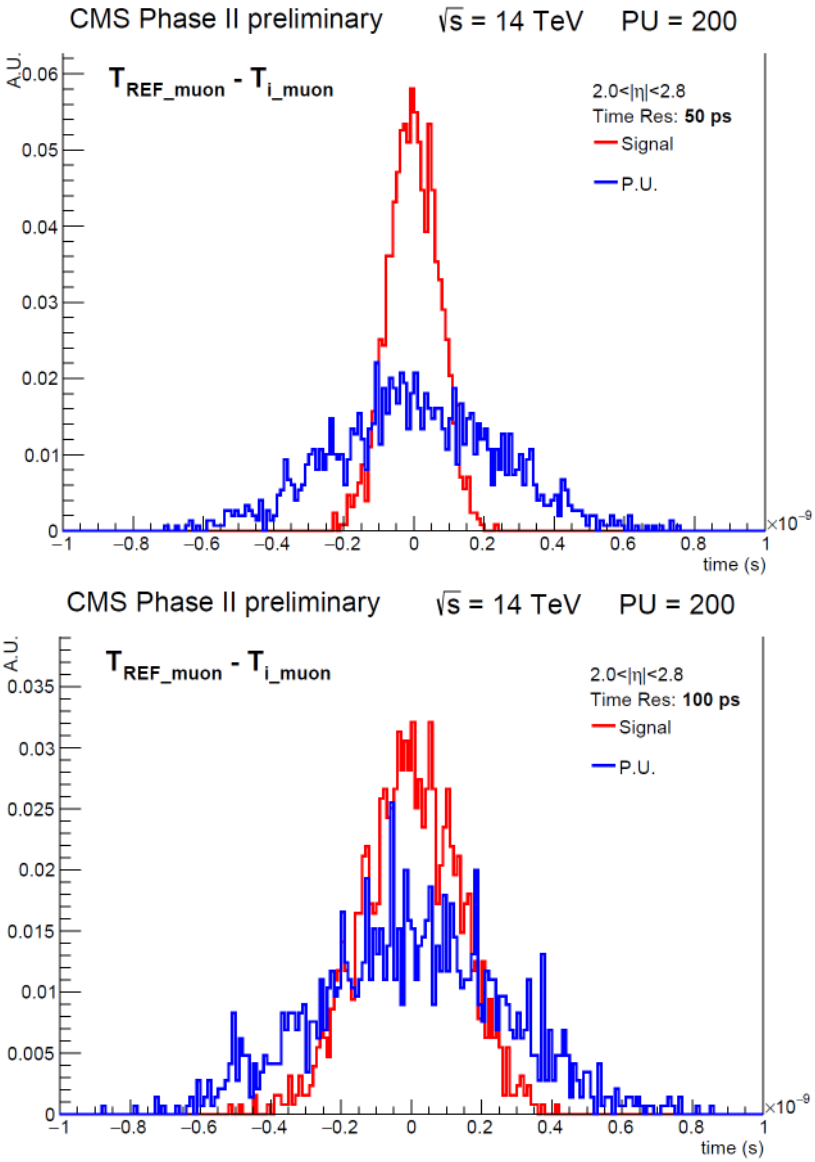

Figure 1.34: Time distribution of signal (in red) and IT pileup (in blue) with detector time resolution of 50 ps (left) and 100 ps (right).

as the number of PU events not rejected with a particular cut, i.e. $S/\sqrt{B}$ with respect to the time resolution, has an exponential shape, decreasing with the worsening of the time resolution of the detector.

These motivations are at the basis of the R&D program that is ongoing on the so-called *Fast Timing Micropattern* detector, the technology *optional solution* for the ME0 station that will be described in detail in Chapter 5.

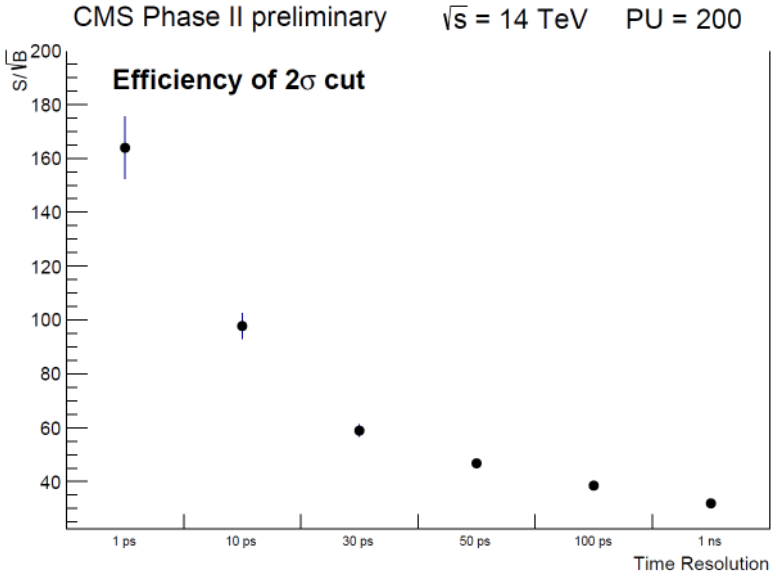

Figure 1.35: Cut at 2σ on the signal difference distributions ($\sim$ 95% efficiency on the signal).

1.4.2.4 RE3/1 and RE4/1

For the high-η region of the 3rd and 4th muon stations, the installation of two new detectors has been proposed in the region $1.8 < \mid \eta \mid < 2.4$ (RE3/1) and $1.9 < \mid \eta \mid < 2.4$ (RE4/1) respectively. The technology proposed is generally of RPC kind, that could be classical RPCs or improved RPCs (iRPCs) with for example low-resistivity glass electrodes [38].

The motivations in support of their installation are, as for GE1/1 and GE2/1, related to the improvement in redundancy, in particular to enhance trigger and reconstruction capabilities.

Fig.1.36 shows how the installation of RE3/1 station could help in recovering the stub reconstruction efficiency in the third station, characterized, with the presence of ME3/1 alone, by drops in correspondence of the high voltage spacers of the CSC chambers. Similar results can be obtained in the fourth station.

Moreover, Fig.1.37 and 1.38 are focused on the quality of the standalone muon reconstruction, which can be analyzed studying the width of the q/p_T distribution (RMS), expected to have a gaussian shape, but actually characterized by a large tail.

The study have been performed for all the stations, ME1/1 to ME4/1, removing one CSC station per time and focusing on the recovery that could

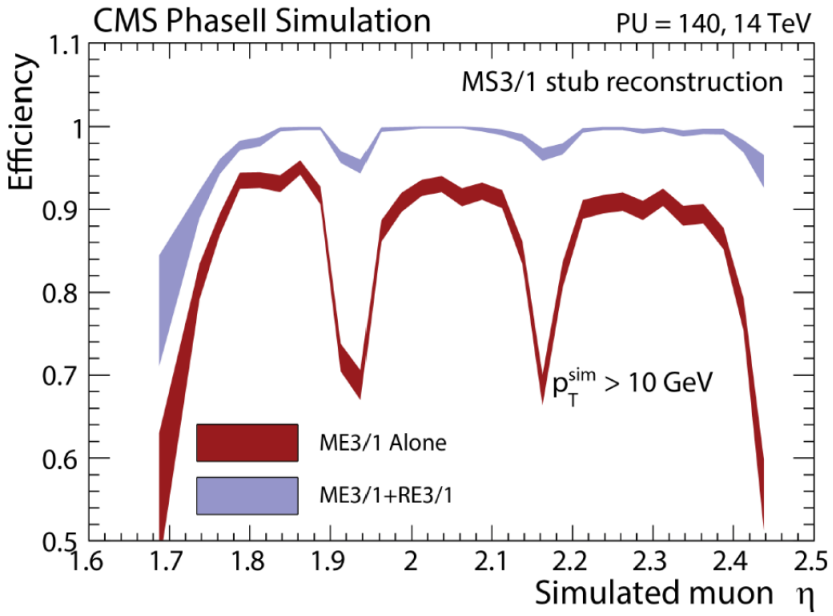

Figure 1.36: Stub reconstruction efficiency in the third muon station with ME3/1 alone (in red) and ME3/1 + RE3/1 (in blue). A similar improvement is obtained also in the fourth station with the RE4/1 station installation [6].

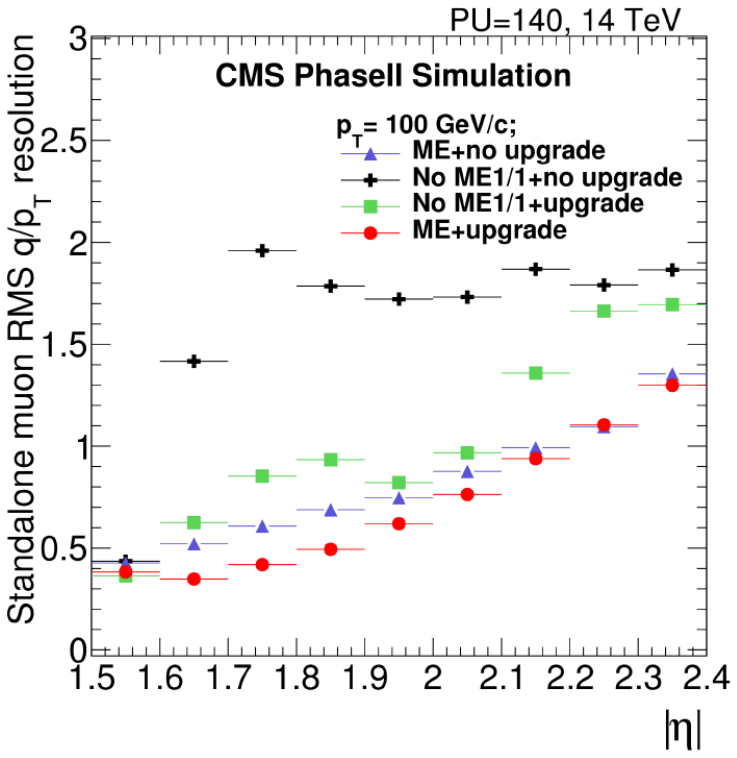

Figure 1.37: Standalone muon RMS q/p_T resolution as a function of η for different upgrade scenarios.

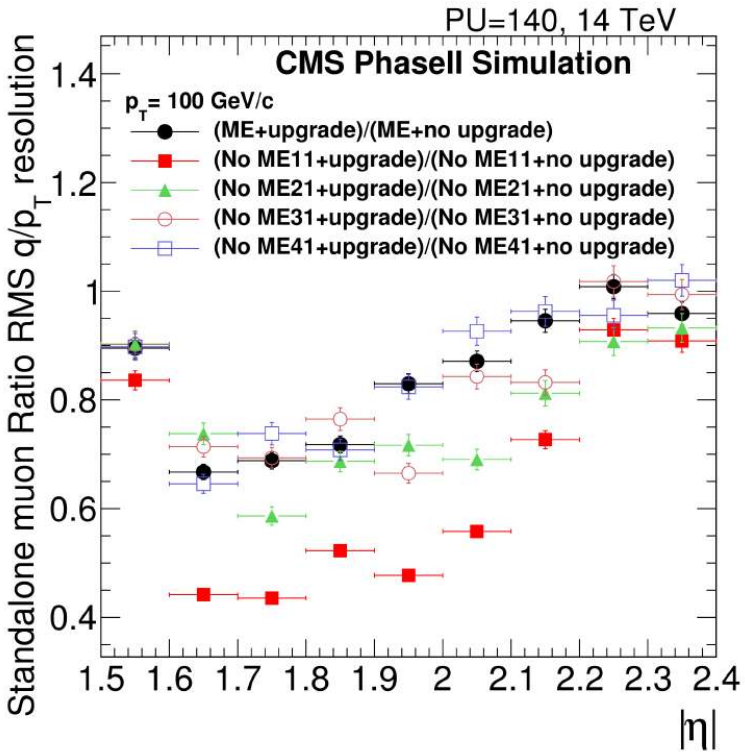

Figure 1.38: Standalone muon ratio RMS q/p_T resolution as a function of η for different upgrade scenarios [6].

be reached with the upgrade in each situation: removing one MEX/1 station the upgrade is able to recover completely the RMS in a condition of 0 PU, and nearly completely for 140 PU. However, if the recovery is defined as

$$\frac{No\,MEX/1\,station\,+\,Upgrade}{No\,MEX/1\,+\,No\,Upgrade} \lesssim 1 \tag{1.8}$$

it is clear that the recovery effect is strongest for missing ME1/1 recovered by GE1/1 and lower for REX/1.

Finally, considering the standalone muon reconstruction efficiency, Fig.1.39 shows the results with a Phase I geometry, top plot, and an upgraded geometry, bottom plot, for a fully efficient detection (in black) and different percentage of inefficiency. From the top plot, it is clear that the higher η regions suffer from the worst consequences of a possible inefficiency: it could be greatly recovered with the upgraded geometry, as shown in the bottom plot even with a significant percentage of detector inefficient [6].

Moving to the technological aspect, standard RPCs, like those installed in other regions of CMS, could not be installed here, as improvements in rate

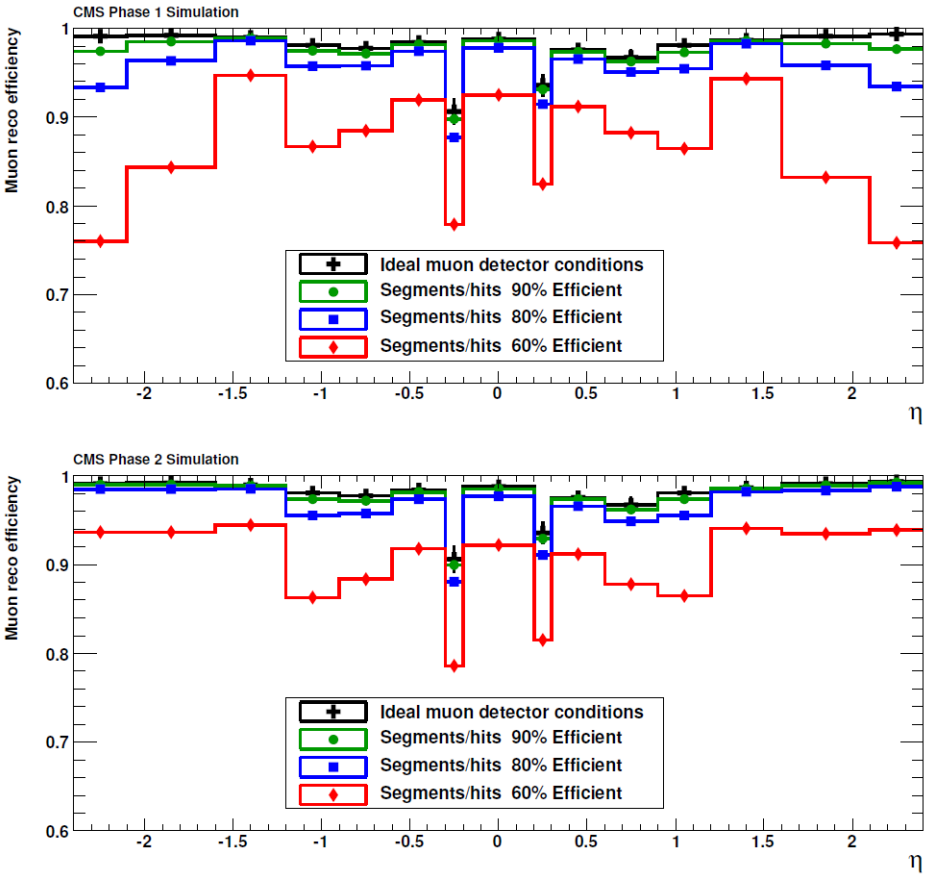

Figure 1.39: Standalone muon reconstruction efficiency as a function of η with ideal muon detection conditions and for different degradation percentage for all the detectors involved [6].

capability are needed. The first results provided by FLUKA simulations, and the comparison with data from the CSCs, provide an estimate of the rate around 700 Hz/cm^2 in the hottest points of RE3/1 and RE4/1. Taking into account an additional safety factor, a rate capability of around 2 kHz/cm^2 should be required for the new chambers, while standard CMS double-gap RPCs have been tested to reach around 1 kHz/cm^2 [22].

For this reason, improved RPC are being developed, working on the following characteristics:

- The electrode resistivity ρ can be reduced in order to reduce the recovery time needed for the electrodes to be charged up again after a discharge in the gas gap
- The average charge generated in the avalanche can be reduced partially transferring the amplification from the gas to the front end electronics

- Changing the detector configuration, which includes many possible options, like changing the electrode thickness or their number (multigap).

Moreover, if multi-gap RPCs will be used, their excellent time resolution of the order to $\sim$ 100 ps can be used for pileup mitigation too [6].

Chapter 2

Comparison between classical gas detectors and MPGD

Gaseous detectors are widely used in HEP experiments, thanks to their flexibility and relatively low cost. However, the improved performance of the colliders are going to put in great discussion the usefulness of their installation and lead to the development of new generation of detectors, like for example Micropattern Gaseous Detector (MPGD). In this chapter the principles of gaseous detectors and MPGD will be introduced. This will be the basis of the discussion about strong points and limitations of both the technologies, that lead to the choice for the installation in the CMS detector.

2.1 Introduction to gaseous detectors

Gaseous detectors are based on the collection of the ionization electrons and ions produced in a gas by the passage of a radiation. Three basic kinds of gaseous detectors were developed in the first half of the twentieth century, the *ionization chamber*, the *proportional counter* and the *Geiger-Muller counter*.

2.1.1 Ionization and transport phenomena in gases

The energy loss of a charged particle in matter is due to two kinds of reactions: excitation and ionization of the atoms, in which electrons and ions couples are

created. The excitation of an atom, X

$$X + a \rightarrow X^* + a \tag{2.1}$$

where a is a charged particle, is a resonant reaction, which requires the correct amount of energy to be transferred and is characterized by a typical cross section of the order of $\sigma \simeq 10^{-17}$ cm^2. The ionization instead

$$X + a \rightarrow X^* + a + e^- \tag{2.2}$$

has a slightly higher cross section, of the order of $\sigma \simeq 10^{-16}$ cm^2. The electrons and ions produced in the reaction are known as *primary* ionization. If a sufficiently amount of energy is transferred to the electron, it can be able to produce itself ion-electron pairs, known as *secondary* ionization.

Another important mechanism to be considered is the *Penning effect* [44]: in some atoms, metastable states can be excited and can be unable to deexcite immediately with the emission of a photon, due to a large spin-parity difference with respect to the ground state. In this case, a deexcitation can occur through a collision with a second atom resulting in the ionization of the latter, an example is

$$Ne^* + Ar \rightarrow Ne + Ar^+ + e^-. \tag{2.3}$$

In any case, in order to be collected in a detector in an efficient way, it is important that the produced pairs remain free for a sufficient long time. Two processes could prevent this possibility: the *recombination* and the *electron attachment*.

If there is no electric field, electron and ion recombine under the effect of their electric attraction, emitting a photon in the process

$$X^+ + e^- \rightarrow X + h\nu \tag{2.4}$$

The rate of recombination depends on the concentrations of positive and negative ions

$$dn = bn^- n^+ dt \tag{2.5}$$

where b is a constant dependent on the type of gas, n^+ and n^- are the positive and negative ion concentrations respectively. If we set $n^+ = n^- = n$, the

integration gives

$$n = \frac{n_0}{1 + bn_0 t} \tag{2.6}$$

where n_0 is the initial concentration at $t=0$ [40].

The other effect, the *electron attachment* consists in the capture of free electrons by electronegative atom to form negative ions.

The atom, which has almost a full outer electron shell, with the addition of an extra electron goes in a stable state and releases an amount of energy, known as *electron affinity* [40].

2.1.2 Transport of electrons and ions in gases

The motion of electrons and ions is extremely important as it influences the operating conditions of the detectors. The most important phenomena are the *diffusion* and the *drift* in electric field, as well as the development of avalanche in the gas.

2.1.2.1 Diffusion

When there is no electric field applied, electrons and ions released by the ionization diffuse uniformly from the point of creation. They can suffer multiple collisions with the gas molecules and lose their energy, coming quickly in thermal equilibrium and eventually recombining. At thermal energies the average speed of the particles can be obtained as

$$v = \sqrt{\frac{8kT}{\pi m}} \tag{2.7}$$

where k is the Boltzmann's constant, T the temperature and m the mass of the particle. At room temperature the electron speed is few times 10^6 cm/s, while the positive ion speeds are of the order of 10^4 cm/s.

The linear distribution of charges after a time t of diffusion is

$$\frac{dN}{dt} = \frac{N_0}{\sqrt{4\pi Dt}} \exp\left(\frac{x^2}{4Dt}\right) \tag{2.8}$$

where N_0 is the total number of charges, x the distance from the point of creation and D the *diffusion coefficient*. D is a parameter that can be calculated

from the kinetic theory as

$$D = \frac{2}{3\sqrt{\pi}} \frac{1}{p\sigma_0} \sqrt{\frac{(kT)^3}{m}} \text{ [40]}. \tag{2.9}$$

where p is the gas pressure and σ_0 is the total cross section for a collision with a gas molecule.

2.1.2.2 Drift

In presence of electric field, electrons and ions are accelerated along the field lines towards the anode and the cathode respectively. The acceleration is in general stopped by the collisions with the gas molecules, therefore a maximum average velocity can be reached, known as *drift velocity* of the charge, superimposed to its random movement.

The *mobility* of a charge is defined as

$$\mu = \frac{u}{E} \tag{2.10}$$

where u is the drift velocity and E is the electric field. For ideal gases, the mobility is related to the diffusion constant by

$$\frac{D}{\mu} = \frac{kT}{e} \tag{2.11}$$

The mobility for ions depends linearly on the ratio E/p, while the mobility for electrons is much greater and depends from E [40].

2.1.2.3 Avalanche multiplication

When the primary ionization electrons gain enough energy from the electric field to ionize other gas molecules, multiplication can occur. The secondary electrons can then produce tertiary ionization and so on, resulting in an avalanche, which will have the typical liquid drop shape shown in Fig.2.1 left, due to the greater mobility of electrons with respect to ions.

If α is the mean free path of electrons for a secondary ionizing collision, $1/\alpha$ is the probability of an ionization per unit path length, called also *first Townsend coefficient*, whose behavior as a function of the electric field for a typical gas is shown in Fig.2.1 right.

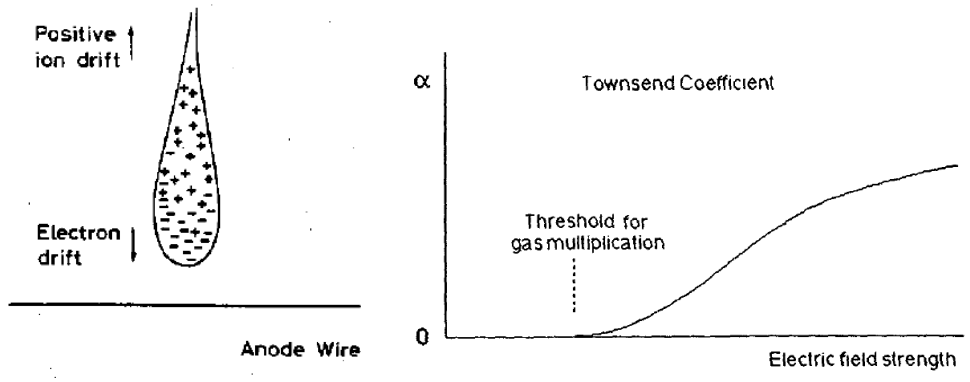

Figure 2.1: Left: Avalanche formation. Since the electrons are more mobile that the ions, the avalanche takes the form of a liquid drop with the electrons at the head [40]. Right: A plot of the first Townsend coefficient as a function of electric field for a typical gas [41].

If n is the number of electrons, in a path dx there will be

$$dn = n\alpha dx \tag{2.12}$$

new electrons created. Integrating, the total number of electrons created in a path x is

$$n = n_0 \exp(\alpha x) \tag{2.13}$$

where n_0 is the initial number of electrons. The multiplication factor is so

$$M = n/n_0 = \exp(\alpha x) \tag{2.14}$$

o, generally, for non uniform electric fields

$$M = \exp\left[\int_{r1}^{r2} \alpha(x)dx\right] \tag{2.15}$$

The multiplication factor is physically limited at about $M < 10^8$ or $\alpha x < 20$, after which a breakdown occurs: this limit is called *Raether limit* [40].

2.2 Classical gaseous detectors

The classical gas detectors, i.e. ionization chambers, proportional counters and Geiger-Muller counters, are essentially the same device working under different operating parameters and exploiting different phenomena.

The classical configuration of a gaseous detector consist of a cylinder, filled with a suitable gas, selected following particular criteria explained in Section 2.2.1. Along its axis is suspended a conducting wire at positive voltage, $+V_0$, with respect to the walls. The electric field is radial

$$E = \frac{1}{r}\frac{V_0}{\ln(b/a)} \tag{2.16}$$

where r is the radial distance from the axis, b the inner radius of the cylinder and a the radius of the central wire.

If a particle enters in the cylinder and ionizes the gas, the electrons and ions produced in the ionization will move towards the anode and the cathode respectively, where they will be collected.

The current signal observed depends from the field intensity, as shown in Fig.2.2, which plots the charge collected as a function of the amplification electric field. The applied electric field defines different regimes in which gaseous detectors can operate.

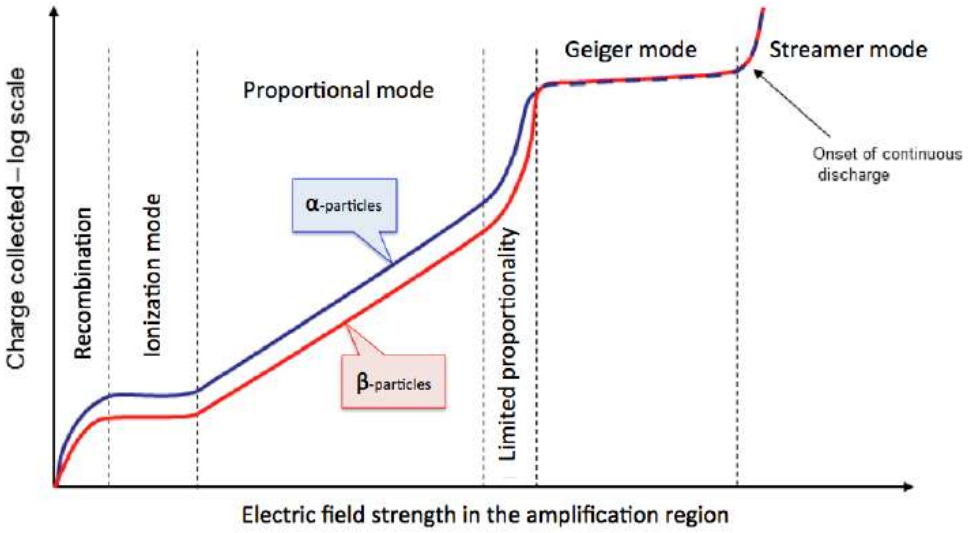

Figure 2.2: Gain-voltage characteristics for gaseous detectors showing the different operating modes.

Ionization chamber At zero voltage applied the charge is not collected and the electron-ion pairs recombine under their own electrical attraction. Raising the voltage, the recombination is overcome and, at some point, all the pairs created are collected.

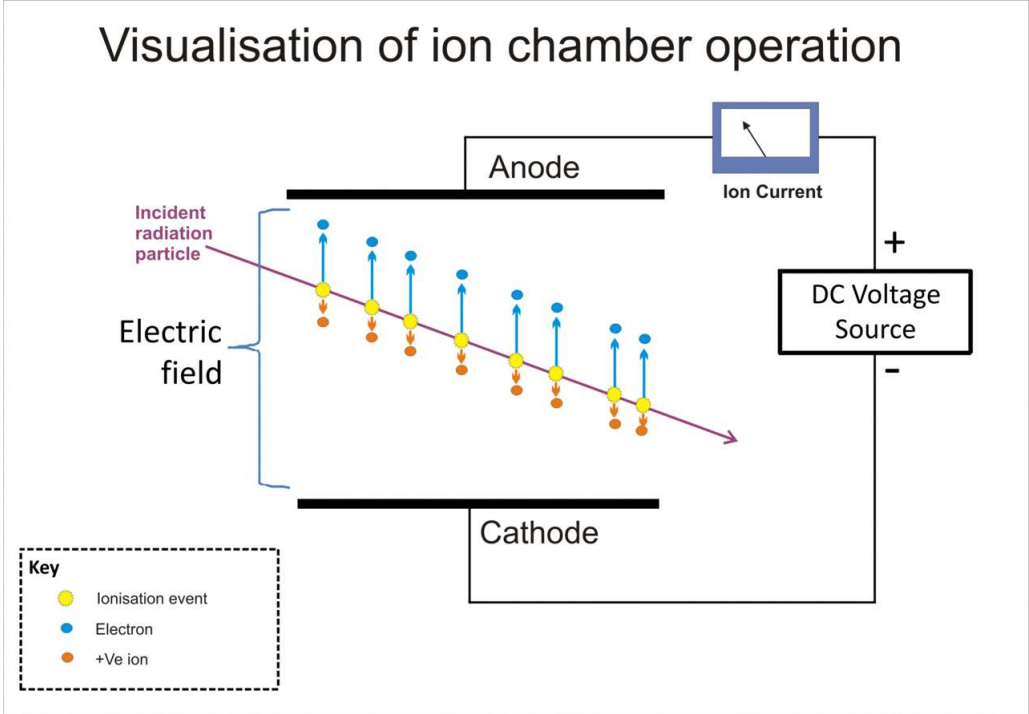

Figure 2.3: Schematic diagram of an ionization chamber, showing drift of electrons and ions.

A further increase in the voltage shows no other effects as the detector is operating in the first flat region of the plot in Fig.2.2, called *ionization* region. A detector working in this region is called *ionization chamber* and its operation is schematically shown in Fig.2.3.

Ionization chambers are preferred for high radiation dose rates because they have a very low *dead time*. The advantages of this kind of detector are:

- Good uniform response to gamma radiation and an accurate overall dose reading
- High rate capabilities
- The exposure to a sustained high radiation levels do not degrade fill gas

On the other hand, its very low electronic output requires a sophisticated readout circuit [43].

Proportional chamber If we increase the electric field enough to enter in the so-called *proportional mode* region, the electric field would be sufficient to accelerate the electrons produced in the first ionization and to produce an avalanche. The number of electron-ion pairs produced in the avalanche is directly proportional to the number of primary electrons, with a multiplication

factor that depends from the voltage applied, up to 10^6. A detector working in this region is called *proportional chamber*. The main advantage of this kind of detector is that it can measure the energy of the radiation and provide spectrographic information.

An example of proportional chamber widely used in particle physics is the *Multiwire Proportional Chamber (MWPC)*, sketched in Fig.2.4.

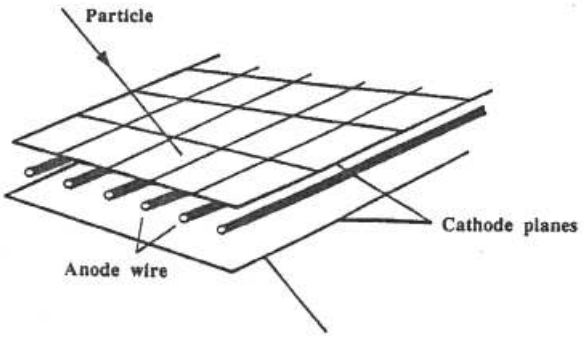

Figure 2.4: Sketch of a Multiwire Proportional Chamber

It consists of a plane of equally spaced anode wires centered between two cathode planes. If a negative voltage is applied to the cathode planes, the electric field gets a particular configuration, in which the field lines are essentially parallel and almost constant far from the anode wires. Near the anode wires instead the field takes a *1/r* dependence. When electrons and ions are freed in the constant field region they drift along the field lines: when the electrons reach the high field region around the anode wire they are accelerated and produce an avalanche; the positive ions produced in the multiplication process then induce a negative signal on the anode wire as well. The neighboring wires are affected too, but the signal induced there is positive and of small amplitude.

Geiger-Muller chamber If the voltage is so high that the space charge created distorts the electric field near the anode, the proportionality starts to be lost. This region is called of *limited proportionality*. After this, a further increase of the voltage applied, allows the production of a quantity of charge sufficient to develop discharges in the gas. Instead of a single avalanche, in the gas a chain reaction happens, with many avalanches spread out along the entire anode. The output current is then saturated and gives a signal with always the

same amplitude, whatever is the energy of the initial event. Detectors working in this region are called *Geiger-Muller* or *breakdown* counters.

The current pulses produced in this kind of device by the ionising events are elaborated by electronics which can derive a visual display of count rate or radiation dose. The detectors working in this conditions are generally cheap but robust devices, with a large variety of sizes and applications. Moreover they can give a large output signal requiring minimal electronic processing for simple counting. Due to the loss of proportionality of course they cannot measure energy of radiation and they cannot measure high radiation rates due to the high dead time.

2.2.1 Gas mixtures

In order to have a complete overview of the classical gaseous detectors it is important also to understand how the fill gases are selected. Generally the factors that influence the decision are few, like working voltage, high gain, good proportionality and high rate capability. These conditions could not be easily achieved with pure gases, so gas mixtures are usually used. As basis, noble gases are chosen, since they require the lowest electric field intensities for avalanche formation. In particular the use of Argon is very widespread, thanks to its high specific ionization and low cost. Argon however cannot be used as single component of the mixture, because it would not be possible to reach gain higher than 10^3-10^4 without continuous discharges: due to the high excitation energy, the excited argon atoms formed in the avalanche can de-excite, producing high energy photons able to generate secondary avalanches.

The problem is solved adding to the mixture an adequate percentage of a polyatomic gas, which acts as a *quencher*: it absorbs the radiated photons and dissipates the energy through dissociations and elastic collisions. In this way, gains up to 10^6 can be easily achieved.

Another improvement can be obtained inserting in the mixture a small amount of electronegative gas, which can also trap electrons extracted from the cathode before they can reach the anode to cause an avalanche [40].

Recently, the question of the choice of the gas mixture had to include a new aspect related to the use of greenhouse gases (GHG). Indeed, numerous mixtures selected for the operation of gaseous detectors include fluorinate-gases (F-gases), subjected, from 1st January 2015, to a new regulation of the

European Union [46] which can be summarized as:

- Limiting the total amount of the most important F-gases that can be sold in the EU from 2015 onwards and phasing them down in steps to one-fifth of 2014 sales in 2030.
- Banning the use of F-gases in many new types of equipment where less harmful alternatives are widely available.
- Preventing emissions of F-gases from existing equipment by requiring checks, proper servicing and recovery of the gases at the end of the equipment's life [48].

GHG are generally gases which absorb and emit radiation within the thermal infrared range and as a consequence are responsible for the greenhouse effect. Two are the parameters that are considered in this context for the evaluation of their dangerousness: the *Global Warning Potential (GWP)*, that is normalized to the effect of CO_2 (GWP = 1) and the *Ozone Depletion Potential (ODP)*, normalized to the the effect of CCl_3F (ODP = 1), which describes the effect on the ozone layer [47].

At CERN, the overall GHG contribution comes from $C_2H_2F_4$ (71%), CF_4 (20%) and SF_6 (9%), which have GWP equal to 1430, 7390 and 23900 respectively and are employed by RPCs, CSCs and GEMs systems. The experiments could adopt different strategies to face this issue: one possibility is to modify the gas system in order to foresee the recuperation of the highest possible fraction of gas mixture after being used in the detectors and re-injected into the supply lines (*recirculation system*). An even more complex solution is to recuperate also a fraction of the gas that is sent to the exhaust in a recirculation system (*recuperation system*) [48]. In case the application of these solutions is not possible or is not completely efficient, for example due to leaks in the detectors, the alternative is to find a different gas mixture, GHG-free, able to reach the same performance. Many studies are going on right now on this item. For example for RPC detectors, the standard gas mixture with which they are operated in CMS and ATLAS is composed by $C_2H_2F_4/iC_4H_{10}/SF_6$ 94.7%/5%/0.3%. More than 50 different mixtures have been tested, with the aim of removing or at least reducing the presence of both $C_2H_2F_4$ and SF_6, using alternative gases from the families of the Hydro-Fluoro-Carbon (HFC) and of the Hydro-Fluoro-Olefine (HFO). The difficulty of this activity can be understood by the fact that the majority of these new mixtures were classified as not suitable because they needed the

detectors to be operated at a too high voltage or showed the presence of a large quantity of discharges, well above the limit acceptable for a safe and long term operation. Interesting results were obtained only with one candidate mixture, $HFO{-}1234/C_2H_2F_4/iC_4H_{10}/SF_6/He$ 37.45%/37.45%/4.5%/0.6%/20%, which allowed the RPCs tested to reach performance comparable to those obtained with the standard mixture. However, this is just a first hint and further test are necessary to understand if this mixture will really be apt for the application in high energy physics experiments [49].

2.3 Limitations of classical gaseous detectors

Gaseous detectors technology had a great success in high energy physics thanks to few important features that characterize them. First of all, gaseous detectors are generally cheap and it is possible to produce large area detectors at low price. These detectors can also have flexible geometries, which can be adapted for the installation in different regions of the biggest high energy experiments. Finally, considering proportional detectors like MWPC, they have a very good energy resolution.

However, gaseous detectors are at the same time affected by few weak points, that led to the development of the Micropattern Gaseous Detectors (MPGD) technology.

The first strong limitation is of mechanical nature: considering a detector like the MWPC described above, one problem arises from the stability of the anode wires when an electric field is applied between the anode and the cathode. In fact, if one wire is displaced from the middle plane, it is attracted more to one side and less to the opposite, and the movement would continue indefinitely if there is no restoring force (the mechanical tension on the wires). It has been observed in large chambers that, above a certain value of the applied voltage, the wires become unstable, moving off the middle plane and reaching a new equilibrium with all wires alternately displaced towards the cathodes. Due to the reduction of the distance of the wires from the high voltage electrodes, a discharge may occur and propagate to the whole chamber, breaking most of the anode wires, as experienced in one of the first large MWPCs. Considering the geometry of the chamber, the maximum wire length can be calculated as

$$L_c = \frac{s}{CV_0}\sqrt{4\pi\epsilon_0 T_M} \tag{2.17}$$

where L_c is the wire critical length, s is the wire spacing, CV_0 are the two equal linear charges representing the wires and T_M is the maximum tension allowed by the elasticity module of a given wire. For example, a MWPC with 2 mm spacing between tungsten wires, 20 μm-diameter, operated at 5 kV, we obtain a maximum wires' length of 90 cm [42]. It is clear that it imposes a constraints on the dimensions of the chamber or, on the other side, on the wire spacing. Generally 2-3 mm is the typical spacing used for this kind of technology in order to be able to find a stable operational condition, but this introduces a strong limitation on the achievable spatial resolution: considering for example a digital readout, the space resolution can be estimated as

$$\sigma = \frac{d}{\sqrt{12}} \tag{2.18}$$

where d is the wires spacing: for $d = 2 - 3mm$, $\sigma = 600 - 900\mu m$.

In addition, in general a great quantity of ions is produced in all the active area of the detector during the development of an avalanche: in a MWPC, the positive ions create a sheath around the wire, resulting in a local drop of the electric field, with a consequent reduction of the gain; the normal field is restored only when the ions leave the proximity of the wire and are neutralized at the cathode, but it happens only after several hundred microseconds due to their slow motion. The gain is affected at each interaction and the effect of course increases with the increase of the incident flux, as can be seen from Fig.2.5, which shows the normalized gain of a MWPC as a function of the incident field. This is an intrinsic limitation of gaseous detectors, that prevents them from working in very high rate environment, like the high-η region of the CMS muon system.

Coming to a CMS-related example, for RPC detectors, whose geometry and working principle are deeply described in [17], the limit in rate capability is strongly related to the bulk resistivity ρ of the bakelite plates that compose the electrodes. The effects are mainly two: on one side, the time constant τ of an RPC cell involved in an avalanche is given by

$$\tau = \epsilon_0(\epsilon_r + 2)\rho \tag{2.19}$$

so it is smaller for lower values of ρ. On the other side, at very high rate, the flow of total current through the plates becomes important and produces

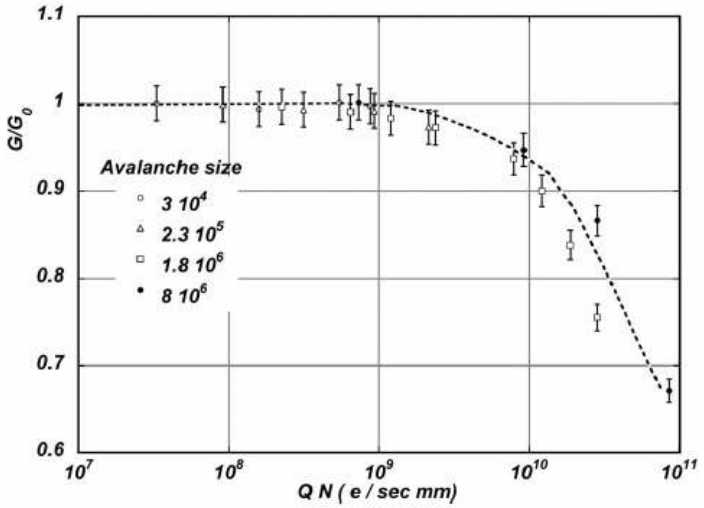

Figure 2.5: Normalized gain measured with a wire chamber as a function of the particle flux, expressed in terms of charge production rate per mm of wire [42].

a drop of voltage V_d across them, that can be estimated from:

$$V_d = 2 < Q_e > rs\rho \tag{2.20}$$

where r is the rate expressed in part/cm^{2}s, s is the electrode thickness and $< Q_e >$ is the mean charge produced by the avalanche. As a consequence of this voltage drop, a lower *effective voltage* is applied to the gas gap, resulting in a lower gas amplification. With the resistivity value selected for the CMS RPC, the achievable rate was between 500 Hz/cm^2 - 1 kHz/cm^2, lower than what was expected from the high-η region of the muon system.

Finally gaseous detectors are generally affected by ageing effects that could prevent them from working properly. For example, when gas mixtures enriched with hydrocarbon quenchers are used, the ageing effect can be due to polymerization processes that happen in the gas during the development of the avalanche. These polymers, in liquid or solid phase, deposit on the electrodes, causing as visible effect an increase of the noise or in the dark current. Fig.2.6 shows the typical effects on an anode wire. Similar effects can be obtained also with non-hydrocabon enriched gas mixtures, where for example CO_2 is used as quencher, if plasticizers, silicone and sulphur compounds enters in the mixture through the gas flow by the flux regulators, tubes and connections [42].

Returning to the CMS RPC example, ageing effects could come from the

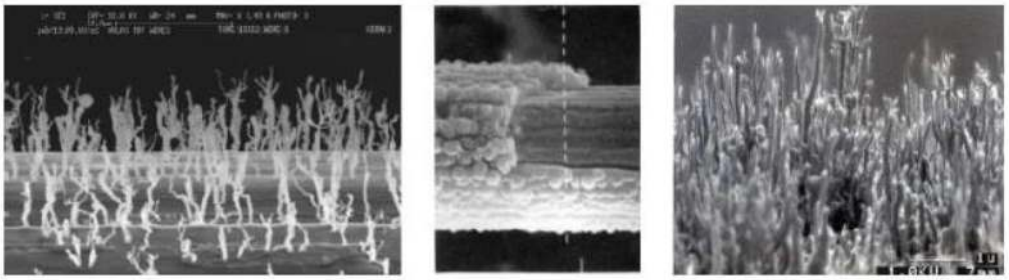

Figure 2.6: Pictures of aging effects on an anode wire.

used freon-based mixture ($C_2H_2F_4/i - C_4H_{10}/SF_6$ 96%/3.5%/0.5%): the F^- radicals contained in the freon-based component can produce corrosive HF-compounds during an avalanche, with the consequent chemical damage to the RPC electrodes [45].

2.4 Micropattern gaseous detectors

In order to overcome the limitations of classical gaseous detectors a new concept was introduced in 1982 by Oed [51], the Microstrip Gas Chamber (MSGC). The detector consisted of a set of tiny metal strips engraved on a thin insulating substrate and alternately connected as anodes and cathodes, as shown in Fig.2.7. The processes of production of the signals is the same of MWPC, but the photo-lithographic techniques used in this device allows the reduction of the electrode spacing of at least one order of magnitude. In addition, the fast collection of positive ions by the nearby cathode strips reduces space-charge buildup and increases the rate capability [50].

MSGC were the first prototype of a new family of gaseous detectors, called Micropattern Gaseous Detectors (MPGD), high granularity gaseous detectors with small (below 1 mm) distances between the anode and the cathode electrodes.

In MPGD the ionization happens in a region with low electric field, called *drift region*, while the multiplication takes place in a well localized region with a very high electric field, called *amplification region*.

This separation allows in general a great improvement, of at least one order of magnitude, of the spatial resolution. In addition, also the rate capability benefits from the separation between the drift region and the amplification region, because generally this allows a more localized avalanche development,

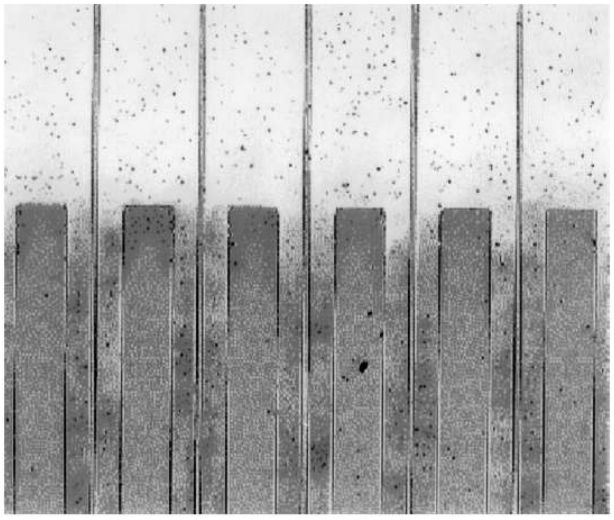

Figure 2.7: Close view of one of the first microstrip plates developed by Oed. On an insulating substrate, thin metallic anode strips alternate with wider cathodes; the pitch is 200 μm [50].

with a consequent faster evacuation of the charge. On the other hand new problems are introduced, the most important one is the occurrence of *sparks*. Indeed, as the inter-electrode spacing is very small, the presence of dust can induce sparks and, as the electrodes are so thin, they risk to be damaged.

The so called *Classical MPGD* are in particular the well-known *Micromegas* and *GEM*, chosen by LHC experiments for the installation during their upgrades.

2.4.1 Micromegas

Micro-mesh gaseous detectors (Micromegas) were developed starting from the observation that in thin, sub-mm gaps, due to the saturation of the Townsend coefficient at very high fields, large gains can be reached with a decreased sensitivity to gap variations and imperfections [55].

The detector, shown in Fig.2.8 left, is composed by a thin metal grid stretched at a small distance, 50 - 100 μm, from the readout electrode; a high electric field ($>$ 30 kV/cm) is applied across the gap, as shown in Fig.2.8 right, so that the electrons released in the upper drift region are collected and multiplied with large gains. Due to the small gap and high field, positive ions and electrons move very quickly and induce fast signals with only a small ion tail; as the drift field is generally much smaller than the amplification one, most

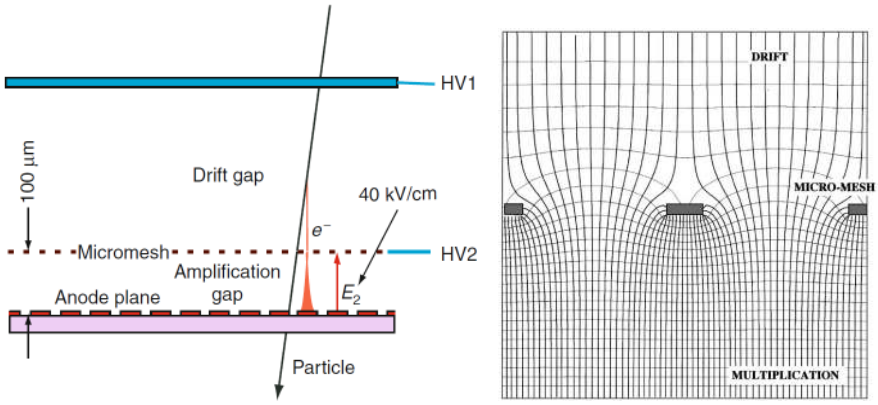

Figure 2.8: Left: Basic principle of a Micromegas detector [39]. Right: schematics and electric field map in the micromegas. A metallic micromesh separates a low-field, or drift, region from the high-field multiplication region[50].

ions are collected on the cathode mesh, reducing the charge backflow into the drift gap [42]. In addition, defining as *electron transparency* the ratio of the electrons that cross the mesh over the total number of the primary electrons created in the drift region, the mesh turns out to be transparent to more than 95% of the electrons.

While the drift of the electrons in the conversion region is quite a slow process, that takes several 10's of ns, the amplification process is very fast, lasting only a fraction of ns: as a consequence the pulse that arrives at the readout strips is a very fast pulse.

As already introduced above, the weak point of this kind of detectors is the vulnerability to sparks, that happen when the total number of electrons in the avalanche reaches 10^7. In a detector like Micromegas, a high detection efficiency for minimum ionizing muons requires a gas amplification of at least 10^4. Therefore, ionization processes producing more than 1000 electrons over distances comparable to the typical lateral extent of an avalanche (a few hundred microns) carry the risk of sparking. The result of a discharge can be a damage to the detector itself or to the readout electronics; in alternative it can lead to a large dead time as a result of HV breakdown.

The Atlas Collaboration, which decided to implement Micromegas detectors in their muon system [56], deeply focused the R&D program on the spark protection system. They inserted a layer of resistive strips on top of a thin insulator added directly above the readout electrode, in order to make the detectors spark-insensitive. Indeed the readout electrode is no longer directly

exposed to the charge created in the amplification region as the signals are capacitively coupled to it. A consequence is that some fraction of the signal height is lost, but on the other hand the chamber can operate at a larger gain without discharge problems.

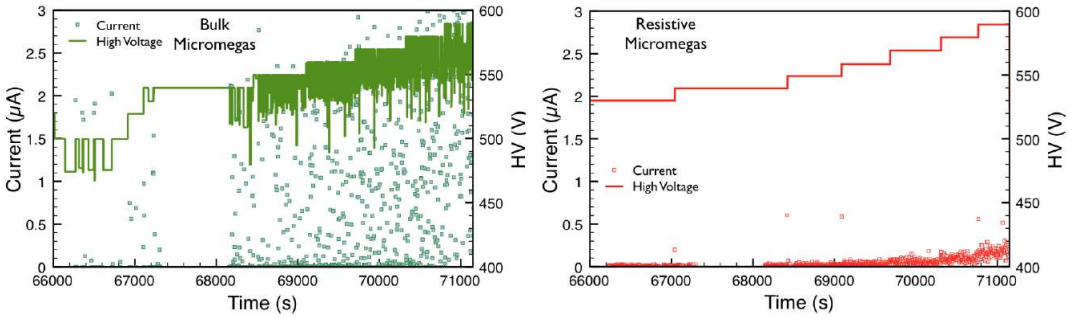

Figure 2.9: Monitored HV (continuous line) and current (points) as a function of the HV mesh under neutron irradiation, left a non-resistive micromegas; right a micromegas with resistive-strip protection layer [56].

The results of this work can be observed in Fig.2.9, where the results of irradiation with neutrons of a standard micromegas (left) and a spark-protected micromegas (right) are compared: in standard micromegas we can observe large currents, large HV drops with recovery times of the order of 1 s and as a consequence the chamber cannot operate in a stable condition. On the other hand, the spark-protected micromegas shows low currents, without HV drops and the chamber can work permanently up to the maximum HV value [56].

2.4.2 GEM

A Gas Electron Multiplier (GEM) consists of a thin, metal-clad polymer foil, named Kapton, cladded on both sides with a suitable layer of copper, usually 5 μm-thick, chemically perforated by high density of holes, typically 100/mm^2 [42]. A common holes' pattern is the one shown in Fig.2.10 with 70 μm diameter and 140 μm pitch.

With a suitable choice of voltages producing a field map like the one displayed in Fig.2.11, the electrons generated in the ionization in the gas layer above the GEM foil are swallowed up into the holes, where the amplification occurs thanks to the high electric field. The electrons generated in the avalanche are then transferred into the lower gas layer.

The maximum gain, that is a feature of the GEM structure, depends on the

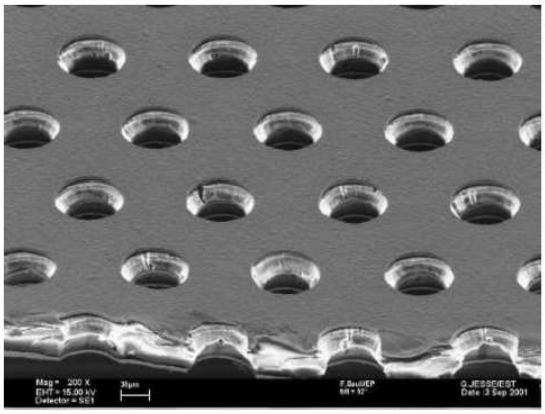

Figure 2.10: Microscopic view of a GEM electrode. The holes' diameter and pitch are 70 μm and 140μm respectively. [42].

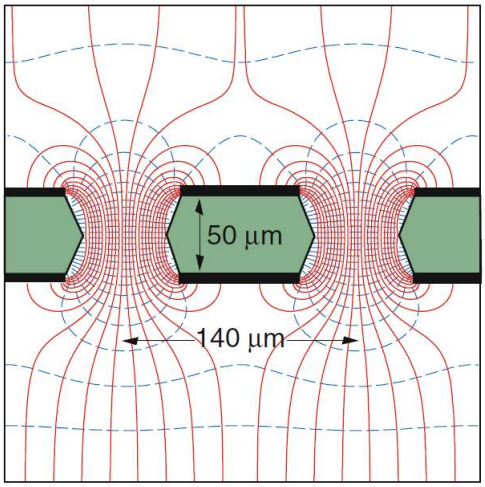

Figure 2.11: GEM electric field near the holes in typical operating conditions [42] [39].

thickness of the polymeric support, the diameter of the holes, the gas mixtures and the applied voltages. Excellent performances has been obtained with 50 μm-thick polymer foils, hole diameters of 50-100 μm and pitch of 100-200 μm, like those shown in Fig.2.10.

Gain of the order of 10^4 have been measured coupling a GEM foil with a printed circuit board (PCB) used to collect the charge; the results are shown in Fig.2.12.

As for the other micropattern detectors described in the previous section, GEM devices experience an increasing discharge rate under exposure to high radiation flux or highly ionizing radiation. The solution that has been adopted in this case is to share the amplification between two or more foils used in cas-

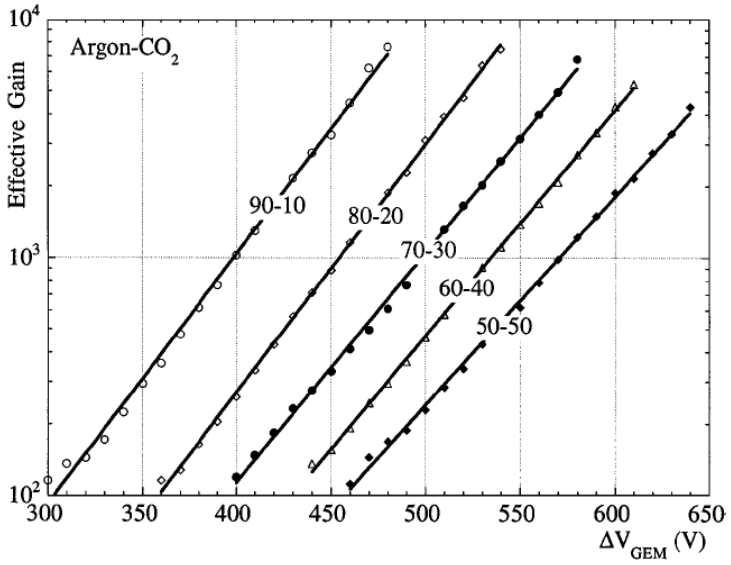

Figure 2.12: Effective gain curves measured with the single GEM+PCB detector in various Ar/CO_2 mixtures. ΔV_{GEM} is the potential difference across the multiplier [50].

cade. Fig.2.13 shows the Triple-GEM solution, adopted also for the installation in the CMS muon system, as will be discussed in Chapter 3.

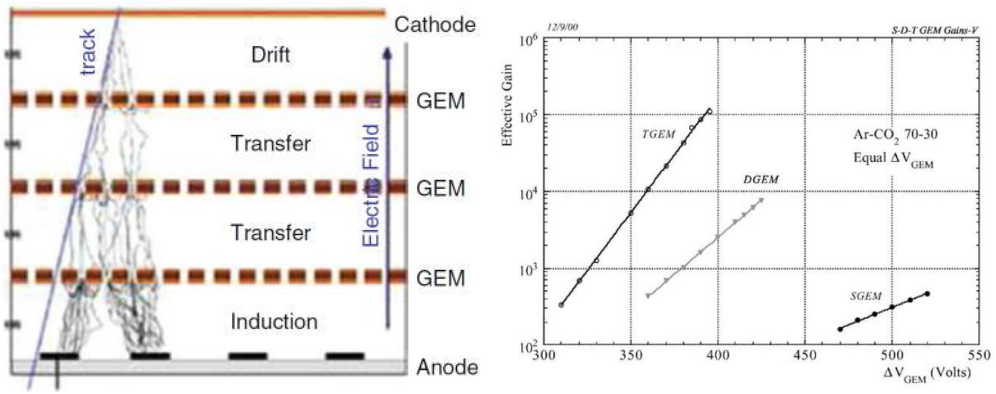

Figure 2.13: Left: schematic view of the Triple-GEM detector [39]; Right: Total effective gain on anodes for a single, double and triple GEM detector [58].

In case of a single GEM the two gas gaps are called *drift gap* and *induction gap*, where the first one is the one above the GEM foil in which the first ionization happens, while the second one is the one between the GEM foil and the readout PCB. In case of a double or triple structure, the name of the first and of the last gap remains the same, while the second and the third gap (in

case of a triple-GEM) are called *transfer gaps* [50].

As already shown in Fig.2.12, the *effective* gain of a GEM device increases exponentially with the applied voltage. Other parameters that influence the reachable gain are the geometry of the GEM foil and the external fields. For GEM structures generally two kinds of gain are defined, the *real* or *absolute* gain and the *effective* gain. The *real* gain is simply the amplification factor related to the avalanche that develops inside the GEM holes. However, this is not the value that really contributes to the signal formation and that can be measured: indeed a part of the electrons produced in the avalanche can recombine, or even more they can be reabsorbed by the GEM electrodes, in particular the bottom one. This is the main reason that cause the *effective* gain to be lower than the absolute one, where the *effective* gain is then defined as the fraction of electrons collected by an electrode following the multiplier [57]. It strongly depends on the electric fields outside the GEM holes, as it will be described in Section 2.4.2.2.

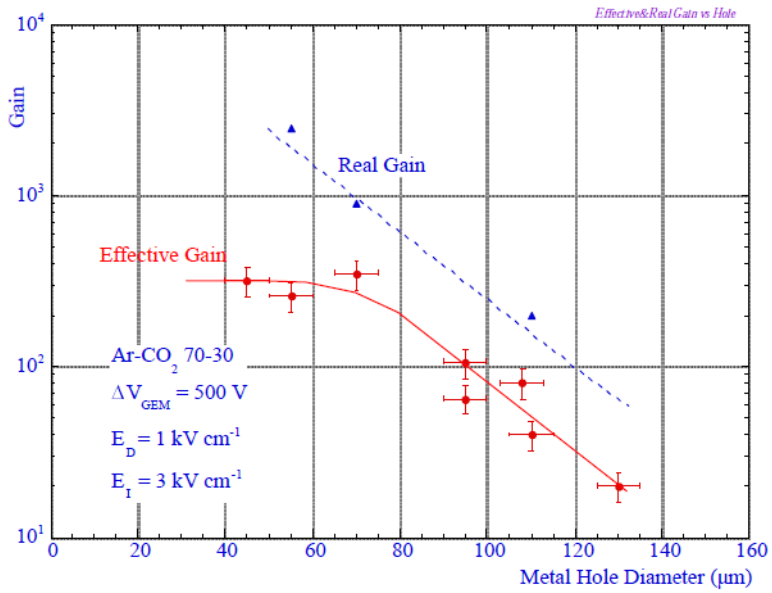

Figure 2.14: Effective and real gain as a function of the holes diameter in a single GEM [57].

Starting from the geometry contribution, Fig.2.14 displays the effective gain measured for different values of holes diameter (red points): the gain increases with decreasing diameter until around 70 μm and reaches a plateau for lower values. The blue triangles instead are an estimation, from the measurement of the currents in the structure, of the *real* GEM gain for three diameters.

The behavior of the effective gain can be explained as a increasing losses of electrons produced in the avalanche, that are reabsorbed from the bottom GEM electrode, when the hole diameter is reduced below a value similar to the GEM thickness. This observation also suggests that, even if using a thicker GEM could be useful to increase the real gain, due to the longer multiplication path available for the electrons, there might be no improvement in the effective gain since saturation will probably occur at larger hole diameters [57]. This issue has been deepened in the last years with the development of THGEM, structure similar to the GEM foils, but up to 1-2 mm-thick.

2.4.2.1 Effect of the induction field

The dependence of the effective gain from the induction field is shown in Fig.2.15 where the results of measurements performed in different gas mixtures (Ar-DME [1] from 90%/10% to 50%/50%) are plotted.

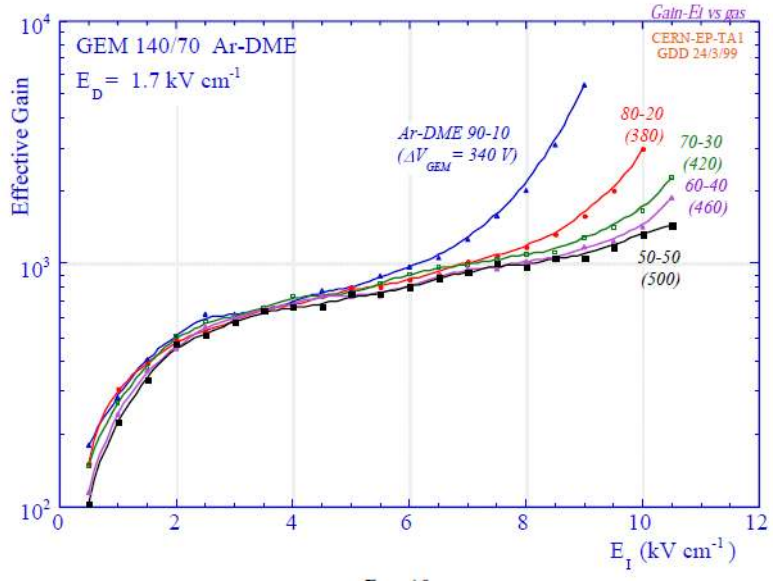

Figure 2.15: Effective gain of a single GEM as a function of the induction field, for different gas mixtures. [57].

In all the curves the point in which the parallel plate multiplication is reached can be noticed: it corresponds to a fast increase in the gain and the appearance of a (positive) ion current on the bottom GEM electrode, overtaking the electron current. Even if it is an interesting region due to the increase of the gain, it is considered an unsafe region as it may allow a

[1] DME is *Dimethyl ether*, a good quencher used in some gas mixtures.

discharge developed inside the GEM foil to propagate to the readout electrode. In addition, signals detected on the anode develop a characteristic ion tail, with a consequent increase in occupancy.

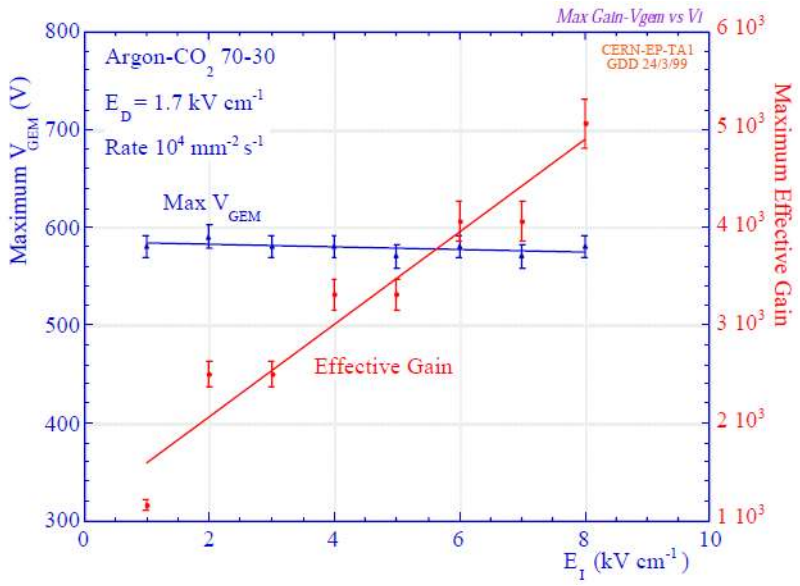

Figure 2.16: Effective gain (red) and maximum voltage (blue) as a function of the induction field for a single GEM in Ar/Co_2 70/30 [57].

The maximum potential difference achievable on GEM under strong X-ray irradiation (10^4 Hz/mm^2) before discharge presents only a small decrease towards high values of induction field as shown in Fig.2.16, consistent with a slight increase of the real gain. This confirms that the discharge is generated by a transition mechanism that depends on the avalanche size, and not by other charge transfer properties.

The induction field has also an influence on the gain stability under strong irradiation as it influences the charge collection [57].

2.4.2.2 Effect of the drift field on charge collection

The ratio between the number of electrons that enter the holes and the number of electrons lost on the copper is known as the *collection efficiency*. When the electric field in the drift region is greater that ~ 3 kV/cm, some of the electrons cannot reach the GEM holes and terminate on the top copper layer. This fraction increases when increasing the strength of the field. In a similar way, when the electric field below the GEM hole is low, some of the electrons cannot be extracted and are lost on the bottom copper layer. The ratio between the

electrons exiting the holes and the ones lost on the copper is called *extraction efficiency*.

The *transparency* of the GEM foil, shown in Fig.2.17 as a function of the drift field, is the combination of the collection and the extraction efficiencies. It is a function of the electric fields above and below the GEM, but also depends on the internal electric field and the diameters of the holes [87].

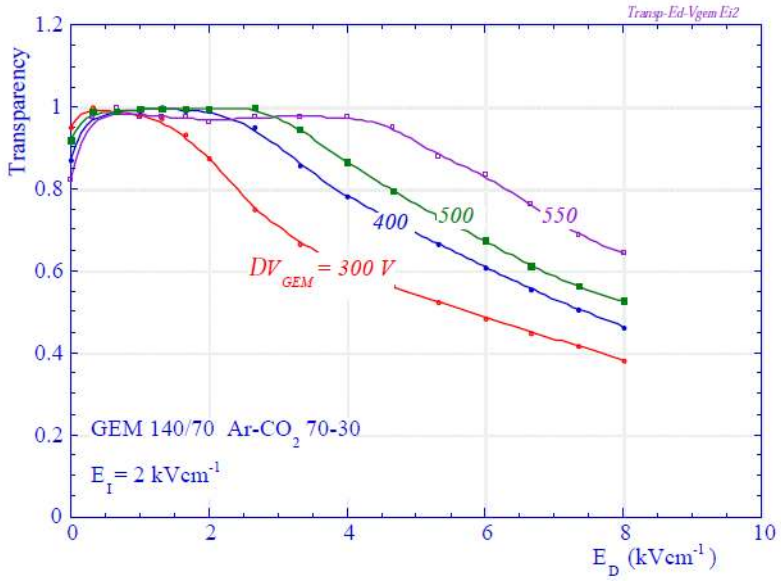

Figure 2.17: Electron collection efficiency (transparency) as a function of drift field for several values of GEM voltage and a low induction field [57].

For example, Fig.2.18 compare the dependence of the detected signal on the drift field, for three GEMs having increasing optical transparency: 140/50 (τ= 0.12), 90/60 (τ=0.4) and 140/100, (τ= 0.46). For both GEMs with large optical transparency, the efficient collection region extends almost to 10 kV/cm; the gain of the GEM with smaller holes is however five times larger. This is important for the use of detectors in strong magnetic fields, requiring the use of high values of drift field to reduce the Lorentz angle.

The fractional ion feedback, defined as the ratio of drift to total currents, increases with the drift field and depends on the GEM voltage, as shown in Fig. 2.19. A more substantial suppression of the ion feedback can be obtained with multiple structures [57].

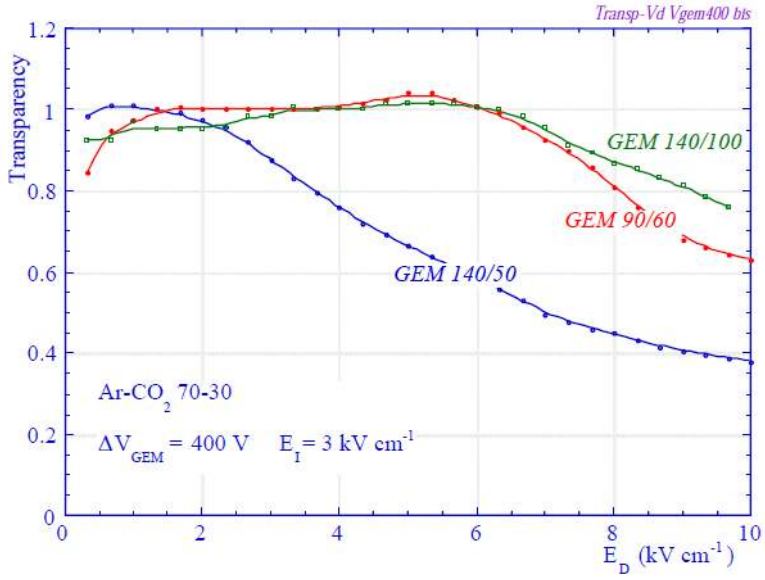

Figure 2.18: Transparency as a function of drift field measured on three GEMs with different geometry for low GEM field [57].

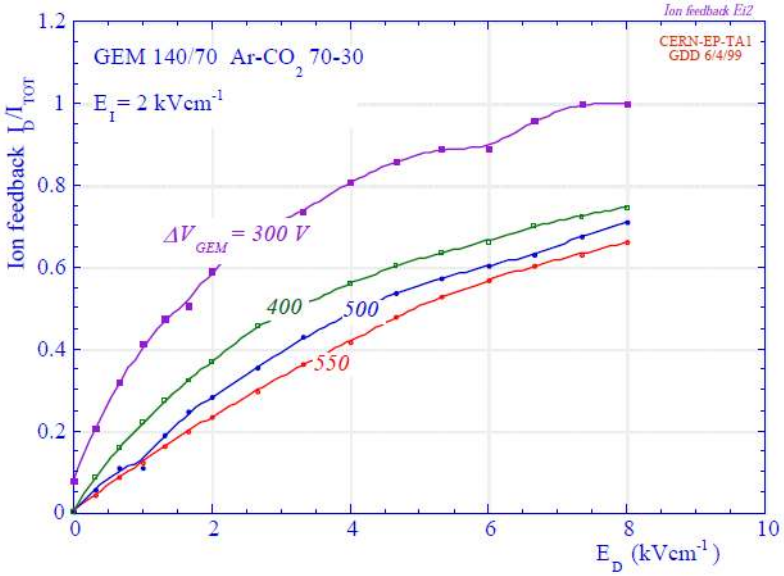

Figure 2.19: Ion feedback ratio as a function of drift field for several GEM voltages, at a low induction field [57].

2.4.2.3 Discharge probability

As already discussed above, the main general problem of MPGD and GEM in particular, is the development of discharges that can prevent the detector from working properly. In case of a GEM structure, the discharge starts with a sudden, radiation-induce breakdown of the gas rigidity in one GEM, normally

the last one in a cascade of multipliers. The probability of this initial discharge appears to depend on the primary ionization density and on the overall gain of the structure, but not directly on the external fields [2] [58].

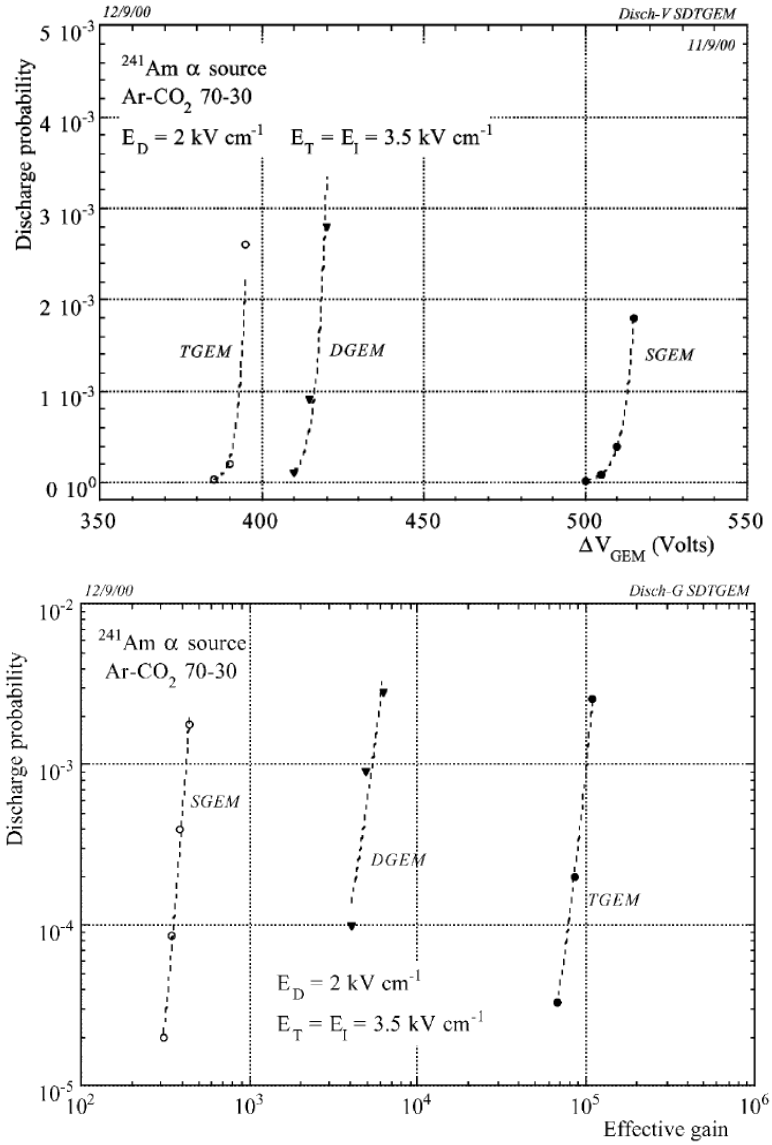

Figure 2.20: Top: discharge probability on α in single, double ad triple GEM detectors as a function of the applied voltage (equal to all GEMs); Bottom: discharge probability as a function of the total effective gain for single, double and triple GEM detectors [58].

A measurement of the discharge probability in single, double and triple GEM structures has been performed using an ^{241}Am α source, directly placed over the drift electrode and releasing $\sim 2 \times 10^4$ ionization electrons per track

[2] Here the *external fields* are the fields in the gas gaps.

in the drift gap at a rate of about 100 Hz. Fig.2.20 top shows the results of the discharge probability measurement as a function of the voltage applied to each GEM foil, for single, double and triple GEM structures. One thing that can be noticed is the decrease in the discharge voltage when moving from a single GEM structure to a multiple GEM structure, due to the fact that the avalanche size for multiple device is bigger than for a single foil device. On the other hand, looking at Fig.2.20 bottom, the maximum gain achievable before discharge is increased by almost an order of magnitude at each addition of a multiplier, reaching about 10^5 for a triple GEM structure [58]. Many discharge probability measurements have been performed in the last years, with GEM detectors of different geometries. The results obtained often vary also by orders of magnitude, underling that this phenomenon is strongly dependent from the geometry of the detector, the gas mixture used and the operational conditions [59, 60].

2.4.3 Other GEM-like detectors

Many detectors have been developed based on the GEM working principle. Two of them, the Micro-WELL detector and the Thick-GEM are the starting point of resistive devices considered for the Phase-II upgrade of the CMS muon system.

2.4.3.1 The Micro-WELL detector

The WELL detector is based on a kapton foil with etched holes, similar to those used in GEM detectors, but the bottom part of the foil is directly in contact with metallic anode readout strips. A schematic of the WELL structure is shown in Fig.2.21.

Results obtained with this prototype are well described in [62]. Here we would underline only that the detector was able to reach gains above 10^4 with different Neon/DME mixtures, with a uniformity within the 15% over the surface. In addition the rate capability has been measured with a X-Ray tube (Cr target) and no detectable gain drop has been observed up to an incident rate of 1.6×10^6 photons/mm^{2}s [61, 62].

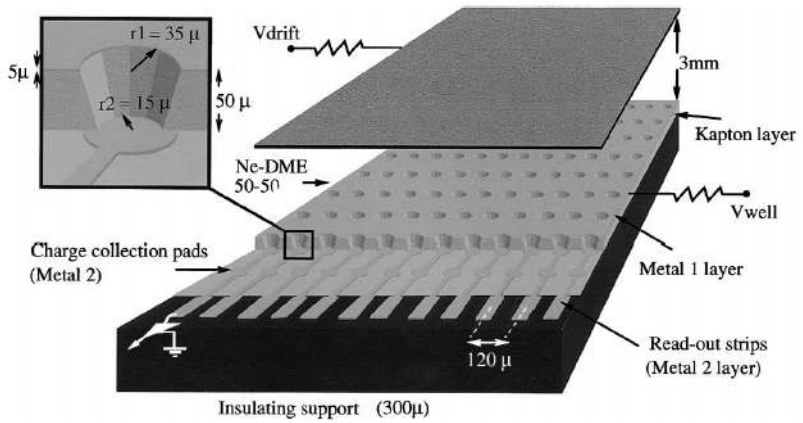

Figure 2.21: Schematic diagram of a WELL detector [62].

2.4.3.2 The THGEM

The THGEM has a hole-structure similar to the GEM, but with about 10-fold expanded dimensions (see Fig.2.22). It is economically produced by mechanically drilling sub-millimeter diameter holes, spaced by a fraction of a mm in a thin printed circuit board. A Cu hole's rim is then etched on the holes' border in order to reduce edge discharges.

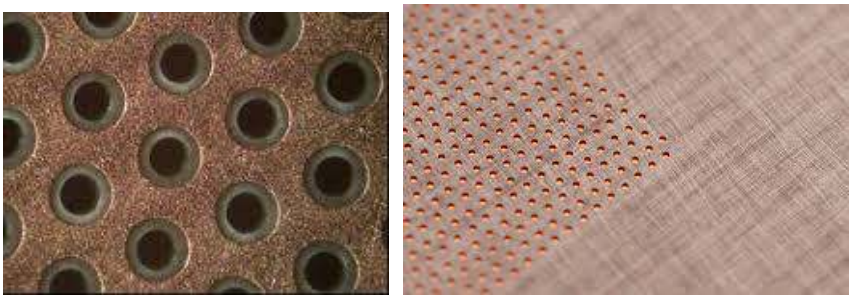

Figure 2.22: Examples of THGEM structure

The THGEM's operation principle is similar to the one of GEM: an electric potential is applied between the electrodes and creates a strong electric field within the holes. The shape of the field is responsible for an efficient focusing of ionization electrons into the holes and their multiplication by a gas avalanche process. The electron collection is more effective than in GEM because the THGEM's hole-diameter is larger than the electron's transverse diffusion range when approaching the hole. The efficient collection and transmission of electrons offers the possibility to use several THGEM elements in cascade. This leads to higher detector gains at lower voltage bias per single

THGEM element and thus to higher operation stability [63].

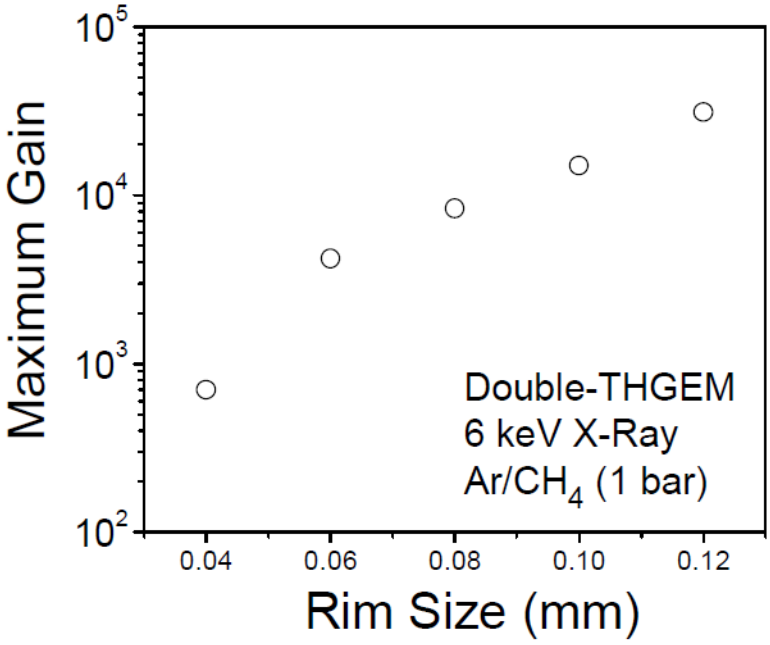

Figure 2.23: Maximum gain achievable versus rim size. Detector parameters: thickness = 0.4 mm, holes pitch = 1 mm, holes diameter = 0.3 mm [63].

As shown in Fig.2.23, the size of the etched rim around the THGEM holes is fundamental in order to reduce the discharge probability and to reach higher voltages and higher detector gains. The maximum attainable gain increases exponentially with the rim-size. This effect, as well as the gain stability in time, is due, for example, to the electric field distribution outside the hole, the charging up of the insulator, the type of material, the quality of hole's wall surface, the surface-quality of the Cu-edge [63].

Due to the large hole's size, efficient electron transport and negligible photon and ion feedback, the THGEM has shown to reach stable operation in a different gas mixtures. High gains, $>10^4$ and $>10^5$, were reached with single photoelectrons in single- and in double-THGEM detectors, respectively, with Ar/CH_4 95%/5% and Ar/CO_2 70%/30%. For few hundreds of primary electrons induced by a X-Ray (5.9 keV), the same detectors reached gains of $>10^3$ and $>10^4$ in Ar/CH_4 95%/5%. With this last gas mixture, the THGEM reached rate capabilities greater than 1 MHz/mm^2 at effective gains of $\sim 10^4$. Moreover, gains above 10^4 were also achieved with a double-THGEM operated in pure Ar, Kr, Xe, Ne and Ar/Xe 95%/5% [63].

2.4.4 New generation of MPGD

As GEM and Micromegas have been considered for the application in many high-energy physics experiments, a lot of R&D have been dedicated to these technologies. However many new ideas were developed in recent years (an exhaustive review is given in [61]), here we will introduce only the micropattern gas detectors with resistive electrodes. As already extensively stressed above, the main problem in operating MPGD is that, without taking precise precautions, they can easily be damaged by sparks. Among the several methods developed for protecting MPGD, one possibility is to use resistive electrodes instead of metallic ones, in order to reach higher gains in the single structure without the problem of discharges. Example of these new devices are the μRWELL detector [89] and the Fast Timing Micropattern (FTM) detector [106] that are being considered as *optional solution* for the GE2/1 and ME0 stations of the CMS muon system respectively and will be presented in detail in Chapter 5.

2.5 Detector sensitivity to background

One parameter that is often taken in consideration before the installation of a particular technology in an experiment is its behavior in a radiation-filled environment. The main components are often neutrons and gammas produced by the interactions of the particle generated in the collisions with the material composing the apparatus. Apart from the radiation hardness, the *sensitivity* of the detector to neutrons and gammas is a fundamental standard to be evaluated: it represents the probability for a given particle to generate a spurious signal in the detector. Indeed, not only charged particles can induce a signal into a gas detector, but also neutrals: they interact mainly with the material composing the structure of the detector, producing secondary charged particles that can ionize the gas and induce a detectable signal. Of course all these interactions disturb the operation of the chambers and act as an irreducible background for the measurements to be performed. In particular the expected *hit rate* can be defined as the convolution between the sensitivities of the detector and the background fluxes in the region in which they should be installed: if the hit rate is too high and considered not affordable for the kind of measurements the Collaboration wants to perform, the sensitivity can

become a key point for the choice of the technology.

The sensitivity depends on the materials that compose the detector, as well as on the energy and the direction of the particle that crosses the chamber, as different processes are in this way involved in the interaction.

We will discuss here the examples of two different detectors interesting in the framework of the CMS muon system, RPCs and Triple-GEMs. In the CMS muon system, both technologies are exposed to a background composed mainly by neutrons and gammas. For this reason, the CMS Collaboration developed intensive studies focused on the evaluation of the sensitivity, both through simulations and measurements.

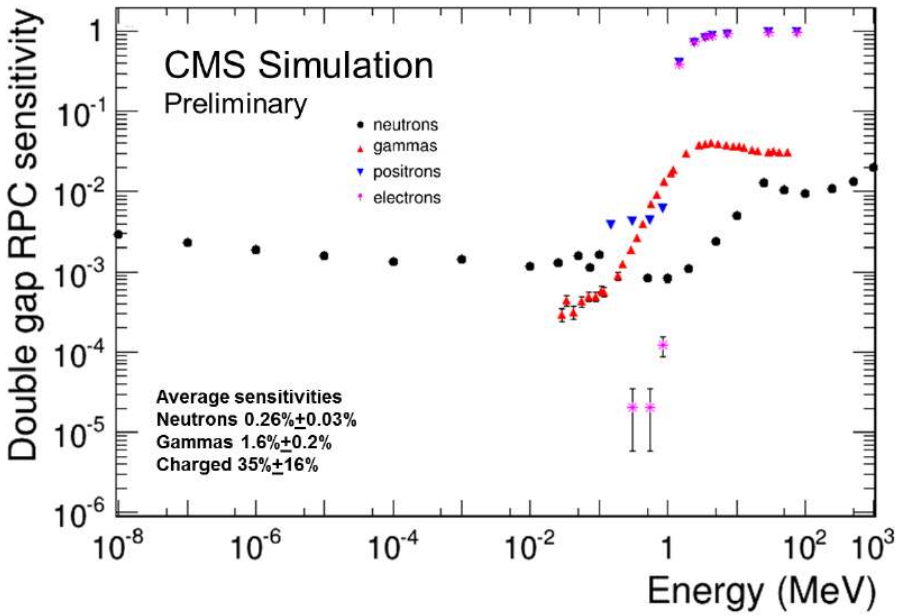

Figure 2.24: Sensitivity of double gap RPC detectors as a function of the energy of the incident particle, for neutrons, gammas, electrons and positrons [66].

Starting from RPCs, a neutron and gamma sensitivity measurement on a CMS double gap RPC was performed with a ^{252}Cf source, releasing neutrons of average energy of about 2.1 MeV and gammas of average energy 1.5 MeV. The results obtained are a neutron sensitivity of $(0.63 \pm 0.02) \times 10^{-3}$ and a gamma sensitivity of $(14.0 \pm 0.5) \times 10^{-3}$ [65]. Even if dedicated simulations were performed at the time of the measurement, recently they have been re-proposed in order to extend the study to Triple-GEM detectors. The simulation computes

the sensitivity as

$$sensitivity = \frac{\#\ of\ events\ generating\ a\ signal\ in\ the\ detector}{\#\ of\ generated\ events} \tag{2.21}$$

where a signal is considered generated when at least one charged particle is produced inside the active gas gap. This is in general an overestimation of the sensitivity value, as it assumes that every time a charge is created inside the gap a detectable signal is developed.

The results of the sensitivity of double gap RPC over the whole range of energies expected in the CMS muon system is shown in Fig.2.24.

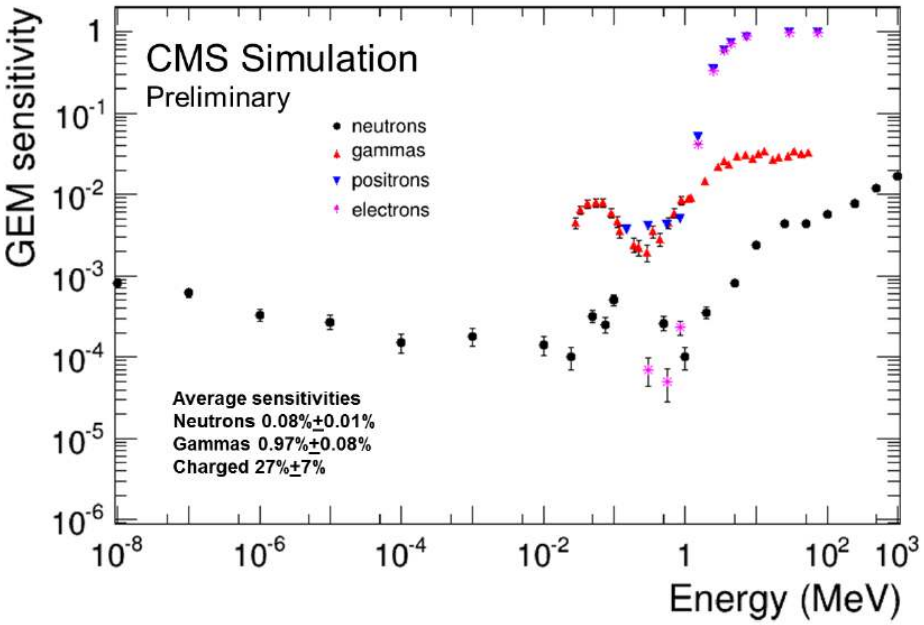

Figure 2.25: Sensitivity of Triple-GEM detectors as a function of the energy of the incident particle, for neutrons, gammas, electrons and positrons [66].

The study was then extended to Triple-GEM detectors, in order to understand if such a different technology would provide different results in this field. The results of the simulation performed with a Triple-GEM chamber are shown in Fig.2.25.

Even if the order of magnitude of the sensitivities between the two technologies is comparable, the different trend of the two plots underlines the differences between the processes involved in the interactions.

Fig.2.26 shows the processes involved in the interactions of neutrons with a double gap RPC, on the top, and a Triple-GEM, on the bottom, as a function

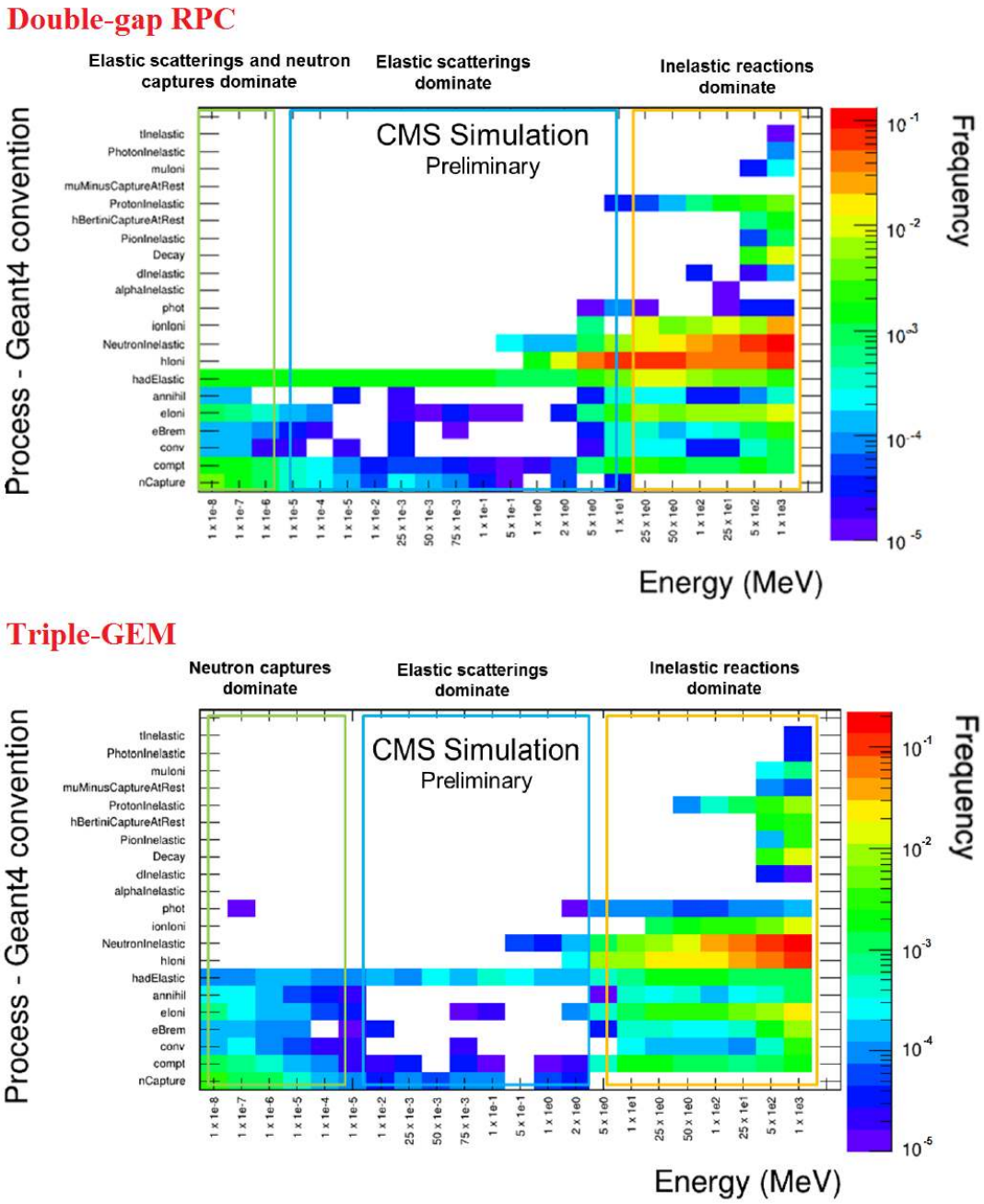

Figure 2.26: Processes involved in the interactions of neutrons in double gap RPC (top) and Triple-GEM (bottom) [66]

of the energy of the incident particle. Both the plots can be divided in three regions: for incident neutron energies between 10 meV and 10 eV the prevalent interactions are neutron capture on hydrogen and other heavy nuclei: in such a reaction, generally represented by $A(n,\gamma)A+1$, the nucleus absorbs the neutron and goes into an excited state, finally returning to the stable state

with the emission of a γ-ray [43]. The other possible reaction in this region is the elastic scattering on hydrogen nuclei with the production of a recoil photon, which become dominant in the intermediate energy range, up to few MeV. Indeed, as we can observe from the cross section of the two processes in Fig.2.27 and 2.28, the contribution of radiative capture is relevant at very low energies, then it decreases linearly, while the scattering cross section has a plateau in the intermediate region that enhances its importance.

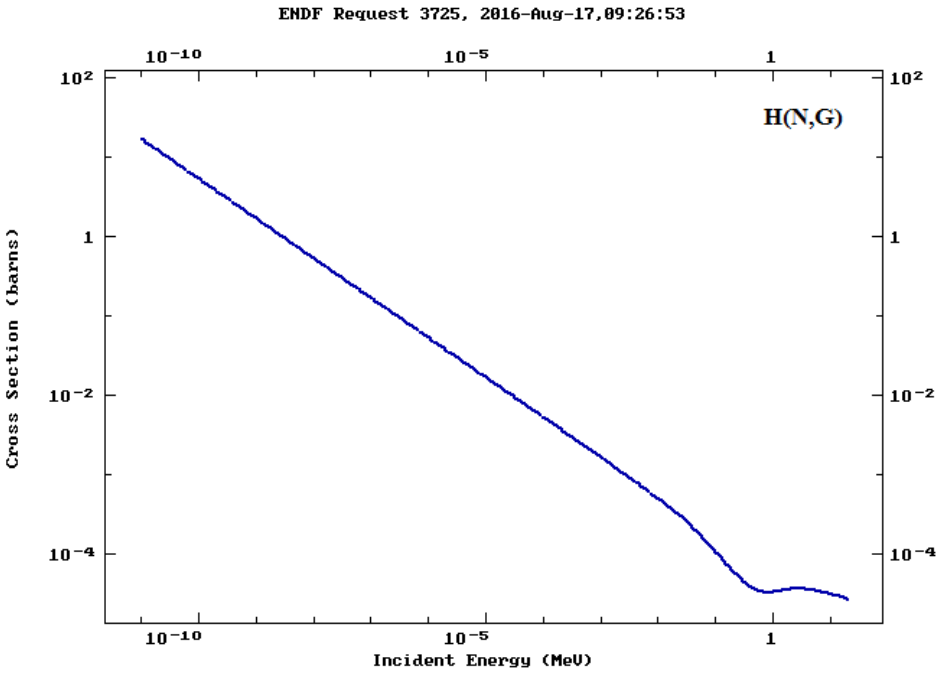

Figure 2.27: Radiative capture neutron cross section on hydrogen as a function of the incident neutron energy (database ENDF/B-VII).

Finally, the high energy range includes neutron-induced nuclear reactions, leading to the fragmentation of the target nucleus and the production of nuclear fragments.

The main difference in the two technologies is in the elastic scattering process, which is enhanced in double gap RPCs with respect to Triple-GEM. This is a consequence of the presence of bakelite in RPC, which is a material richer in hydrogen with respect to those included in a Triple-GEM. The outcome is an increase in neutron sensitivity in RPCs with rispect to GEMs, as can be observed in Fig.2.24 and 2.25 [66].

Moving to the gammas instead, in the low energy range, up to 0.3 MeV, the interactions are dominated by the photoelectric effect, which consists in

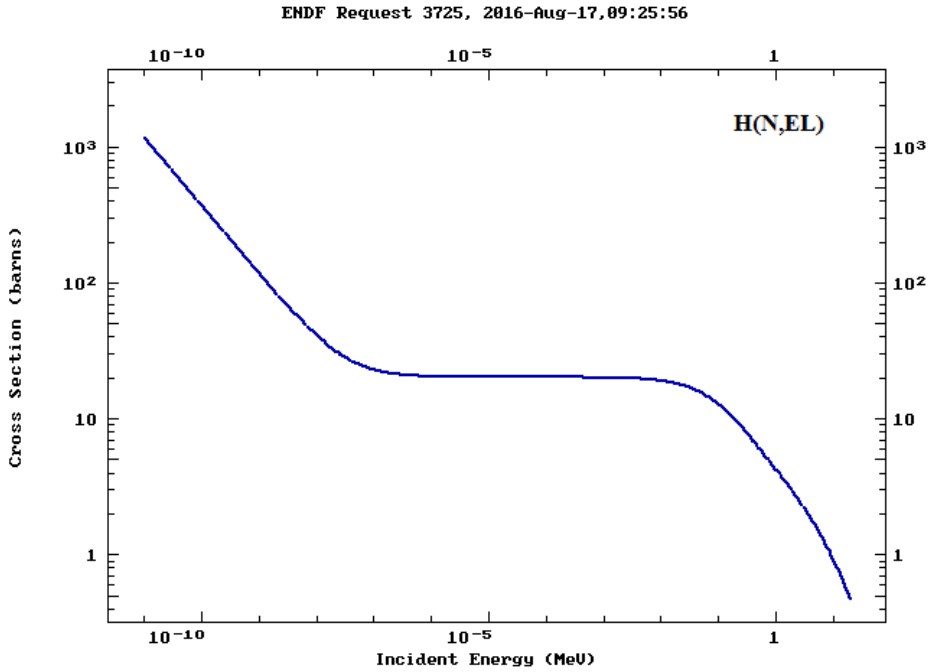

Figure 2.28: Elastic scattering neutron cross section on hydrogen as a function of the incident neutron energy (database ENDF/B-VII).

the absorption of a photon by an atomic electron with the subsequent ejection of the electron from the atom. The energy of the outgoing electron is

$$E = h\nu - B.E. \tag{2.22}$$

where $B.E.$ is the binding energy of the electron [40]. The cross section of the photoelectric effect has a strong dependence for the Z of the target nucleus, while it has a strong inverse relationship with the energy of the incident photon

$$\sigma_{pe} \propto \frac{Z^n}{E_\gamma^{3.5}} \tag{2.23}$$

where n is between 4 and 5.

Compton scattering, i.e. the inelastic scattering of photons from free or loosely bound electrons at rest, is enhanced in the intermediate energy region. Its probability per atom of the absorber depends on the number of electrons available as scattering targets, so it increases linearly with Z [41]. Moreover it has a strong dependence from the scattering angle θ and its differential cross

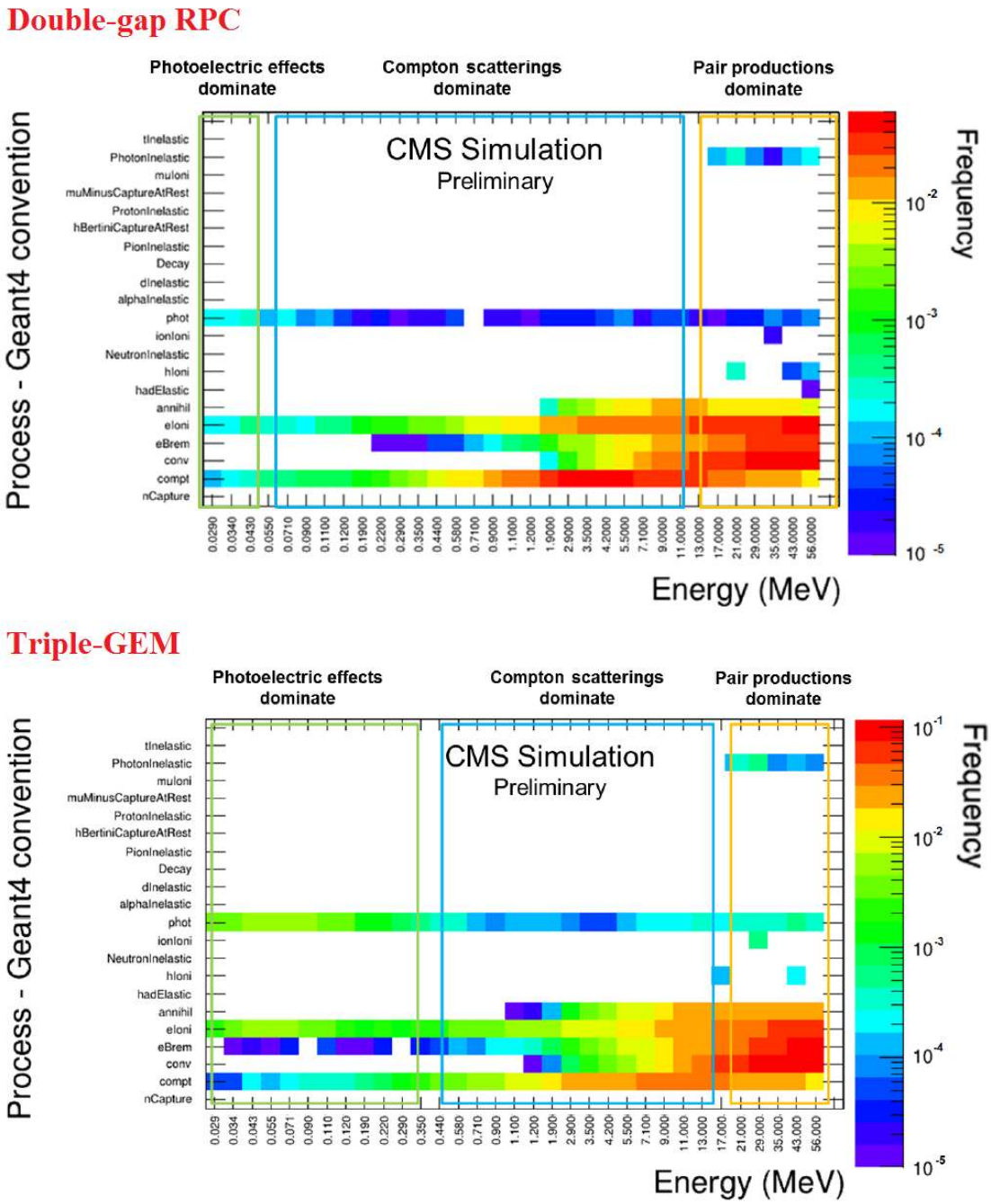

Figure 2.29: Processes involved in the interactions of gammas in double gap RPC (top) and Triple-GEM (bottom) [66].

section can be calculated through the Klein-Nishina formula [43]

$$\frac{d\sigma_c}{d\Omega} = \frac{r_0^2}{2}\left[\frac{1+\cos^2\theta}{(1+\alpha(1-\cos\theta))^2}\right]\left[1+\frac{4\alpha^2\sin^4(\theta/2)}{(1+\cos^2\theta)(1+\alpha(1-\cos\theta))}\right] \quad (2.24)$$

For energy higher than 13 MeV the dominant process becomes the pair production, which is in general energetically possible when the energy of the the photon exceeds twice the rest-mass energy of an electron (1.02 MeV), but which actually remains of very low probability until the photon's energy reaches several MeV. In this reaction the photon disappears and is replaced by an electron-positron pair: there is not a simple expression for the probability of pair production per nucleus, but its magnitude varies as the square of the atomic number of the absorber [41].

What can be observed is that in double gap RPCs, the photoelectric effect is suppressed with respect to GEMs: indeed RPC materials have generally a lower Z and the gas mixture does not contain argon, which is the main responsible for photoelectric effect in Triple-GEM. The enhancement of photoelectric effect on argon in Triple-GEM chambers can be observed also in Fig.2.25 in the energy range 50-100 keV, where a bump in the gamma sensitivity is clearly noticeable [66].

This brief analysis demonstrates that, due to quite different materials contained in the two technologies, the processes involved in the generation of spurious signals can be various. However, the difference in the total expected sensitivity is not relevant, so the installation of both the technologies can be considered affordable in the CMS environment.

Chapter 3

GEM detectors and the GE1/1 station

The GE1/1 station is the first high-η region station foreseen in the upgrade plan of the CMS muon system. It will be installed in LS2, in a gap originally foreseen for RPC detectors between the hadron calorimeter and the CSC ME1/1 chambers. Its aim will be the reduction of the L1 muon trigger, allowing the measurement of the bending angle at trigger level, as well as the improvement of the tracking performance in this harsh environment region. Moreover it will re-establish the missing redundancy in the region $1.6 < | \eta | < 2.2$ [29].

3.1 GEM detectors for the GE1/1 station

The GE1/1 station will be instrumented with Triple-GEM detectors, whose principle of operation and characteristics have been already discussed in detail in Section 2.4.2. The mechanical design of a complete GE1/1 Triple-GEM detector is shown in Fig.3.1. The detector is composed by drift board made of PCB, three GEM foils and a readout board, again of PCB, and it is laterally closed by an outer frame. The structure is completed by a cooling system, made of a copper pipe together with copper pads thermally connected with the heat sources, an optical board for the transmission of the signals and an aluminum shielding to protect the detector (in blue in the picture).

In the GE1/1 muon station, a pair of Triple-GEM chambers is combined to form a *superchamber*, shown in Fig.3.2 left, that provides two measurement

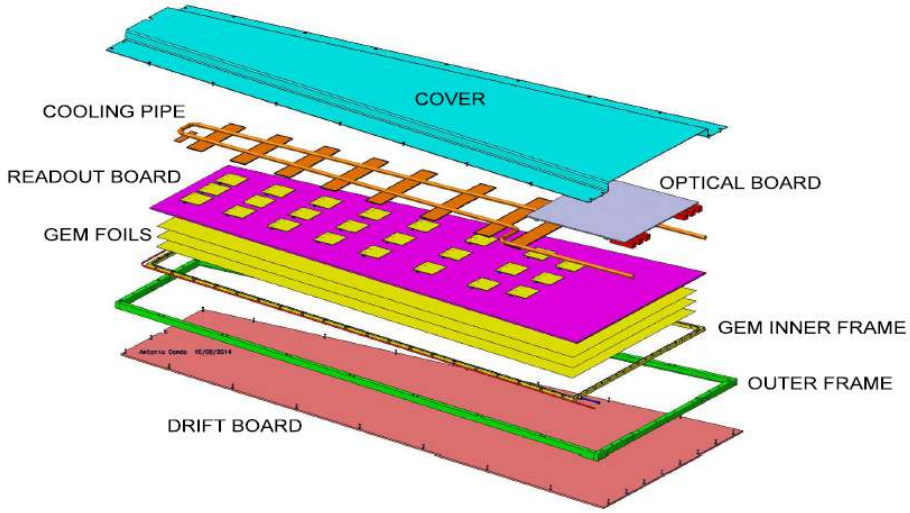

Figure 3.1: Exploded view of the mechanical design of a single GE1/1 chamber [29].

planes in the muon endcap to complement the existing ME1/1 detectors and maximizes the detection efficiency.

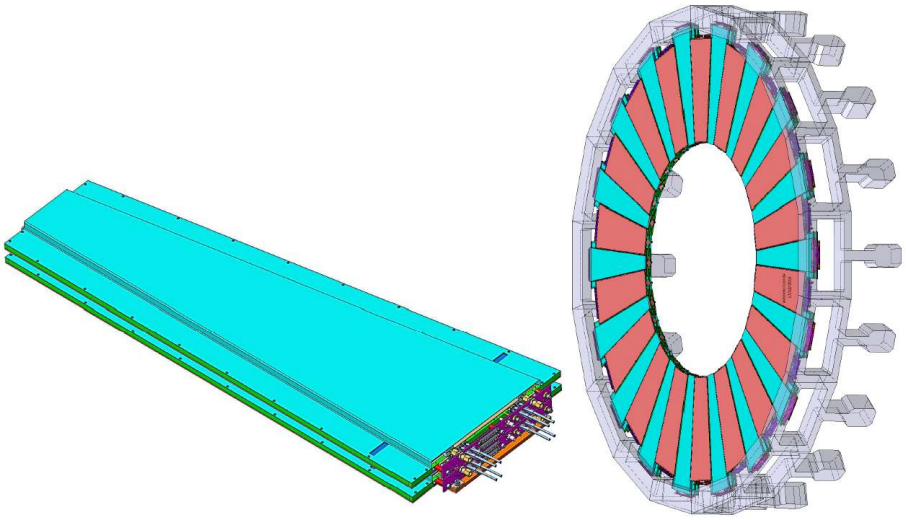

Figure 3.2: Left: A pair of GEM chambers form a superchamber. Right: Long and short chambers are combined to maximize the instrumentation within given mechanical constraints in the endcap [29].

The superchambers alternate in ϕ between long ($1.55 < |\eta| < 2.18$) and short ($1.61 < |\eta| < 2.18$) versions, as requested by the mechanical envelope of the existing endcap, in order to maximize the η coverage. Each endcap holds

18 long and 18 short superchambers, for a total of 72 ten-degree chambers per endcap of CMS. One endcap is represented in Fig.3.2 right. The superchambers will be installed in slots originally foreseen for RPC chambers, in the gap between the hadron calorimeter and the CSC ME1/1 chambers in the YE1 *nose* (see Fig.3.3).

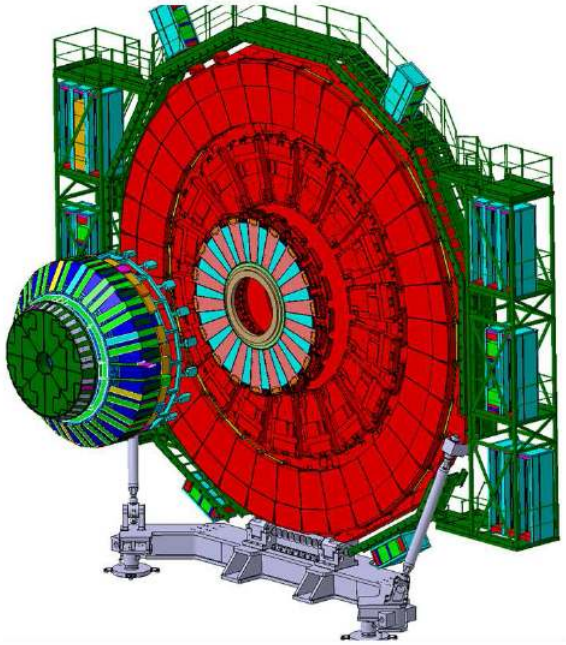

Figure 3.3: Overview of the GE1/1 station [29].

3.1.1 Detector development

The fundamental step in the R&D program for the GE1/1 station was the demonstration that large-area GEM foils could be manufactured reliably and that Triple-GEM detectors built with such foils could satisfy the performance requirements. Five generations of prototype detectors (see Fig.3.4) were built and tested in 2010-14 with one generation being developed every year based on the experience with the previous generation [67, 68, 69, 70].

The GE1/1-I prototype was the first 1 m-class GEM detector ever constructed and operated [70]. Components were glued together and spacer ribs were used to keep the GEM foils apart; it had only 8 readout sectors in total. In the GE1/1-II the readout segmentation was increased to 24 sectors arranged in eight η-partitions and three columns. Each η-partition comprised 384 radial strips with 455 μrad angular pitch. The foil gap configuration was

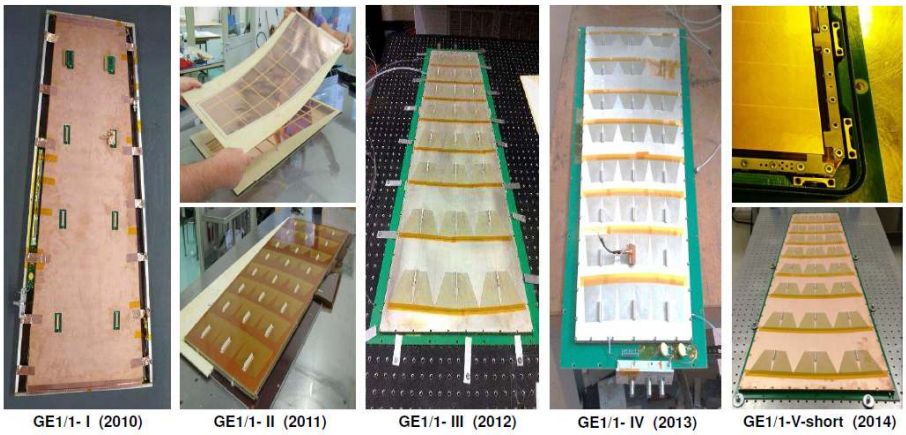

Figure 3.4: Five generations of GE1/1 prototype chambers constructed and tested by the GEM collaboration in 2010-2014. The split figures for GE1/1-II and GE1/1-V demonstrate the evolution from construction using spacer frames to purely mechanical stretching of GEM foils without any spacers [29].

changed from 3/2/2/2 mm to 3/1/2/1 mm to speed up the signal [67]. The GE1/1-III prototype was the first detector in which foils were stretched purely mechanically against the outer detector frame, but this frame was made from several pieces and was glued to the drift board [68]. This generation was also the first prototype to use a miniaturized ceramic high voltage divider for powering. When bolting the readout board onto the outer frame in this design, the O-ring acted as a fulcrum creating a torque on the board as the bolts were tightened. This caused the readout board to deform slightly after assembly, which in turn provoked a response non-uniformity across that chamber prototype, as the foil gap sizes were not kept uniform enough. In the GE1/1-IV prototype, before assembly both readout and drift boards were pre-bent in the direction opposite to the bowing observed in the GE1/1-III in an attempt to compensate for the bending that occurs after assembly. They were bolted to the outer frames and sealed with O-rings making the GE1/1-IV the first large-area GEM detector produced without gluing any components. The problem has been rectified in the GE1/1-V prototype design by tensioning the foils against independent *pull-out* pieces. The drift and readout boards are now bolted onto the pull-out pieces. The outer frame is made from a single piece and only serves as a wall for the gas volume; it is sealed against readout and drift boards with O-rings. The planarity of the foils stretched with this new method has been verified using a system of Fiber Bragg Grating (FBG), a kind of distributed Bragg reflector made of short segments of optical fibers. FBG

are able to reflect particular wavelength of light and transmit all the others, therefore they can be used as a strain measurement tool, since variation of the Bragg grating translate into a different light frequency response. With this system, the Collaboration was able to demonstrate that applying the correct tension across the GEM stack with the new tensioning system, a uniform gaps spacing is obtained [71], fundamental in order to get uniform performance all over the detector area.

This last prototype design with a few improvements of details, finally called GE1/1-VI and produced in the two versions, *long* and *short*, is being adopted as the final design of the GE1/1 Triple-GEM chambers [29].

3.1.2 Obtained performance

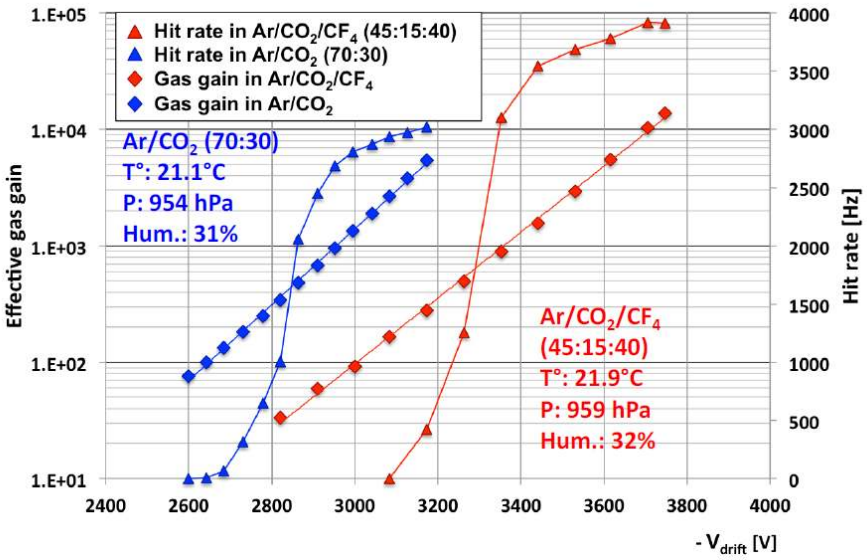

Figure 3.5: Measured gas gains (diamonds) and hit rates (triangles) as a function of high voltage applied to the drift electrode of a GE1/1-IV. Measurements with Ar/CO_2 70%/30% (blue) and with $Ar/CO_2/CF_4$ 45%/15%/40% (red) gas mixtures are displayed. The log scale (left) applies to the gain whereas the rates are plotted on a linear scale (right) [29].

One of the fundamental parameters for the operation of GEM detectors is the gas gain, which was measured for each GE1/1 prototype generation. A high-rate X-ray generator is used to irradiate the GEM chamber, then the gas gain can be calculated from measured hit rates and anode currents, with the

formula

$$G = \frac{I_{net}}{R_{net}^{max} \times N_p \times e} \tag{3.1}$$

where I_{net} is the net current, i.e. with noise subtraction, with the detector powered, R_{net}^{max} is the maximum net measured rate, e is the electron charge and N_p in the number of primaries produced in the interaction of the incident particle.

Fig.3.5 shows gain measurements performed at CERN for a GE1/1-IV operated at different high voltages applied to the drift electrode for both Ar/CO_2 70%/30% and $Ar/CO_2/CF_4$ 45%/15%/40% gases. The plot also shows the hit rates observed in the GE1/1-IV for a fixed rate of incident X-rays, underlining the beginnings of rate plateau where the chamber starts operating with full efficiency.

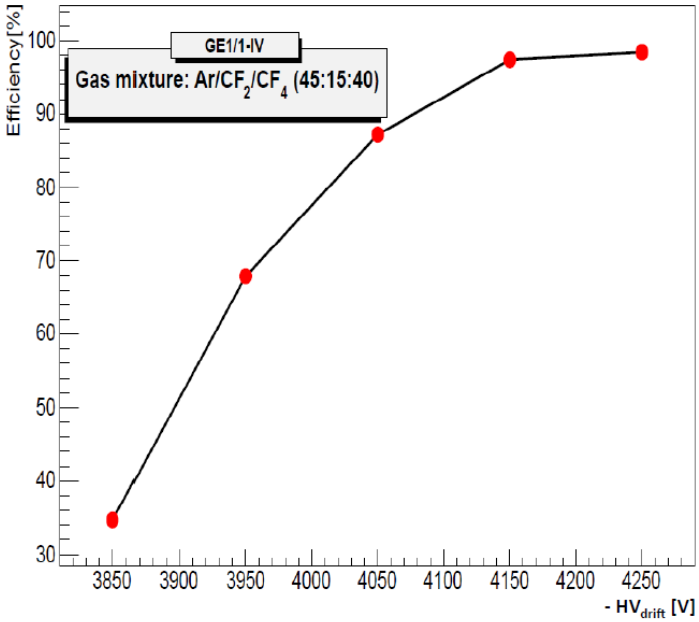

Figure 3.6: Measured detection efficiencies of GE1/1 prototypes for charged particles. Eff. vs. HV applied to drift electrode when GE1/1-IV is operated with $Ar/CO_2/CF_4$ 45%/15%/40% and read out with VFAT2 chips configured with 0.8 - 1.2 fC strip-hit thresholds [29].

Efficiency measurements for charged particles is displayed in Fig.3.6. A GE1/1-IV prototype is able to reach a plateau efficiency of 98% for pions when operated with $Ar/CO_2/CF_4$ 45%/15%/40% and read out with VFAT2 chips [99]. Similar results have been obtained with Ar/CO_2 70%/30% and

analog readout [69].

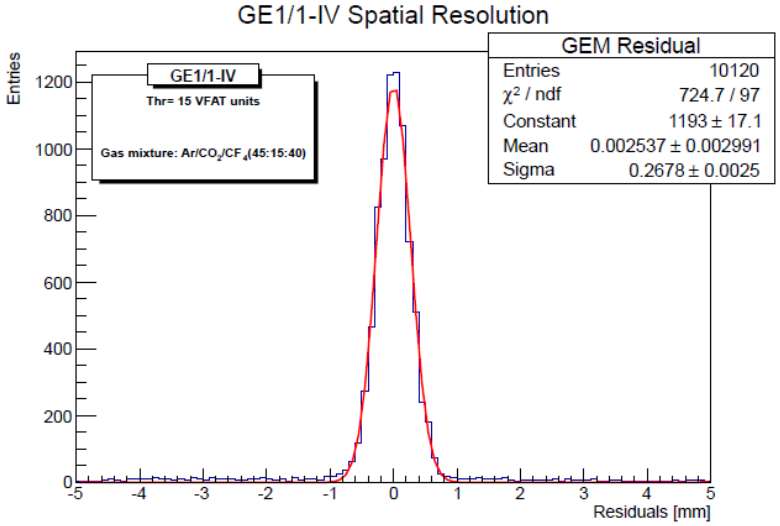

Figure 3.7: Track-hit residuals measured in central sectors of GE1/1 prototypes at r $\sim$ 1.9 m. Exclusive residuals in azimuthal ϕ-direction measured with a pion beam at CERN when a GE1/1-IV is operated with $Ar/CO_2/CF_4$ 45%/15%/40% and read out with binary-output VFAT2 chips [29].

The required angular resolution is 300 μrad as an upper limit imposed by the trigger. Indeed it is the minimal precision with which the difference $\Delta\phi$ = ϕGE1/1 - ϕME1/1 of the angular muon positions measured in GE1/1 and ME1/1 must be determined to achieve the intended trigger rate reductions. In addition to the intrinsic GEM resolution, the intrinsic ME1/1 resolution as well as the ME1/1 and GE1/1 chamber alignments will contribute to the uncertainty in the $\Delta\phi$ measurement. For this reason, the intrinsic GE1/1 resolution must be significantly better than 300 μrad to provide a comfortable safety margin for this crucial performance parameter. The angular resolution for GE1/1 prototypes with an angular strip pitch of 455 μrad and binary signal readout was measured to be 137 $\pm$ 1 μrad. As shown in Fig.3.7, in a central sector of the GE1/1 this correspond to a spatial resolution of $\sim$ 270 μm[1]. As this is an appropriate performance, the final GE1/1 design adopts an angular strip pitch very close to that value.

[1]The GE1/1 chambers are trapezoidal in shape as they are designed to cover a ring in the CMS endcap. Each η-partition of the readout board of a chamber contains 384 radial strips, which have a constant angular dimension and, as a consequence, are narrower in the high-η region and broader in the low-η region. For this reason, the angular resolution remains constant over the whole chamber, while the spatial resolution varies in the different η-partition. The estimation of the spatial resolution, in μm, is so usually performed in a

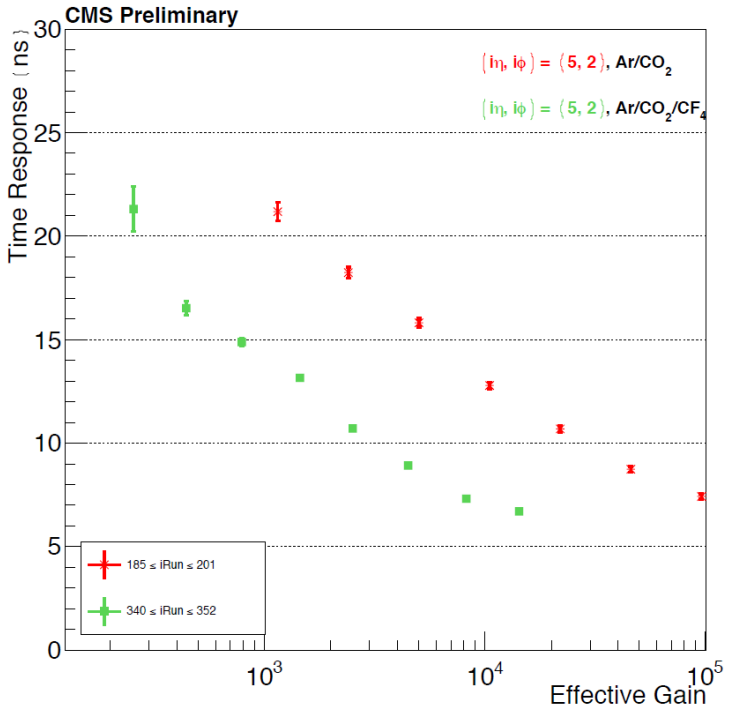

Figure 3.8: Time resolution measured with a GE1/1-IV prototype as a function of the gain.

The time resolution was measured with a GE1/1-IV, during the 2014 test beam: in Fig.3.8 the red series represents the results obtained with Ar/CO_2 70%/30% in a central sector of the chamber. Pushing the detector at very high gain it is even possible to reach 7 ns time resolution, while operating the detector at a standard gain value (2-3 $\times$ 10^4) the time resolution is of the order of 10 ns. With $Ar/CO_2/CF_4$ gas mixture, instead, GE1/1 could reach 6 ns time resolution at a reasonable gain, compatible to what measured in the past by other Collaborations developing Triple-GEM detectors, like LHCb [103, 105].

Another feature to be confirmed was the high-rate capability of the GE1/1. The gain vs. incident rate was measured using a medium-intensity 22 keV Ag X-ray source and a high-intensity 8 keV Cu X-ray source. A GE1/1-III detector, operated with Ar/CO_2 70%/30%, was illuminated with the Cu source and the gas gain was measured via the anode current produced in the chamber during this irradiation. The gain has been calculated with the formula 3.1: results in Fig.3.9 show that it is observed to be constant for an incident

central η-partition of the chamber, in order to have a reliable average value.

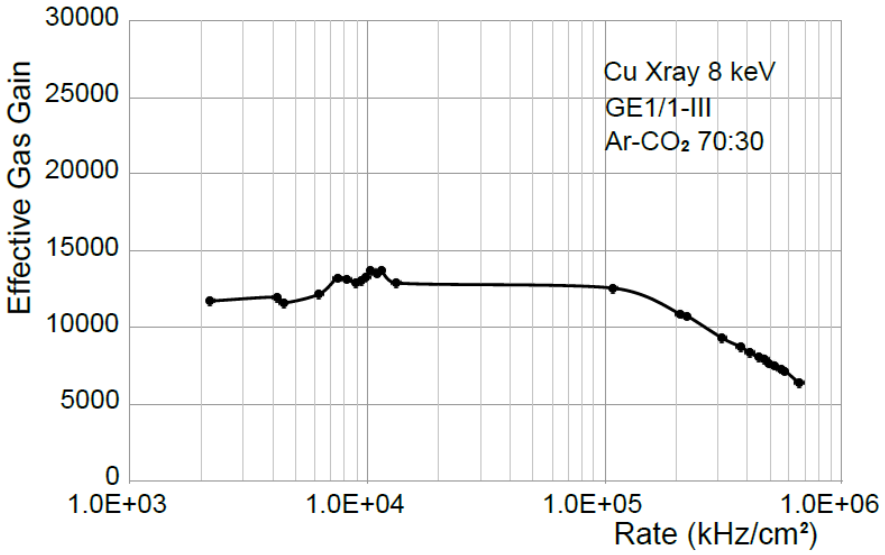

Figure 3.9: Effective gas gain as a function of the incident photon rate measured in a GE1/1-III detector operated with Ar/CO_2 70%/30% and irradiated with an 8 keV X-ray source with Cu anode [29].

particle rate up to 100 MHz/cm^2. The gain begins to drop only above that value. This result confirms that the GE1/1 chambers will easily operate in the $1.6 < \mid \eta \mid < 2.2$ forward muon region of CMS, where a maximum rate on the order of 10 kHz/cm^2 is expected [29].

3.2 Behavior of GEM detectors in the CMS background

The high collision rate at the new energy and luminosity regime of the LHC gives rise to an extreme radiation environment. High background particle rates complicate signal identification and can have a significant impact on the performance of the detectors themselves, in extreme cases making them inoperable. The dominant contribution to the CMS cavern backgrounds is due to neutrons and the secondary particles arising from neutron interactions with matter. This background has a long lifetime as neutrons can propagate for seconds without interacting. Neutrons arise from the interactions of hadrons produced in primary $p-p$ collisions with the material of the beam pipe and the structures positioned in the very forward region. The spectrum of these long-lived neutrons ranges between the thermal region and a few GeV: it is

simulated using the FLUKA simulation tool [26] and is shown in Fig.3.10. The slow neutron capture by nuclei with subsequent photon emission in the detector material yields photons and, consequently, electrons and positrons capable of producing detectable amounts of ionization in gas detectors [29].

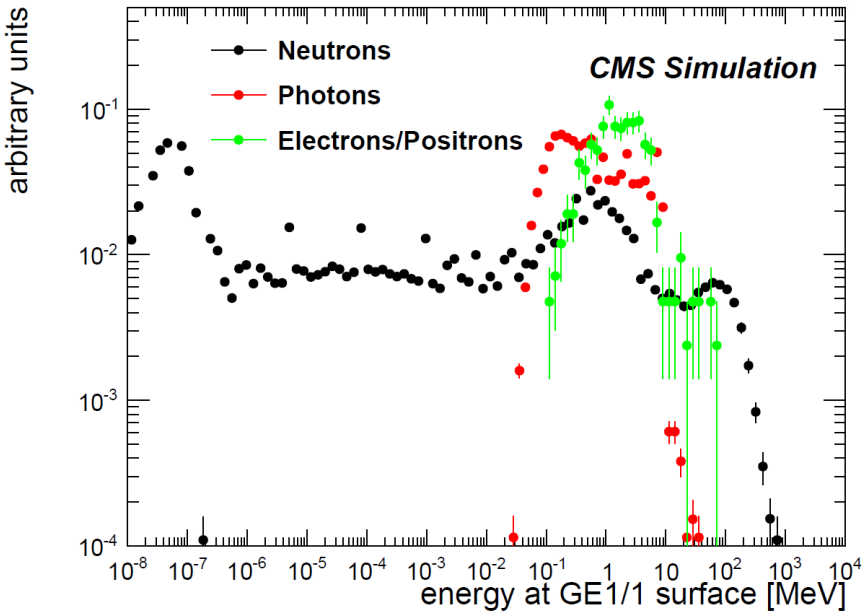

Figure 3.10: The energy spectrum of incident particles crossing the GE1/1 chambers predicted using FLUKA [29].

In order to calculate the expected hit rates in the GE1/1 station, the fluxes simulated with FLUKA have to be convoluted with the chamber sensitivities in order to obtain the hit rates. The sensitivity of the GE1/1 chambers to neutrons, photons, electrons and positrons has been evaluated with a standalone simulation using Geant4 [77].

The modeled detector was a GE1/1 superchamber complete with a full material description. In the simulation, particles of fixed energy and given type cross the outer surfaces of the superchamber with uniform density over the outer surface of the chamber frame and with the incident angles distributed according to the angular distribution obtained in the FLUKA simulation study. The simulation is repeated for each particle type over a broad range of energies. Events, in which at least one charged particle reaches the drift volume or the first transfer gas gap of one of the two GEM chambers included in the superchamber, are assumed to generate a valid signal in that chamber. The results of this simulation is shown in Fig.3.11.

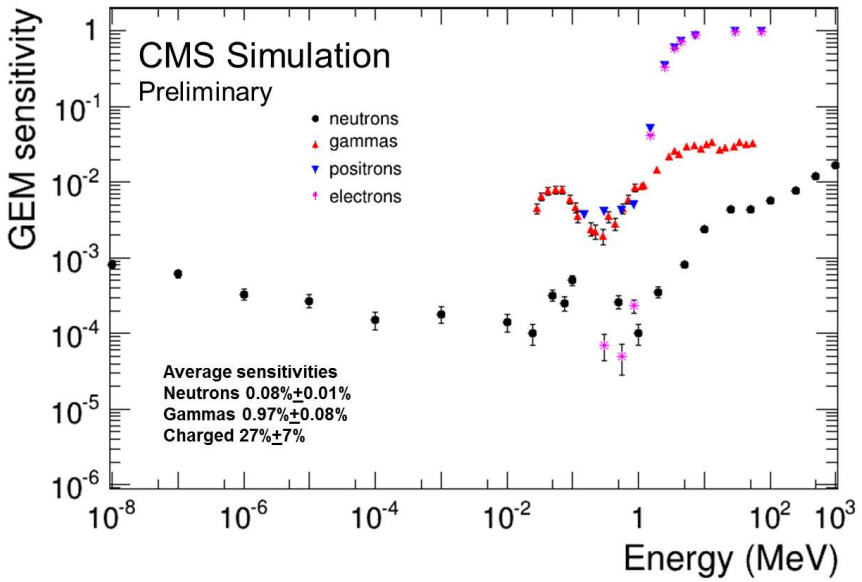

Figure 3.11: Energy-dependent sensitivity, defined as the probability to produce a measured hit in the chamber, of the GE1/1 chamber to neutrons, photons, electrons, and positrons, as a function of the incident particle energy. [29].

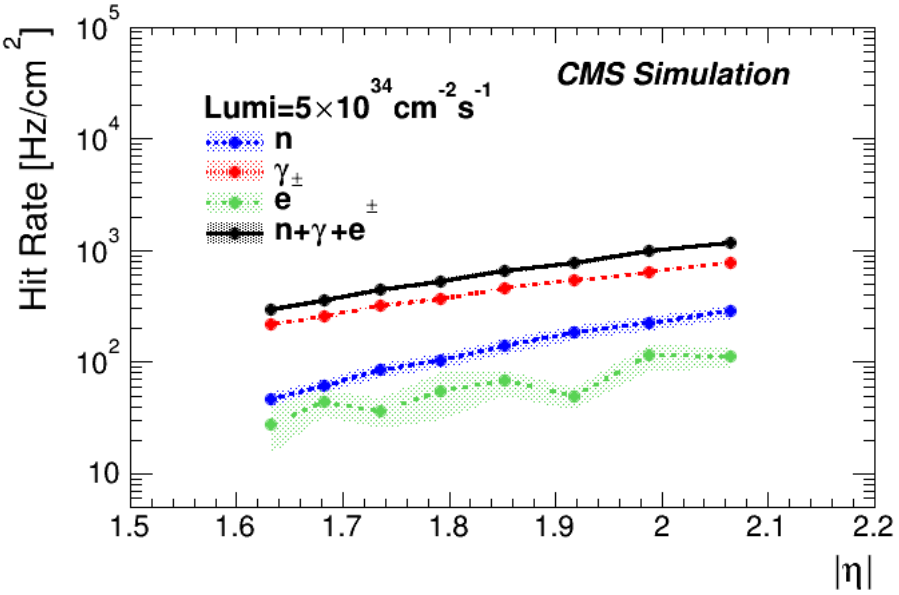

Figure 3.12: The expected contribution to the GE1/1 detector per chamber hit rate associated with the backgrounds induced by long lived neutrons for instantaneous luminosity of 5 $\times 10^{34} cm^{-2} s^{-1}$ as a function of pseudorapidity [29].

The final detector sensitivities is then obtained averaging over both the angular and energy spectra of the background particles. The detector hit rates are then calculated as the particle flux weighted by the corresponding average sensitivity. The results for the GE1/1 case are plotted in Fig.3.12 [29].

3.3 Study of behaviour of GEM detectors in gamma field at GIF++ facility

A long-term aging test was performed by the Collaboration at the Gamma Irradiation Facility (GIF) at CERN, with a ^{137}Cs source emitting gamma rays of 662 keV. A GE1/1 prototype detector was placed 30 cm from the source (see Fig.3.13), where it received an incident gamma rate on the order of 100 kHz/cm^2 with an observed pulse rate from gammas interacting in the detector of a few kHz/cm^2. The detector was operated at a gas gain of 2×10^4 and was flushed with the standard $Ar/CO_2/CF_4$ 45%/15%/40% gas mixture at 0.5 liters/hr.

After the GIF closure, the entire setup was moved to the GIF++ facility, where it was subjected to the intense flux of a ^{137}Cs source of 14 TBq. A second step of the study was performed with a GE1/1 supplied with Ar/CO_2 70%/30%, placed at 50 cm from the irradiator, where the estimated incident flux was just below 10^8 Hz/cm^2 [87].

The analysis was then focused on the identification of possible variation of the gain of the chamber, induced by a radiation damage. The effects of temperature and pressure, which can cause a variation of the density of the gas and, as a consequence, of the gain, were taken into account too.

With $Ar/CO_2/CF_4$ 45%/15%/40% gas mixture, the GE1/1 detector accumulated a total charge of 53 mC/cm^2, without significant variation of its gain, apart from small fluctuations within 3% of its initial value [87, 29]. Partial results of this irradiation campaign is shown in Fig.3.14, where no ageing effects can be observed up to 10 mC/cm^2. Similar results were obtained with the Ar/CO_2 70%/30% gas mixture: the GE1/1 detector accumulated a total charge of 55 mC/cm^2 in 6 months of continuous irradiation, without relevant variations in its gain.

Both the tests therefore proved that the Triple-GEM technology, in the GE1/1 configuration, will be able to survive to the harsh CMS environment,

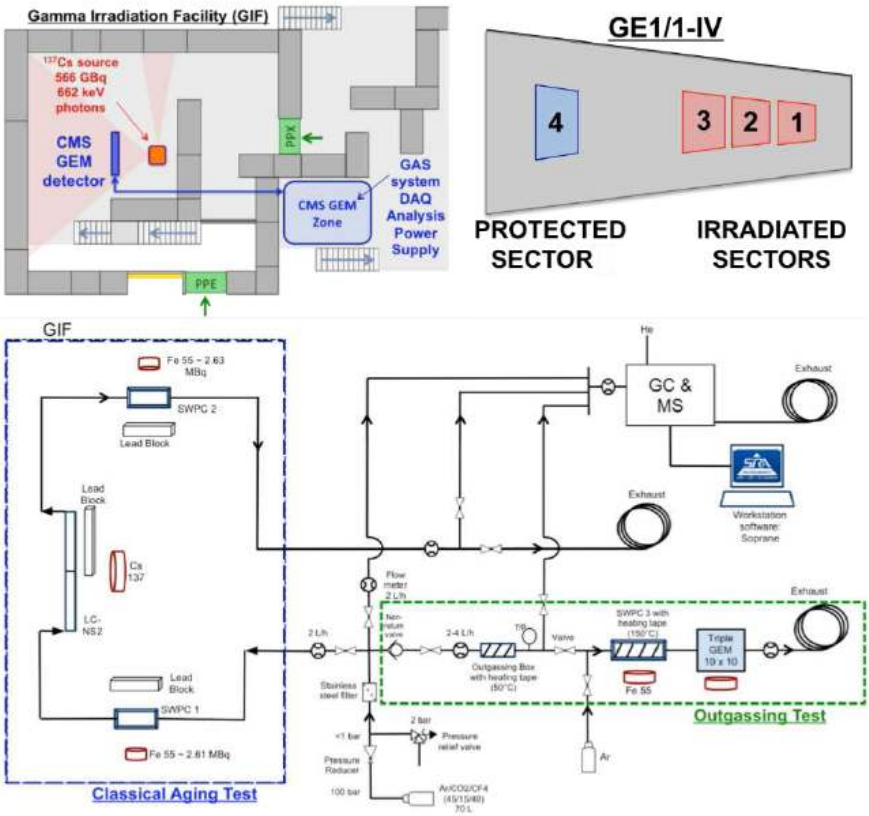

Figure 3.13: Schematic view of the aging test setup at the Gamma Irradiation Facility (GIF) at CERN and of the irradiated and shielded sections of the GE1/1 detector under test (top). Overview of the gas system for the classical aging test in blue and the outgassing studies in green (bottom) [29].

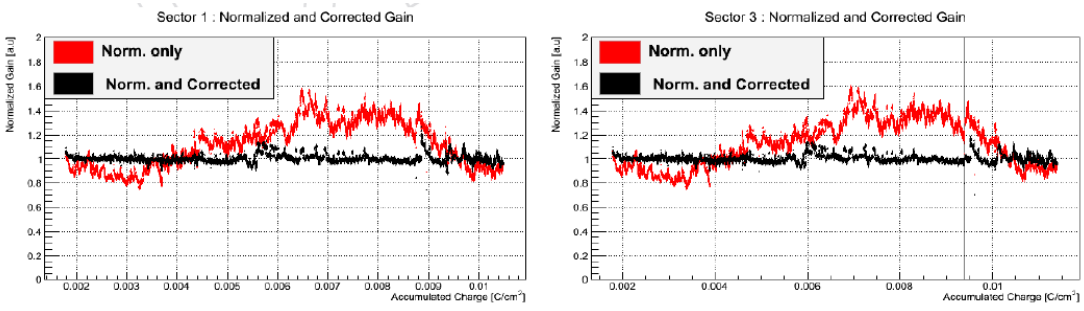

Figure 3.14: Corrected and normalized gain in irradiated GE1/1-IV sectors 1 (left) and 3 (right) as a function of the total charge accumulated in the detector during the GIF aging test. No aging effects have been observed after a total accumulated charge of about 10 mC/cm^2 [29].

without significant losses in performance. Indeed the accumulated charge ref-

erence value in the GE1/1 position can be obtained as

$$Q_{GE1/1} = R \times t_{HL-LHC} \times n_p \times e \times G \tag{3.2}$$

where R is the average expected hit rate in the GE1/1 region, of the order of 1 kHz/cm^2 from simulations, t_{HL-LHC} is a 10-years HL-LHC operation time, equal to 6 $\times$ 10^7 s, n_p is the number of primaries, 31, from the the energy deposited by a MIP traversing the gas gap and G is the gain, whose reference value is assumed to be $2{\times}10^4$. With these numbers, the expected accumulated charge value in CMS in the GE1/1 region is about 6 mC/cm^2, i.e. both the tests performed at the GIF and GIF++ accumulated a sufficient charge, with a safety factor of $\sim$ 10.

3.4 Study of behaviour of GEM detectors in neutron field at the Louvain facility

A complementary test was performed at the Louvain facility in Belgium, with the aim of evaluating the sensitivity of GEM detectors to neutrons in the energy range 5-50 MeV.

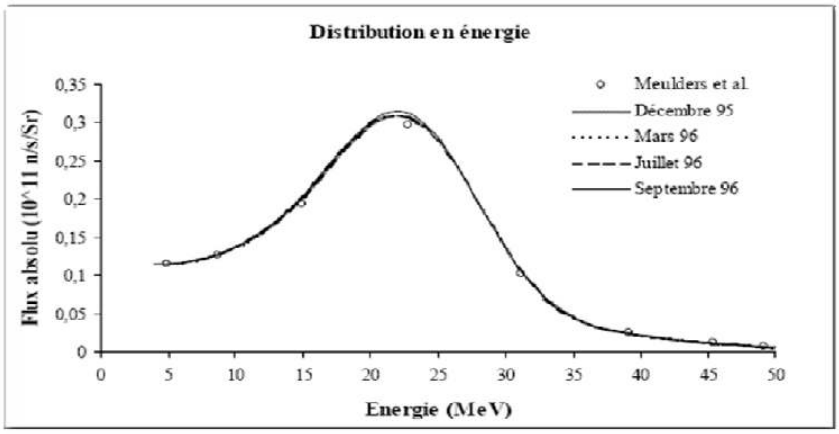

Figure 3.15: Energy distribution of the neutron beam at the Louvain facility [78].

The high flux neutron beam of the Louvain-la-Neuve facility is produced through spallation of a primary 50 MeV deuteron beam from a Cyclotron over a thin beryllium target. The neutron beam is produced through the high cross section reaction ^{9}Be(d,n)^{10}B [78].

The spectrum of the resulting neutron beam is shown in Fig.3.15: the neutrons have energy between 5 and 50 MeV, peaked around 20 MeV.

Even if three layers of filters (1 cm-thick polyethylene, 1 mm-thick Cadmium, 1 mm-thick Lead) are placed outside the target box, the neutron beam is contaminated by the presence of protons, electrons and gamma, with the fraction displayed in Table 3.1.

Particle	**Fraction**	**Average Energy (MeV)**	**Maximum Energy (MeV**
Neutron	1.0	16.56	50
Proton	1.5×10^{-4}	12.61	25
Electron	1.6×10^{-4}	1.57	6
Gamma	2.4×10^{-2}	1.93	10

Table 3.1: Gamma and charged particle contamination of the neutron beam [78].

The neutron fluence can be evaluated monitoring the deuteron current on the target, through the formula

$$fluence = \frac{10^{14} \times I}{0.079 \times d^{1.902}} \tag{3.3}$$

The fluence (n/cm^2) is so directly proportional to I, the integrated deuteron current, expressed in μA $\times$ hour, and inversely proportional to the distance d between the target and the irradiated sample (in cm) [78].

3.4.1 Dedicated sensitivity simulation

A dedicated sensitivity simulation was developed in order to perform a straightforward comparison with the experimental results. In this simulation, neutrons were generated in front of the GEM chamber with a simulated energy spectrum consistent with the one expected in Louvain and shown in Fig.3.16.

The beam spot in the simulation as a square with 10 cm side, placed at the center of the chamber surface. The geometry of the chamber simulated reproduced exactly the one of the detector used in the test and is shown in Fig.3.17.

Moreover, as the beam was contaminated by other particles, as summarized in Table 3.1, we studied the sensitivity of the chamber also to these background components, simulated with the energy spectra plotted in Fig.3.18.

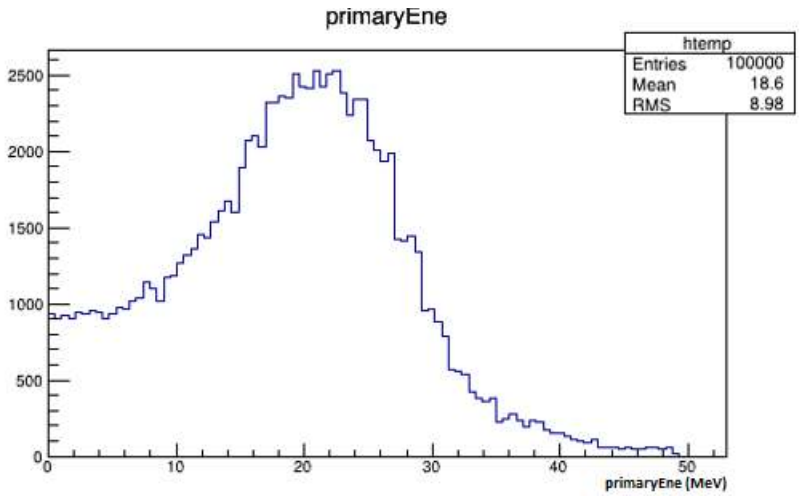

Figure 3.16: Louvain neutrons simulated spectrum.

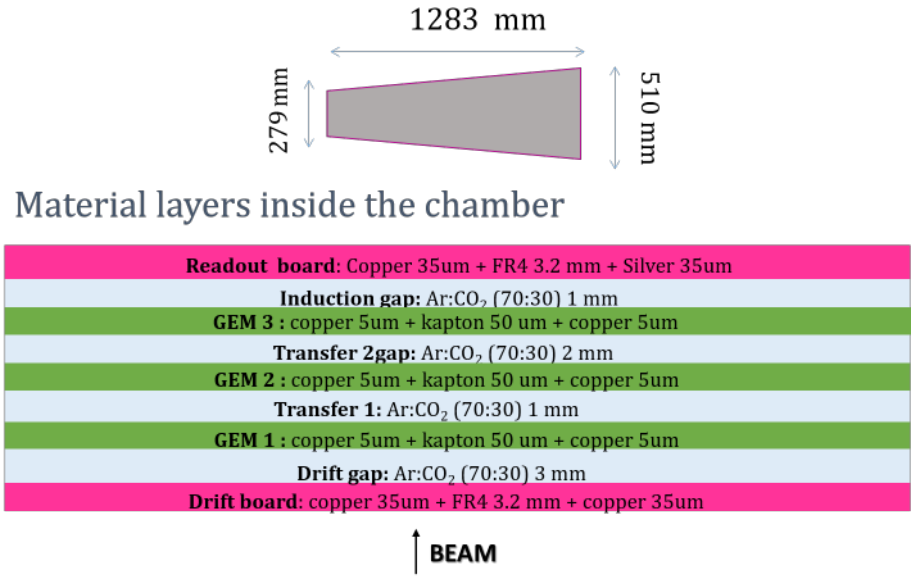

Figure 3.17: Simulated geometry of the Triple-GEM irradiated in the Louvain test.

The results obtained for the sensitivity to neutrons as well as for background particles are summarized in Table 3.2.

The neutron sensitivity value will be then compared with the results obtained from the irradiation test. An accordance between the two would also validate the whole GE1/1 results, as the simulations for the GE1/1 superchambers and for this particular case are identical in principle, with modifications only related to the geometry of the detector and the incident particles spectra.

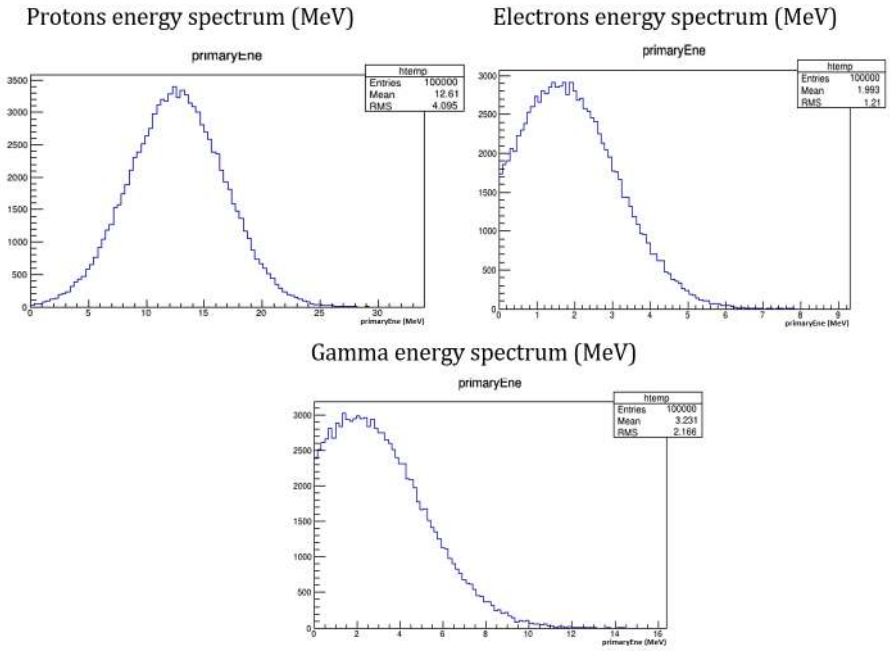

Figure 3.18: Louvain background simulated spectra. Top left: protons. Top right: electrons. Bottom: gamma.

Particle	**Sensitivity**
Neutron	$(2.6 \pm 0.2) \times 10^{-3}$
Gamma	$(1.42 \pm 0.04) \times 10^{-2}$
Protons	$(4.0 \pm 0.2) \times 10^{-3}$
Electrons	(0.396 ± 0.001)

Table 3.2: Results of the simulation performed for the Louvain test.

3.4.2 Experimental setup

The experimental setup used for the test is shown in Fig.3.19. The detector was a GE1/1-III, operated with Ar/CO_2 70%/30% gas mixture at a flow rate of 1.8-2 l/h. The power was supplied though a module CAEN HVN1470, controlled by LabView 8.5. The readout system was composed by one board with 4 Gastone_32 chips [79], for 128 channels in total. The output analog signal was discriminated by 8 Constant Fraction Discriminators CAEN V812 [80]. Every module returned an OR signal from 16 channels. A general OR was then obtained through a module Benney 32 IN LOGIC [81] and then counted with a VME scaler CAEN V560E [82]. At the same time the current was measured in a nearby sector, reading directly the current induced on the 128 strips using a Panasonic connector and a Keithley 6487 picoammeter [83]. All

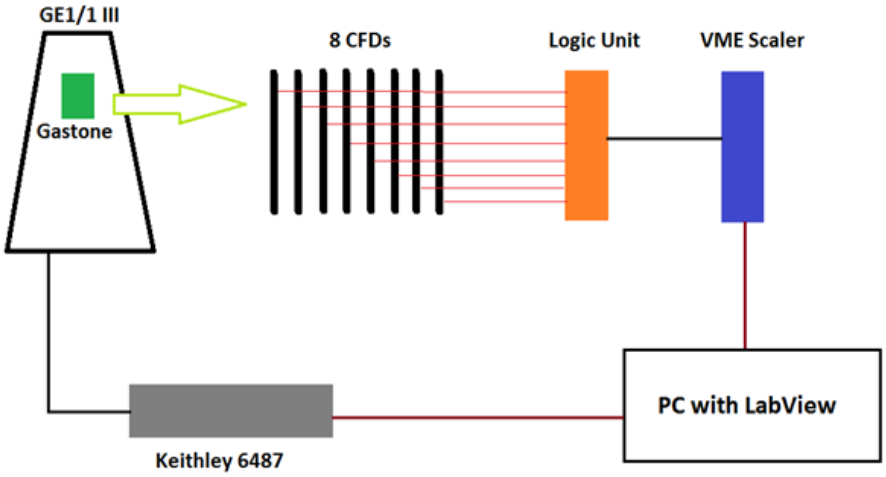

Figure 3.19: Experimental setup used in laboratory and in Louvain.

the acquisition system was controlled by LabView [84], with software developed on purpose for CFDs and Scaler. The software for the HV module was provided by CAEN.

3.4.2.1 HV System

The GEM was supplied through a CAEN HVN1470 module: the voltage arrived at the chamber through a single channel and was distributed to the different gas gaps and amplification foils through a voltage divider like the one shown in Fig.3.20. The 10 MΩ resistors connected to the top (T) of every GEM foil are protection resistors, used to avoid possible discharges that could damage the divider.

The HVN1470 module was remotely controlled with a LabView software, developed by CAEN, whose front panel is shown in Fig.3.21. It allowed the control of the HV channel setting the voltage to be applied or, alternatively, the current that should pass through the divider. Both the voltage and the current were constantly monitored and could be visualized through the two plots *Vmonitor* and *Imonitor* on the front panel.

3.4.2.2 Readout and Data Acquisition system

The first element of the readout system was the Gastone_32 chip [79], an analog circuit, developed starting from the previous Gastone version implemented in the Kloe experiment [85]. It was chosen instead of the VFAT_V2 chip [99]

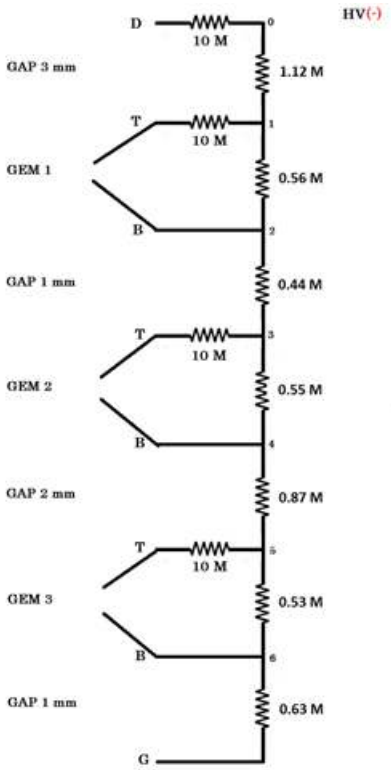

Figure 3.20: GEM voltage divider.

standardly used by the Collaboration, as the DAQ system available at that moment was not able to handle the expected rate of particle (up to 10^5 Hz/cm^2 assuming a sensitivity of 10^{-3}); Gastone instead was developed in order to be able to handle a rate of 10 MHz/channel. Gastone_32 is a CMOS 350 nm, composed by a charge preamplifier, with a gain of 5.6 mV/fC, followed by a shaper with a gain of 4. The peaking time is between 10 e 70 ns for an input capacitance between 10 and 50 pF. In total, the circuit has a charge sensitivity of 20 mV/fC [79].

The output signals from Gastone have a maximum amplitude of 1.3 V, whatever is the input charge, so the chip should be characterized by a region of linear response, followed by a saturation region. An expected calibration curve could be the one in Fig.3.22, which shows the amplitude of the output signal V_{out} (mV) as a function of the input charge C_{in} in fC. In a brief test performed in the laboratories of the University of Bari and Bari Politecnico, it was demonstrated that, also with saturated signals, the time duration of the signal itself does not change and remains shorter than 1 μs. As a consequence, the rate capability of Gastone should not be deteriorated in case of saturated

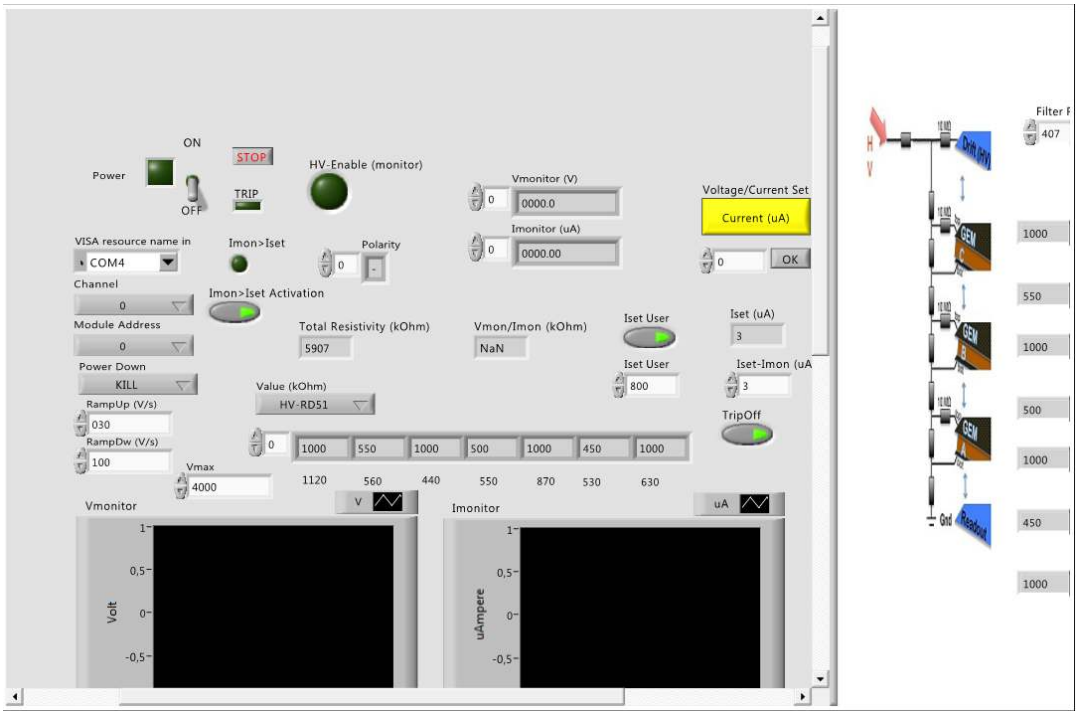

Figure 3.21: Front panel of the LabView software developed by CAEN and used for the remote control of the HVN1470 module.

signals.

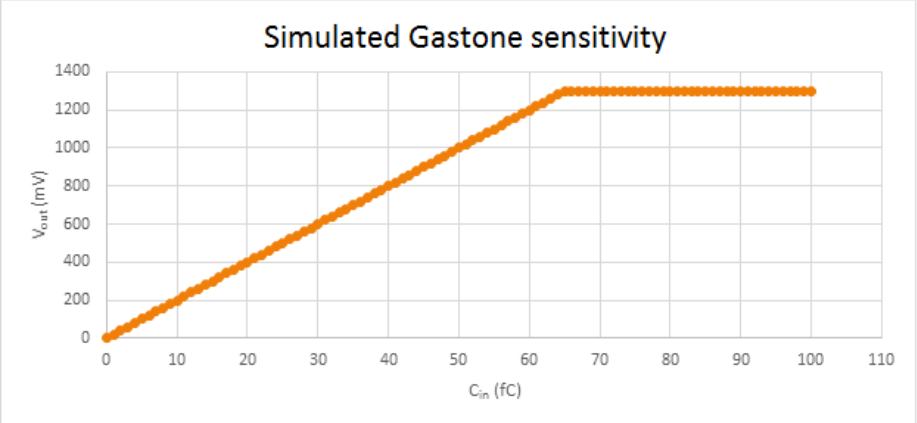

Figure 3.22: Simulated sensitivity curve of Gastone.

Some tests on Gastone performances had been performed also in the laboratories of the University of Pavia, with the aim of understanding the behavior of Gastone when used with big input charge (>50 fC), like the one that can be produced by neutrons and X-Ray.

The setup used for the test on Gastone is shown in Fig.3.23 left. The attenuated signal from a voltage generator passed through a 1 pF capacitor,

directly soldered to one channel of the readout board. In this way, a charge signal of the order of fC could be injected into one channel of Gastone (Fig.3.23 right).

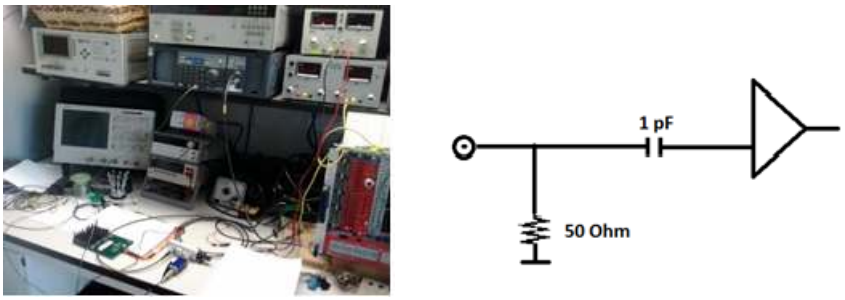

Figure 3.23: Left: Experimental setup used for the test on Gastone. Right: Diagram of the connection to one channel.

The output signal from Gastone was then observed with an oscilloscope and its amplitude was measured. Starting from the input charge and the amplitude of the output signal, the sensitivity (or gain) of Gastone could be calculated as

$$S = \frac{V_{out}(V)}{C_{in}(fC)} \tag{3.4}$$

The results of the first measurement of Gastone sensitivity is shown in Fig.3.24: the three data series correspond to three different values of attenuation applied to the input signal (input width 100 ns, leading and trailing edge 1 ns) in order to extend the input charge range as much as possible.

The input charge value is calculated as

$$Q_{in}(fC) = V_{att}(V) \times C(F) \times 10^{15} \tag{3.5}$$

where C is the capacitor value (1 pF) and V_{att} is the attenuated voltage from the generator, evaluated from

$$A = -20 \log_{10}(\frac{V_{att}}{V_{in}}) \tag{3.6}$$

where V_{in} is the input from the generator and A is the attenuation, as

$$V_{att} = V_{in} \times 10^{-\frac{A}{20}} \tag{3.7}$$

The curve is characterized by a linear region, up to 50 fC, in which the sensitivity is about 18-20 mV/fC. The region of saturation can be divided into

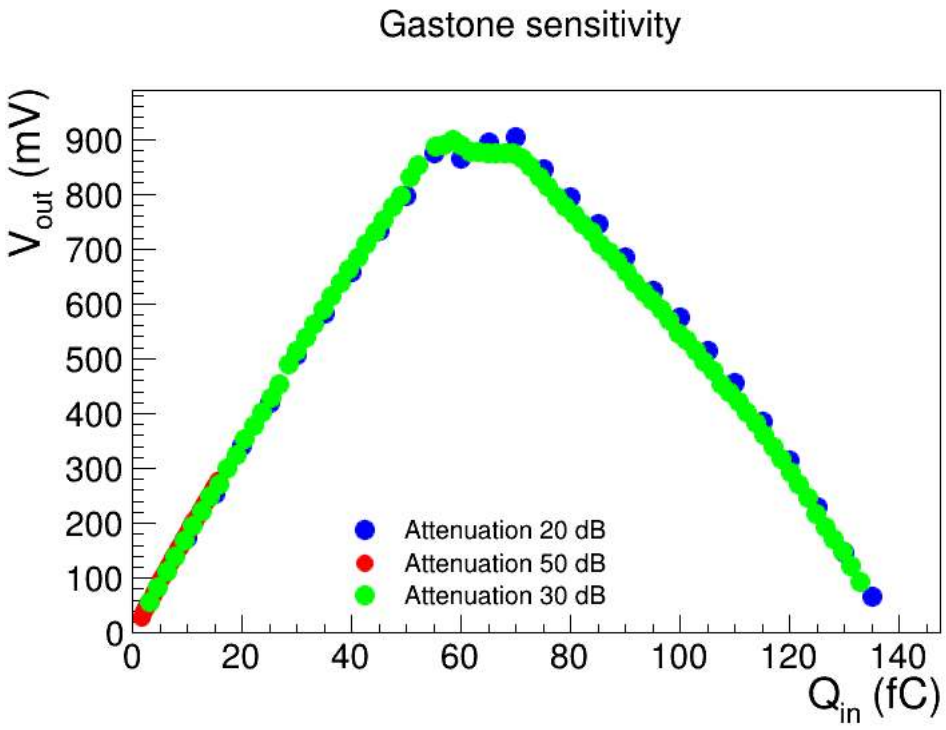

Figure 3.24: Results from the test on Gastone sensitivity.

two parts: in the first one, up to 70 fC, the output signal keeps the same amplitude of about 900 mV with the increase of input charge. In the second part instead, the signal amplitude starts to decrease with the increase of the input charge: in this region the gain of Gastone is decreasing and reaches 0 at about 140 fC. The ideal region of operation of Gastone from these results can be then identified with an input charge up to 50 fC, slightly lower than what expected from Fig.3.22.

The output signal from Gastone was then discriminated with VME Constant Fraction Discriminators Mod. V812 CAEN. Each module can discriminate up to 16 channels, with LEMO inputs and ECL output. In addition, a LEMO OR output is present, together with a Majority output, which is activated only when a certain number of channels go over threshold at the same time. The threshold can be selected in a range from 5 to 255 CFD units for each channel. Moreover, also the signal width and the dead time (or VETO) that must be applied after a signal over threshold can be selected.

In order to remotely control the CFDs, I developed a dedicated LabView interface, whose basic unit is shown in Fig.3.25. The software was designed in

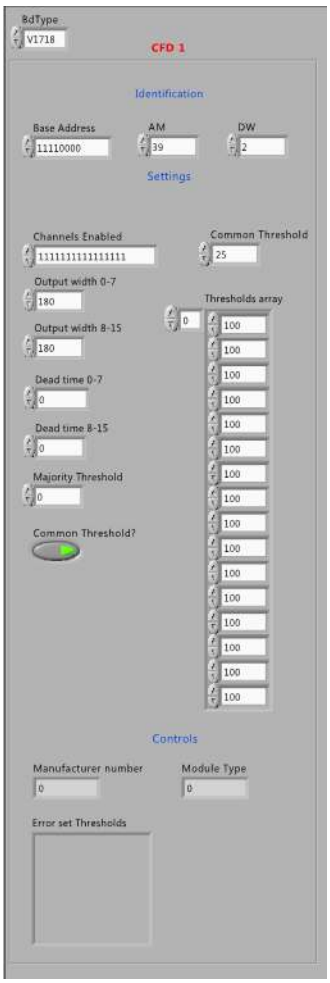

Figure 3.25: Partial view of the front panel of the LabView software used to control the CFDs. The complete panel foresees 8 structures, identical to the one shown in this picture, each dedicated to one CFD.

order to allow the selection between a threshold common to all the channels and an independent setting of the threshold of each channel. However the threshold value applied via LabView is not directly equivalent to the threshold value in mV applied. The characterization has been performed with a CFD and a pulse generator in the Pavia laboratory: the obtained linear relation between the applied threshold and the effective threshold is

$$V_{th}^{real}(mV) = 1.83 \times V_{th}^{app}(CFD\ units) + 11.85\ mV \tag{3.8}$$

in average over 16 channels. As a consequences, the threshold values actually applied are approximately those shown in Table 3.3.

Another important parameter is the delay: the constant fraction discrim-

$\mathbf{V}_{th}{}^{app}$	$\mathbf{V}_{th}{}^{real}$
10	30.15
15	39.3
20	48.45
25	57.6
30	66.75
35	75.9
40	85.05
45	94.02
50	103.35

Table 3.3: Relation between threshold in CFD units and threshold in mV.

inator splits the signal in two; one of the two signals is then inverted and attenuated by a costant fraction (20%) while the other signal is delayed. The two signals are then added together, creating a bipolar signal that crosses the zero in a definite instant, independent from the signal amplitude, giving a time information free from errors due to time walk. The delay between the two signals is connected to the rise time of the signal through the relation

$$T_{delay} = T_{rise} \times (1 - F) \tag{3.9}$$

where F is the attenuation factor. Considering that Gastone produces signals with rise time of the order of 100 ns, from the relation above the ideal delay should be of the order of 80 ns. The standard version of the module however has a delay range from 8 to 20 ns. We have performed some tests in Pavia laboratory, using signals with long rise time, between 100 and 200 ns, from a generator and with different amplitudes, in order to understand if the CFD works also in this condition. The discrimination function still survives, just the time information is degraded.

The functioning of the CFD is guaranteed only with signals from -5 mV to -5 V. Using the results from Geant4 [77] simulations (Fig.3.26), we can make a guess on the amplitude of the signals that arrive to Gastone.

From simulations, the mean value of the energy deposited in the drift gap by neutrons is 27 keV: assuming 28 eV for the ionization energy of Ar/CO_2 gas mixture, it corresponds to 964 pairs produced in the drift gap. With a supposed gain of 1000, 9.64×10^5 pairs are obtained at the readout. It corresponds to a charge at the readout equal to 142 fC and, if Gastone sensitivity is 20 mV/fC, it would produce a signal of 2.8 V, i.e. saturation of Gastone. In reality, as we

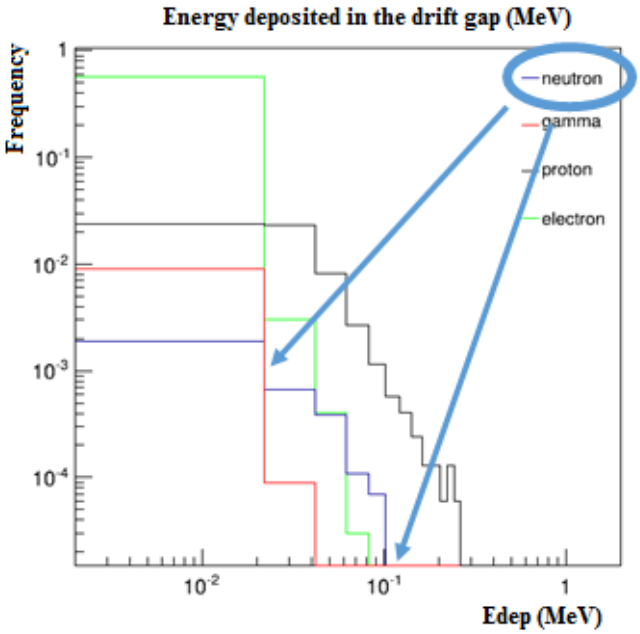

Figure 3.26: Energy deposited in the drift gap from Geant4 simulations.

have already underlined before, Gastone can produce signals with a maximum amplitude of 1.3 V, for every input charge greater than 50 fC. As a consequence, we can assume that the CFDs have always worked in a safe region. In addition, we have performed a test with a generator producing signals up to -12 V and we did not observe any loss in the rate, neither with fast signals nor with signals with long rise time (100 ns), up to 100 kHz. We have also checked the right functioning of the OR of the CFD using both signals from a generator and signals from scintillating fibers readout by SiPM: the result is that the OR works properly, even when signals with a long fall time (15 μs) are used, as shown in Fig.3.27.

The other characteristics that must be considered for the CFD are the dead time and the output width: starting from the dead time, the datasheet of the module [80] reports a dead time that goes from 150 ns to 2 μs. If we set the dead time at the minimum we would have 150 ns + 4.5 ns due to the uncertainty and signal formation time, in total we have $\sim$ 160 ns: the rate capability is so 6 MHz for each channel approximately. Considering instead the output width of the discriminated signal, the datasheet reports a range from 15 ns to 250 ns, with the relation between CFD units and ns shown in Fig.3.28.

After the CFD, the acquisition chain was composed by a NIM logic used

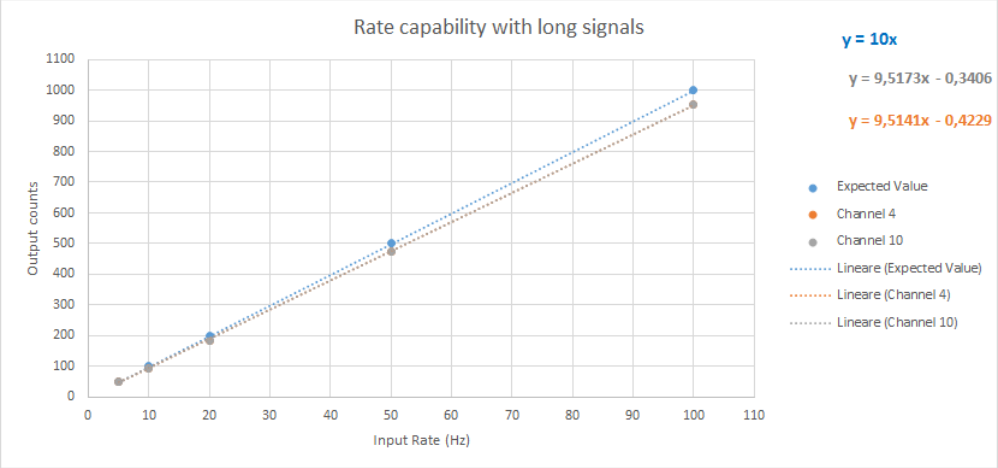

Figure 3.27: Results of rate capability tests performed with CFD V812: the signal from a ORTEC 448 Research Pulser was characterized by 200 ns rise time, 16 μs fall time and an amplitude of -1.2 V.

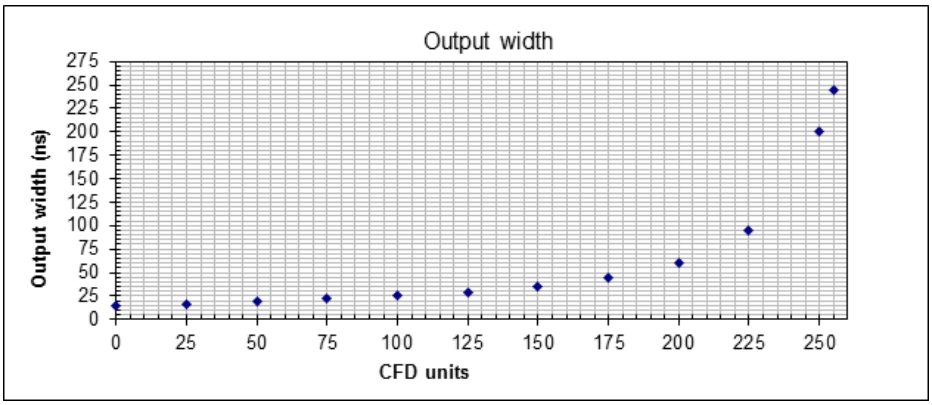

Figure 3.28: Calibration of the output width of the CAEN V812 discriminator.

to make the total OR of the strips, with a dead time of the order of 10 ns and a NIM-ECL converter N92 with a delay input-output of 4 ns, both negligible for the rate capability estimation.

Considering finally the scaler, its role was to open a window, store all the signals that Gastone produces in a certain time and return the number at the end of the time window. Also the scaler was remotely controlled with LabView, with a dedicated software that I developed on purpose.

3.4.3 Characterization of the detector before the neutron test

During the period preceding the Louvain test, we have performed many preliminary tests at the TIF[2] with the X-Ray source. Different HV scans and current measurements were performed, with different functioning parameters of the X-Ray. The procedure used for every HV scan is the following:

- Set the HV at the lower value, usually ranging from 2300 and 2500 V corresponding to 460-500 μA on the divider.
- Measure the rate for that HV value, with a proper acquisition time.
- Increase the HV value of 50-100 V and repeat the procedure

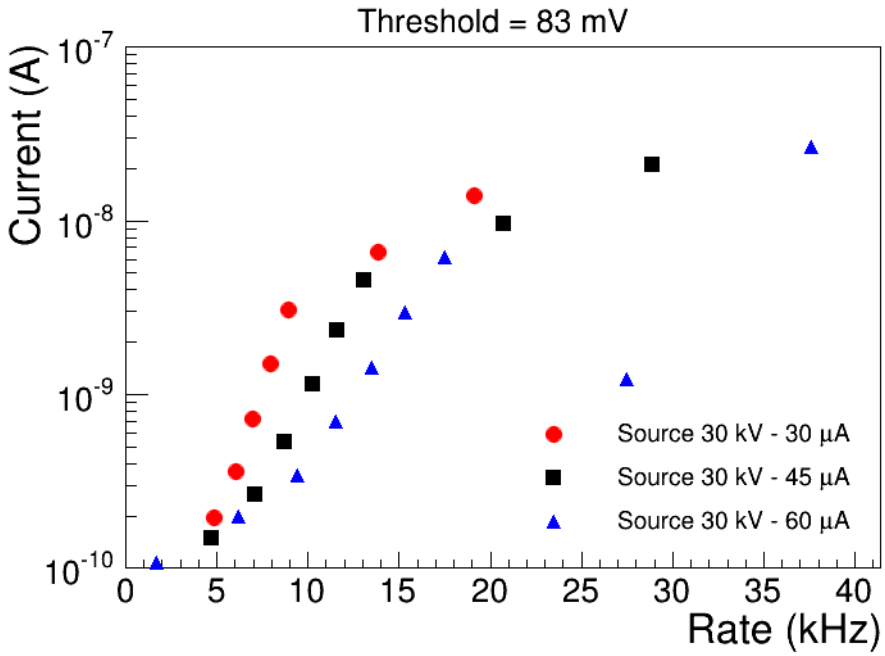

Figure 3.29: Behaviour of the anode current as a function of the measured rate, with three different current values of the X-Ray.

Considering the current measurement instead:

- Set the HV at the lower value, usually ranging from 2300 and 2500 V corresponding to 460-500 μA on the divider.

[2]The Tracker Integration Facility (TIF) is the laboratory at CERN in which the greatest part of the R&D of GE1/1 detectors has been carried out. It presently hosts a part of the quality control chain of the GE1/1 chambers.

- Install the Panasonic connector in a sector near the one used for the rate current and connect it to the triax cable that goes to the picoammeter.
- Measure 10 currents value for each HV step with a dedicated LabView software, developed on purpose, then calculating the mean value.

These methods were employed also during the Louvain tests and for the cross-check measurements after the irradiation[3].

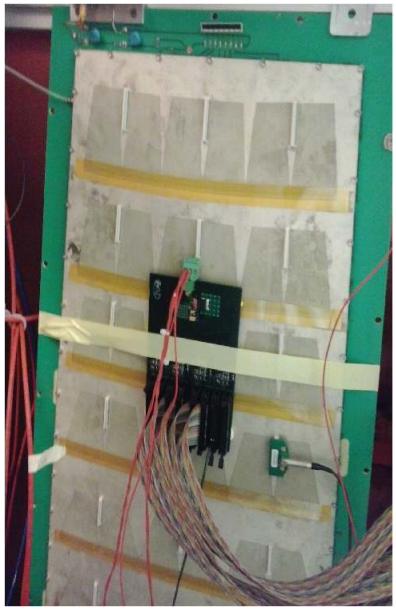

Figure 3.30: Position of Gastone and of the Panasonic connector during some measurements performed at the TIF.

In Fig.3.29, an example of the behavior of the current as a function of the measured rate is plotted, in three runs performed with the X-Ray source at 30 kV and 30, 45 and 60 μA, fixing the photon energy and increasing just the flux. We can observe that the three curves are exponential at the beginning and at the end and, in particular, in the last part they seem to have all the same slope. It seems that at higher voltages, corresponding to the points and higher rate, the current reaches a saturation, with a maximum value around 2-3 $\times$ 10^{-8} A.

[3]In all the current measurements we have used a Panasonic connector with a 100 kΩ resistor between the signal and the ground points. In case of current measurement, it creates a current divider with the input resistor of the picoammeter, distorting the measurement. From the picoammeter manual [83], the voltage burden for the model Keithley 6487 is reduced at a value lower than 200 μV for every current range except 20 mA, for which is less than 1 mV. In order to calculate this effect, the manual uses a 5 kΩ resistor. If we assume this value for the input resistor, the *real* current is 1.05 the measured current, with a variation of just 5%.

In the correspondent rate plots there is not a clear plateau, as those observed in a typical rate curve of a Triple-GEM detector like in Fig.3.5. For this reason, in this case we used the maximum rate for the gain estimation with formula 3.1. It turned out to be of the order to 2×10^4 at the highest high voltage value applied. The rate was typically measured in sector 3-2, while the current in sector 4-3[4], as shown in Fig.3.30.

3.4.4 Preliminary results from Louvain measurement

The GE1/1-III to be irradiated was installed at the Louvain facility as shown in Fig.3.31. The chamber was positioned just at the end of the beam line after a polystyrene box used for previous tests.

Figure 3.31: GE1/1-III Triple-GEM detector installed at the Louvain-la-Neuve facility.

A hole was made into the box, in order to minimize the contamination of the beam and to allow the alignment of the chamber with the help of a dedicated laser system.

The measurements were performed at three different values of incident flux and at different applied thresholds. They are summarized in Table 3.4.

The noise level was evaluated through a threshold scan with different voltages applied at the chamber: already at $V_{th} \sim 55$ mV the noise is at the

[4]The sectors of the GE1/1 chamber readout are numbered in lines, following the η partition, and in column, following the segmentation in ϕ. There are 8 lines, numbered from 1 to 8 from the top to the bottom of the chamber and 3 columns, numbered from 1 to 3 from left to right facing the readout board.

Beam Current (nA)	Flux (n/cm^{2}s)	Threshold (CFD units)	Threshold (mV)	HV scan	Current measurement
85	4.44×10^6	10	30	✓	✓
		15	39	✓	✓
		20	49	✓	✓
		30	67	✓	✓
200	1×10^7	30	67	✓	✓
		40	85	✓	✓
2000	1×10^8	30	67	✓	✓
		40	85	✓	✓
		80	158	✓	✓

Table 3.4: Summary of the measurements performed during the Louvain test.

order of some Hz. All the results presented in the next sections come from background subtracted data.

In Fig.3.32 and in Fig.3.33, we can see the results of the measurement with threshold 30 CFD units with incident neutron flux of 4.44×10^6 n/cm^{2}s. In this measurement, as in all the others performed during the preparation of the test in Louvain, the rate never reaches a plateu and the behaviour is always increasing. The charge, calculated as

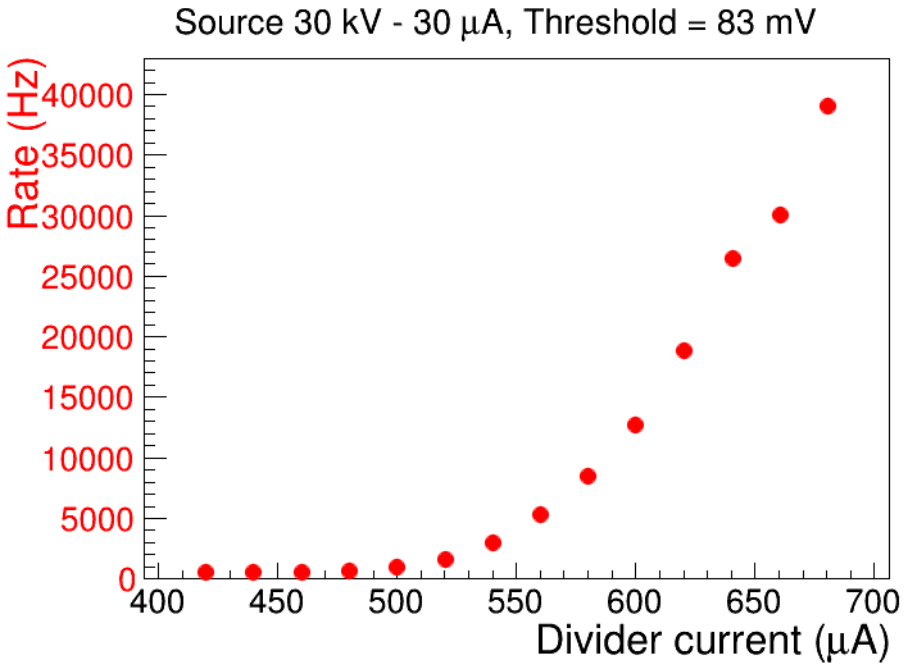

Figure 3.32: Results of the rate measurement with threshold 30 CFD units (67 mV). (The error bars are included in the markers)

$$Q = 10^{15} \frac{i_{true}}{R_{true}} \tag{3.10}$$

decreases with the increase of the HV applied to the GEM. Considering the current instead, as we can see from Fig.3.33, we can observe a region of exponential behaviour, always in the range 520-640 μA. After this region, the current seems to be saturated, as we have already observed in Fig.3.29 and it may explain the behavior of the charge. Indeed, at high HV value, where the rate continues to increase, the current saturates instead, so the ratio between current and rate, used to calculate the charge, starts to decrease.

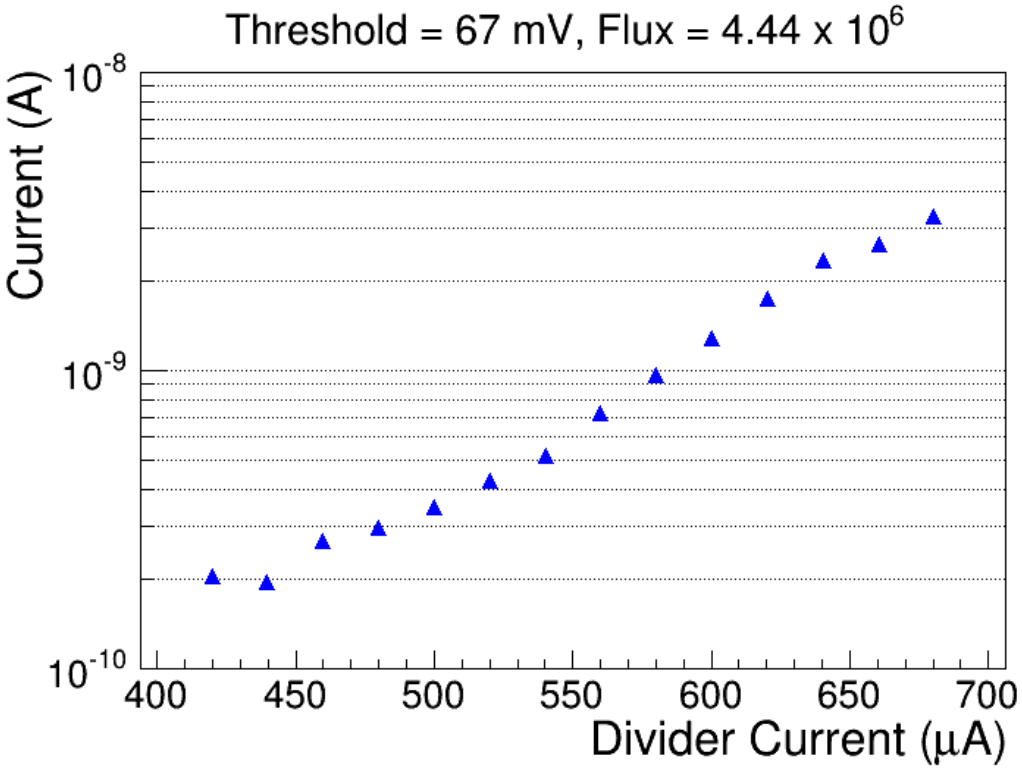

Figure 3.33: Results of the current measurement. (The error bars are included in the markers)

With the irradiation at higher fluxes (1×10^7 n/cm^{2}s and 1×10^8 n/cm^{2}s), the behavior observed is exactly the same described above.

3.4.5 Estimation of the sensitivity from the Louvain data

An estimation of the sensitivity to neutrons can be performed starting from the data acquired in Louvain. Fig.3.34 shows the results of the sensitivity measurement as a function of the threshold applied and for different HV values of the chamber.

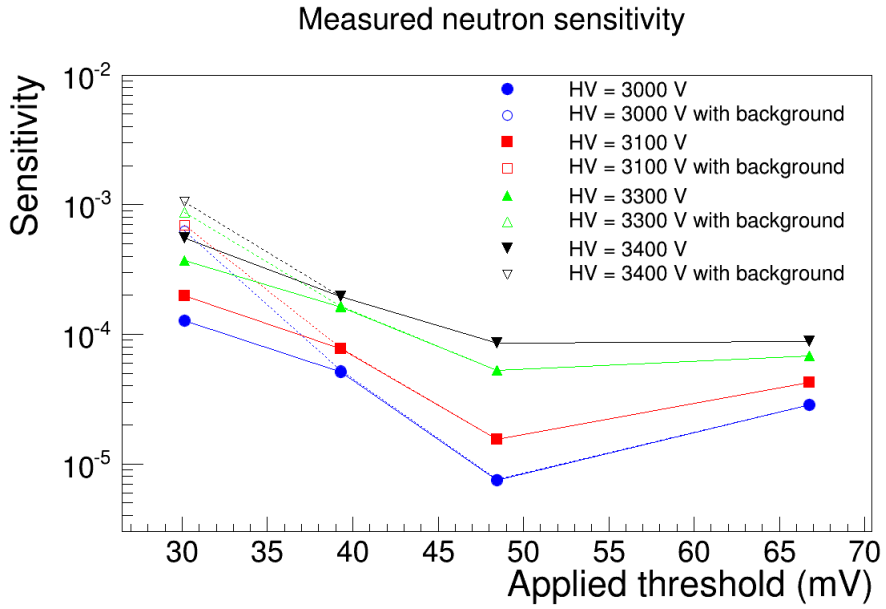

Figure 3.34: Results of the sensitivity measurements performed in Louvain-la-Neuve with a neutron beam. The full line and markers refer to background subtracted data, while the open markers and dashed lines to data including the background. (The error bars are included in the markers; the lines were added just to guide the eyes.)

The full line and markers represent the results from background subtracted data, while the open markers and dashed lines still include the contribution of the background. The contribution of the background is relevant only at the lower thresholds, confirming what already noticed with the noise runs.

Comparing the results of this measurement with the simulation performed with Geant4 and shown in Table 3.2, we can observe a difference: the simulated value is $(2.6 \pm 0.2) \times 10^{-3}$, while the highest value obtained from the measured data, background subtracted, is $(5.552 \pm 0.002) \times 10^{-4}$. This value is calculated at the highest HV value, 3400 V (equivalent to a divider current of 680 μA), with the lowest threshold, $\sim$ 30 mV. The results are not compat-

ible within the errors and the discrepancy is even higher if we consider lower working voltages or higher applied thresholds. For this reason, a set of complementary studies was performed after the Louvain test to find possible weak points on both the simulation and hardware aspects.

3.4.5.1 Complementary simulation studies

In order to find a justification of the difference in sensitivity between the simulation and the experimental result, many analysis have been performed afterwards the Louvain test.

First of all an energy cut was added into the simulation, i.e. only the events that were depositing into the drift gap an energy greater than a fixed value were considered as good. It was introduced to mimic the effect of the threshold set in the electronics chain and was calculated as follow: assuming a Gastone sensitivity of 20 mV/fC, a threshold of 39.3 mV corresponds to a minimum charge that must reach the readout of $\sim$ 1.97 fC. With a detector gain of 1000, this correspond to $\sim 1.97 \times 10^{-3}$ fC produced in the drift gap, i.e. 12.4 e-ion pairs. If the primary ionization energy in Ar/CO_2 is 28 eV, the minimum energy deposition in the drift gap must be then 349.13 eV. The same calculation has been performed for the different threshold values applied in Louvain: Table 3.5 shows the threshold applied, the correspondent energy cut and the sensitivity value obtained from the simulation.

Threshold (mV)	**Energy cut (eV)**	**Sensitivity**
39.3	349.13	$(2.63 \pm 0.16) \times 10^{-3}$
67	584.06	$(2.46 \pm 0.16) \times 10^{-3}$
85	700.44	$(2.32 \pm 0.12) \times 10^{-3}$

Table 3.5: Summary of the energy cut applied and results of the sensitivity from simulation.

The study was then extended to values of gain of the chamber, from 1000 to 50. The results are shown in Fig.3.35.

As can be noticed from Table 3.5 and from Fig.3.35, the effect of the energy cut is negligible, then the recorded difference between the simulation and the experimental results cannot be ascribed only to the presence of an electronics threshold.

The possibility that one of the gaps was not working properly was considered too: it could be due to a problem related to the powering, discharges or

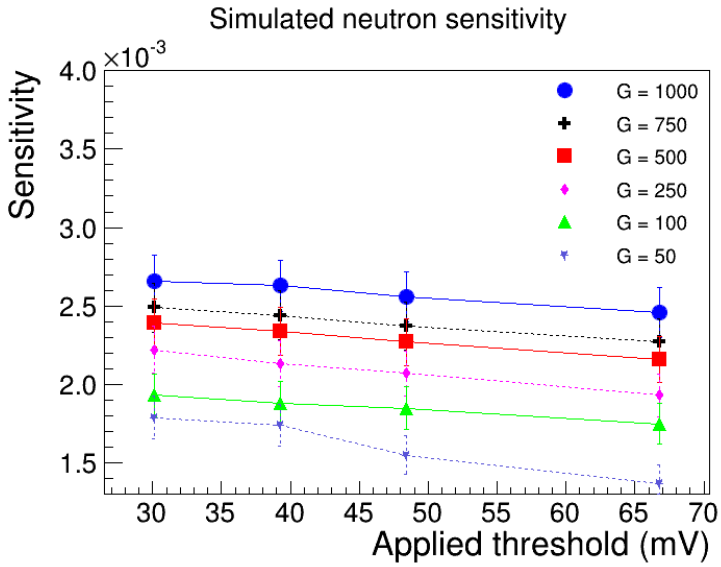

Figure 3.35: Simulated neutrons sensitivity as a function of the applied threshold, for different gain values of the detector (the lines were added just to guide the eyes).

foils defects. From the hardware point of view it would translate into a reduced gain, or into a loss of events, which could even justify a lower sensitivity. From the simulation point of view instead, only the *drift* and *transfer1* gaps are relevant: indeed, the simulation, in its original feature, considers an event as good only if it produces charges into these first two gaps. If the charges were produced in one of the other two instead, the gain was considered not enough for the signal to be amplified and detected. For this reason we made two complementary simulations, one considering the *drift* gap not active, i.e. damaged, the second one considering the *transfer1* not active. The results show that, when the *transfer1* gap is considered dead, the sensitivity from simulation is slightly reduced, to $\sim 2.3 \times 10^{-3}$; when instead is the *drift* gap not active, the difference is more relevant, with a decrease in sensitivity up to $\sim 2 \times 10^{-3}$. This difference can be understood from Fig.3.36, which shows the z coordinate (in mm) of the interactions of primary neutrons in a Triple-GEM detector.

The majority of the interaction happens in the drift and readout boards, which have the greatest material budget of all the detector. If the *drift* gap is active, all the charged particles produced in the drift board can be detected. If it is not, these particles can be reabsorbed before reaching the first active gap, which would be the *transfer1*, loosing good events, with a consequent reduction in the sensitivity. The effect is clearly lower in case the *transfer1* gap is dead,

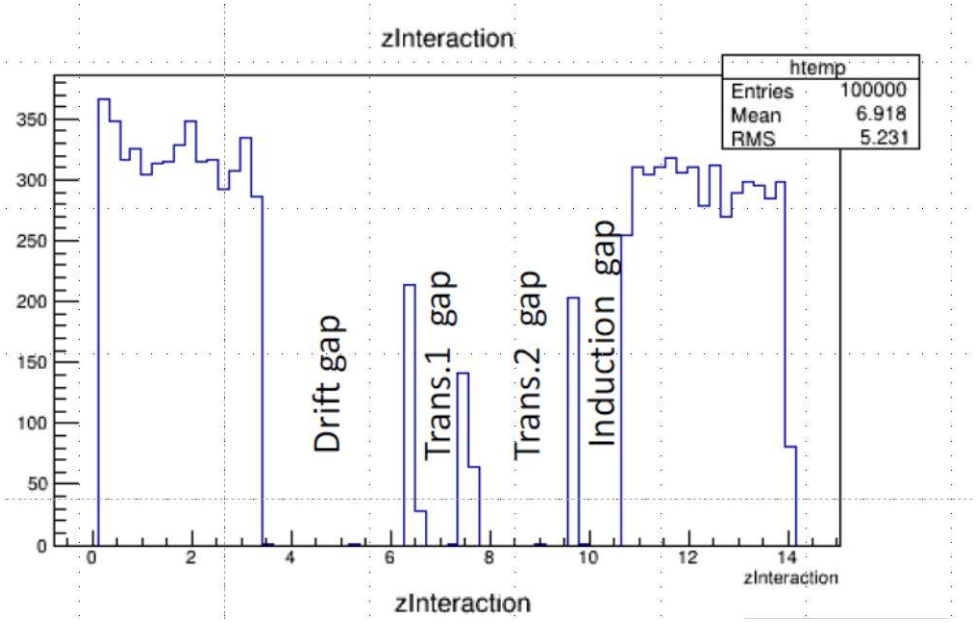

Figure 3.36: z coordinate (in mm) of the interactions of primary neutrons in a Triple-GEM detector.

because the number of interactions produced in the material surrounding it is smaller with respect to the *drift* gap case.

Apart from these considerations however, also this effect can be considered negligible as the sensitivity from simulation still remains higher that the experimental value.

A rough estimation of the average charge produced by neutrons interaction can be obtained from the slope of the linear fit of the current, measured at the anode, as a function of the rate acquired. In Fig.3.37 we can see the result for the run with threshold 39 mV and incident flux 4.44×10^6 n/cm^{2}s. The slope of the linear fit, which was limited to the linear part of the plot, gives an average charge of ~ 28 fC. Using the same kind of calculation already explained above and assuming an average value of the energy deposited in the drift gap from simulation of 27 keV, we can derive a gain of ~ 182, a very low value that could explain the low sensitivity measured.

Repeating the same exercise for all the threshold value applied we can obtain an estimation of the average charge produced in each run and verify if the electronics was working in a saturation region or not. In Table 3.6 we can see the results for thresholds from 30 to 67 mV, at a flux of 4.44×10^6 n/cm^{2}s.

Assuming the behavior of the Gastone sensitivity in Fig.3.22, we can affirm that the electronics was working in the linear region, except for a possible

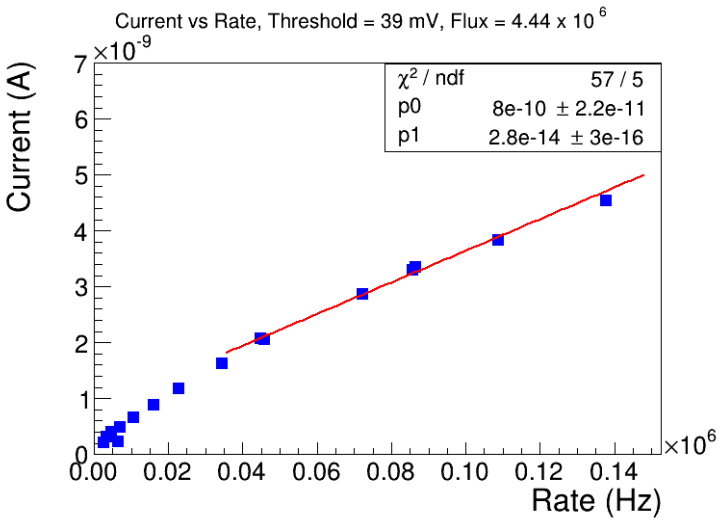

Figure 3.37: Current at the anode of the Triple-GEM as a function of the rate measured, with a threshold of 39 mV and an incident neutron flux of 4.44 × 10^6 n/cm^{2}s. The fit was limited to the linear part of the curve; the error bars are included in the markers.

Threshold (mV)	**Estimated charge (fC)**
30.15	20
39.3	28
48.45	50
67	70

Table 3.6: Summary of the estimated charge from the fit between the current from the anode and the rate measured.

saturation for thresholds 67 mV and higher.

During the irradiation moreover, an increase of the dark current, i.e. the current with the detector not powered, was observed and is quantified in Table 3.7.

The hypothesis of a possible activation of the material was discarded because the current from the anode measured immediately after the end of the test, i.e. with HV = 0 on the chamber and without the neutron flux, was compatible with the current measured before the beginning of the test.

We then supposed that the neutron flux could induce a charging up effect in the detector, that could influence the gain and, as a consequence the measured sensitivity. For this reason, we performed two additional simulations, which were taking into account a possible variation of the gain: the first one in which we suppose that the gain was reduced by the charging up effect, the second

Time	**Current at HV = 0 (A)**	**Picoammeter Accuracy**	**Flux (n/cm^2s)**
12:40	4.19×10^{-11}	1.00×10^{-11}	4.4×10^6
13:20	4.90×10^{-11}	1.00×10^{-11}	4.4×10^6
14:35	7.74×10^{-11}	1.01×10^{-11}	4.4×10^6
15:52	8.64×10^{-11}	1.01×10^{-11}	4.4×10^6
16:36	2.49×10^{-10}	1.02×10^{-11}	1×10^7
17:11	2.27×10^{-10}	1.02×10^{-11}	1×10^7
17:51	1.18×10^{-9}	1.12×10^{-11}	1×10^8
18:14	2.86×10^{-9}	1.29×10^{-11}	1×10^8

Table 3.7: Summary of the estimated charge from the fit between the current from the anode and the rate measured. The picoammeter accuracy was estimated from [83].

one in which the gain was increasing.

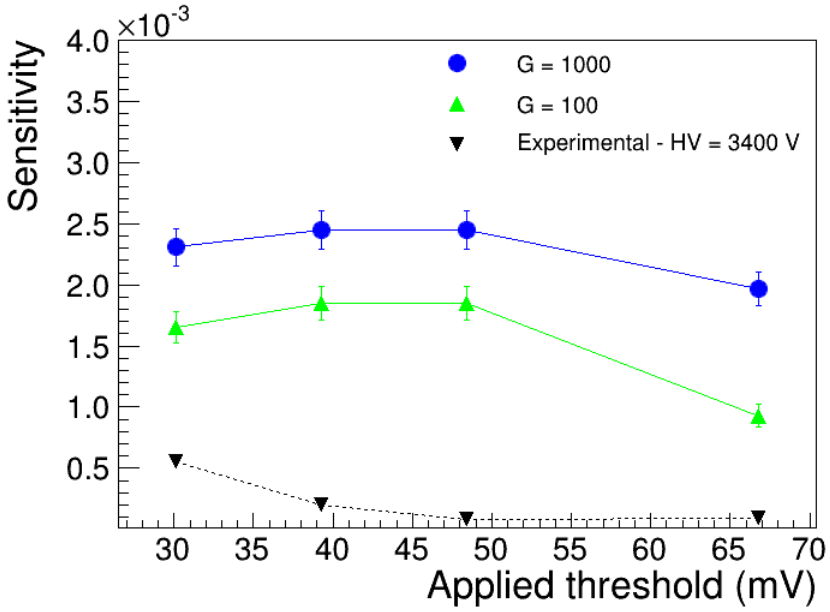

Figure 3.38: Effect of the reduction of the gain due to charging up effect on the simulated sensitivity (the lines were added just to guide the eyes).

In Fig.3.38 we can see the results of the first simulation: the gain is reduced by the charging up effect, with a variation proportional to the variation of the current in Table 3.7. The procedure has been repeated for two different values of initial gain, 100 and 1000. From the plot we can notice that the difference with respect to the experimental values is still relevant and, moreover, the behavior of the sensitivity as a function of the threshold is different with respect

to the experimental curve.

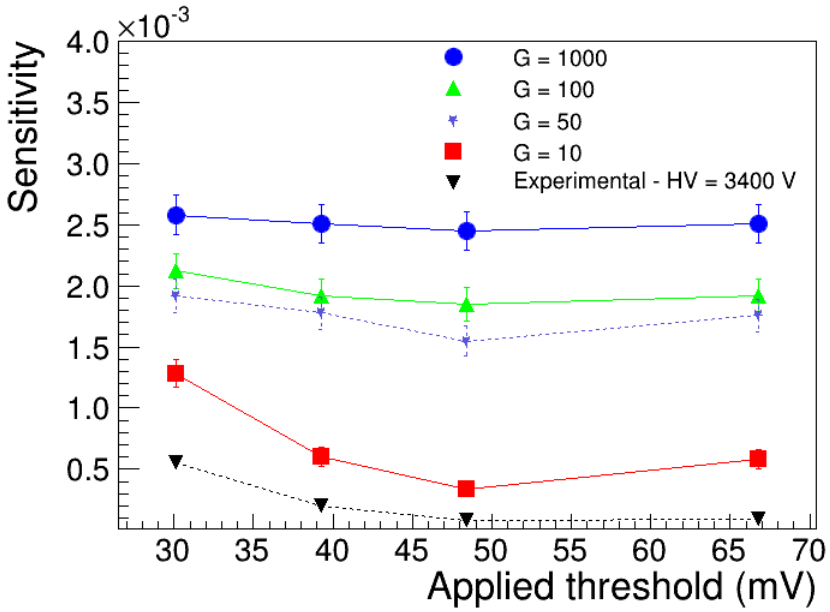

Figure 3.39: Effect of the increase of the gain due to charging up effect on the simulated sensitivity (the lines were added just to guide the eyes).

If instead we suppose an increase of the gain related to the charging up effect, we obtain the results in Fig.3.39. Also here the variation of the gain is proportional to the variation of the current in Table 3.7 and the procedure was repeated for four different values of initial gain. The behavior of the sensitivity here is the same of the experimental values, but the simulation approaches the experimental results only for very low gain values.

Both the simulations were performed taking into account also the variation of the sensitivity of Gastone for the higher threshold value, 67 mV: from Fig.3.22 a sensitivity value reduced to 18.6 mV/fC can be obtained.

These tests seem all to indicate that a better accordance between the simulation and the experimental result would have been reached with the detector operated at higher gain and then efficiency.

3.4.5.2 Validation of the DAQ and chamber operation after the neutron test

Complementary to the simulation studies, after the Louvain irradiation an intense campaign of test was performed at the TIF laboratory to validate the

operation of the chamber and of the data acquisition system.

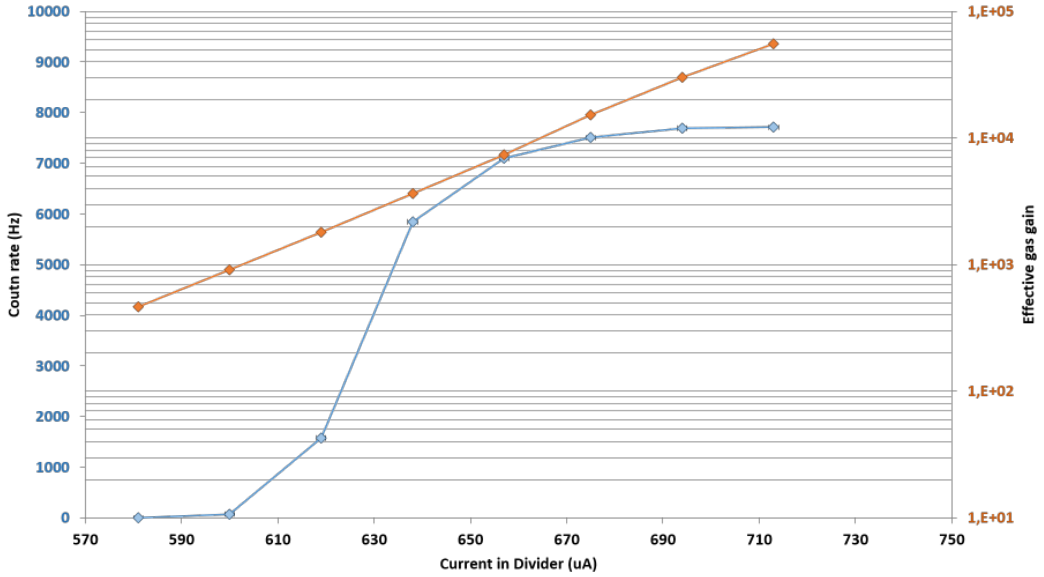

Figure 3.40: Results of the characterization performed with the GE1/1 chamber irradiated in Louvain after the test (the lines were added just to guide the eyes).

To exclude any possible effect from the electronics, a full characterization of the chamber was performed with an analog readout chain. The preamplification and amplification stages were performed with a ORTEC 142PC [93] preamplifier and an ORTEC 474 [94] amplifier respectively. The signals were then discriminated with a NIM constant fraction discriminator and counted with a NIM scaler.

The results of the rate and gain measurements performed in one central sector of the GE1/1 chamber with the X-Ray source powered at 30 kV-10 μA are plotted in Fig.3.40, while Fig.3.41 shows a spectrum obtained with the same sector of the chamber irradiated with the X-Ray source.

The detector proved to be fully operational: with this simpler electronics chain it is able to reach the plateau, with gain up to 5×10^4. Moreover also the shape of the spectrum from the X-Ray source is the one expected and can be compared with similar results in [87].

In order to understand the reason why it was not possible to reach the plateau during the Louvain test a full analysis of the electronics chain was performed, comparing step by step the rate measured with the analog chain with the one measured with the chain adopted in Louvain. These steps of the

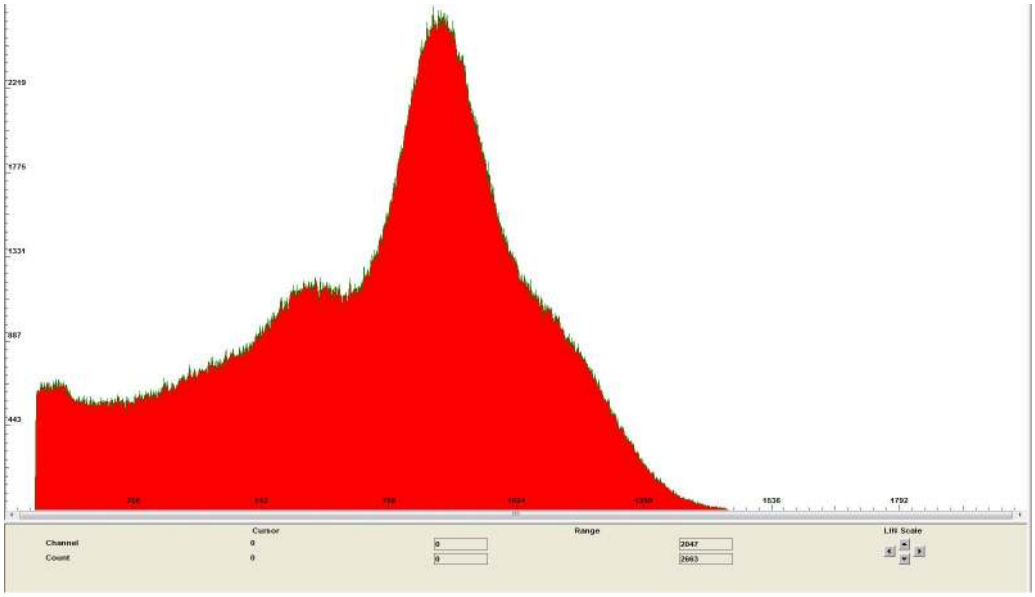

Figure 3.41: X-Ray spectrum acquired with the GE1/1 chamber irradiated in Louvain after the test.

validation were performed with a ^{109}Cd source, emitting photons of the same energy of the X-Ray generator (main emission 22 keV), but at a lower rate.

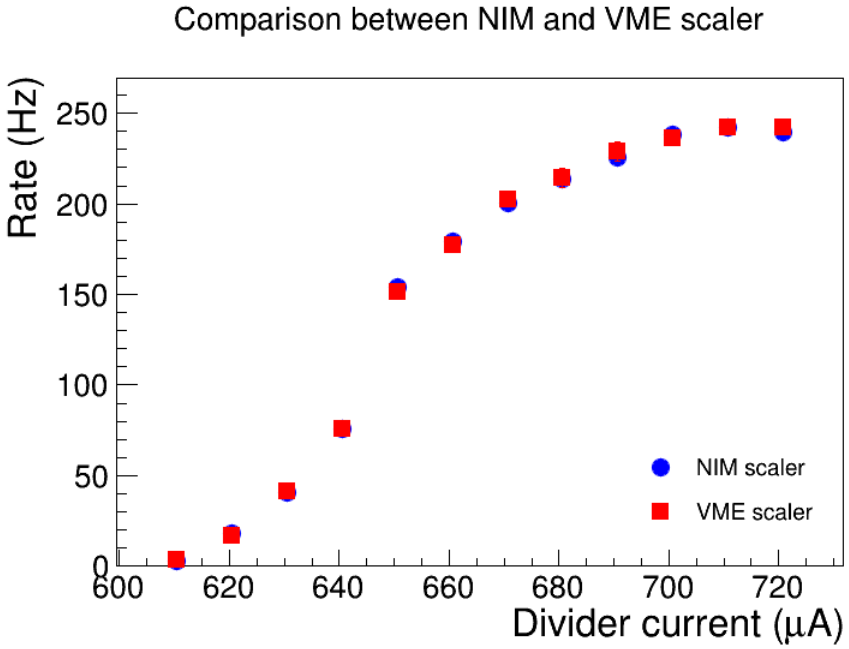

Figure 3.42: Comparison between the rate measured with a NIM scaler and a VME scaler (the error bars are included in the markers).

Fig.3.42 for example shows a comparison between the rate measured with

the full analog chain and the analog chain in which the NIM scaler was substituted with the VME scaler used in Louvain: the results are fully compatible, excluding the possibility of a hardware or software problem in the scaler. Similar results were obtained also for the VME constant fraction discriminator.

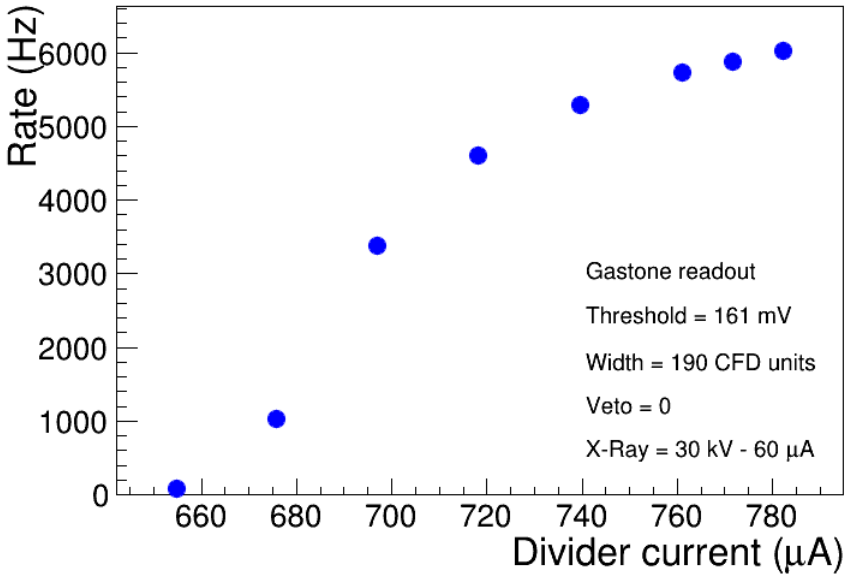

Figure 3.43: Rate curve obtained with a Triple-GEM detector read out with the Gastone chip in the laboratories of the University of Bari (the error bars are included in the markers).

Initial doubts about the operation of the Gastone chip were erased during a test performed in the laboratories of the University of Bari: the results, plotted in Fig.3.43, show that also with the use of this chip it is possible to reach a plateau with a Triple-GEM chamber. The reason why the plot in Fig.3.43 is not directly comparable with the previous, in particular for what concerns the current through the divider, is that the chamber used in this test was a GE1/1-IV, not the one used in Louvain.

From this validation tests also the electronics and data acquisition chains appear to be not responsible for the lack of plateau in the Louvain data. However, both with the analog chain and with Gastone during the test in Bari, the plateau was reached at a higher divider current with respect to the maximum reached in Louvain: the maximum value of the current through the divider in the Louvain test was 680 μA, which is just at the beginning of the efficiency

plateau observed in Fig.3.40 and 3.42. This observation agrees with the hypothesis of operation at low gain that was suggested by the simulation studies and could be an explanation for the low sensitivity measured.

3.4.6 Calculation of the integrated charge

To conclude, considering the irradiation time of the Louvain test, it is possible to calculate the total neutron fluence absorbed and give an estimation of the accumulated charge. The irradiation time is summarized in Table 3.8 so, the

Beam Current (nA)	**Flux (n/cm^2s)**	**Time (h)**
85	4.44×10^6	6
200	1×10^7	1.5
2000	1×10^8	1.5

Table 3.8: Summary of the irradiation time of the Louvain test.

total fluence, estimated as

$$F = \phi \times T \tag{3.11}$$

where ϕ is the flux in n/cm^2s and T is the irradiation time in s, is $\sim 6.9 \times 10^{11}$ n/cm^2 [5].

Assuming an average number of primaries n_p, from Fig.3.26, of 964, a gain G of 1000 and a sensitivity S from simulation of 2.6×10^{-3}, the accumulated charge can be estimated as

$$Q_{acc} = n_p \times G \times F \times S \times e \sim 0.27\, mC/cm^2 \tag{3.12}$$

where e is the electron charge.

The accumulated charge reference value from the Collaboration, already discussed in Section 3.3 is about 6 mC/cm^2.

3.4.7 Conclusions

During the test performed in Louvain-la-Neuve with a neutron beam the maximum measured sensitivity value was $(5.552 \pm 0.002) \times 10^{-4}$, of a factor ∼4.6

[5]The expected neutron flux in the harshest region of GE1/1 is $\sim 2 \times 10^5$ n/cm^2s for a total fluence in 10 HL-LHC years (T = 6×10^7 s) of $\sim 10^{13}$ n/cm^2.

lower with respect to the value foreseen by a dedicated simulation. From the simulation point of view, the result is overestimated, because the simulation assumes that once a charge is produced in the *drift* or *transfer1* gap a signal always develops into the chamber. On the hardware side, from a comparison between the data acquired in Louvain and during the validation tests after the irradiation, it seems that a better accordance would have been reached with the detector operated in a higher gain condition.

However, we can affirm that the detector and the electronics were both able to survive to an accumulated charge of ~ 0.27 mC/cm^2, as their full operation was completely proved after the Louvain test. This value, even not enough to completely qualify the operation of the chamber in the HL-LHC luminosity neutron environment, confirms the results obtained at the GIF and GIF++ with gammas.

Chapter 4

The Slice Test and the Detector Control System of the GE1/1 station

CMS approved in June 2013 the installation of a limited number of GE1/1 chambers into the muon endcaps. Four superchambers were originally foreseen for the installation in YE1/1 during the Year-End Technical Stop (YETS) 2016-2017, as shown in Fig.4.1: a fifth chamber, that will be powered with a multichannel power supply from CAEN [75] instead of the standard voltage divider, has been included in the design.

The main motivations of this early installation are gaining operational experience and demonstrating the integration of the GE1/1 system into the trigger [29].

The insertion of this new station into the CMS environment implies a series of technical interventions, aimed at integrating the chambers into the whole system. These activities comprehend the routing of cables for the low voltage and high voltage, as well as the signal cables. Moreover a dedicated gas system has to be implemented to supply the Triple-GEM. Among these integration activities, an important role is occupied by the development of the Detector Control System (DCS), which will allow the control and monitoring of the station from the CMS control room. This activity, in which I am deeply involved, with the development of the DCS part related to the gas system, has been initially focused only on the detectors to be installed in the Slice Test and will be later enlarged to the whole GE1/1 station.

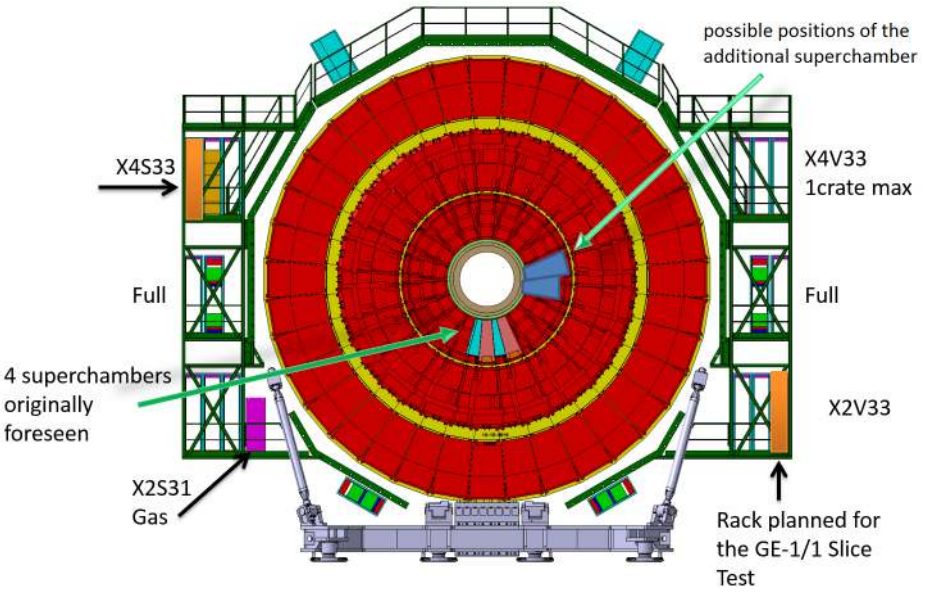

Figure 4.1: Positioning of the GE1/1 superchambers in the Slice Test.

4.1 Role of the Detector Control System

The Detector Control System (DCS) is responsible of ensuring the safe and optimal operation of the experiment so that high quality physics data can be recorded by the data acquisition system. The DCS input data rate is in the range of 10^4 MB/s. This data is not only stored to a database but it also needs to be processed at this rate in order to take automatic decisions and sequence commands that are sent to different parts of the system.

The DCS of the CMS experiment has to deal with some challenging requirements derived from the scale and characteristics of the experiment: for example, some of its hardware needs to operate in an environment with radiation doses up to 10^4 Gy/year and a high magnetic field.

The DCS system has to run without interruption, eventually only stopping for long shutdown periods. It should provide an interface intuitive and powerful enough to allow a single operator to control and monitor the whole experiment. The system should work in synchronization with the LHC machine state so that the experiment is ready for data taking whenever LHC is delivering stable colliding beams and, at the same time, it makes sure that the experiment is in a safe mode for other non-stable LHC conditions [72].

From the DCS point of view the CMS building complex, shown in Fig.4.2, can be divided in three main areas: the surface buildings, the underground

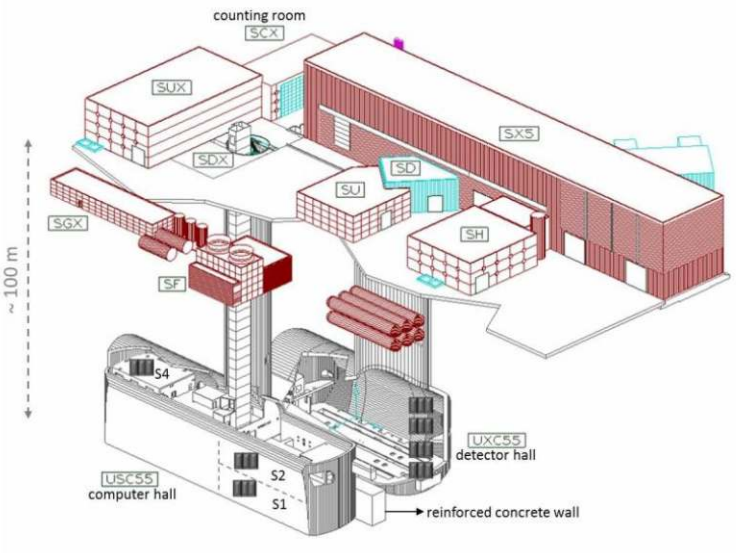

Figure 4.2: The CMS experimental facilities [72].

detector hall and the underground computer hall. In the surface counting room (SCX) sits the experiment online database together with the web servers, sharing room with a 3000 server farm used for the physics event building and filtering. The experiment control room (also on surface in SCX) contains the DCS human-machine interface. The detector is installed in the detector hall (UXC55) where there are a few hundreds of electronics racks. The DCS equipment in these racks needs to be radiation tolerant. The computer hall (USC55) hosts the power supply mainframes and cannot withstand the detector hall environment.

The DCS includes all the equipment supplying power, both low voltage and high voltage, together with CERN-made solutions used for many different services. For example, Programmable Logic Controllers (PLCs) are used to control critical processes involving safety aspects. Another important element is the Distributed Information Management system (DIM) [73] created at CERN and used by the custom hardware to communicate via Ethernet with the distributed control system PCs. A DIM server can be configured to publish DIM services containing information relative to the monitored hardware. These services can also be used to send information, like commands or settings, to the hardware. Any number of DIM clients can connect to a DIM service. PLCs are connected to the DCS system using industrial communication drivers over Ethernet [72].

In order to fulfill all the requirements, the CMS DCS system is divided

in many subsystems, each controlling one subdetector in all its features. For the GE1/1 system, it will be mandatory to provide a dedicated DCS system able to control the whole station in all its aspects. The GE1/1 DCS has been developed in a first version, able to control all the detectors to be installed in the Slice Test foreseen for the end of 2016.

4.2 General design

The DCS system of the GE1/1 station has been developed with the SIMATIC WinCC Open Architecture SCADA software, released by ETM [74], already used for the design of the entire CMS DCS system.

The main panel of the CMS GEM DCS is shown in Fig.4.3: it gives a general overview of the status of the system, through the graphical representation of two wheels of chambers, called *SC-TOP* and *SC-BOT*, referring to the Top and the Bottom chamber of each superchamber respectively[1].

On the bottom right of the panel there is a main overview of the status of the LV system, while on the top right a series of *Panic Buttons*, able to kill the HV, the LV or the entire system in case of emergency.

This panel, by means of a log in with authorized credential, gives a direct access to all the subpanels, shown in Fig.4.3, dedicated to different aspects of the operation of the station. It can be generally divided into two main parts: the first one, related to the operation of the chambers in the CMS environment includes the control and monitoring of the high voltage, low voltage, cooling and gas system as well as some environmental parameters, like the temperature. The second part instead has been developed to control the chambers in laboratory during the quality control procedures needed for their qualification.

Starting for the first part, the role of the high voltage panel is to permit a continuous monitoring and control of the HV applied to each chamber. It is an *active* panel, in the sense that the operator is actually able to send commands to the HV modules and change the values set. This first version of the HV panel, to be used for the Slice Test, right now foresee only the possibility to supply the chambers through a single HV channel: the voltage is then distributed to the foils through a ceramic divider. For each chamber two

[1]Here Bottom (B) and Top (T) indicates the single chamber inside the superchamber. The Top chamber is the chamber facing the interaction point, while the Bottom chamber is the one behind. Only the positive endcap is represented right now as the Slice Test does not foreseen the installation of chambers in the negative one.

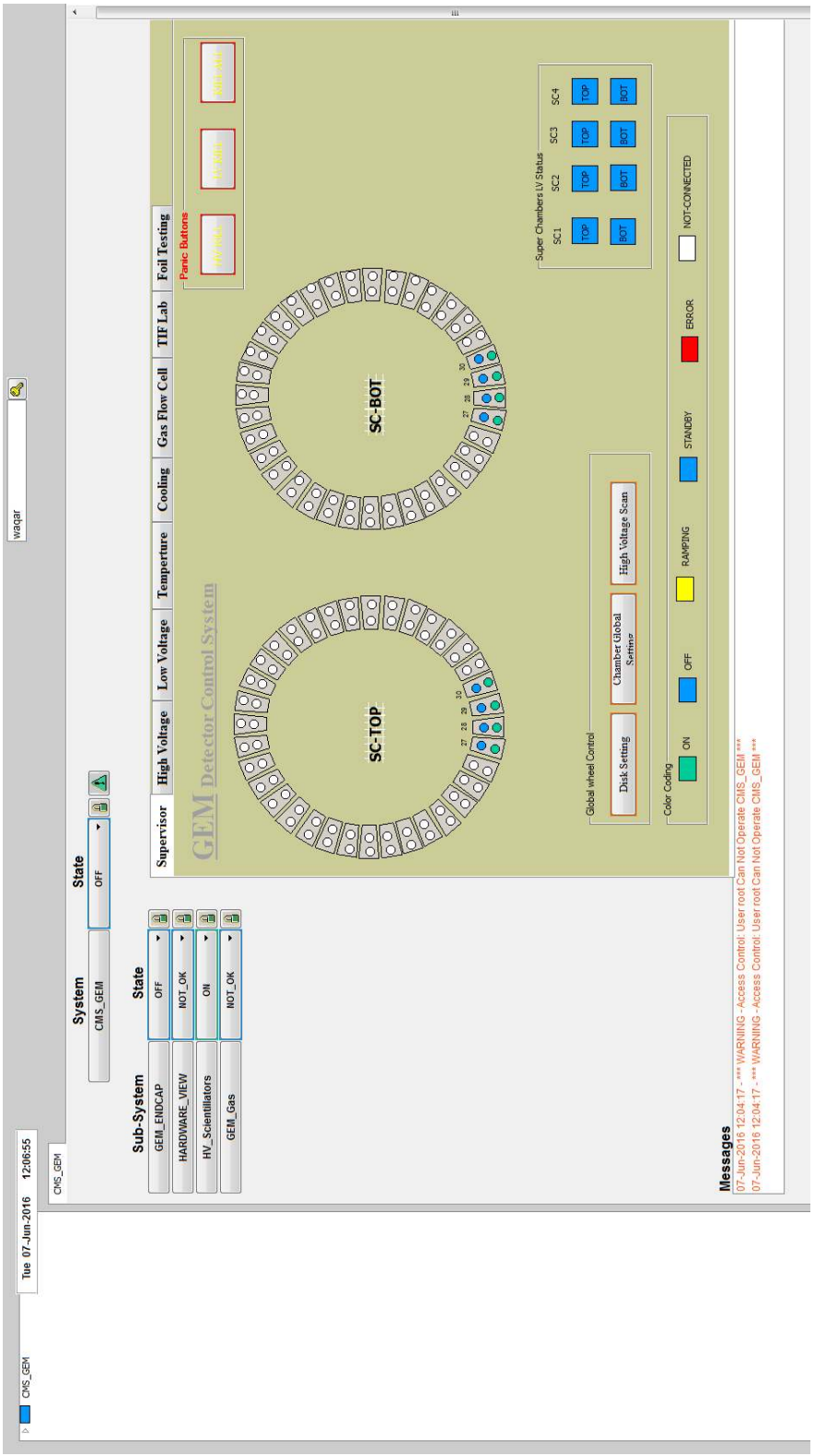

Figure 4.3: Main panel of the CMS GEM DCS.

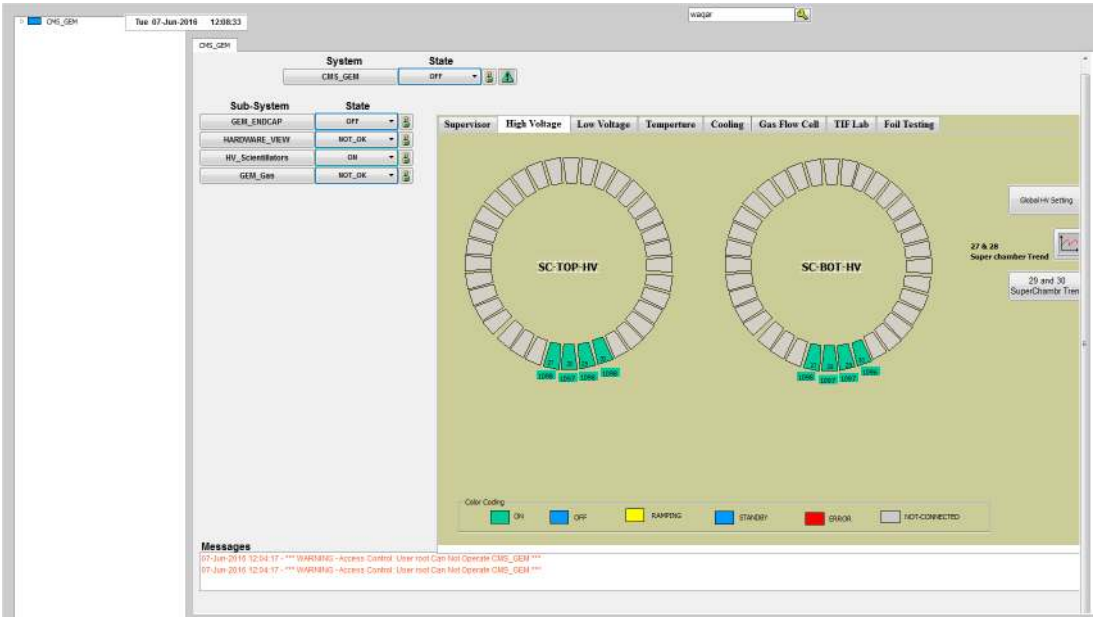

Figure 4.4: HV panel of the GEM DCS.

parameters must be continuously monitored: the HV applied and the current through the divider, which assure that the voltage is distributed correctly to the foils and gaps. The presence of divider itself prevent the possibility to monitor the current though each foil of the chamber. The total resistance of the divider is known and with a simple calculation, assuming an Ohmic behavior of the system, it is possible to foresee the current value that should pass through it. A wrong divider current value measured could be therefore used as indication of the rupture of one of the resistors, causing a wrong distribution of the voltages, which can lead to a damage or even rupture of the detector.

The configuration of the high voltage panel is shown in Fig.4.4: it has a structure similar to the main panel, with the station represented by two wheels of chambers. For each chamber the panel shows the status indicated by the color of the trapezoid, following the color code green for *OK* status, blue for *Not-OK* status and red for *Error* status. Together with the status, also the HV value applied to the chamber is displayed, in the text box under the relevant trapezoid.

The situation will be more complex for the last superchamber of the Slice Test and for the complete GE1/1 HV panel, as the chambers will be powered through a CAEN multichannel power supply [75]. It will allow the powering of each foil and gap independently, for a total of seven HV channels for each detector. The main advantage will be the possibility of monitoring the behavior

of each foil independently, looking for discharges, as well as slightly modifying the different applied fields to enhance the performance. On the other hand, the architecture of the system, and consequently, the one of the DCS panel, will be more problematic, as the number of channels to be checked will explode. The additional panel is going to be developed right now, in order to be ready for the Slice Test.

The low voltage panel instead has the role of control and monitoring the behavior of the electronics system: the main components of the low voltage system are the VFAT_V3 chip, developed on purpose for the readout of GE1/1 Triple-GEM detector, and the optohybrid. Its main tasks are to synchronize the data sent by the VFAT_V3 chips, zero-suppress the trigger data, encode the data and send them via optical links to the trigger electronics. A comprehensive description of the GE1/1 electronics system can be found in [29]. Also this panel is an *active* panel, as it allows the direct intervention on the different parts of the system. The structure of the panel is similar to the one of the high voltage but in this case the values expressed in the text boxes are related to the VFAT and optohybrid status. Moreover, the low voltage panel includes a dedicated subpanel with a summary of the status of all the LV elements considered in the system.

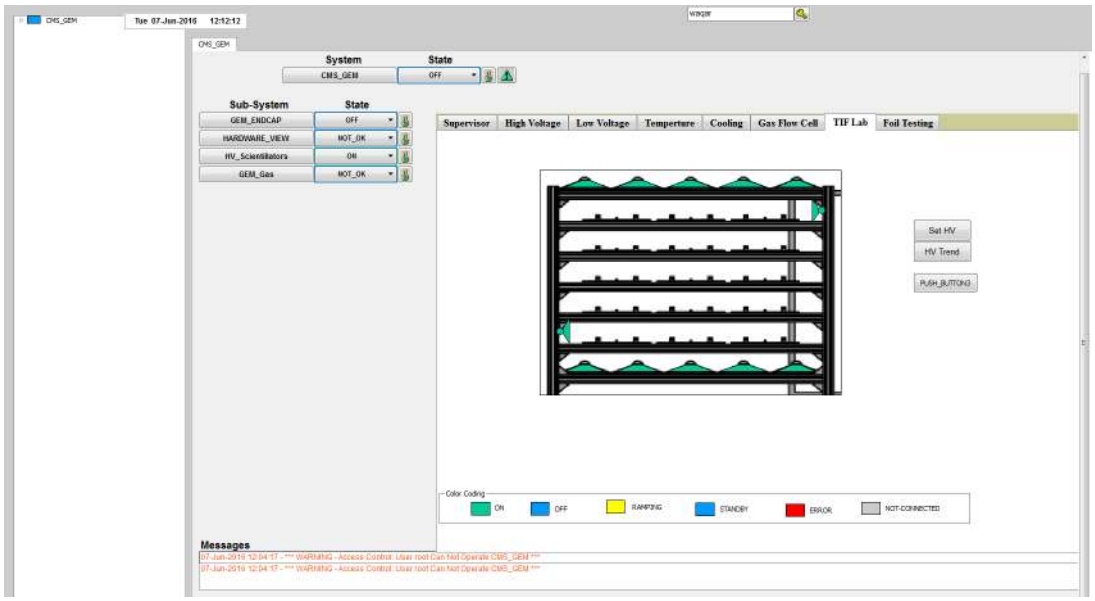

Figure 4.5: DCS panel dedicated to the TIF laboratory activity.

The role of the cooling panel is to control the system that avoid the overheating of the chambers. Indeed, the on-detector electronics together with the

powering of the detector itself act as heat power source, for about 78 W for each chamber and a total of 11.2 kW for the whole station. The design of the on-detector cooling system is finalized and is based on the use of copper pipes, thermally connected to the heat sourced with copper strip plates. Water coming from the YE1/1 cooling circuit should flow into the pipe to cool down the entire system [29]. However a discussion is still on-going between the GEM Collaboration and the CMS Technical Coordination (TC) for what concern this last point, i.e. the connection to the general cooling system. For this reason the complete hardware schema is not fully defined, preventing also the development of the complete DCS cooling panel.

The Temperature panel should be used to monitor the environmental temperature in which the detectors must operate, as it can influence the performance, like for example the gas gain. However also in this case the hardware system has not been completely defined, therefore the DCS panel is still to be developed.

The second part of the DCS system hosts two panel dedicated at the operation of Triple-GEM in laboratory.

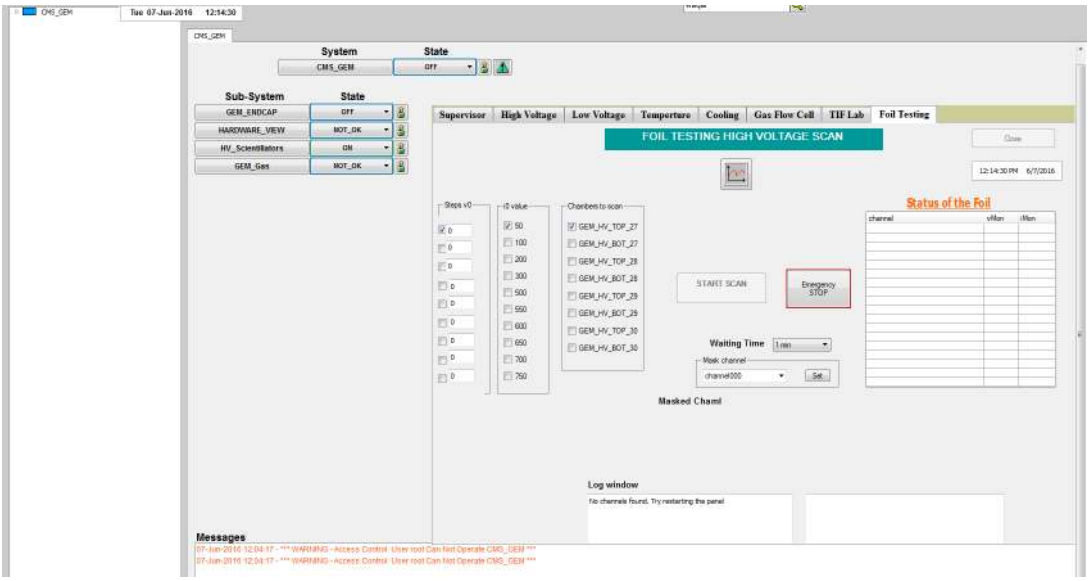

Figure 4.6: DCS panel dedicated to foil testing.

The TIF lab panel, shown in Fig.4.5, has been developed in order to control the scintillators mounted on the cosmic stand in the TIF laboratory, fundamental element for the quality control chain of the GEM detectors.

Finally the Foil Testing panel has been developed to be used for the high

voltage scan to be performed on the GEM foils during the quality control and is displayed in Fig.4.6.

4.2.1 The gas panel

The purpose of the gas panel of the DCS is to monitor the status of the gas system of the GE1/1 station. The structure of the gas system is shown in Fig.4.7: in the Gas Building SGX at Point 5 CMS, the gas is stored and then sent into the mixer, where the correct gas mixture is created.

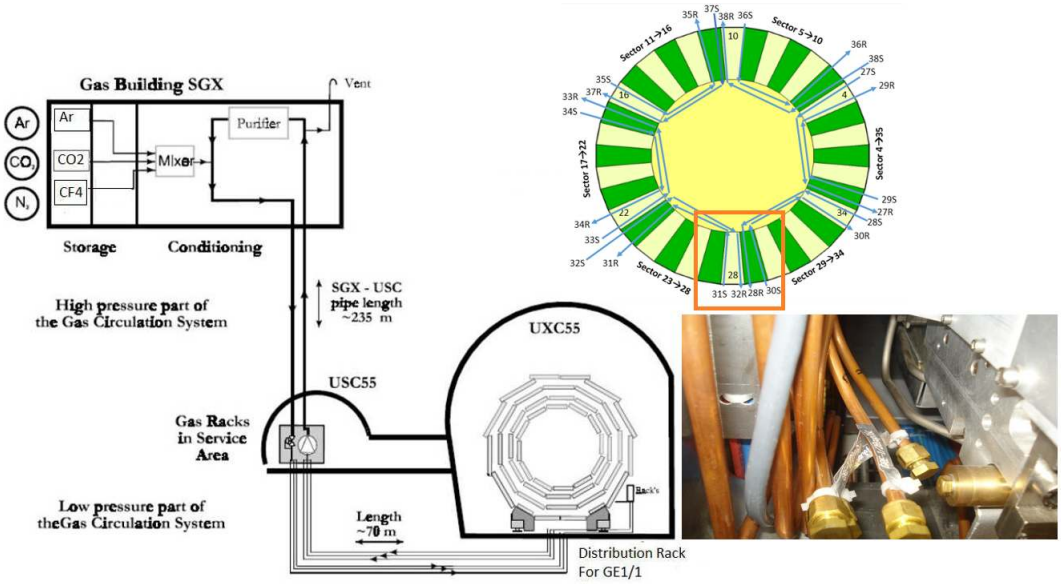

Detector gas volume	Volume [cm^3]	Gas flow [Volume/h]	Gas mixture [%]
Single GE1/1 detector - Long	3120	1	$Ar/CO_2/CF_4$ 45 : 15 : 40
GE1/1 superchamber -Long	6240		
Endcap disk	224640		
Full installation	449280		

Figure 4.7: Overview of the gas system for the GE1/1 station. In red is highlighted the region in which the chamber for the Slice Test will be installed, with the relevant gas lines.

The mixture is then sent, through a of 235 m lenght pipe, in the USC, where it enters in the gas racks in the service area. The connection between the USC and the UXC is obtained through a 70 m-long pipe. In the UXC, the gas is finally distributed to all the detectors of the station.

The structure of the gas lines to be used for the Slice Test is shown in the top of Fig.4.7: the region that will host the first four superchambers that will be installed in 2016-2017 is highlighted in red, the relevant gas lines are the number 28, 30, 31 and 32. Each gas line supplies two adjacent chambers, for

example the line 28 supplies the chambers 29 Bottom and 30 Bottom. The line that will supply the fifth superchamber is not yet defined: as soon as it will be selected, it will be inserted in the DCS in a straightforward way, as well as the rest of the GE1/1 gas system.

Differently from the other panels, the gas system panel is completely *passive*, i.e. it allows only the monitoring of the system and not a direct action on it. Indeed the hardware of the entire CMS gas system is centrally controlled by the CERN gas group [76], not by the single subsystems: the CERN gas group installs the components, sets them and intervenes in the case a problem is detected by one of the users.

The role of the gas panel is fundamental for the correct functioning of the station, as of course the detectors cannot operate without a proper gas supply. Indeed, the composition of the mixture must be check continuously, as it influences the performance of the chambers: for example, if a too low percentage of argon is supplied (being equal the voltages applied) the chamber will not reach the expected efficiency. On the opposite, a too high percentage of argon can lead to the development of discharges, which can eventually damage the detector. The gas flow must also be supervised: the normal operation is obtained with a gas flow of the order of 2-3 l/h (ideally 1 Volume/h $\sim$ 3.1 l/h for a Long GE1/1 chamber), while a difference between the input and output volume can be an indication of a leak in the detector. Finally, another important parameter is the pressure, as the GE1/1 chambers are designed to operate in a slight overpressure, typically of the order of 20 mbar. In case a too high gas overpressure, higher than 50 mbar, is reached into the detectors, they could be damaged irremediably. In order to fulfill the aim of monitoring the entire gas system, the main gas panel of the DCS, shown in Fig.4.8, controls many subpanels, each dedicated to a different aspect of the system: the Services, the Gas Racks and the Flow Cells.

The Services include the Mixer, the Exhaust and and Expert section, dedicated so far to the alarm settings and other configurations with access restricted only to system experts. The button *Alarm Set* opens a new subpanel, called *Alarm Settings* panel, that is dedicated to the definition of the error and warning ranges of operation.

Shown in Fig.4.9, it is divided in four sections, each corresponding to one portion of the gas system. Starting from the top left we can find the Mixer, with all the parameters related to the components of the gas mixture. The

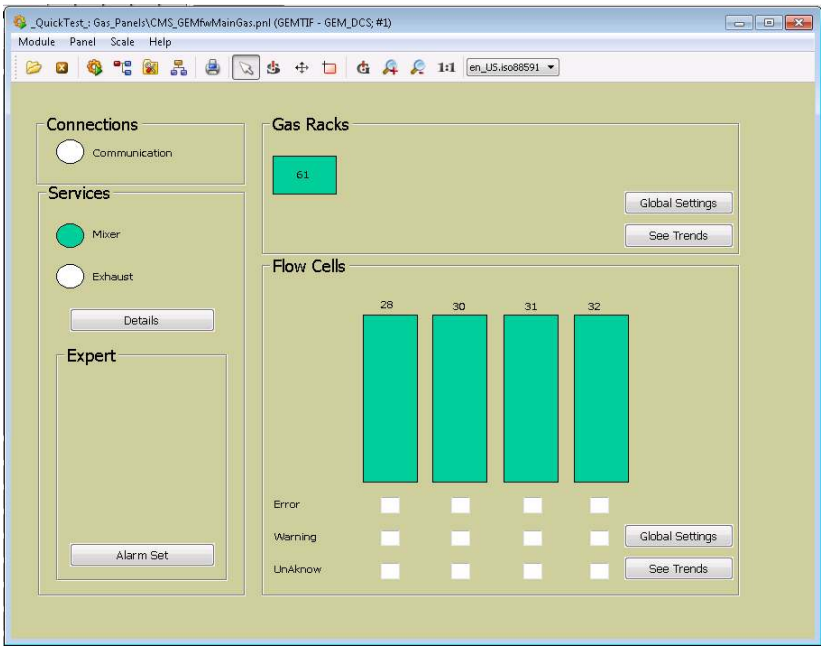

Figure 4.8: Main DCS gas panel.

Mixture drop-down menu allows the expert to select between the Ar/CO_2 mixture and the $Ar/CO_2/CF_4$ mixture. In case Ar/CO_2 is selected, all the parameters related to CF_4 are automatically deactivated when the *Check* button is pushed. The relevant parameters for the mixer are the *Line Ratio* for each gas component, which corresponds to the percentage of that particular gas in the mixture, the *Input pressure* of each gas and *Output pressure*.

The other two completed parts of this panel are related to the rack and the flowcells. The role of this last item is actually to provide the right gas flow to the chambers, so the relevant parameters are the input flow and the difference between the input and output flows, useful to detect for example gas losses.

The exhaust section in not completed yet because the Collaboration has not defined so far the schema of the exhaust system. Indeed, while for the Slice Test probably an *open system* will be implemented, i.e. a system in which the output gas from the chamber is simply released in the atmosphere, for the complete GE1/1 station a more complex solution should be implemented. The reason of this is the fact that one of the two gas mixtures considered by the Collaboration is $Ar/CO_2/CF_4$ 45%/15%/40%, which contains a high concentration of CF_4 that is in the list of banned gases due to the presence of fluorine. If this mixture will be finally selected for the operation, it will not be possible anymore to release the exhaust in the atmosphere, but a system

that foresees the recirculation or the recuperation of the CF_4 will have to be implemented (see [48] for details concerning the gas system structures).

The expert that is going to work with the DCS gas panel has to define the ranges in which a value is considered correct, suspicious or wrong. For this reason, in the Alarm Settings panel the expert should define two ranges, called *Warning* and *Error*. The read datapoint value is compared with these reference values: if it is outside the Warning limits, the variable goes in the Not-OK status. If the value is outside the error limits set, the variable goes in the Error state. In order to help the expert in setting the reference values correctly, each section of the Alarm Settings panel is equipped with the *Check* button, already mentioned above. When it is pressed, the software compares the Warning and Error reference values of each datapoint and check their consistence. For example, Fig.4.9 shows a particular case in the rack portion, where the combination minimum value higher than the maximum value is considered as an error. All the other couples that are considered consistent, are instead colored in green.

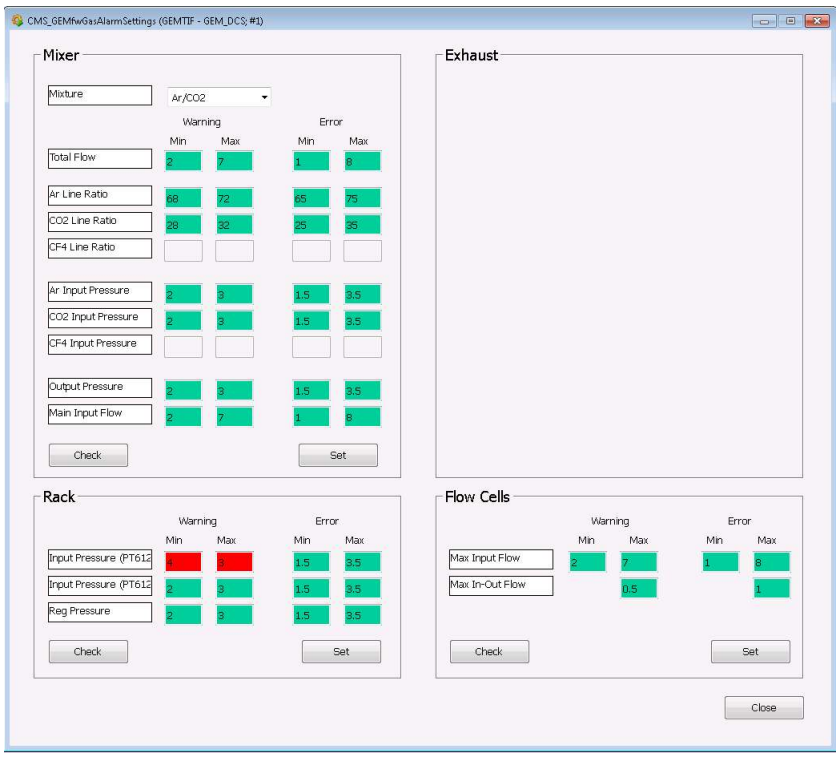

Figure 4.9: Alarm settings panel: the red color of two text fields indicates that those values are not consistent (i.e. Min > Max).

Once that the expert has selected the Warning and Error reference values

and checked their consistence, through the *Set* button they can be stored in the *Datapoint parametrization module* shown in Fig.4.10, from where they are recalled every time a datapoint value read from the system has to be checked.

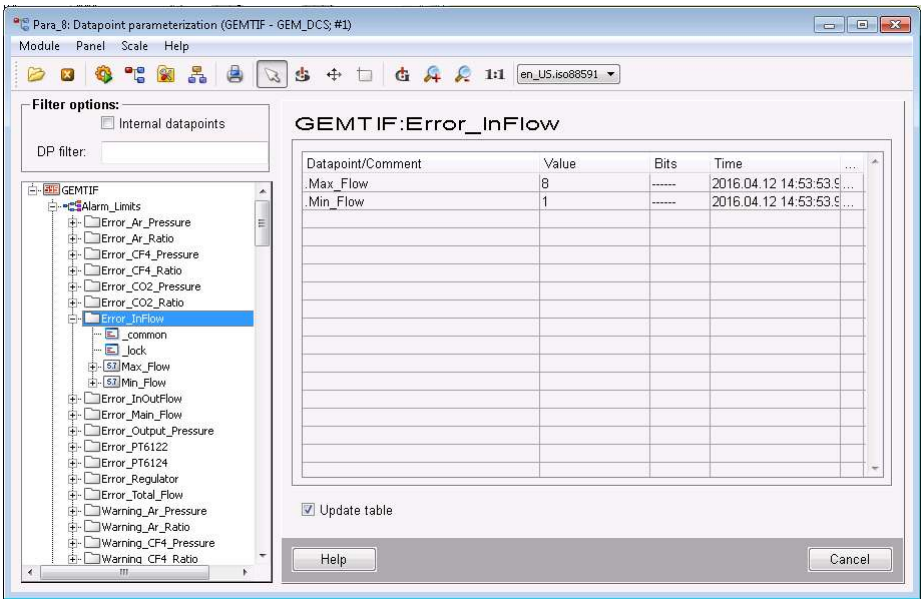

Figure 4.10: Para module showing that the values set in the alarm settings panel are actually applied to the reference datapoints..

Moving to the other parts of the services section of the Main Gas panel, the Details button opens the Gas Services panel, shown in Fig.4.11. This panel contains all the current values of the datapoints read from the gas system concerning the Mixer, the Environmental parameters and the Exhaust.

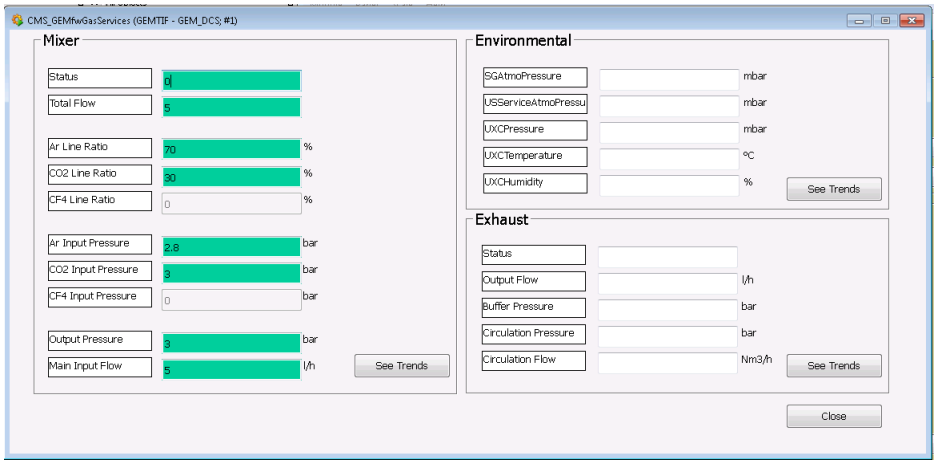

Figure 4.11: Gas services panel.

Every time that the panel is opened, it is automatically filled with the

current values of the datapoints. Each box is then refreshed automatically every time that one value changes. The color code of the boxes is related to the alarm value set by the expert in the Alarm Settings panel and follows the structure already explained above.

Figure 4.12: Panel showing the trend of the gas mixer parameters.

The trend in time of the most important datapoint is also graphically shown in a plot as in Fig.4.12. The datapoints plotted are the input pressure of the three possible components of the gas mixture, with the Y axis on the left in red, blue and green respectively for Ar, CO_2 and CF_4, and the ratio of each component in the mixture, the Line Ratio, with the Y axis on the right in light blue, brown and orange respectively.

On the top right part of the Main Gas panel, the Gas Racks section is displayed: on the Main Gas panel we can find an indicator showing the general status of the rack, represented as a colored rectangle identified with the rack number. As shown in Fig.4.13, right now the only rack implemented in the gas system is the number X2S31/61, that should be used to supply the chambers during the Slice Test, while it is still on discussion the possibility to introduce a second rack, the number 62. The relevant datapoints here are monitored though the Rack Status subpanel, opened with the Global Settings button in the Rack Status section.

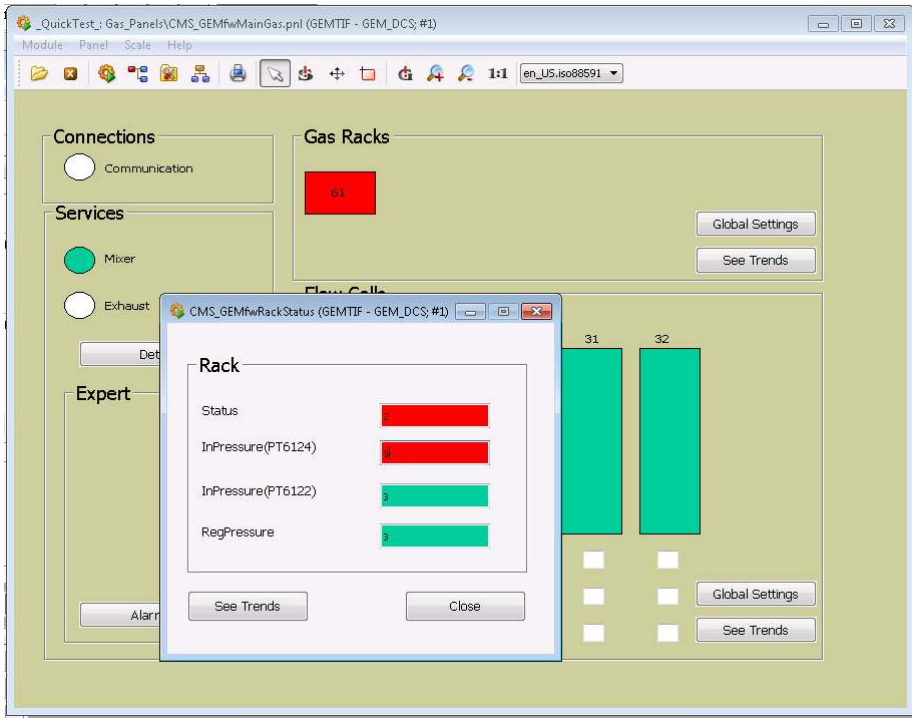

Figure 4.13: Rack status panel.

Also for the rack status, a trend panel is implemented, the Rack Trend panel, with the same characteristics of the Mixer Trend panel described in detail above.

The bottom right part of the Main Gas panel includes the Flow Cells section. Each rectangle in Fig.4.8 represents one of the gas lines that physically supplies the gas to the chamber. Right now only the four lines to be used with the first four superchambers foreseen in the Slice Test are implemented. The four lines, numbered to 28 to 32, as already explained above will supply two chambers each.

The detail of each line is shown in a table in the Gas Settings panel, opened with the Global Settings button. As shown in Fig.4.14 for each gas line, the table contains the names of the chambers supplied, the current input flow of the line, with the timestamp of the last read value, and the current output flow of the line, with the relative timestamp. The table is automatically updated every time at least one value changes.

A trend plot panel, associated to this table, shows then the behavior of the input and output flow of each line.

Concerning the alarm implementation for this section of the gas panel, as can be observed in Fig.4.9, the relevant variables are three: the input flow,

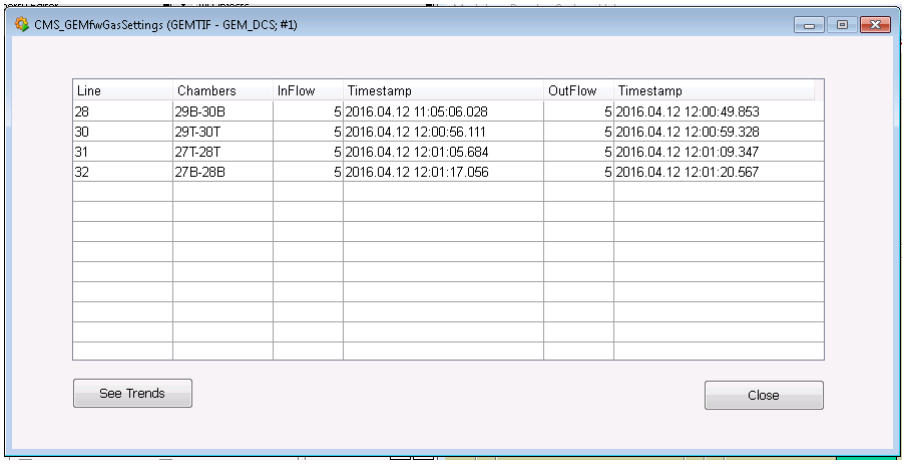

Figure 4.14: Panel showing the current values of input an output flow of each flowcell.

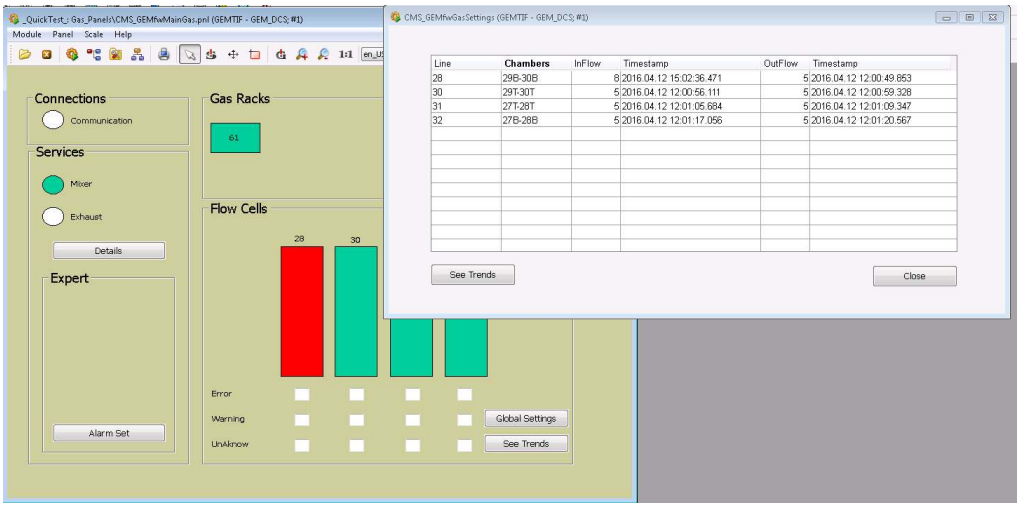

Figure 4.15: Example of response of the panels to a variation in a datapoint.

the output flow and the difference between input and output, where the last one is fundamental to detect possible leaks in the detectors or in the line or possible wrong calibration of the flowcells. Exactly as in all the rest of the gas panel, the color of the flowcell indicator in the main gas panel is linked with the status of that flowcell defined through the ranges given by the expert in the Alarm Settings panel. If for example the input flow value is too high with respect to what set by the expert, as in Fig.4.15, the value is displayed in the table and the flowcell indicator in the Main panel goes in Error state.

Finally the entire Gas System panel has been included in the Final State Machine of the GE1/1 DCS, together with all the other panels controlling the high voltage, low voltage and the other parameters, as shown in Fig.4.16. The

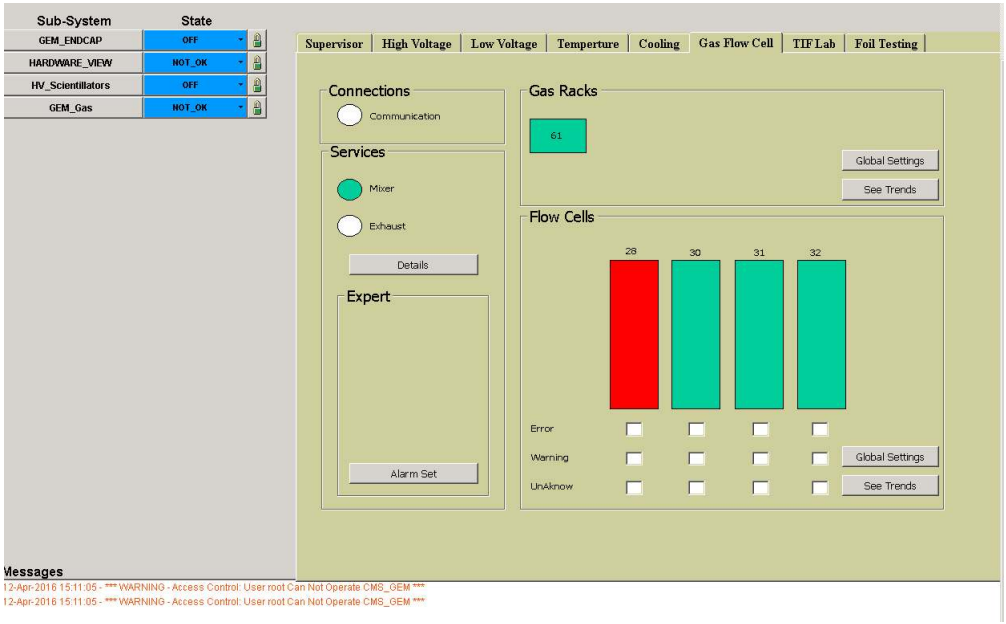

Figure 4.16: Implementation of the gas panel into the final state machine. Here the State of the subsystems in the top left of the page are still in blue, Not-OK state, because the system has not yet been included in the general CMS DCS and is not yet really connected to the hardware.

optimal functioning of the DCS Gas System panel is going to be tested before the beginning of the Slice Test with a complete and working hardware system developed on purpose.

Chapter 5

New MPGD for the GE2/1 and ME0 stations

The GE2/1 and ME0 stations are proposed for the completion of the high η region of the CMS muon system for the operation during the HL-LHC run. The installation of GE2/1 on the back of the YE1, in the second station, is foreseen to be anticipated to the End of Year Technical stop 2022-2023. The proposal instead is to install the ME0 station, to be inserted just behind the forward hadron calorimeter, during LS3 actually planned for 2024-2026.

5.1 The GE2/1 station

The GE2/1 station is proposed to be installed on the back of the YE1, in the second station, in the position shown in Fig.5.1 left. The baseline single GE2/1 detector is designed to have four sub-modules inside, which will be installed layer by layer, in order to form the superchamber configuration.

The two biggest challenges related to the installation of this station are related to mechanical issues: first of all the dimension of the superchambers, more than 1.8 m long and covering 20° each[1]. Moreover, as clear from Fig.5.1 right, the envelop available for the installation is really limited, only 88 mm. If we take as a reference a GE1/1 superchamber, including shielding, cooling and all the services, the thickness is 74 mm, giving a clearance of only 14 mm.

[1]Also the option of 10° chambers was taken in consideration, but it was considered unfavorable as it would include more dead regions. For this reason it was discarded in favor of the 20° solution.

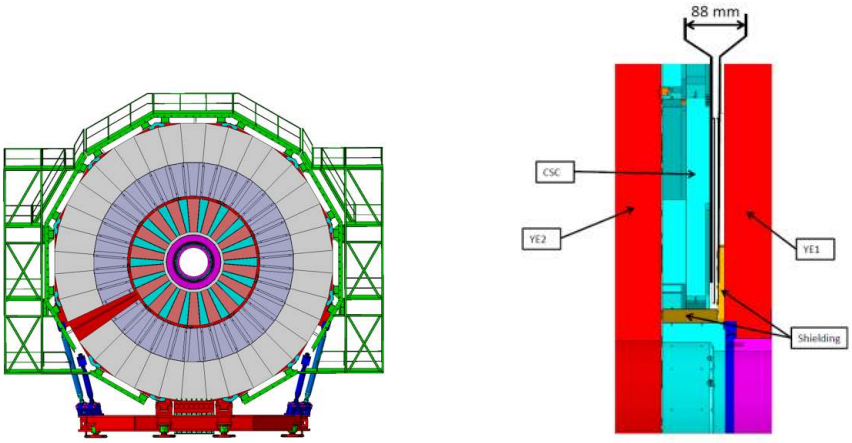

Figure 5.1: Left: positioning of the GE2/1 station in the YE1. Right: space available for the GE2/1 installation.

Notwithstanding these mechanical issues, the technology to be installed in the GE2/1 station should satisfy some minimal requirements in order to achieve the goals already discussed in Section 1.4.2.2, i.e. improve the L1 muon momentum resolution, the reconstruction performance and the efficiency in the second muon station (actually totally driven by CSCs performance) and the L1 tracking trigger on displaced muons.

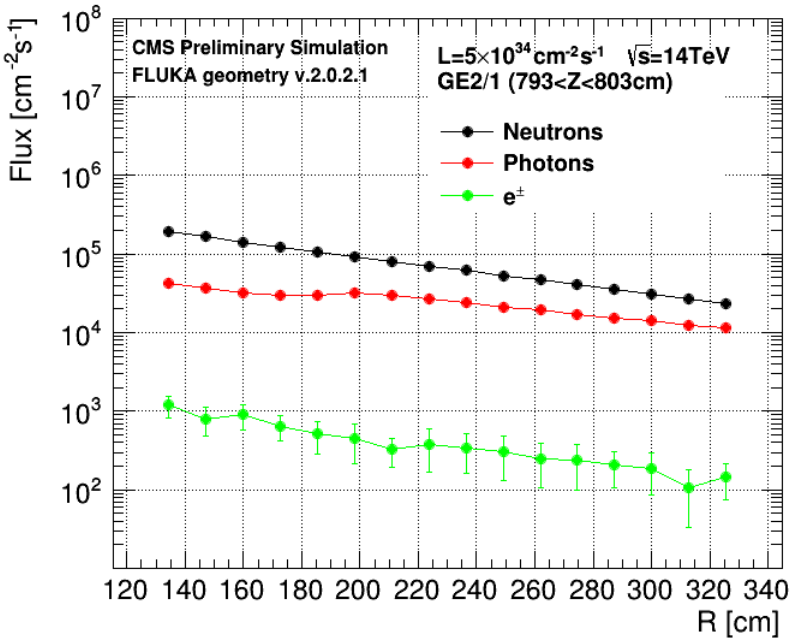

Figure 5.2: Simulated fluxes in the GE2/1 region (FLUKA version 2.0.2.1).

The L1 muon momentum resolution could be enhanced with the addition of a second detector if it would allow the bending angle measurement: this is possible only if the angular resolution of the additional detector is of the order of 1 mrad, which corresponds to a spatial resolution lower than 800 μm. Moreover, for reconstruction, a pitch of at least 450 μrad is requested, which leads to a spatial resolution lower than 433 μm. Finally the timing requirements useful to resolve the ambiguities in CSC reconstruction and efficiency are of the order of 8 ns, not too strict due to multiple redundancy of spatial and timing measurements.

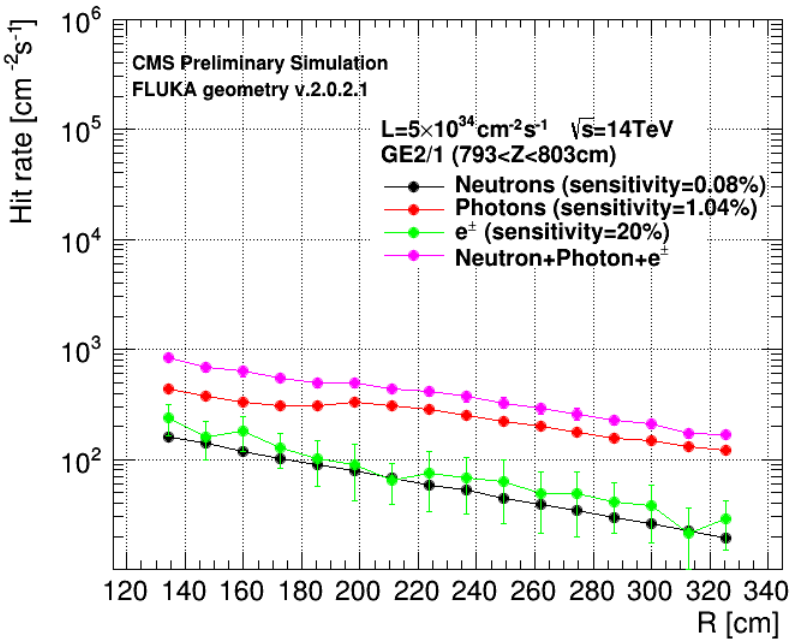

Figure 5.3: Expected hit rate in the GE2/1 region, based on the GE1/1 simulated sensitivity.

Finally the selected technology must be able to survive at the intense background flux expected and shown in Fig.5.2. The expected hit rates in the GE2/1 region, calculated using as a reference the sensitivity of GE1/1 Triple-GEM, are of the order of 1 kHz/cm^2 and are plotted in Fig.5.3. An estimation of the expected integrated charge in this region can be extrapolated from these numbers, using formula 3.2: always considering as a reference a Triple-GEM detector, with gain equal to $2\times$ 10^4, a number of primaries in the gas gap of 31 and a 10-year HL-LHC operation time (6×10^7s), the estimated integrated charge is $\sim$ 6 mC/cm^2, like in the GE1/1 region.

Considering these problems, the Collaboration is evaluating two technological solution for the GE2/1 chambers: the baseline is given by Triple-GEM chambers, with a similar geometry to GE1/1. The optional solution instead is the μRWELL technology.

5.1.1 GEM baseline solution

The baseline solution for the GE2/1 station consists of Triple-GEM detectors, with a layout similar to GE1/1, but covering a much larger surface.

Triple-GEM is a very mature technology and easy to be implemented from the performance point of view. Indeed the results obtained during the R&D performed for the GE1/1 station show that this technology is able to reach both the requested angular and time resolutions (see Fig.3.7 and 3.8). Its operation has been fully validated with the use of a eco-friendly gas, which will be of primary importance in the future, due to the restrictions imposed by the European Union. Moreover rate capability measurements and longevity tests prove that it will be able to cope with the expected hit rate and background without any losses in performance.

The proposed GE2/1 station will be composed by 36 20° superchambers, each formed by two single Triple-GEM detectors, that, with the dimensions shown in Fig.5.4, would be the largest GEM detector ever built.

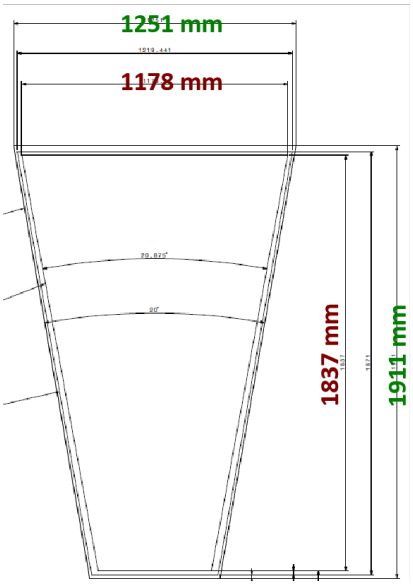

Figure 5.4: Sketch of the GE2/1 chamber dimension.

Due to the dimensions of the single chamber, a unique module solution for

GE2/1 is not possible. In fact on one side the GEM foil base material is limited in size, as the material is produced in pieces 610 mm wide, with a consequent GEM size of 570 mm, including all the external services. On the other side, the PCB producers usually limit the size of the PCB to about 60 cm, even if it is possible to produce larger units.

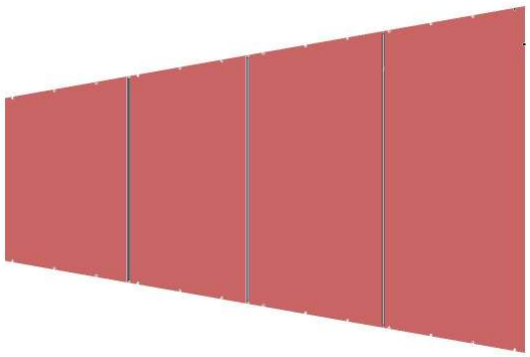

Figure 5.5: GE2/1 chamber divided in modules.

For this reason the GE2/1 chambers will be segmented in four horizontal modules, as shown in Fig.5.5 in order to get a maximum PCB size compatible to what actually produced. The four modules will be coupled together trough external metallic profiles, with a dead area between them limited to 34 mm. In this way, the GE2/1 chamber will be actually composed by four independent detectors, with different gas volumes. In order to reduce as much as possible the total dead area, the two Triple-GEM chambers forming one GE2/1 superchamber will be segmented in different way: one will be composed by four modules all of the same height. The other one will have instead two bigger and two smaller modules. In this way at least one point from one of the two chambers will always be available all over the GE2/1 areas. On the other hand, this choice implies a strong complication from the construction point of view, because eight different kind of PCB will have to be produced, as well as GEM foils of eight different dimensions.

The readout of the GE2/1 chamber will be segmented in eight η-partition and six ϕ-partition, as shown in Fig.5.6, for a total of 768 strip per η-partition. It means that, considering the 20° coverage of the GE2/1 chamber, each strip will cover about 450 μrad, as for GE1/1 chamber. This matching between the two stations allows a better reconstruction of the segment between the two and is compatible with the request for the improvement of the L1 muon momentum

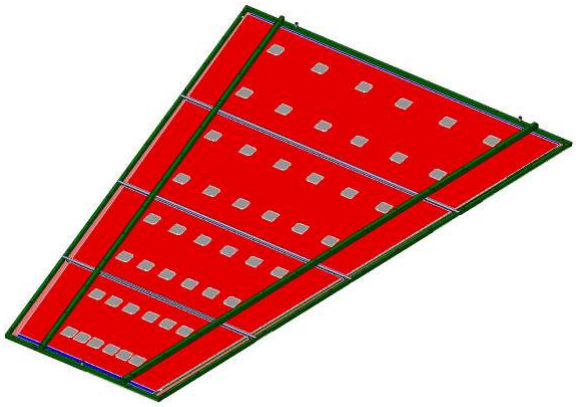

Figure 5.6: Readout partition of a GE2/1 chamber.

resolution.

The readout will be performed with the VFAT3 chip [29] that has been developed for GE1/1 and is going to optimized for the GE2/1 case, which is able to give a trigger signal from a group of strips (two, four or even more). Presuming to make the trigger with groups of two strips, the angular resolution that will be achieved will be lower than 1 mrad, acceptable for the request from trigger. Moreover, this will give an improvement of the trigger rate of a factor from 2.5 in the region $1.6 < \mid \eta \mid < 2.1$ to 1.5 in the region $2.1 < \mid \eta \mid < 2.4$.

5.1.2 μRWELL optional solution

The optional solution for the GE2/1 station consists of μRWELL detector [89].

Based on the μWELL described in Section 2.4.3.1, the μRWELL detector, sketched in Fig.5.7, is obtained merging a suitable etched GEM foil with the readout PCB plane coated with a resistive deposition. A suitable pattern has been created in the copper on the bottom side of the foil, in order to create small copper dots in correspondence of each WELL structure.

The resistive coating can be obtained through a particular sputtering technology called *Diamond Like Carbon (DLC)*[2]. The WELL is obtained with a 50 μm thick polyimide foil, with conical holes of 70 μm (50 μm) top (bottom) diameter and 140 μm pitch. The cathode electrode, defines the drift gap and completes the detector.

[2]Diamond-like carbon (DLC) is a class of amorphous carbon material that displays some of the typical properties of diamond. DLC is usually applied as coatings to other materials that could benefit from some of those properties. Applications of DLC typically utilize the ability of the material to reduce abrasive wear [90]

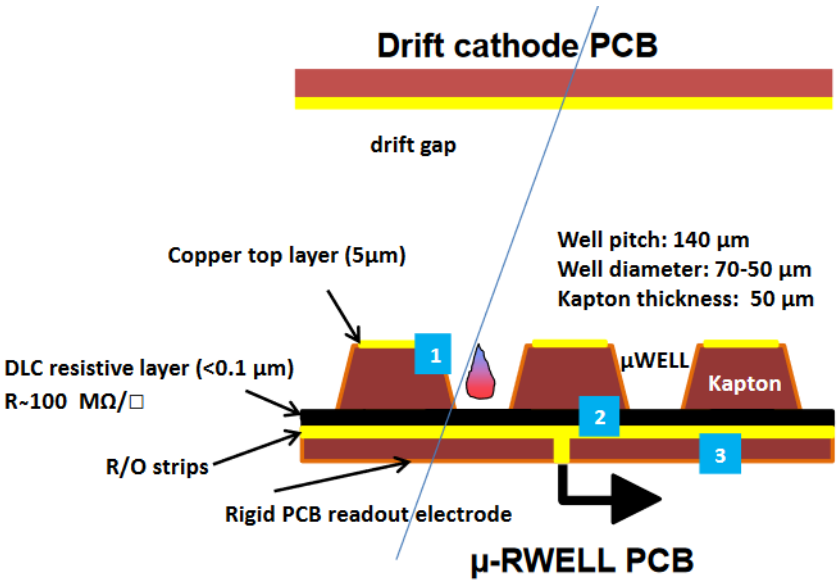

Figure 5.7: Structure of the μRWELL detector [89]

The advantage of this kind of geometry is that the whole electron charge produced in the amplification region, the holes, is directly collected on the resistive layer, that is capacitively coupled with the readout plane, through the copper dot. In addition, also the ionic component contributes to the formation of the signal in a similar way as the electron part.

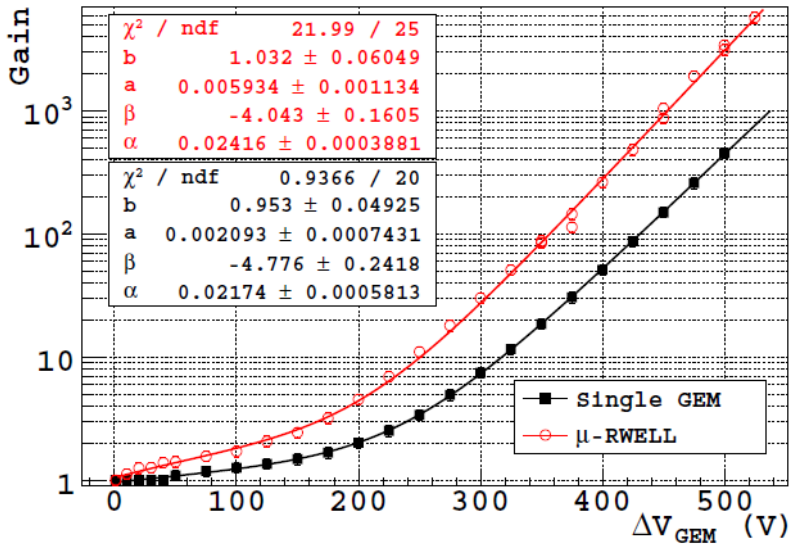

Figure 5.8: Gas gain obtained with μRWELL (red point) and a single-GEM (black points) in Ar/CO_2 70%/30%, as a function of the potential applied [89].

Moreover, in the μRWELL a higher gain can be achieved thanks to the

presence of the resistive electrode which quenches the discharges and allows a higher amplification field inside the channel, as can be observed in Fig.5.8, that shows a comparison between the gas gain reached with μRWELL detector and a single-GEM as a function of the potential applied in Ar/CO_2 70%/30%.

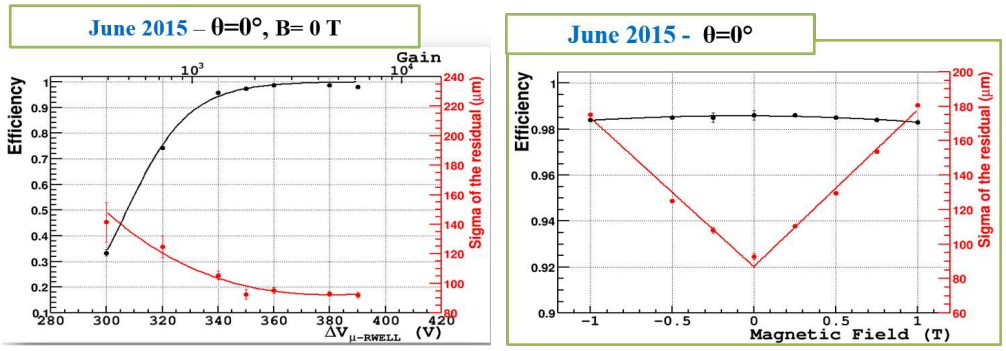

Figure 5.9: Left: efficiency (in black) and spatial resolution (in red) as a function of the applied potential, i.e. of the gain. Right: efficiency (in black) and spatial resolution (in red) as a function of the magnetic field. Both the plots are obtained with a small prototype, with Ar/Iso 90%/10% mixture, with muon beam perpendicular to the chamber surface (Θ=0°) [91].

Focusing on the performance that could be achieved with this new technology, Fig.5.9 displays the results obtained with the first prototypes of μRWELL detector during few test beams carried out at the SPS H4 line in 2014 and 2015, with the Ar/Iso 90%/10% gas mixture. The left plot shows the efficiency and the spatial resolution reached by the detector, without magnetic field, as a function of the potential applied, i.e. the gain. At full efficiency, i.e. gain higher than 3×10^3, the spatial resolution obtained is lower than 100 μm. On the right instead we have the results with magnetic field up to $\pm$ 1 T: the efficiency remains almost stable, with variations of the order of percent at higher magnetic field values; the spatial resolution is degraded with the increase of the magnetic field, up to 180 μm in the worst condition [91].

Similar results can be obtained with the Ar/CO_2 gas mixure, which would be preferred in the CMS context as it is not flammable differently from Ar/Iso 90%/10%[3]. Fig.5.10 left shows the efficiency, in black, and the spatial resolution, in red, obtained with the prototype. In the right plot instead the distribution of the residual is plotted, whose σ represents the spatial resolution: including also the contribution from the trackers, the prototype reaches a

[3]A gas mixture is considered flammable if it contains a flammable component with a percentage greater a fixed value different from gas to gas. In the case of Isobuthane in Argon based mixture, this limit is set to 2.4% [92].

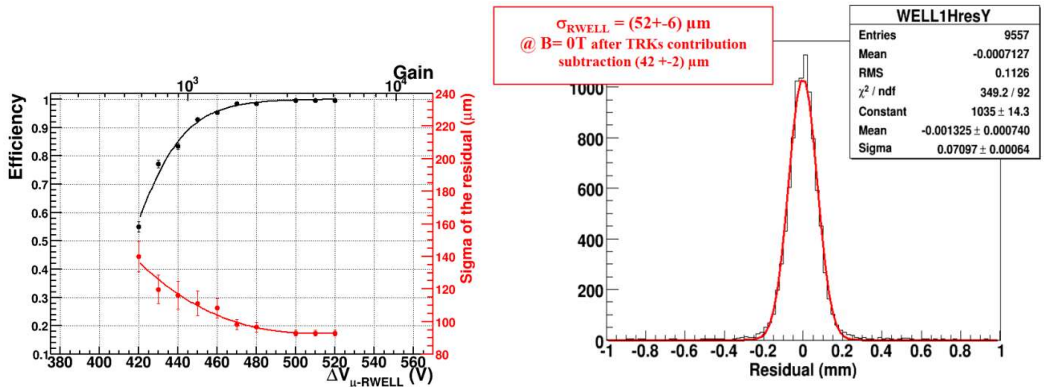

Figure 5.10: Left: efficiency (in black) and spatial resolution (in red) as a function of the applied potenzial, i.e. of the gain. Right: distribution of the residuals. Both the plots are obtained with a small prototype, with Ar/CO_2 70%/30% mixture, with muon beam perpendicular to the chamber surface and with B=0.

resolution of 52 μm, improved up to 42 μm after the subtraction of the trackers contribution.

A fundamental advantage of this technology is the ease of the assembly procedure: the detector is composed by few components and does not require complex and time-consuming procedures: neither stretching, nor gluing, nor internal support frames. The R&D actually ongoing is focused on the analysis of the feasibility of production of large size prototypes, fundamental for the integration in the CMS environment. The prototype that is going to be produced by the end of the summer 2016 is GE1/1 size, in Fig.5.11 a picture of the DLC-coated kapton foil, that will be used for the large size prototype is shown. A test beam at the H8 SPS facility is planned for October-November 2016 aimed at the full qualification of these GE1/1-size prototypes.

For the GE2/1 size detector instead, the idea is also here to splice the bottom PCB into four modules, as for the baseline solution. The four modules will then be glued to a unique support, probably made of carbon fiber, to make the full size detector. In this case however, the whole GE2/1 μRWELL chamber will be a unique gas volume, thanks to the fact that the GEM foils are glued onto the PCB and there is no need of stretching. Therefore the dead area will be greatly reduced with respect to the Triple-GEM solution and it will not be necessary to produce two kinds of chambers with different modules splicing. An exploded view of the GE2/1 size μRWELL detector is shown in Fig.5.12.

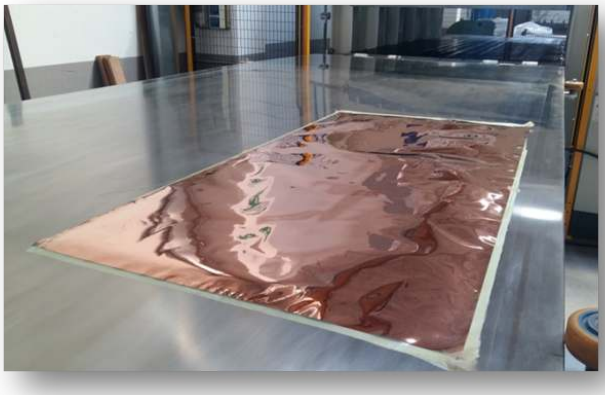

Figure 5.11: DLC-coated kapton foil for the assembly of the GE11-size μRWELL detector.

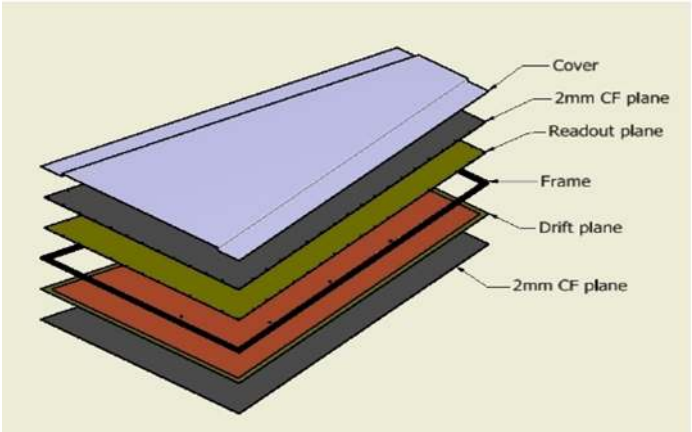

Figure 5.12: Exploded view of the GE2/1-size μRWELL detector.

5.1.2.1 Simulation of the behavior of μRWELL detector in the CMS background

In order to understand the feasibility of the installation of a new technology in the CMS muon system, it is fundamental to understand its behavior in the harsh radiation environment characteristic of those regions and already described in Section 3.2.

For this reason a Geant4 [77] simulation has been developed in order to evaluate the sensitivity of the detector to neutrons, gammas, electrons and positrons, which are the main components of the CMS muon system background.

The sensitivity, already introduced in Section 2.5, has been evaluated for

incident particles of different energies (see Table 5.1). The results as a function of the energies are then averaged over the particle energy spectra expected in the CMS cavern, in order to obtain mean sensitivity values. The results reported in this thesis, here for the μRWELL and later for the Fast Timing Micropattern detector (FTM) are calculated using the GE1/1 energy distributions, obtained with a CMS geometry suitable for Run 1, because the newest energy spectra were still not available.

Particles	Energy ranges (MeV)
Neutrons	10^{-8} - 1000
Gammas	0.03 - 60
Electrons	0.15 - 75
Positrons	0.15 -75

Table 5.1: Energy ranges of background particles considered for the Geant4 sensitivity simulation.

Layer Name	Composition	Depth
Drift Board	FR4Support1 DriftCopper	1 mm 5 um
Drift Gap1	GasGap1	5 mm
µRWELL	Copper Kapton1 DLC1 FR4Support2	5 um 50 um 0.1 um 75 um
Readout Board	ReadCopper Kapton2 FR4Support3	25 um 25 um 1 mm

Figure 5.13: Geometry of the μRWELL detector simulated with Geant4.

Considering the μRWELL detector, the geometry that has been introduced in the simulation is the one shown in Fig.5.13. The thickness of each layer of material reproduces exactly the structure of the real detector, the only difference is in the material called *FR4Support2* in Fig.5.13: this material in reality is *Prepreg*, a composite fiber used to glue the μRWELL structure with the readout board. As it is primarily composed by PCB (FR4) and glue, it has been decided to reproduce it only as normal PCB.

The dimension of the detector simulated are those of GE2/1 chamber, so a trapezoid of 1837 mm height, 1179 mm and 502 mm bases.

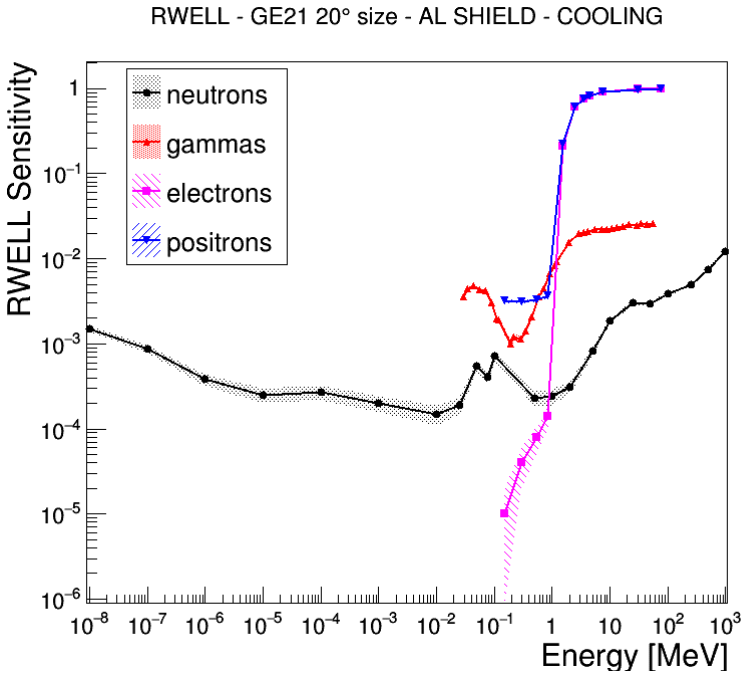

Figure 5.14: Results of the sensitivity simulation of μRWELL detector performed with Geant4

The simulations have been performed for a nude μRWELL detector as well as for a detector covered with a GE1/1-like shielding, made of an aluminum layer 1-mm thick covering both sides of the detector. Finally also a GE1/1-like cooling system was added, composed by a cooling pipe and cooling pads in copper, with water inside[4]. The result of this last simulation is shown in Fig.5.14, while from Table 5.2, showing the sensitivity values averaged over the particles energy distributions, a comparison between the different cases can be done.

The sensitivity to neutrons and gammas increases with the insertion of the aluminum shielding and of the cooling system: this is due to the increase of the total material budget of the chamber, that causes an increase of the number of neutrons and gammas that could interact in one of the external layers of the chamber and produce a charged particle that could reach the active gas gap. On the opposite, electrons and positrons sensitivity decreases with the insertion of the already cited layers, because the probability for them to be

[4]At the time in which this simulation was performed, details like the shielding and the cooling were not yet defined, as also the technology to be used in the GE2/1 station was under discussion. For this reason, the GE1/1 model has been taken as a reference and re adapted to the dimensions of the GE2/1 chambers.

μRWELL	Neutrons	Gammas	Electrons	Positrons
Nude	$(4.38 \pm 1.33) \times 10^{-4}$	$(5.19 \pm 0.11) \times 10^{-3}$	0.519 ± 0.080	0.520 ± 0.080
With Al shielding	$(5.83 \pm 1.77) \times 10^{-4}$	$(7.24 \pm 0.18) \times 10^{-3}$	0.302 ± 0.059	0.305 ± 0.058
With Al shielding and cooling	$(8.03 \pm 2.43) \times 10^{-4}$	$(7.37 \pm 0.19) \times 10^{-3}$	0.287 ± 0.056	0.289 ± 0.056

Table 5.2: μRWELL sensitivity results averaged over the particle energy distribution.

absorbed before reaching the gas gap increases.

In general, the sensitivities to neutrons and gammas for this technology are slightly lower with respect to those obtained for Triple-GEM detectors (see Section 3.2). This is mainly due to the lower material budget of a μ-RWELL detector with respect to a Triple-GEM. On the other hand, sensitivities to electrons and positrons are higher with respect to Triple-GEM, because actually the thickness of material that these particle should traverse to reach the active layer is lower here then in the GEM geometry. However we will see the comparison in detail in Section 5.2.2.7.

5.1.3 Choice of the technology for the GE2/1 station

The choice of the technology to be adopted for the GE2/1 is expected to happen by 2018, in order to start the mass production in time for the installation in 2022. While Triple-GEM technology is a well consolidate technology, thanks to the R&D performed by the CMS Collaboration as well as by other groups, like LHCb, the μ-RWELL detectors are still at an early stage of their development. Even if some basic performance, like efficiency and spatial resolution have been already assessed, other have not been proved yet, like the time resolution and the operation in a radiation environment. Moreover, only small size prototypes have been built so far and the mechanical feasibility of the large size detector still have to be verified.

Triple-GEM detectors are going to face their biggest challenge, i.e. the stretching of GE2/1 size foils, with an intelligent and almost straightforward solution: dividing the active area in four modules actually reduces the dimension of the single foil to be stretched to the GE1/1 size, for which the effectiveness of the stretching methods have been already assessed.

Moreover, considering also the organizational aspect, the GEM Collabora-

tion is training people and developing laboratories out of the CERN site for the construction of Triple-GEM for the GE1/1 station. This great investment of time and resources would actually serve as a basis for the construction of GE2/1 chambers in case the Triple-GEM technology would be selected.

So far, Triple-GEM technology has taken the lead for what concerns the instrumentation of the GE2/1 station. Unless the μ-RWELL prove to give a crucial advantage in the construction, related to the time need or the cost of the chambers themselves, the choice of the Collaboration will probably come down to Triple-GEM detectors.

5.2 The ME0 station

The ME0 station will be inserted in the CMS endcaps in a space that will remain free after the installation of the new High Granularity Calorimeter (HGCal) and the new Backing Hadron Calorimeter (BH), as shown in Fig.5.15. The detector stacks, which are expected to be composed by six layers of chamber, will cover the region $2.03 < | \eta | < 2.82$ and will span over 20°. 18 stacks are foreseen per endcap, for a total of 36 stacks.

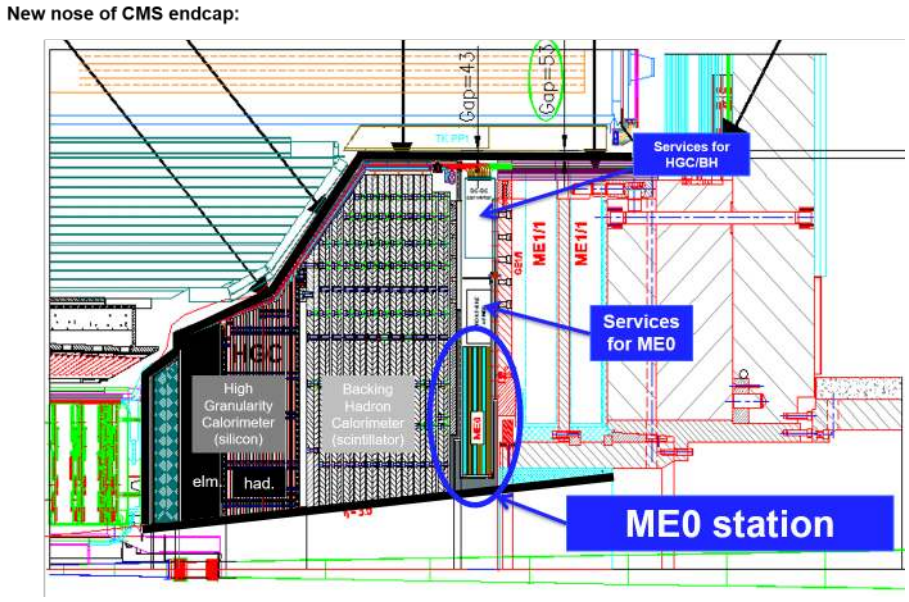

Figure 5.15: Position of the ME0 station in the CMS endcap.

The biggest geometrical constraint comes from the space available for the installation of the station: as highlighted in Fig.5.16, the endcap calorimeters

limit the available space to just 20.5 cm, which must contain not only the detectors but also their services. Moreover, due to the presence of the calorimeter services, that will be placed in the position shown in Fig.5.15, it will not be possible anymore to access the station after the installation.

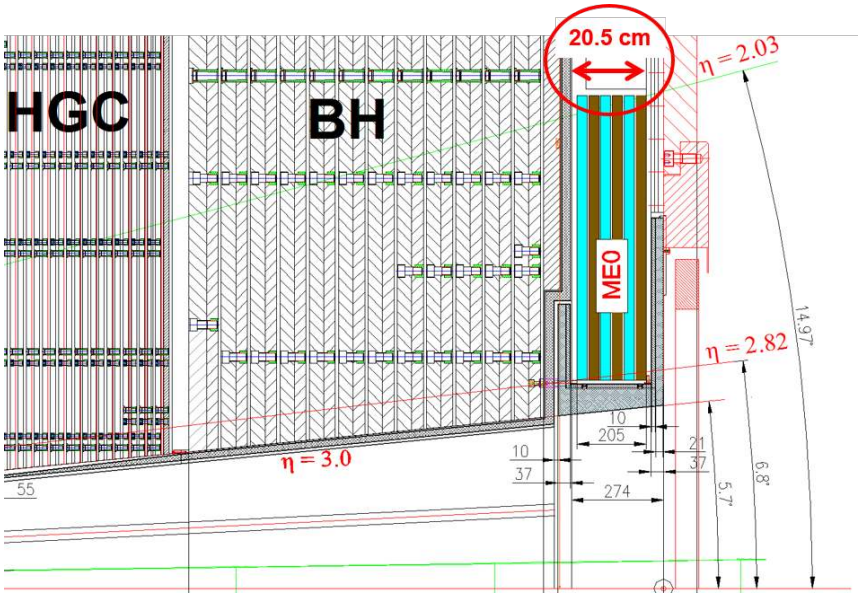

Figure 5.16: Zoom of the position of the ME0 station in the CMS endcap.

Despite these mechanical limitations, the technology to be installed in the ME0 station is required to satisfy few minimal performance requirements needed to fulfill the aims described in Section 1.4.2.3: it should be able to discriminate muons from neutrons and γ of background, finding muon stubs among background hits. The expected background fluxes in the ME0 region are shown in Fig.5.17.

Both the detector and its electronics should be able to handle quite high overall particle rates, as the expected total hit rate from simulation is of $\sim$ 100 kHz/cm^2 and the maximum total hit rate on a single chamber is of the order of 50-100 MHz, as can be deduced from the plot in Fig.5.18, where the hit rates are calculated using the GE1/1 sensitivity values as reference. The expected integrated charge in this region, always obtained using formula 3.2, is $\sim$ 600 mC/cm^2, $\sim$ 100 times higher than GE1/1. More recent simulation, obtained with an improved shielding in that region, would foresee a reduction of a factor 3 of the fluxes and, as a consequence, of the hit rates. In this case the integrated charge will be reduced to $\sim$ 200 mC/cm^2. All these calculations are always performed considering as a reference a Triple-GEM detector, with

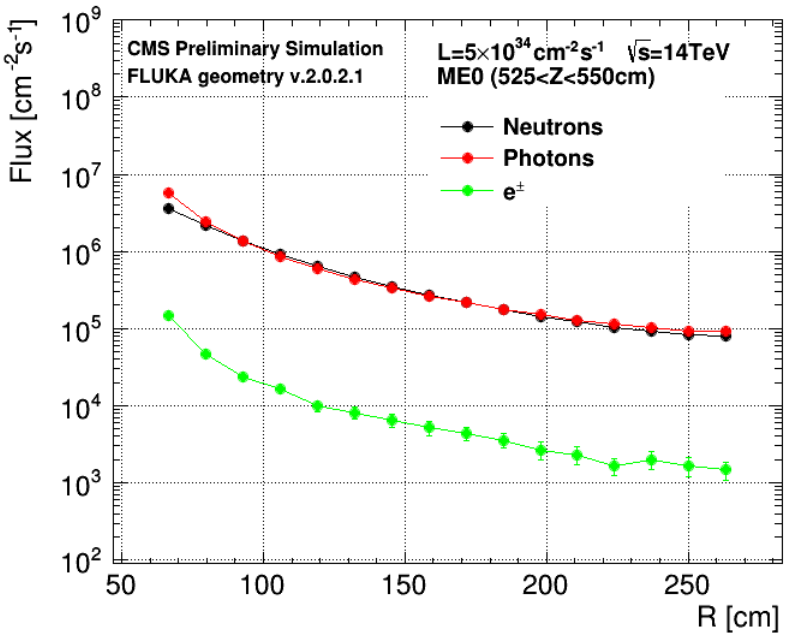

Figure 5.17: Simulated fluxes in the ME0 region (FLUKA version 2.0.2.1).

gain equal to 2×10^4, a number of primaries in the gas gap of 31 and a 10-year HL-LHC operation time (6×10^7s).

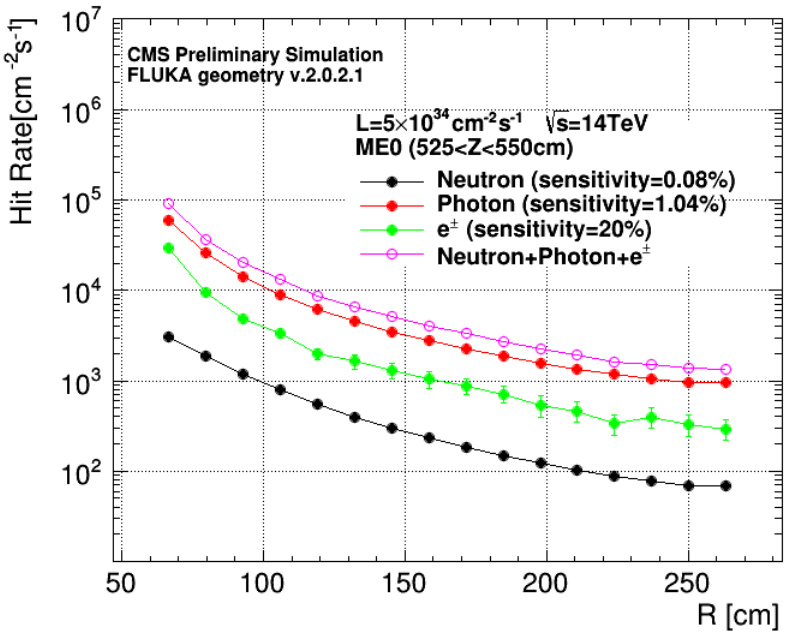

Figure 5.18: Expected hit rate in the ME0 region, based on the GE1/1 simulated sensitivity.

The ME0 station should be able to resolve hit position with a resolution lower than 300 μrad. Concerning the time resolution, the problem has been already discussed in detail in Section 1.4.2.3 and many dedicated studies are still ongoing, however if only the clear identification of the bunch crossing will be requested a time resolution $\leq$ 8 ns will be enough. If instead also the neutron-background and pileup rejection will have to be included, a much more performing technology will have to be developed: it should be able to reach a time resolution of the order of 1 ns if only the Out-Of-Time pileup will be considered, while the In-Time pileup rejection will request $\lesssim$ 100 ps time resolution.

Right now two technologies are taken in consideration by the Collaboration for the installation in the ME0 region: as for GE2/1, the baseline solution is represented by Triple-GEM detectors, in a configuration similar to GE1/1. The optional solution, more focused on the exploitation of the timing information, is represented by the Fast Timing Micropattern detector (FTM).

5.2.1 GEM baseline solution

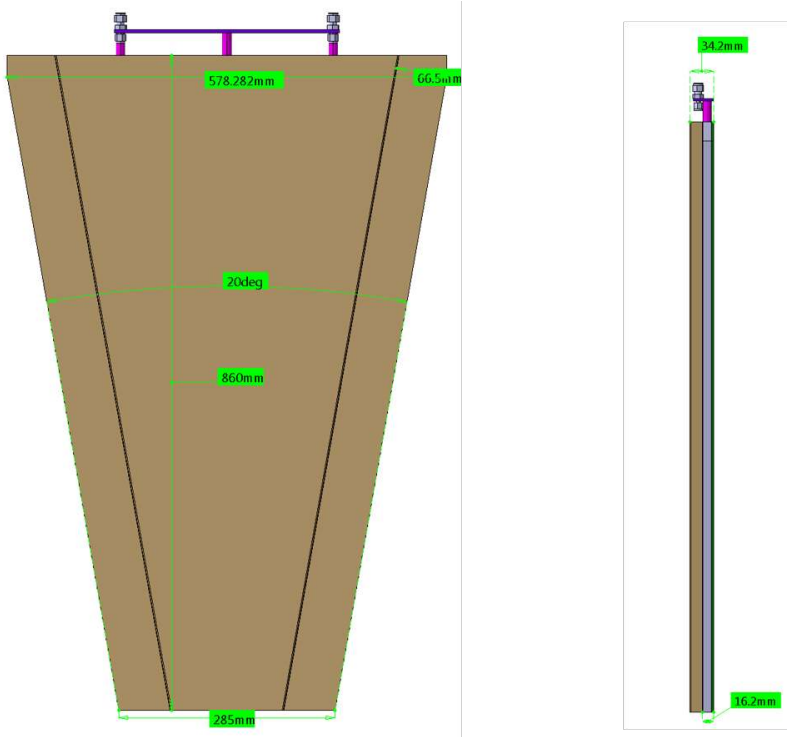

Figure 5.19: Geometry of the ME0 chamber with the baseline solution.

The baseline solution for the ME0 station foresees again the installation of Triple-GEM detectors in a configuration similar to GE1/1.

The geometry of the baseline ME0 chamber is shown in Fig.5.19: as can be deduced from the dimensions, the ME0 Triple-GEM chamber is smaller that the GE1/1, so there are no mechanical issues related to the foils' and PCB's size.

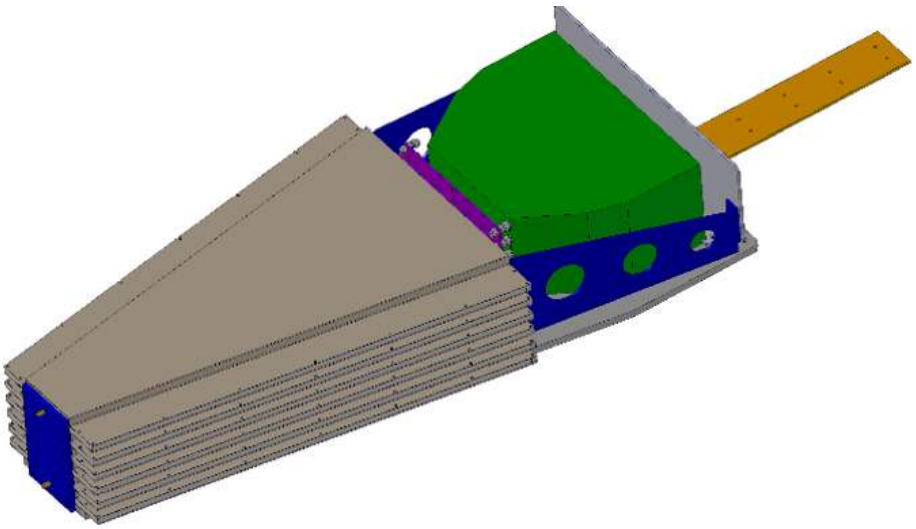

Figure 5.20: Stack of ME0 chambers with the baseline solution.

As said before, each ME0 stack will be composed by six chambers, arranged as in Fig.5.20. The grey part is actually the structure with the six layers of GEM detectors, while the green box is the electronics volume.

Fig.5.21 shows the insertion of the ME0 stack into the station: in order to assure overlap between two adjacent detectors, two subsequent stacks will be installed front-back to each other.

The studies performed for the GE1/1 station already prove that the Triple-GEM technology is able to match the requested performance in space resolution and rate capability. So, beyond the mechanical R&D that should be performed in order to fix a six-layer chamber in the space available for ME0, two are the greatest concerns related to the implementation of the Triple-GEM technology: first of all, the ageing studies performed for GE1/1 qualified the chambers up to an integrated charge of the order of 55 mC/cm^2, so a complementary test should be planned in order to reach the ME0 value. The second topic instead is related to the time resolution achievable by Triple-GEM detector, in particular in the six-layer stack configuration. A first study in this direction has been

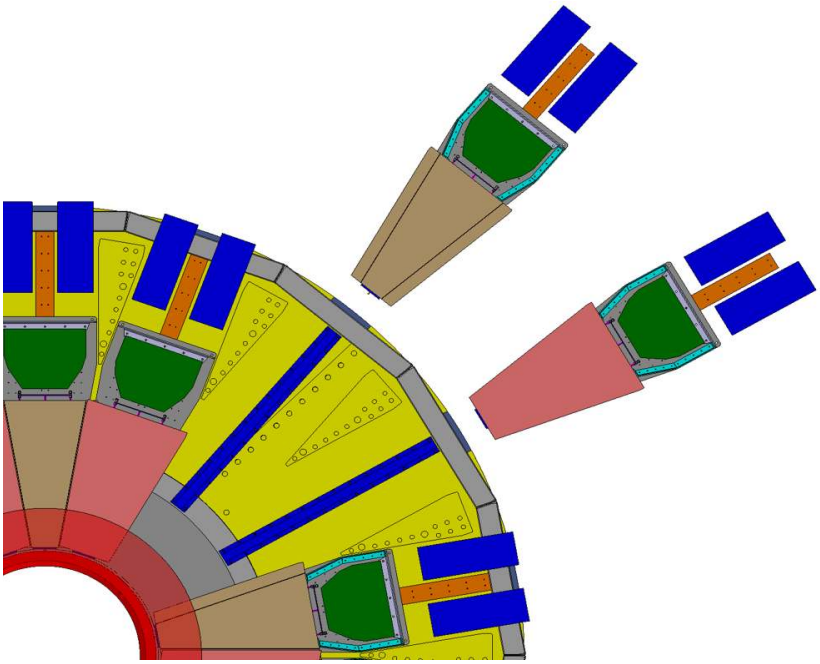

Figure 5.21: Insertion of the stack of ME0 chambers with the baseline solution in the CMS endcap.

developed in two different test beams performed in spring 2016 with the first prototype of Stacked-GEM.

5.2.1.1 Structure and characterization of the first Stacked GEM prototype

The first implementation of the Stacked GEM for the ME0 detector, also called Back-to-Back (B2B), is composed by two Triple-GEM assembled as in Fig.5.22.

The two drift foils were one next to the other, separated only by the nuts closing each stuck, highlighted in Fig.5.23 left, for a total distance of about 3 mm. The two stacks of Triple-GEM developed then symmetrically, with the two readout boards outside. Each readout board had 128 strips read by two Panasonic connectors. The strips were oriented in X on the *Readout GEM1* and in Y on the *Readout GEM2* (see Fig.5.23). The two chambers were completely independent from the powering point of view and two HV dividers were installed on the detectors, one for each Triple-GEM. In Fig.5.23 right, the detector fully assembled is shown.

The first characterization of the prototype was performed in $Ar/CO_2/CF_4$ 45%/15%/40%, with the setup shown in Fig.5.24. The signal from the bottom of the 3rd GEM of one side was sent to a preamplifier ORTEC 142PC [93] and

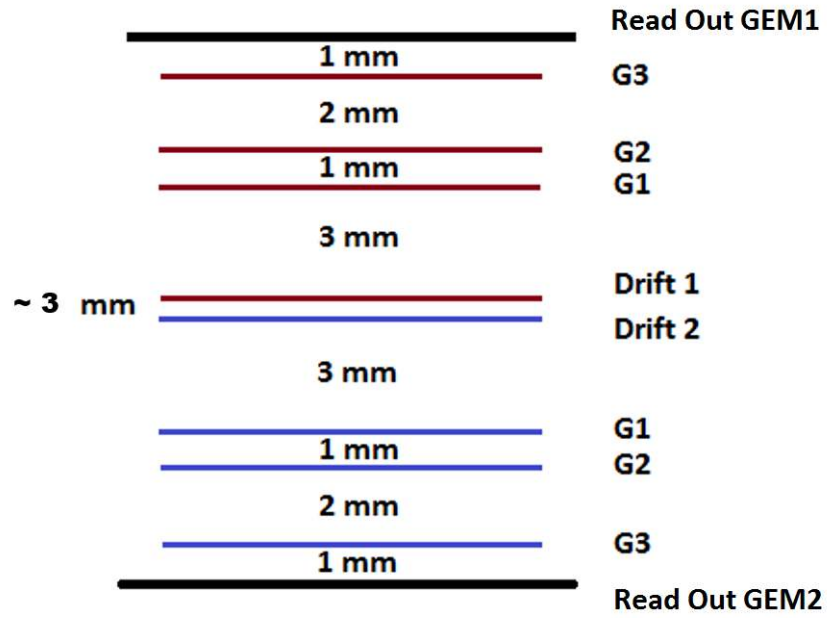

Figure 5.22: Structure of the Back-to-Back (B2B) prototype.

then to an amplifier ORTEC 474 [94]; for the rate and gain measurements the chain was completed with linear fan in - fan out [95] where it was splitted, one output going to the scope and the other one to a discriminator LeCroy 623A [96] and finally to a scaler. For the gain measurement at the same time the signal from the Panasonic connectors was sent to a picoammeter Keithley 6487 [83] to read the current. For the acquisition of the spectra instead, the signal was sent from the amplifier to a Multichannel Analyzer (MCA) [97].

In Fig.5.25 and 5.26 the results of the rate and gain measurements with a ^{109}Cd source are shown for the two sides of the B2B detector.

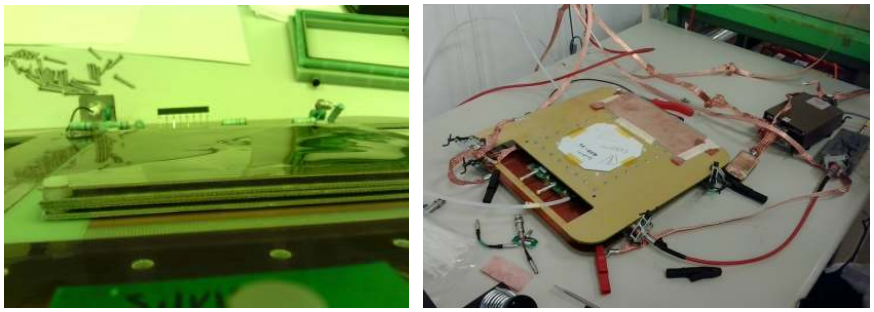

Figure 5.23: Left: picture taken during the assembly of the B2B prototype; Right: B2B prototype assembled.

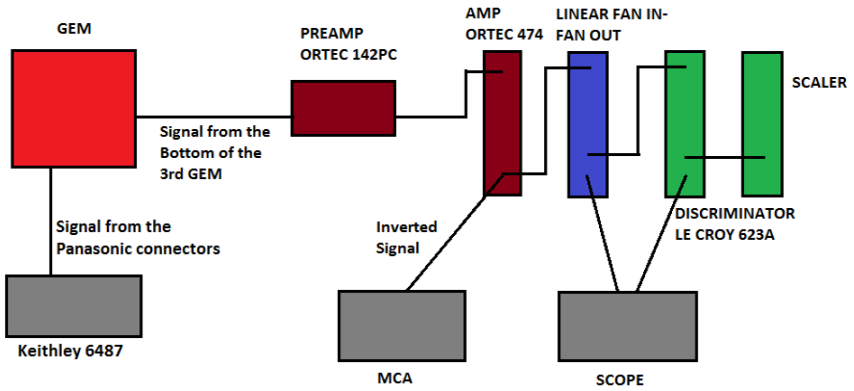

Figure 5.24: Setup used for the first laboratory characterization.

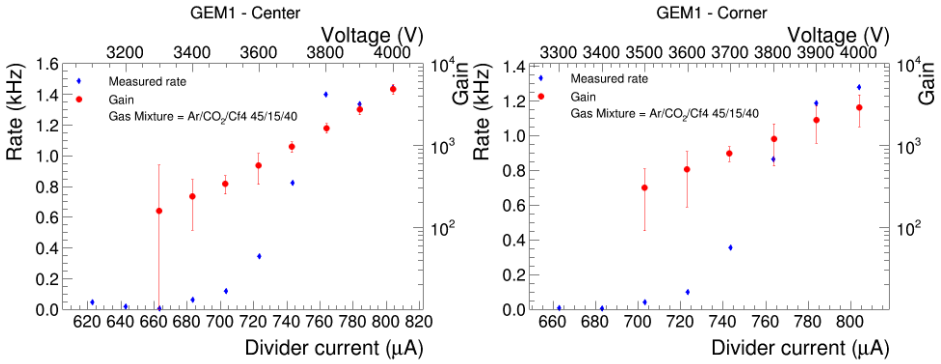

Figure 5.25: Results of the characterization in $Ar/CO_2/CF_4$ mixture of one side of the B2B prototype with ^{109}Cd source. Left: results with the source positioned in the center of the detector. Right: results with the source positioned in one corner of the detector.

For both sides a difference between the rate and gain measured in the center and the corners of the active area was observed: for example, for the *GEM1* side shown in Fig.5.25 in the center the maximum gain reached is about 4800, while in one of the corners is just 2900; for the other side *GEM2* the gain varies from 6300 to 4700 in the center and in a corner respectively.

In order to deepen this first observation of gain non-uniformity, a dedicated measurement was performed with an MCA. The active area of both the sides of the B2B was divided in 100 parts: for each of them, one ^{109}Cd spectrum was acquired and the position of the peak of the ^{109}Cd in the spectrum was observed.

A variation of the channel of the MCA in which the peak is placed is indeed a symptom of a variation in the gain of the chamber. In Fig.5.27 we can see

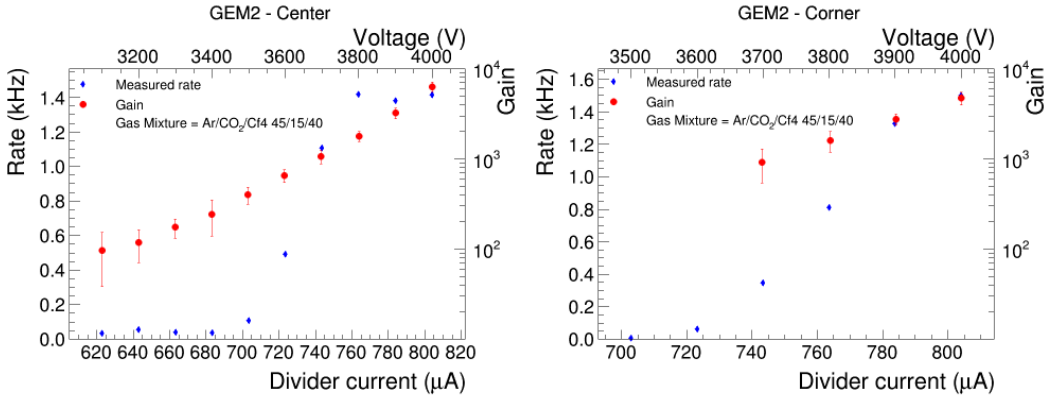

Figure 5.26: Results of the characterization in $Ar/CO_2/CF_4$ mixture of the other side of the B2B prototype with ^{109}Cd source. Left: results with the source positioned in the center of the detector. Right: results with the source positioned in one corner of the detector.

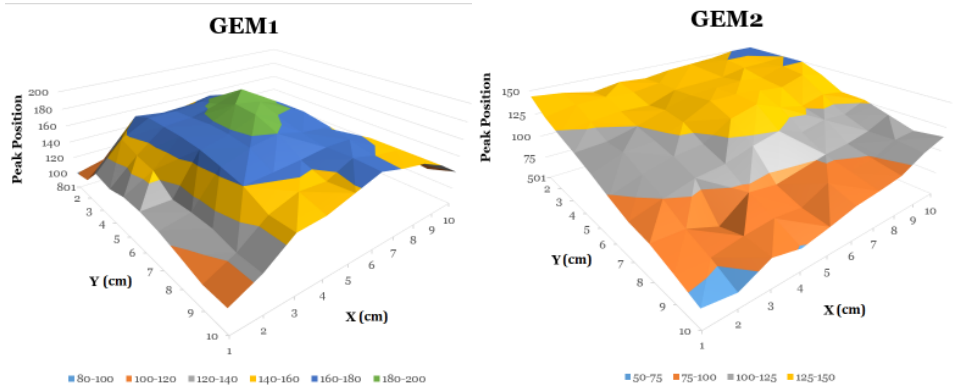

Figure 5.27: Results of the gain uniformity measurement on the two side of the B2B detector.

the results of this test, on the left for the *GEM1* side and on the right for the *GEM2* side. For the side *GEM1* the maximum of the gain is in the center of the active area and then it decreases towards each corner; in the side *GEM2* instead the maximum gain is in one corner and decreases towards the opposite one. For both sides the gain varies of a factor between 2 and 2.5.

The cause of this gain non-uniformity was supposed to be in the non-flatness of the drift foil and of the GEM foils, already noticed during the assembly and only partially solved. For this reason the two separated drift foils were replaced with a more rigid PCB foil, copper-coated on both sides. The two sides were short circuited, with the consequence that the two chambers were not anymore independent from the powering point of view.

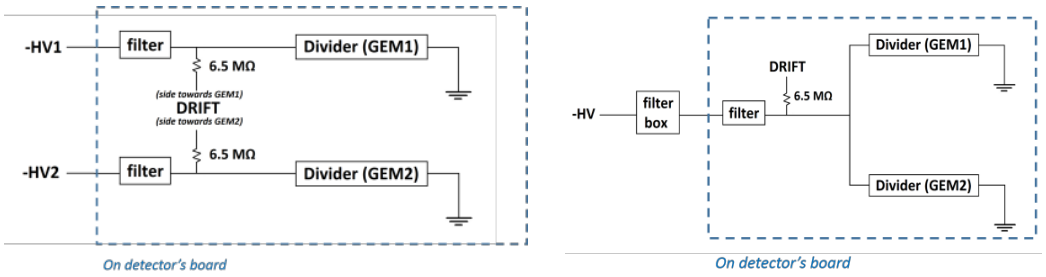

Figure 5.28: HV circuit of the B2B detector. Left: the old circuit, that allowed an independent powering of the two GEMs; Right: new HV circuit, modified after the introduction of the new drift foil.

In order to deal with the new configuration of the drift cathode, also the rest of the HV circuit had to be modified, as shown in Fig.5.28. On the left the old HV circuit configuration is shown, where the two GEMs were completely independent and powered through two HV lines and two HV dividers. On the right instead the new configuration foresees only one HV line, that supplies the common drift cathode. It is then is split in two to supply the two HV dividers in parallel. For this reason the total current drawn by the stack is double with respect to a standard Triple-GEM.

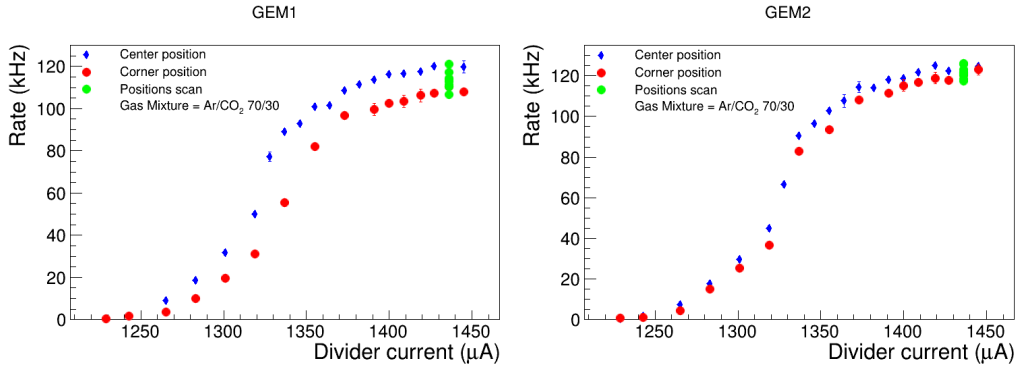

Figure 5.29: Results of the characterization in Ar/CO_2 mixture of the B2B prototype with ^{109}Cd source after the introduction of the new drift foil. The two plots represent the two side of the detector.

The new characterization was performed with a setup similar to the one in Fig.5.24 and the results are shown in Fig.5.29 and 5.30. Fig.5.29, in which the two plots represent the two sides of the detector, illustrates the rate measured with a ^{109}Cd source in the middle of the chamber, in blue, and in one corner, in red. The green points are the result of the scan in position, i.e. the rate measured, at a fixed divider current value of the chamber, with the source

placed in nine different positions of the active area of the detector.

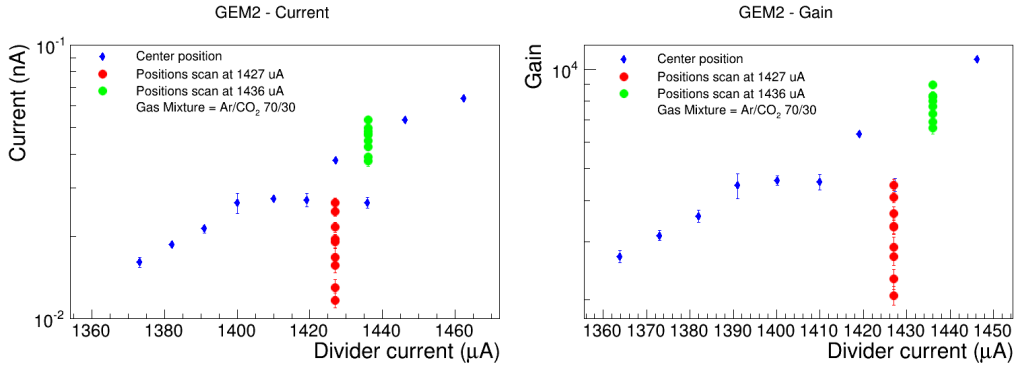

Figure 5.30: Results of the current (left) and gain (right) measurements in Ar/CO_2 mixture of the B2B prototype with ^{109}Cd source after the introduction of the new drift foil.

Fig.5.30 instead represent the current at the anode measured with one of the two GEM in the stack (GEM2) on the left and the consequent calculated gain, from Formula 3.1, on the left. In blue we see the results in the center of the chamber, while in red and green two scans in position performed at two different values of the divider current. Focusing on plot in Fig.5.30 right, an estimation of maximum variation of the gain over the area of the detector can be done with the points at 1427 uA and 1436 uA. The result is that there is still a non-uniformity of the gain of a factor between 1.3 - 2.2.

There is a small improvement with respect to the previous geometry, but the problem is not completely solved. The rest of the non-uniformity could be due to a non-flatness of the readout boards which means a non-uniformity of the induction gap and then of the induction field. As already highlighted in Section 2.4.2.1 the effective gain as a function of the induction field, plotted in Fig.2.15, is not characterized by plateau regions, which would assure an induction field range of operation without significant variation of performance. On the opposite, it is clear that even a small variation of the induction field, which could be due for example to a non-flatness of the readout board, can induce an important variation of the effective gain of the detector.

5.2.1.2 Back-to-Back prototype test beam results

After the replacement of the drift foils, the response of the prototype has been studied in two test beams at the SPS beam lines H2 and H4 [98] with muons

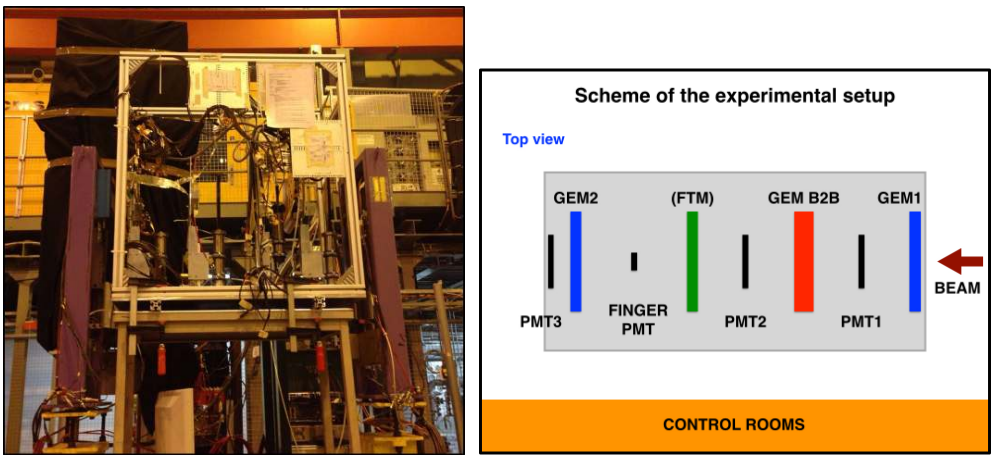

Figure 5.31: Left: Picture of the installation at the test beam in the SPS-H2 beam line in May 2016. Right: schematic of the positioning of the detectors in the H2 test beam.

and pions beams, with two different gas mixtures, Ar/CO_2 70%/30% and $Ar/CO_2/CF_4$ 45%/15%/40% respectively.

In Fig.5.31 left the setup installed in the H2 test beam area is shown: the stand, housing the B2B prototype, two GEMs 10x10 cm^2 for the tracking and four scintillators for the triggering, was installed between two beam chambers, in order to obtain a better alignment with the beam. On the right picture instead a schematic of the position of the detectors in the stand is shown. An identical configuration was used also in the H4 test beam.

The beams provided in the H2 and H4 beam lines, as anticipated above, were a muon beam and a charged hadrons beam, or simply pions beam. In Fig.5.32 the beam profiles of the muons and pions beam taken with the B2B detector are displayed: the muons, on the left, are less collimated, with beam spot of the order of 4-5 cm in diameter; the pions, on the right, instead, are very well collimated, with a beam spot diameter of the order of 2 cm.

The readout of the B2B and of the two tracker's GEMs was done with four VFAT_V2 chips for each detector, controlled by three Turbo boards. Details about the VFAT_V2 and the Turbo readout system can be found respectively in [99] and [100]. Focusing on the B2B, one pair of VFAT chips was used to readout one side of the detector in the X direction, while the other pair read the other side in the Y direction. The detail of the VFATs connected during the H2 and the H4 test beams is shown in Fig.5.33. The VFATs mounted on the detectors are identified following the numeration of the slot on the Turbo

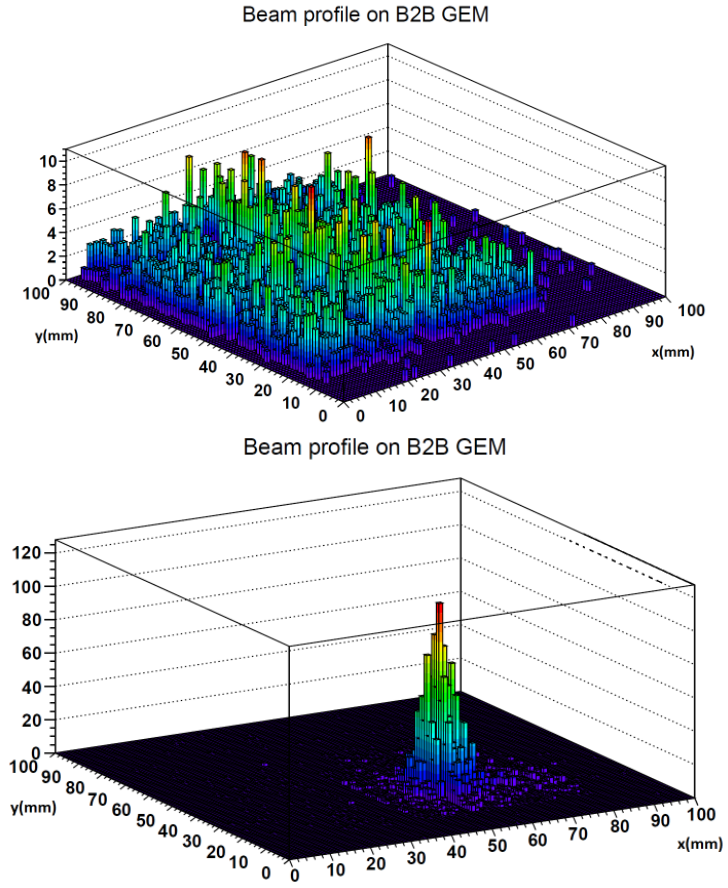

Figure 5.32: Beam profiles obtained during the H2 test beam in May 2016 with B2B detector. Top: muon beam; Bottom: pion beam

board, which goes from 0 to 7 (i.e. VFAT0, VFAT1...), i.e. the number of the VFAT here is not related to the version of the chip used, which is always VFAT version 2. For the sake of clarity, the version of the VFAT will be indicated here as VFAT_V2 [99] or VFAT_V3 [29].

5.2.1.3 Time resolution with Ar/CO_2

The timing data were acquired with a TDC with intrinsic time resolution of about 120 ps: an example of raw data acquired from the OR of 128 strips of one VFAT is in Fig.5.34. The raw data contain a time response distribution whose major contributions are the intrinsic time resolution of the detector and the VFATs signal sampling of 40 MHz. In order to obtain the intrinsic time resolution of the detector is so necessary to deconvolve the raw data from the VFAT contribution. The time resolution is then estimated as the standard deviation of the curve used as fitting function.

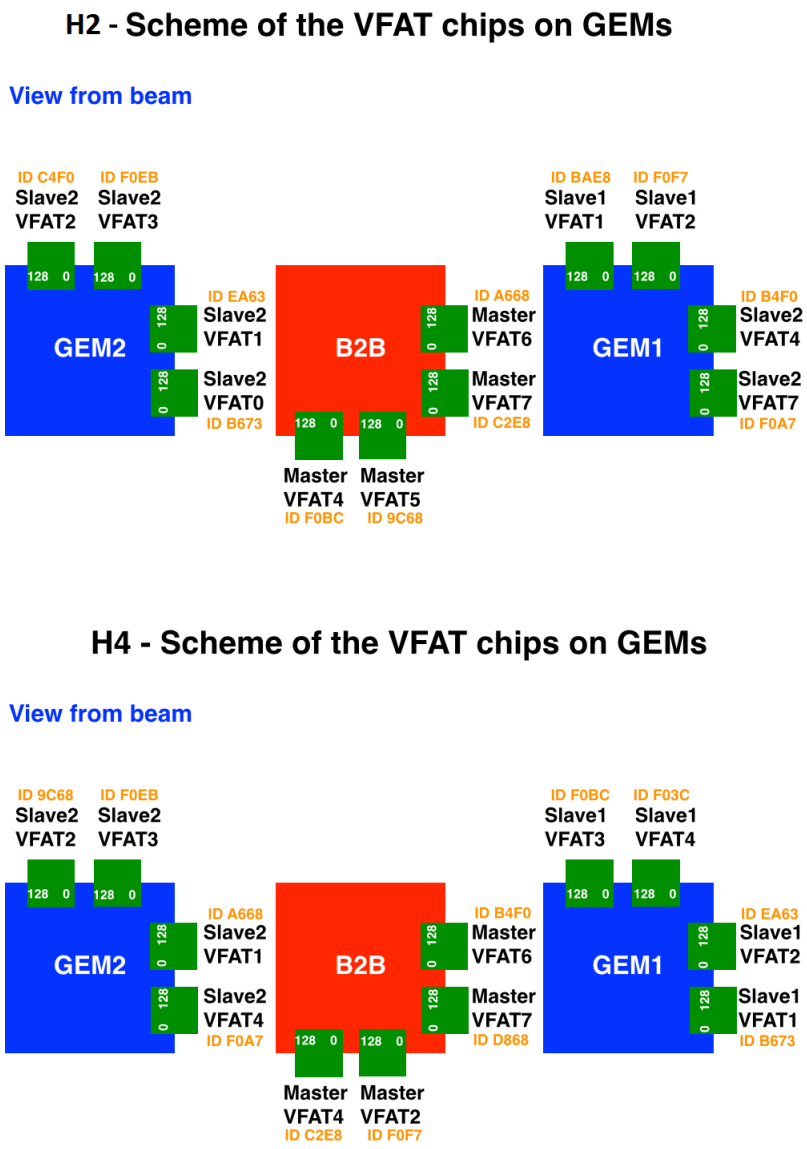

Figure 5.33: Schema of the VFATs connected to the B2B and tracker's GEMs during the H2 test beam (top) and the H4 test beam (bottom). The VFATs mounted on the detectors are identified following the numeration of the slot on the Turbo board, which goes from 0 to 7 (i.e. VFAT0, VFAT1...), the number of the VFAT here, and in all the following plots, is not related to the version of the chip used, which is always VFAT version 2. For the sake of clarity, the version of the VFAT will be indicated here as VFAT_V2 [99] or VFAT_V3 [29].

The effect of the deconvolution is shown in Fig.5.35 where the time resolution is plotted as a function of the threshold applied to VFAT5, mounted on one of the two Triple-GEM in the Back-to-Back stack (see Fig.5.33 top), with

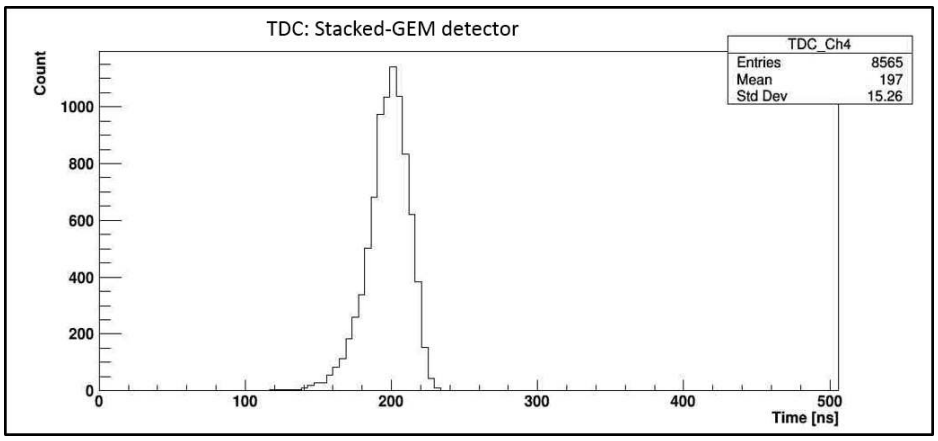

Figure 5.34: Time distribution of the signals induced by muons in the B2B detector. The data represented in this plot are the raw data coming from the TDC. It was working in a COMMON-STOP method, i.e. it was measuring the time of arrival of the B2B signal with respect to a trigger, given by the scintillators. For this reason the time scale in this plot is reversed with respect to the real time verse.

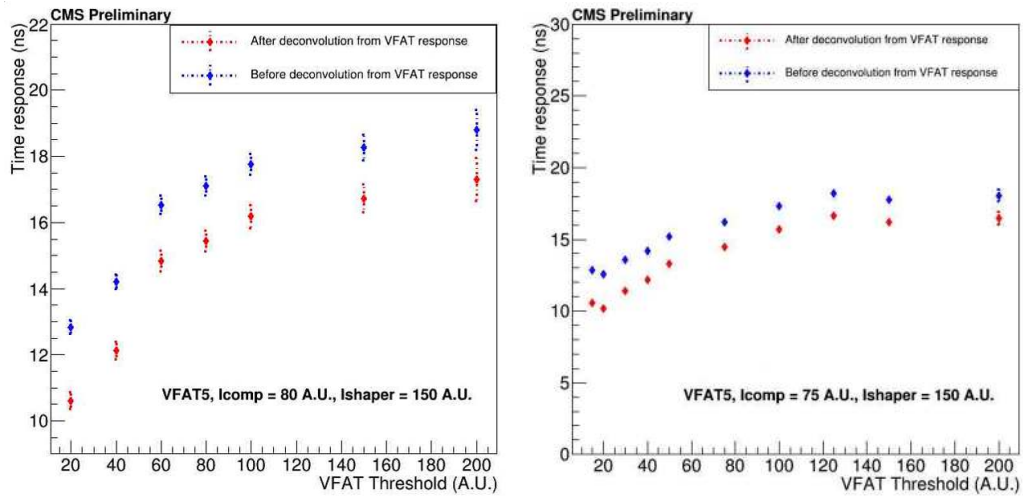

Figure 5.35: Time resolution as a function of the threshold applied on the VFAT5, in the left plot with muon beam, in the right with pion beam, with Ar/CO_2 70%/30% mixture. The blue curve shows the time resolution before the deconvolution from the VFAT response, the red curve after the deconvolution.

muons on the left and with pions on the right. The threshold in the plots is expressed in VFAT units, which correspond to a charge through the relation 1 VFAT unit = 0.08 fC. The blue curve is the time resolution obtained fitting with a Gaussian the raw data from the TDC, while the red curve is obtained

from the sigma of the fitting function

$$func = a \times c \times \sqrt{\pi/2} \times Erf(\frac{(12.5 + (x-b)}{c \times \sqrt{2}}) - Erf(\frac{(x-b) - 12.5}{c \times \sqrt{2}}) \quad (5.1)$$

where *a, b* and *c* are three parameters of the time distribution, the *maximum*, the *mean* and the *RMS* respectively. This fitting function is obtained making the convolution between a $f(t)$ and a $g(t)$, where $f(t)$ is a gaussian in this case, representing the pure response of the detector, and $g(t)$ is a square wave representing the 40 MHz clock of the VFAT, so $g(t) = 1$ for $-12.5 \leq t \leq 12.5$ ns and 0 elsewhere.

From the two curves it's clear the improvement of time resolution of about 2 ns due to the deconvolution from the VFAT response. The same results are shown also in Fig.5.36 for the VFAT7, mounted on the readout board of the other GEM of the stack, as shown in Fig.5.33. From the plots in Fig.5.35 and 5.36 also the behavior of the time resolution at different VFAT thresholds applied can be deduced.

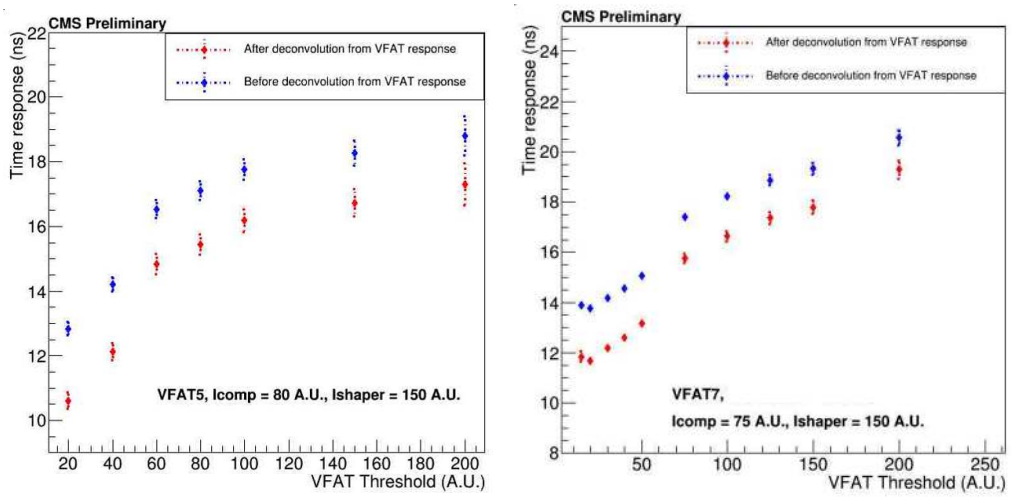

Figure 5.36: Time resolution as a function of the threshold applied on the VFAT7, in the left plot with muon beam, in the right with pion beam, with Ar/CO_2 70%/30% mixture. The blue curve shows the time resolution before the deconvolution from the VFAT response, the red curve after the deconvolution. The threshold in the plots is expressed in VFAT units, which correspond to a charge through the relation 1 VFAT unit = 0.08 fC.

Different operational parameters of the VFAT have been studied in order to optimize the time resolution: for example in Fig.5.37 the time resolution is

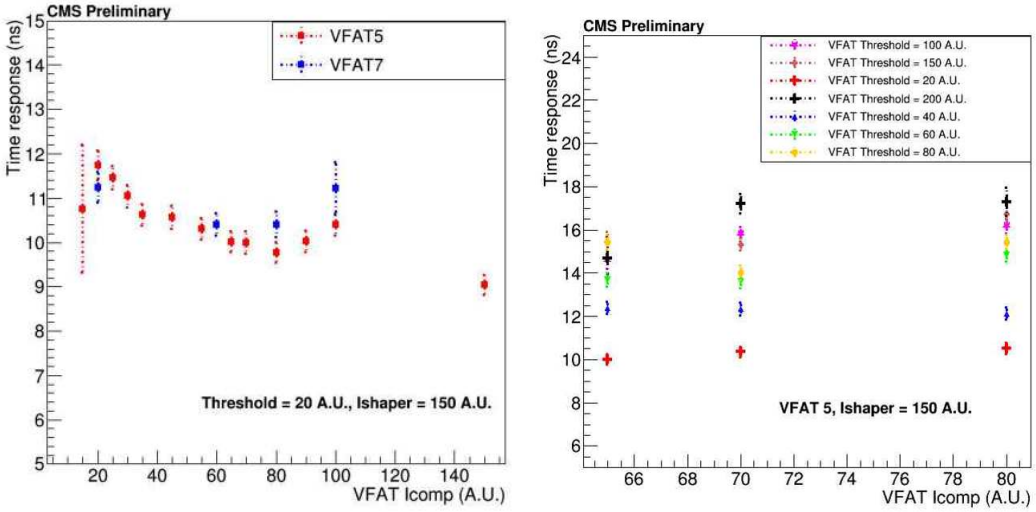

Figure 5.37: Time resolution as a function of the current in the comparator (Icomp) with muon beam, with Ar/CO_2 70%/30% mixture. In the left plot, the red curve correspond to results obtained with VFAT5, the blue one with VFAT7. In the right plot, results obtained at different threshold applied to VFAT5. Icomp is measured in digital units of the VFAT from 1 to 255.

measured as a function of the current of the comparator of the VFAT (Icomp). On the left, the red points are taken with the VFAT5 and the blue points with the VFAT7, which are mounted on the two different GEMs that compose the stack, showing that the time response is comparable between the two chambers. The curves in the right plot instead are taken with VFAT5 at different values of threshold applied: the worsening of the time resolution with the increase of the threshold confirms the result already obtained in Fig.5.35 and 5.36.

Fig.5.38 displays instead the time resolution measured with VFAT5, in red, and VFAT7, in blue, as a function of the current in the shaper of the chip (Ishaper). The two distributions are again compatible, confirming that the two chambers are behaving at the same way. Moreover, the parameter Ishaper seems not to influence deeply the time resolution, as the value measured is always between 10 and 11 ns.

The current on the dividers (Imon) instead seems to influence the time resolution, as it is directly linked with the efficiency of the chamber. As shown in Fig.5.39, at higher divider currents, i.e. higher efficiency, the time resolution is better.

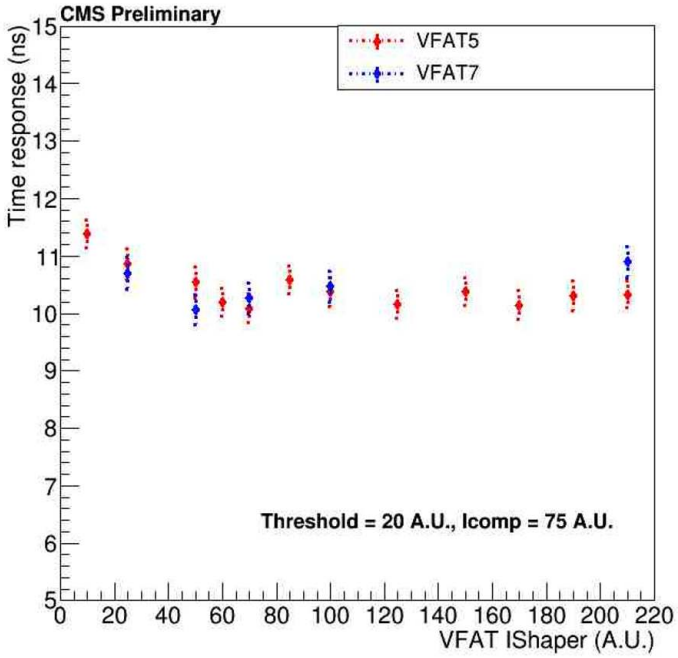

Figure 5.38: Time distribution as a function of the current in the shaper (Ishaper) with muon beam, with Ar/CO_2 70%/30% mixture. The red curve correspond to results obtained with VFAT.5, the blue one with VFAT7. Ishaper is measured in digital units of the VFAT from 1 to 255.

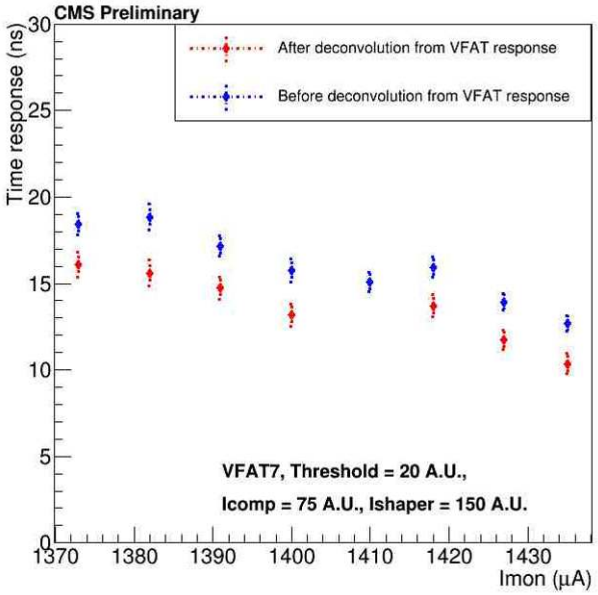

Figure 5.39: Time response as a function of the current through the divider (Imon) with muon beam, with Ar/CO_2 70%/30% mixture. The blue curve correspond to the results obtained before the deconvolution from the VFAT response, the red one after the deconvolution.

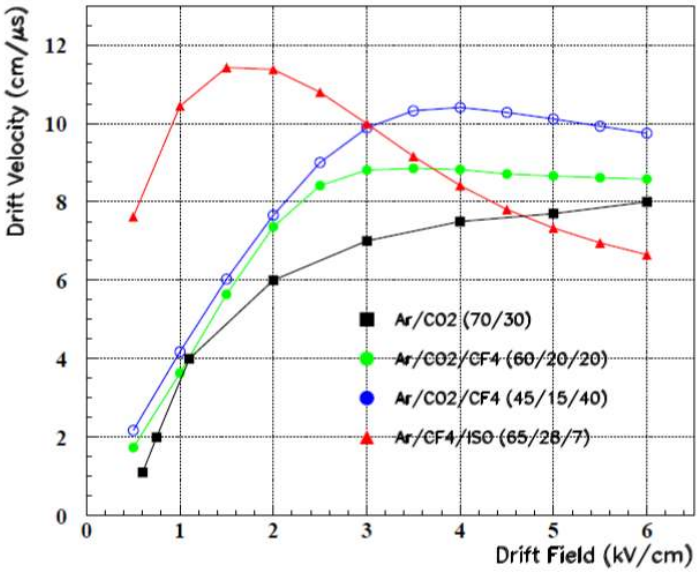

Figure 5.40: Drift velocity for classical gas mixtures used in MPGD [101].

5.2.1.4 Time resolution with $Ar/CO_2/CF_4$

The same kind of analysis has been performed during the H4 test beam with $Ar/CO_2/CF_4$ 45%/15%/40%. Even if the use of this mixture is discouraged, as it contains CF_4, a test with it is nevertheless interesting as it enhances the timing properties of the detector: indeed this mixture is faster than the greenhouse-gas-free mixture (Ar/CO_2), in the sense that the drift velocity (υ_d) here is higher, as shown in Fig.5.40.

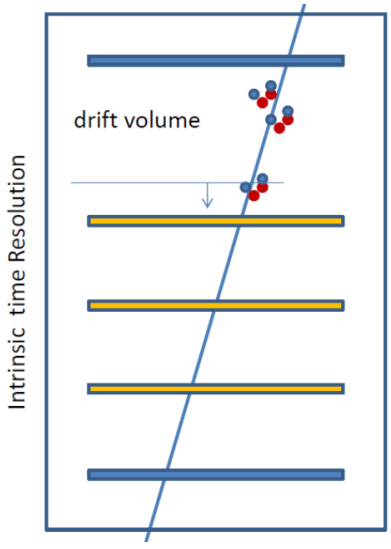

Figure 5.41: First ionization in a classical MPGD.

In general, time resolution of classical MPGD, including GEM, is dominated by the fluctuations on the position on the first ionization cluster in the drift gap. The average time needed for the nearest ionization cluster to reach the amplification stage, as sketched in Fig.5.41, is indeed given by $t = d/\upsilon_d$, where d is the distance of the closest cluster to the first amplification region and follows the distribution $\frac{e^{-\lambda x}}{\lambda}$, where λ is the average number of primary clusters generated by an ionizing particle inside the gas per length; υ_d is the drift velocity, that depends on the gas mixture and the applied drift field. The contribution to the time resolution of the drift velocity is so given by

$$\sigma_t = (\lambda \upsilon_d)^{-1} \tag{5.2}$$

therefore a better time resolution is expected with a faster mixture. A detailed treatise of time resolution on MPGD can be found in [101, 102].

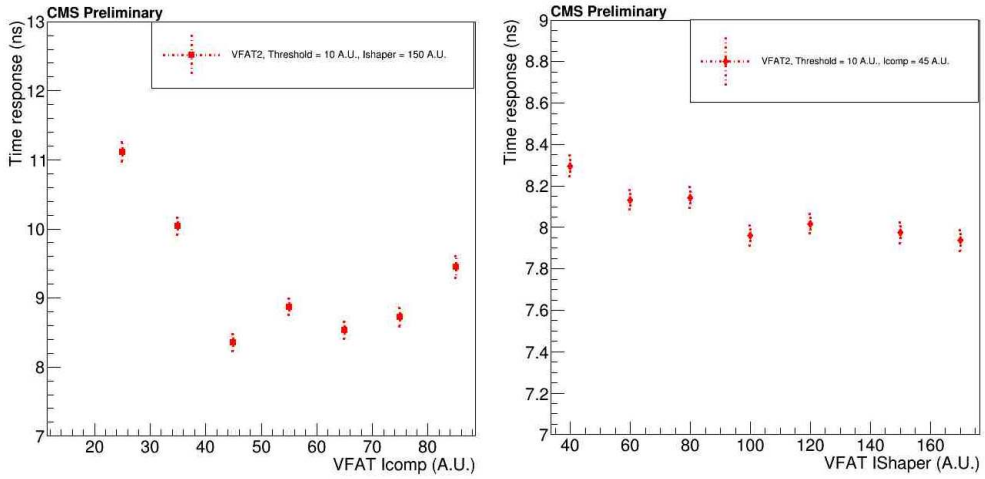

Figure 5.42: Time resolution obtained with muon beam with the $Ar/CO_2/CF_4$ 45%/15%/40% mixture. Left: as function of the current through the comparator (Icomp). Right:as a function of the current in the shaper (Ishaper). Similar results have been obtained with VFAT mounted on the other side of the stack.

The behavior of the time resolution as a function of the current through the comparator and the shaper of the VFAT is, as expected, the same observed with the Ar/CO_2 mixture: starting from the current from the comparator, see Fig.5.42 left, the time resolution distribution has a minimum, that in this plot is around 45 units of the VFAT. Similar results have been obtained also for VFATs mounted on the other GEM of the stack (see Fig.5.33 bottom for the VFAT configuration in H4). Fig.5.42 right instead confirms that the time

resolution is not deeply affected by changes in the current through the shaper of the VFAT.

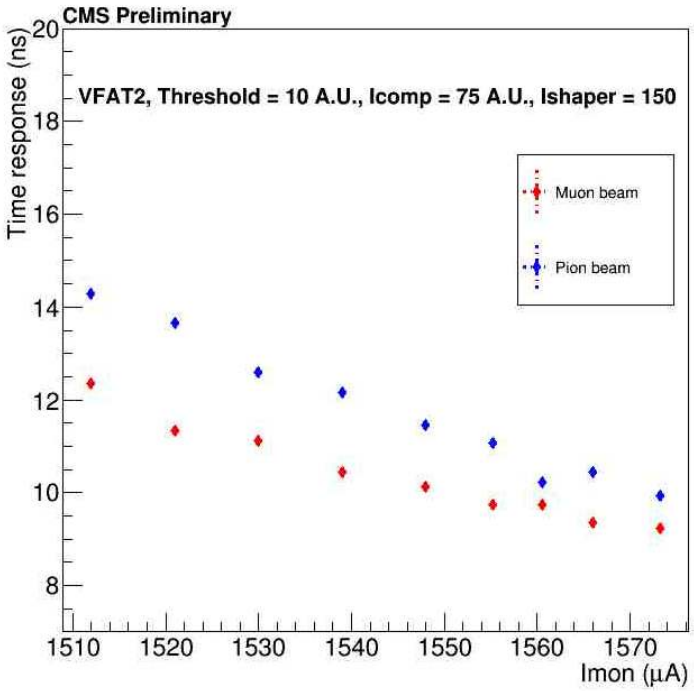

Figure 5.43: Time resolution as a function of the current though the divider (Imon) with muon beam (red) and pion beam (blue) with the $Ar/CO_2/CF_4$ 45%/15%/40% mixture. Similar results have been obtained with VFAT mounted on the other side of the stack.

Also the behavior at different values of the current through the divider (Imon), i.e. different gain of the detector, confirms what already observed with the Ar/CO_2 mixture: the time resolution is improved at higher gains of the detector, as shown in Fig.5.43, where the different colors represent the results obtained with muons (red) and pions (blue). To be noticed is is the fact that with $Ar/CO_2/CF_4$ gas mixture higher current values through the divider must be reached: this is due to the fact that this gas mixture contains a lower fraction of Ar with respect to the Ar/CO_2 mixture (45 % against 70%) so it is necessary to apply higher fields to obtain the same gain values.

5.2.1.5 Comparison with previous results

Fig.5.44 shows the comparison between the time resolutions obtained with Ar/CO_2 in red and $Ar/CO_2/CF_4$ in blue, at different value of current in the shaper on the left and current in the comparator on the right.

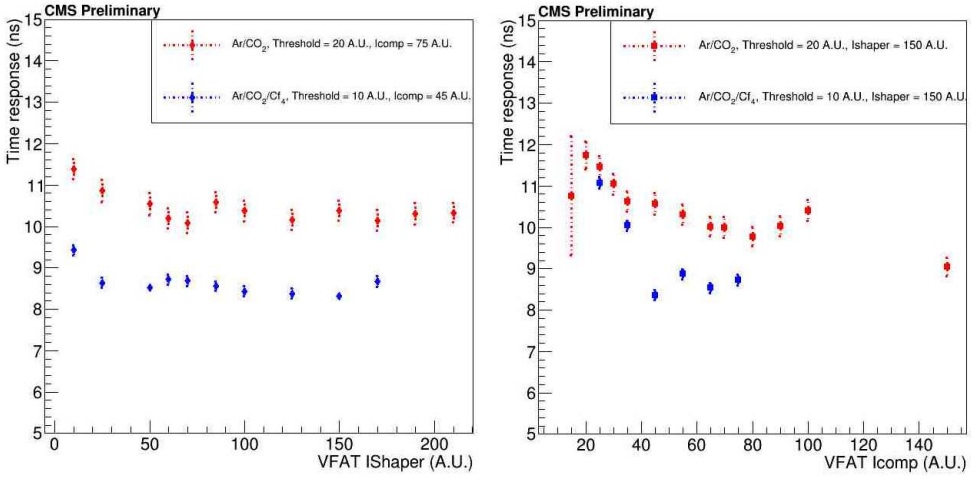

Figure 5.44: Comparison between the time resolution obtained with Ar/CO_2 (red) and $Ar/CO_2/CF_4$ (blue). Left: as a function of the current in the shaper (Ishaper); Right: as a function of the current in the comparator (Icomp).

As expected, the time resolution measured with $Ar/CO_2/CF_4$ is a 2-3 ns better that the one measured with only Ar/CO_2. The comparison is made between two VFATs mounted on the same position on the B2B in the two test beams, however it should be noticed that few operational parameters are different between the two measurements: in the left plot, the value of current in the comparator used was different between the two cases. Moreover in both the plots, the threshold applied during the test with $Ar/CO_2/CF_4$ was lower, due to the better grounding performed in the H4 test beam that allowed to have a lower noise level. The first parameter should not affect the time resolution, as the values in the two cases were selected in order to get the best time resolution in the two situations. On the other hand it is possible that the lower threshold applied in the H4 case helped in obtaining a better time resolution, as the threshold is not negligible parameter as already shown in Fig.5.35.

The results obtained with both the gas mixtures however are worse than what previously measured with GE1/1 prototypes, as well as with prototypes developed for other experiments. Starting from GE1/1, in Fig.3.8 we have seen that, with Ar/CO_2, pushing the detector at very high gain it is possible to reach 7 ns time resolution, 3-4 ns lower than the best value measured with B2B. Operating the detector at a standard gain value (2-3 $\times$ 10^4) the time resolution is of the order of 10 ns, comparable to the result obtained with the B2B. The biggest differences between GE1/1 and B2B are obtained with $Ar/CO_2/CF_4$, as GE1/1 could reach 6 ns time resolution at a reasonable gain,

while with B2B it is not possible to go below 8 ns.

A possible explanation could be found in the way the two detectors are powered: indeed, even if both mount a divider to apply the voltages at the foils and gaps, the models used are different between the B2B and GE1/1. In particular, the most relevant distinction is that the drift field that is actually applied to the B2B Triple-GEMs is lower with respect to the drift field applied in a GE1/1 chamber.

We can try to quantify the effect: if we suppose to have 700 μA flowing in both the divider versions, in GE1/1 we would obtain a drift field of 2.6 kV/cm, while in the B2B just 2.2 kV/cm: looking at Fig.5.40, these values are in a region in which the drift velocity, in particular for $Ar/CO_2/CF_4$ 45%/15%/40% mixture, is changing quickly. Looking at the blue dots indeed, moving from 2.6 to 2.2 kV/cm means reducing the drift velocity from 9 to 8 cm/μs, about 11-12% variation. Considering the proportionality of the drift velocity to the time resolution from formula 5.2.1.4, in the case of the B2B, a 11% variation would reduce the time resolution measured with $Ar/CO_2/CF_4$ to $\sim$ 7 ns, approaching the GE1/1 performance.

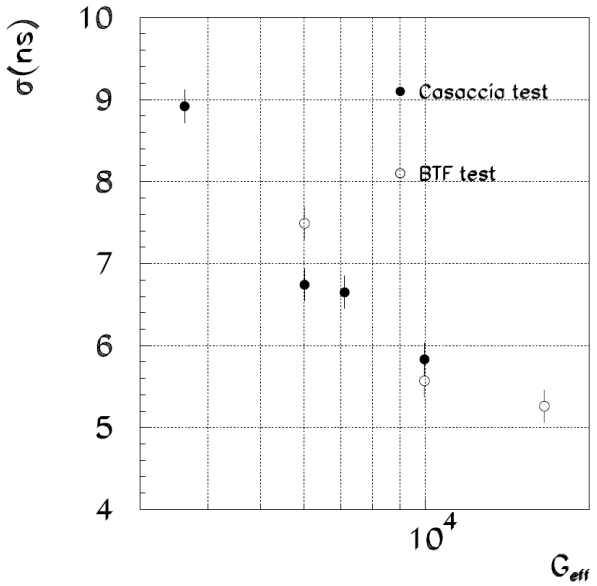

Figure 5.45: Time resolution measured with the Triple-GEM LHCb prototype in laboratory (white dots) and in the Enea-Casaccia facility with background radiation (black points) vs. effective gain [105].

An interesting comparison can be done also with Triple-GEM detectors developed for other experiments: LHCb [103] is using Triple-GEM in its muon

system since the beginning of its operation. In 2004 the time resolution of these detectors, geometrically identical to what actually selected by CMS and to what is implemented in the B2B (3/1/2/1 mm gaps geometry), was measured with $Ar/CO_2/CF_4$ 45%/15%/40% mixture both in a radiation-free laboratory environment and in presence of γ background at the Calliope facility of ENEA-Casaccia laboratories [104]. The results are shown in Fig.5.45: also in this case the time resolution reached, at a gain of the order of 10^4, is lower than 6 ns, even in a high radiation environment [105].

If the reason of the worse time resolution obtained by the B2B will be clearly identified and fixed, it will be in line with the requests for the ME0 station, at least for what concerns the bunch crossing identification. The $\lesssim 1$ ns time resolution needed for the neutron background and pileup rejection instead seems to be beyond the limits of this technology in its classical configuration.

5.2.2 FTM optional solution

The possibility to introduce an incisive method of pileup and background rejection through the use of ultimate precision timing forced the development of new detectors able to reach sub-nanosecond time resolutions. The candidate developed in the framework of the muon system upgrade and chosen as optional technological solution for the ME0 station is the Fast Timing Micropattern detector (FTM) [106].

5.2.2.1 FTM concept and working principle

With a typical drift gap of the order of 3-4 mm and with a proper choice of the gas mixture, like those shown in Fig.5.40, from equation 5.2.1.4, classical MPGDs can reach a time resolution of the order of 5-10 ns .

In order to reach the 1 ns scale or better, an improvement can be obtained working on the segmentation of the drift gap: the principle is to divide a single thick drift region in many thinner drift regions, each coupled to its amplification stage, as in Fig.5.46.

In this way, the uncertainties related to the position of the first ionization in the drift gap are reduced, as the thickness of the single gap itself is reduced. Moreover, in an efficient device, each drift-amplification stage is in competition with all the others, for a total reduction in time resolution proportional to the

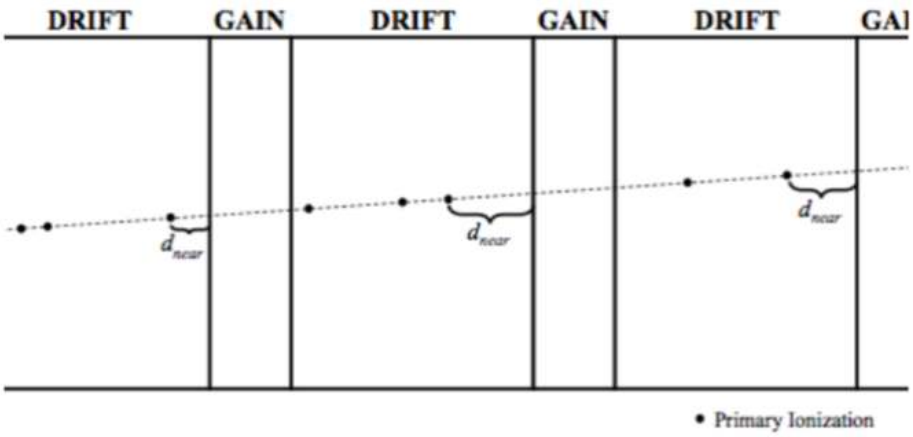

Figure 5.46: Principle of the time resolution improvement for FTM detector [106].

number of stages N_D employed:

$$\sigma_t = (\lambda \upsilon_d N_D)^{-1}. \tag{5.3}$$

The construction of consecutive drift-amplification stages is allowed by the use of resistive layers to polarize drift and multiplication volumes. The overall structure is then transparent[5] to the signal that can be extracted from every amplification stage and is induced on the top and bottom readout, as in Fig.5.47 [107].

5.2.2.2 Structure of the first FTM prototype

The first prototype of Fast Timing Micropattern detector is composed by two independent drift-amplification stages and is shown in Fig.5.48.

Each amplification region is based on a pair of kapton foils stacked due to the electrostatic force induced by the polarization of the foils: the first foil, perforated with inverted truncated-cone-shaped holes (with top base 100μm and bottom base 70μ m and pitch 140μm), is a 50μm thick polyimide foil (Apical) from KANECA [108], coated with DLC technique, to reach a specific surface resistance of up to 800 M$\Omega/\square$ (200 M$\Omega/\square$ measured); the second foil is 25 μm thick XC Dupont Kapton [109], with a resistivity of 2 M$\Omega/\square$. The drift

[5]The transparency considered here is different from what already discussed for GEM detectors in Chapter 2. Indeed here we are talking about *electrical transparency*, i.e. the possibility for the signal to be induced on the top and bottom readout even if powered resistive layers are present in the middle of the structure.

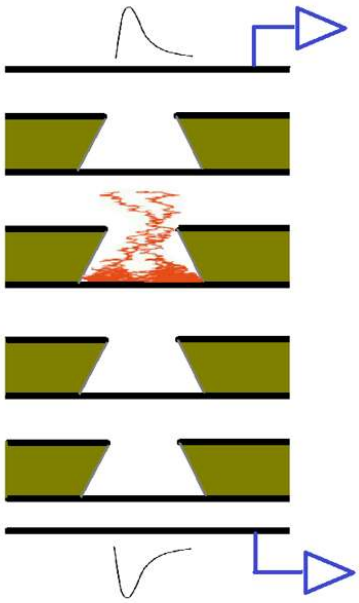

Figure 5.47: Principle of the induced signal in FTM detector.

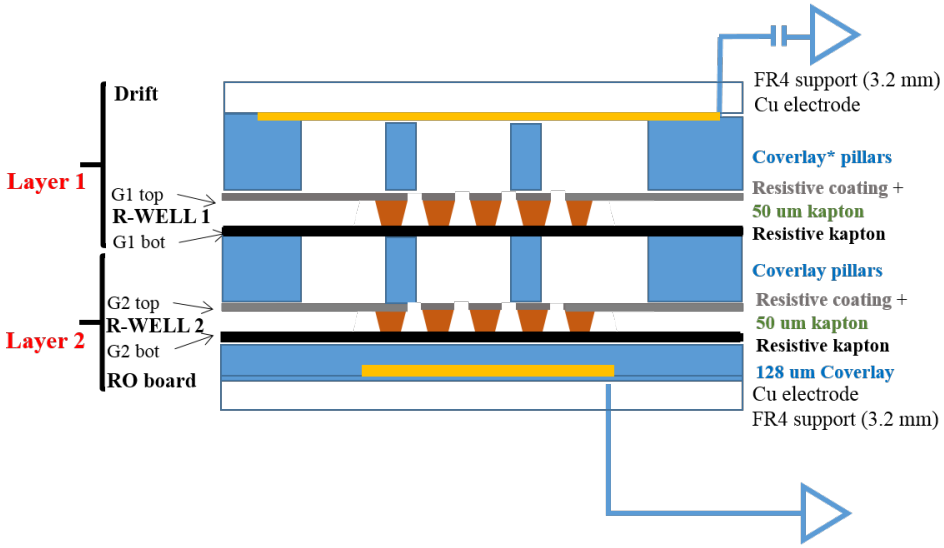

Figure 5.48: Structure of the first prototype of FTM detector.

volumes are 250 μm thick, with planarity ensured by coverlay pillars, with 400 μm diameter and pitch of 3.3 mm. The two layers can be powered together or in a separate way, in order to compare their performance and the improvement that can be obtained with the full structure. The active area of the prototype is of the order of 20 cm^2. The induced signal can be picked up from the readout electrode, but also from the drift electrode, through a capacitive coupling.

5.2.2.3 Characterization results

The first characterization of the FTM prototype was performed at CERN with an X-ray generator [86], with Ag cathode filament (22 keV X-Rays). Examples of signals picked up from the drift and readout electrodes and read out with an electronics chain composed by a preamplifier ORTEC 142PC [93] and an amplifier ORTEC 474 [94], are shown in Fig. 5.49.

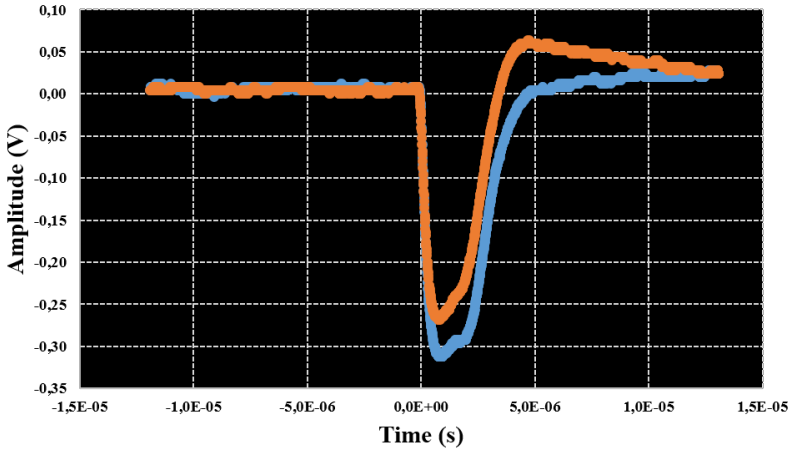

Figure 5.49: FTM signals: in blue the signal pickup from the readout electrode, in red from the drift electrode (inverted). Each point in this plot is obtained as the average of 10 acquisitions of the scope.

Linearity and transparency The measured rate from both the readout and drift electrodes at different values of current from the X-Ray gun, i.e different values of incident flux up to the maximum available from the source, is shown in Fig. 5.50.

The response of the detector, for both the electrodes, is linear; in addition the two data sets are comparable, giving an indication of the electrical transparency of the layers.

Fig.5.50 was obtained with all the detector powered, i.e. applying both the drift fields and the amplification fields. If we look instead at the behavior of the single layer, the results are shown in Fig.5.51, on the left for *Layer 1* and on the right for *Layer 2*. Even if the behavior is still linear in both the cases, it is clear that there is a difference between the two: the applied fields being equal, the maximum rate measured on *Layer 1* is twenty times higher than the rate measured on *Layer 2*. This is a first indication of a defect or a problem on *Layer 2*, then confirmed by the results obtained during the test beam.

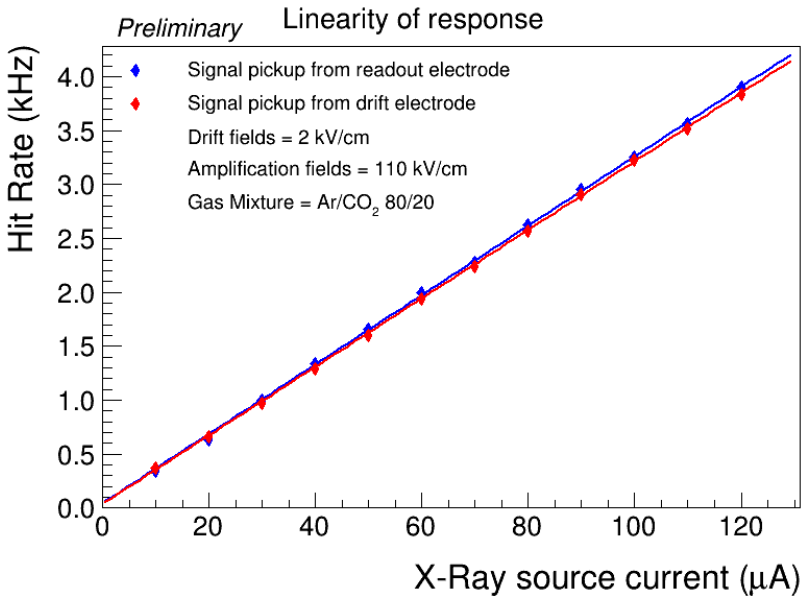

Figure 5.50: Rate measured with the FTM detector as a function of the X-Ray source current, i.e. of the incident flux. The blue curve is obtained with the signal pickup from the readout electrode, while the read curve with the signal from the drift electrode. This plot is obtained with all the detector powered.

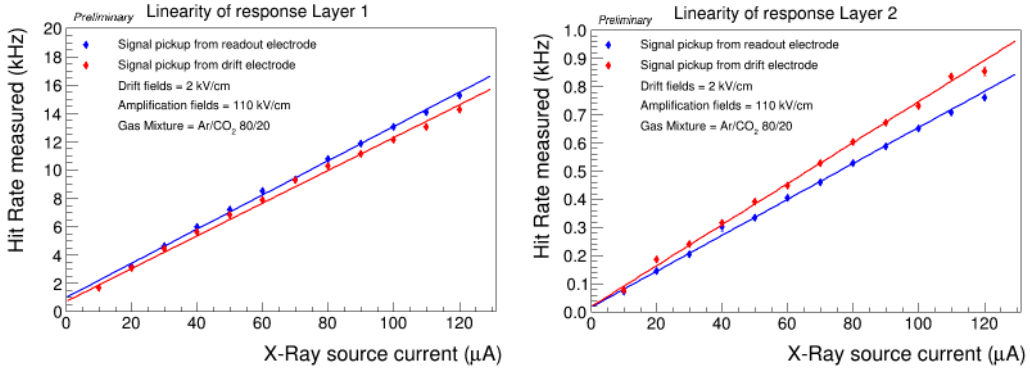

Figure 5.51: Rate measured with the FTM detector as a function of the X-Ray source current, i.e. of the incident flux. The blue curve is obtained with the signal pickup from the readout electrode, while the read curve with the signal from the drift electrode. The left plot is obtained with only the *Layer 1* powered, the right one instead with only the *Layer 2*. The differences in rate between the readout electrode and the drift electrode are due to a non perfect thresholds setting.

Behaviour at different drift and amplification fields In Fig.5.52 left the rate measured at different values of drift field applied is plotted. From studies performed in similar devices, like the μRWELL (see [89]), the rate is expected to be maximum in the range from 2 to 4 kV/cm, then it should

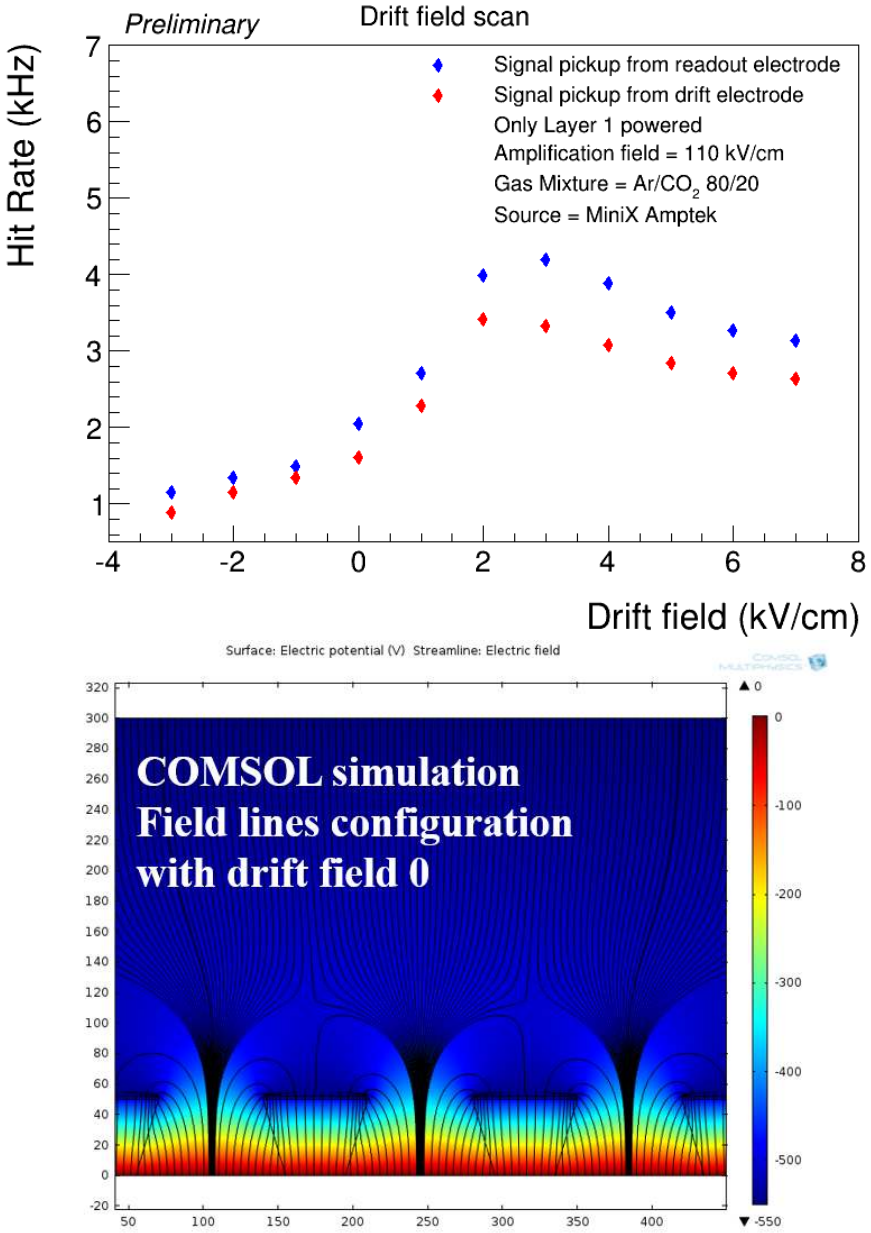

Figure 5.52: Left: Rate measured with the FTM detector as a function of the applied drift field. The blue curve is obtained with the signal pickup from the readout electrode, while the read curve with the signal from the drift electrode. The difference in rate between the two series is due to a non perfect threshold settings. Right: results of the COMSOL simulation with drift field equal to zero.

decrease at lower and higher drift fields. For higher drift fields this is due to the fact that, if the drift field is too high, the field lines guide the electrons produced in the ionization on the top of the kapton foils, instead that in the

holes. The electrons as a consequence are not amplified and the efficiency is lower. For the low drift field side instead, we would expect a decrease up to rate equal to zero when the drift field is zero. What we observed instead is that the rate at zero drift field is different from zero and it is necessary to invert the drift field in order to have the rate decreasing and approaching zero. This is due to the fact that the drift regions in this prototype are only 250 μm thick, so the amplification field lines can enter in the drift zone and play a not negligible role, as confirmed also by COMSOL [110] simulation whose result is shown in Fig.5.52 right: when the drift field is zero, the particle that passes through the drift gap is affected by the residual line of the amplification field and so the ionization can happen. In order to compensate this effect it is necessary to invert the drift field: the rate in this way starts to decrease, we didn't reach the zero because we were operating the detector in an unstable condition.

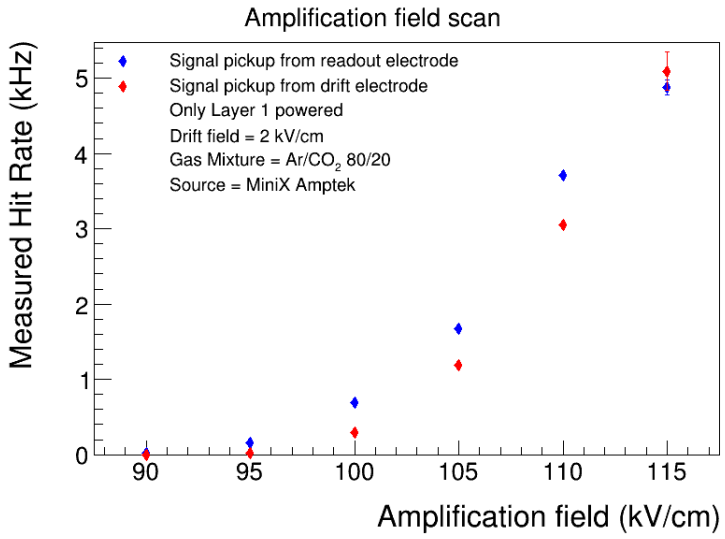

Figure 5.53: Rate measured with the FTM detector as a function of the amplification field applied to *Layer 1*. The blue curve is obtained with the signal pickup from the readout electrode, while the read curve with the signal from the drift electrode. The difference in the rate between the two series is due to a non perfect thresholds settings.

In Fig.5.53 instead the rate is plotted as a function of the amplification field. We would expect to reach a plateau at high fields, but actually we couldn't because the detector started to be unstable at 120 kV/cm. In any case, one thing that is important to notice is that with this detector we are able to go above the limit given by the Paschen curve for Ar/CO_2 70%/30%, showed in

Fig.5.54, that gives the value of the breakdown voltage for a given gas or gas mixture as a function of the thickness of the material and of the pressure [111]. From the Townsend theory indeed we obtain that the breakdown voltage can be calculated as

$$V_b = \frac{Bpd}{\log Apd - \log[\log(1 + 1/\gamma)]} \tag{5.4}$$

where A and B are two coefficients related to the variations of the first Townsend coefficient as a function of the electric field at the cathode and of the distance d from the cathode, p is the gas pressure and γ is the second Townsend coefficient. A and B depends only the gas considered, while γ is slightly dependent also from the material of the electrodes [112].

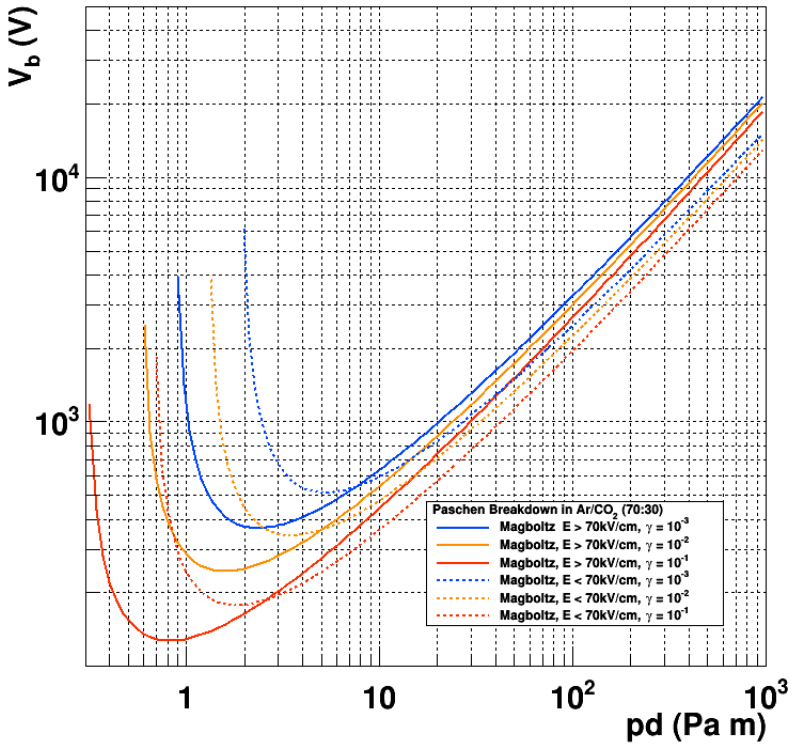

Figure 5.54: Paschen curve for Ar/CO_2 70%/30% gas mixture.

The curves obtained from this relation, i.e. the Paschen curves, are characterized by a minimum, then the breakdown voltage increases for high pressure-distance product. This is due to the fact that when the gas pressure is higher, also the number of collisions between the electrons in the gas is higher. In each collision, an electron looses a part of its energy, so higher fields must be

applied in order to increase the electrons energy in such a way that they would produce a ionization and consequently a discharge. On the other side of the minimum, where pd is small, the mean free path of the electrons in the gas is longer with respect to d. In general there are fewer collisions, then also in this case it is necessary to apply a higher field to produce ionization and then avalanches [112].

In the case of the FTM detector, assuming an environmental pressure of 101325 Pa, a thickness of 50 μm and considering in Fig.5.54 the curves with high field $>$ 70 kV/cm, the highest breakdown voltage that we expect is 450 V (blue line). In order to get 120 kV/cm in the amplification region, we actually applied 600 V, well above the limit. An hypothesis developed to explain this is that the Paschen curves are usually calculated for metallic electrodes, while here we are using a fully resistive device that would have allowed us to overcome this limit.

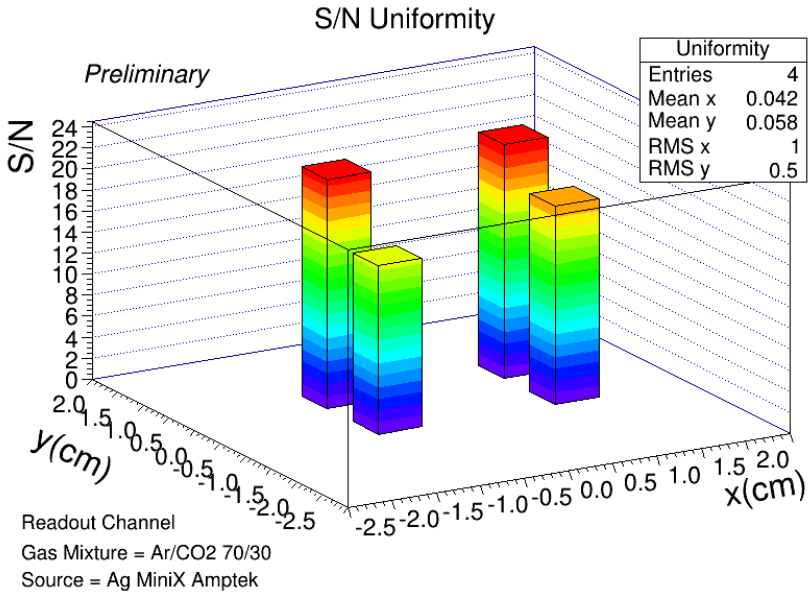

Figure 5.55: Uniformity of signal/noise.

Uniformity Fig.5.55 shows the uniformity of the signal over noise ratio (S/N) over the detector surface. The X-Ray source has been focused in different positions of the detector, over a 0.5 cm diameter surface and, for each position about 50 waveforms have been acquired. The S/N has been calculated

for each waveform as

$$S/N = \frac{maximum\,signal\,amplitude}{rms} \tag{5.5}$$

where

$$rms = \sqrt{\sum_{i=1}^{n} \frac{(y^2)_i}{n}}. \tag{5.6}$$

is the rms of the distribution of the height of the noise. The final result is then obtained as the average over the 50 waveforms.

The S/N is quite high due to the electronics used during the characterization, able to make a good shaping of the signal from the detector and to reach a good amplification. Moreover the response seems to be uniform within 20% over the surface of the detector.

Gain measurement A tentative calculation of the gain of the FTM detector was performed using two different methods:

- *Method 1*: G = $\frac{I_{HV-ON}}{I_{HV-OFF}}$
- *Method 2*: G = $\frac{I_{net}}{R_{net}^{max} \times N_p \times e}$

where I_{HV-ON} and I_{HV-OFF} are the currents measured with the detector ON and OFF respectively with the source ON, I_{net} is the net current (with noise subtraction) with the detector powered, R_{net}^{max} is the maximum net measured rate, e is the electron charge and N_p in the number of primaries produced in the interaction of the incident particle.

Method 1 is the method used for the calculation of the gain of similar devices, like μRWELL. Here the gain is calculated as the ratio between the current with all the detector powered, i.e. both drift and amplification fields different from zero, and the current with only the drift field on, i.e. the ionization current. The gain in this method is actually given by

$$G = \frac{I_{HV-ON}}{I_{HV-OFF}} = \frac{e \times N_p \times G \times R}{e \times N_p \times R} \tag{5.7}$$

where $I_{HV-OFF} = e \times N_p \times R$ because in the ionization regime the $G = 1$ [101]. In this way, $e \times N_p \times R$ can be cancelled and the contribution the gain can be calculated also without measuring the rate and knowing the number of primaries produced by the interaction. These parameters instead are needed

in *Method 2*. This is the classical method used to calculate the gain of Triple-GEM detector, already introduced in Chapter 3. It is important to underline that for this last calculation, the parameter N_p used and is actually fixed at 286 electrons produced in the gap by the interaction of a 8 keV photon that releases all its energy. The 8 keV photon is produced by the interaction of the photons from the source (22 keV peak) with the copper of the drift electrode. Considering that the drift gap in this prototype are only 250 μm thick and assuming that all the energy of the photon is realized in it could be an overestimation that can affect the gain calculation.

All the plots presented below were obtained keeping fixed the value of the drift field at 8 kV/cm.

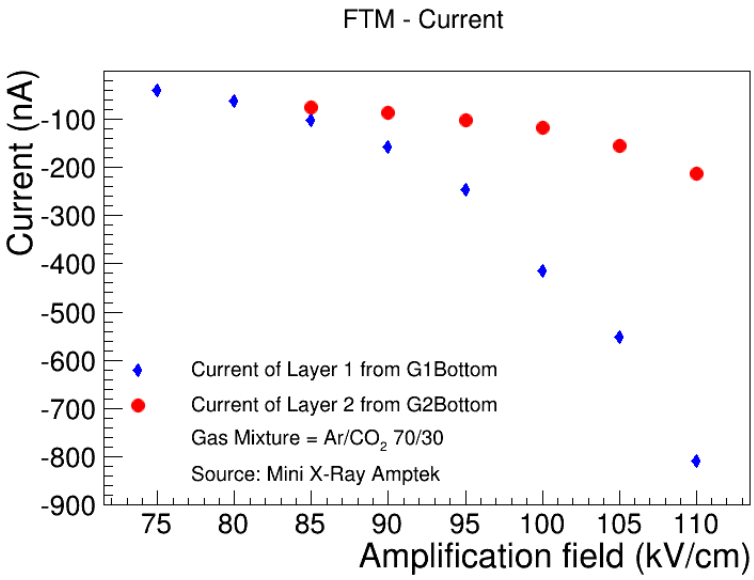

Figure 5.56: Current measured with FTM detector: in blue for *Layer1* from *G1Bottom*; in red for *Layer2* from *G2Bottom*.

For each layer, the current has been measured from the bottom of the amplification region, i.e. *G1Bottom* for the *Layer 1* and *G2Bottom* for the *Layer 2* referring to Fig.5.48, as this is the position nearest to the point in which the avalanche is created and then is collected. From Fig.5.56 we can see that the current measured is of the order of hundreds of pA.

In Fig.5.57 the results of the gain measurement with *Method 1* and *Method 2* respectively are shown. In the right plots, the gain calculated with *Layer 1* is shown in blue, with *Layer 2* in red.

One thing that can be noticed immediately is that with *Method 1* there

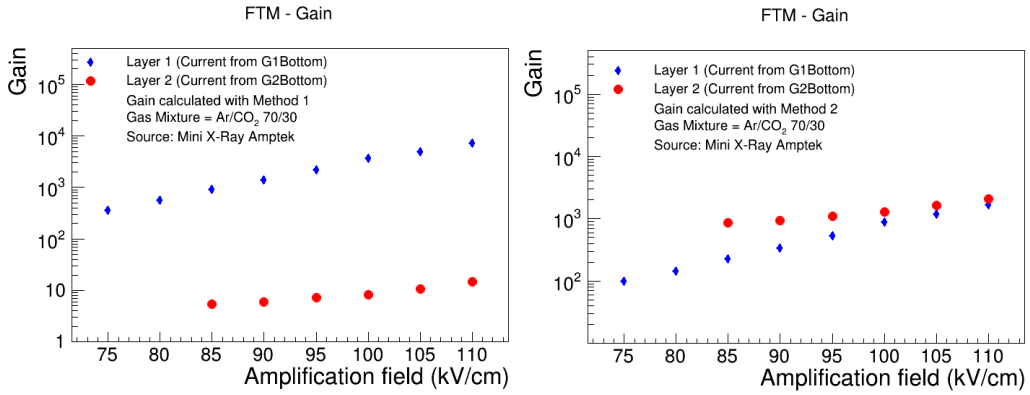

Figure 5.57: Gain measured on the two layers of the FTM. Left: with *Method1*; Right: with *Method2*

is a big difference between the two layers. This would confirm the differences already noticed in the previous steps of the characterization. With *Method 2* instead the gain of the layers are almost equal, but the pertinence and the results obtained with this method are still under discussion.

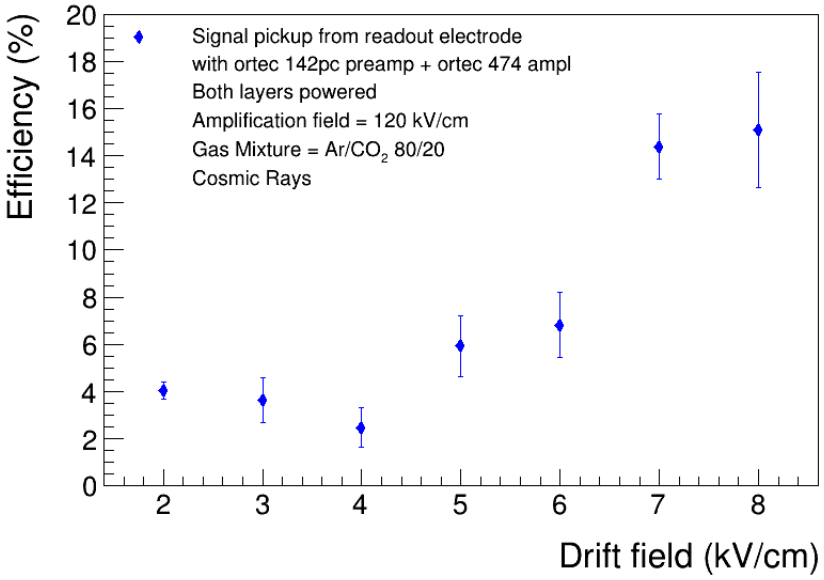

Figure 5.58: Measured efficiency of the FTM detector with cosmic rays as a function of the drift field applied. The results already include the correction for the geometric acceptance.

Efficiency The efficiency was measured with cosmic rays before moving the detector to the 2015 test beam. The signal was taken from the readout electrode and processed with the electronics chain used for all the characterization,

i.e. ORTEC 142PC preamplifier and ORTEC 474 amplifier. The results are shown in Fig.5.58.

The number of primary ionization, for example, for a 3 GeV muon in Ar/CO_2 70%/30%, from Garfield [119] simulation, is about $\sim$33 cm^{-1}, i.e. $\lambda = 300\ \mu$m. The probability to have one ionization in 500 μm is so $1-e^{-\frac{500}{300}} \sim 80\%$, so, if both the layers are working correctly, the detector is already affected by an intrinsic inefficiency of ~ 20 %. Moreover, from the results presented above and then confirmed during the test beam, one of the two layers, *Layer 2* seems to work worst with respect to *Layer 1*. If in first approximation we neglect its contribution, the expected efficiency is already reduced to $\sim$ 57%. The result obtained then is even worse due to the fact that, as Fig.5.57 suggests the detector was working at low gain. Moreover the electronics chain used, even if able to make a good shaping, is optimized to be used with detectors able to produce a big charge at the readout. This is not the case for the FTM, mainly for two reasons: on one side the drift gap is very small, and then the number of primary ionization particles generated. Moreover, each layer of the detector is actually a single-stage amplification, i.e. the presence of the bottom resistive layer prevent the charge to be transmitted to the second gap. For this reason, in order to be able to efficiently use this electronics, the FTM should have provided with a single layer the same charge that a Triple-GEM produces after three amplification stages, with a gain higher than 10^4.

The efficiency measured is even worst when a non-shaping electronics is used: in fact, the advantage of the ORTEC chain is that this electronics is able to make a very good shaping of the signal, with a very good S/N ratio can be observed for the signal shape in Fig.5.49. However it is very slow, not suitable for the timing measurement, then a very fast linear electronics chain was used for this purpose. The S/N noise ratio unfortunately with this last electronics is much lower, forcing to set higher relative thresholds to reject the noise: for this reason the efficiency measured with this last chain is even lower, of the order of fraction of percent.

5.2.2.4 Time resolution with Ar/CO_2

A rough estimation of the expected time resolution of an efficient device with two layers, with a eco-friendly gas mixture like Ar/CO_2 can be obtained with the formula $\sigma_t = (\lambda v_d N_D)^{-1}$: assuming, for example, $\lambda \sim$33 cm^{-1} for a GeV muon in Ar/CO$_2$ 70%/30% mixture, v$_\mathrm{d}$ $\sim$8 cm/μs, the estimated time

resolution is $\sigma_t \sim$1.9 ns.

The two-week test beam carried out in autumn 2015 at the SPS H4 beam line, with muon and pion beams, was focused on the time resolution measurement. The time of arrival of the signals from the FTM, both from the top and bottom readout, together with their coincidence and OR, was measured by a TDC working in COMMON-STOP mode, i.e. the time is measured as the delay of the signal from the detector with respect to a reference signal. The reference was given by a coincidence of three 10×10 cm^2 scintillators with a *finger* scintillator, 2×3 cm^2, readout by PMTs. The finger scintillator was introduced in order to improve the geometrical acceptance of the system as it was mounted just behind the active area of the FTM. Moreover, its signal was slightly delayed with respect to the one of the other scintillators, in such a way that it was always determining the trigger time, reducing as a consequence the uncertainty. The time resolution of the trigger signal itself, built as described previously, was measured and turned out to be of the order of 100 ps. Its contribution has not been subtracted from the data presented later.

The time resolution was evaluated with muon and pion beams in different powering configuration of the detector.

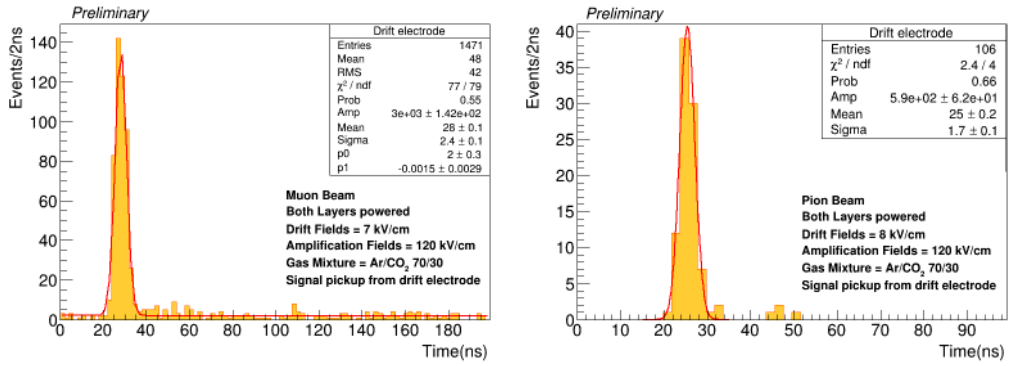

Figure 5.59: Time distribution of signals from the drift cathode of the FTM detector from muon beam on the left and pion beam on the right.

Fig. 5.59 left shows the time distribution of events induced by muons: the signal is taken from the drift electrode and read out by a fast electronic chain composed by a Cividec broadband amplifier [113] and a linear Lecroy 612AM amplifier [114]. The time resolution is the sigma of the gaussian fit to the time distribution and is of the order of 2.4 ns. The same result obtained with pions is shown in Fig.5.59 right: here the time resolution is of the order of 1.7 ns. All these results were achieved using a green-house-gas-free gas mixture,

composed by Ar/CO_2 70%/30%.

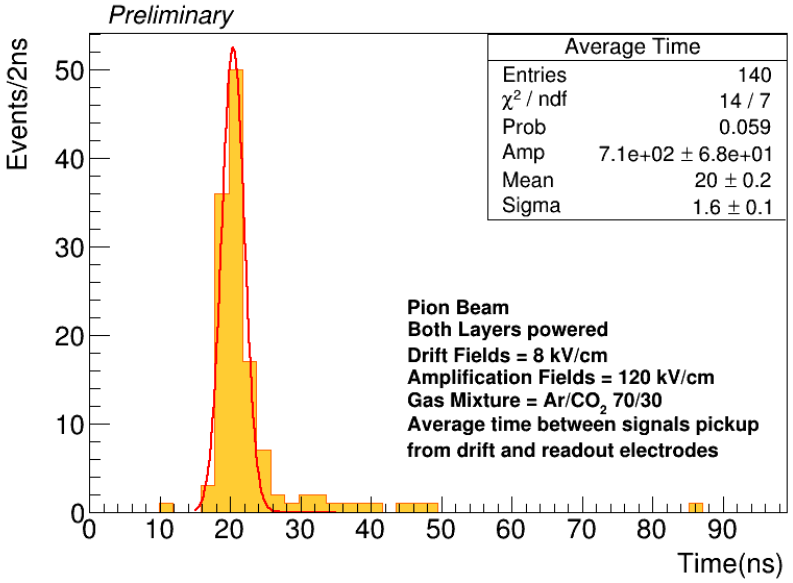

Figure 5.60: Averaged signal between drift and readout with pion beam.

In Fig. 5.60 the average time of arrival of the signals from the drift and readout electrodes of the FTM detector is computed. As a consequence the event is considered good only if there is one signal on both channels. This requirement is used in order to reject all the noise that could have been acquired in the single channel plots due to a non-perfect threshold settings or similar problems. The time resolution obtained is compatible with the one measured with the single drift electrode channel with pions and shown in Fig.5.59 right.

Fig.5.61 displays instead a comparison of the time of arrival of the signals on the readout electrode, on the X axis, and on the drift electrode, on the Y axis. It's clear that the majority of the signals arrives in time between the two channels, in the range 450-470 ns[6]; few events are then distributed along the bisecting line and represent events arrived later with respect to the mean primary ionization time. They could be due to signals induced by secondary ionizations events and are very rare due to the small thickness of the drift gaps.

Fig.5.62 shows the measured time resolution for different values of applied drift fields, keeping constant the amplification fields, with both muon and pion

[6]The time scale in this plot is the one actually created by the TDC, which was working in COMMON-STOP mode, giving the time of arrival of the detector's signals with respect to the time of arrival of the trigger, so the time scale is inverted with respect to the real time versus. In the previous plots the time scale was inverted during the analysis to restore the real time versus.

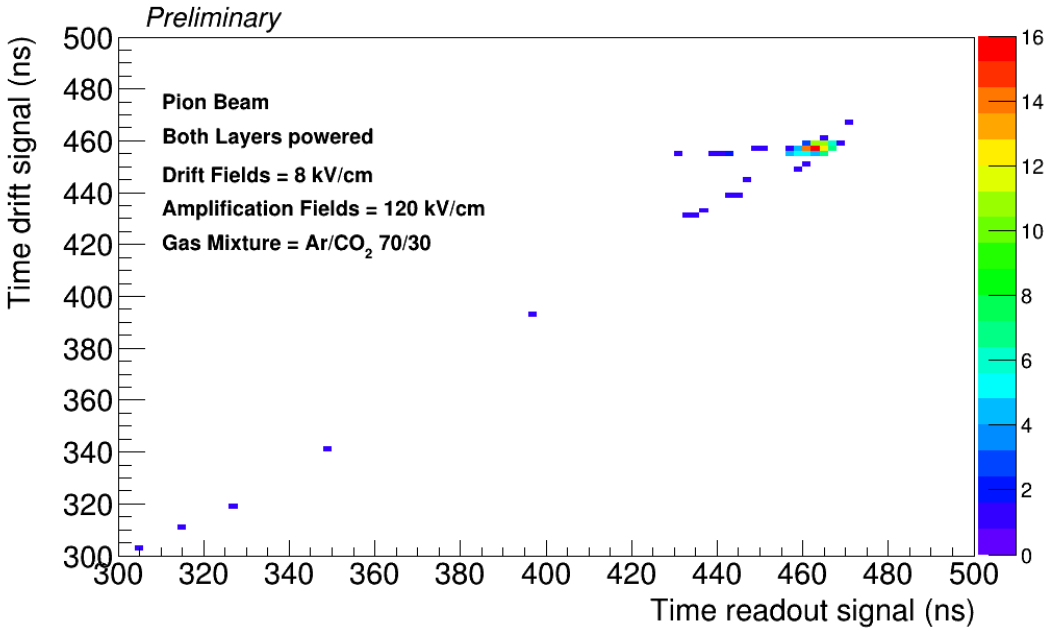

Figure 5.61: Comparison between time of arrival of the signal from the readout cathode and the drift cathode. The time scale on this plot is inverted with respect to the previous ones.

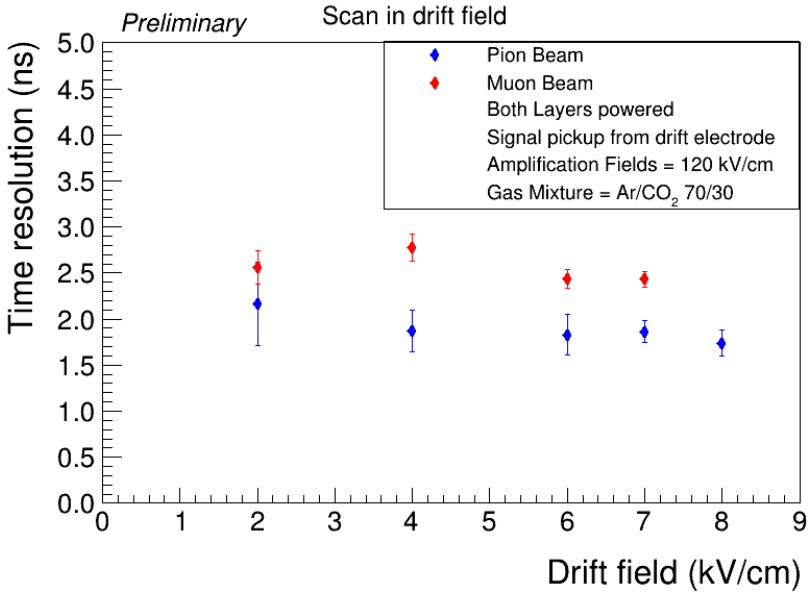

Figure 5.62: Time resolution of the FTM detector as a function of the applied drift field.

beams. The time resolution of the detector seems to be not affected by a change in drift field: this is due to the fact that, with such a small drift gap, even a big change in the drift velocity would not affect significantly the time

needed by electrons to reach the amplification region. Moreover, as shown in Fig.5.40 the drift velocity in Ar/CO_2 70%/30% mixture is nearly constant, with variations of the order of 5% for drift fields between 2 and 10 kV/cm [115].

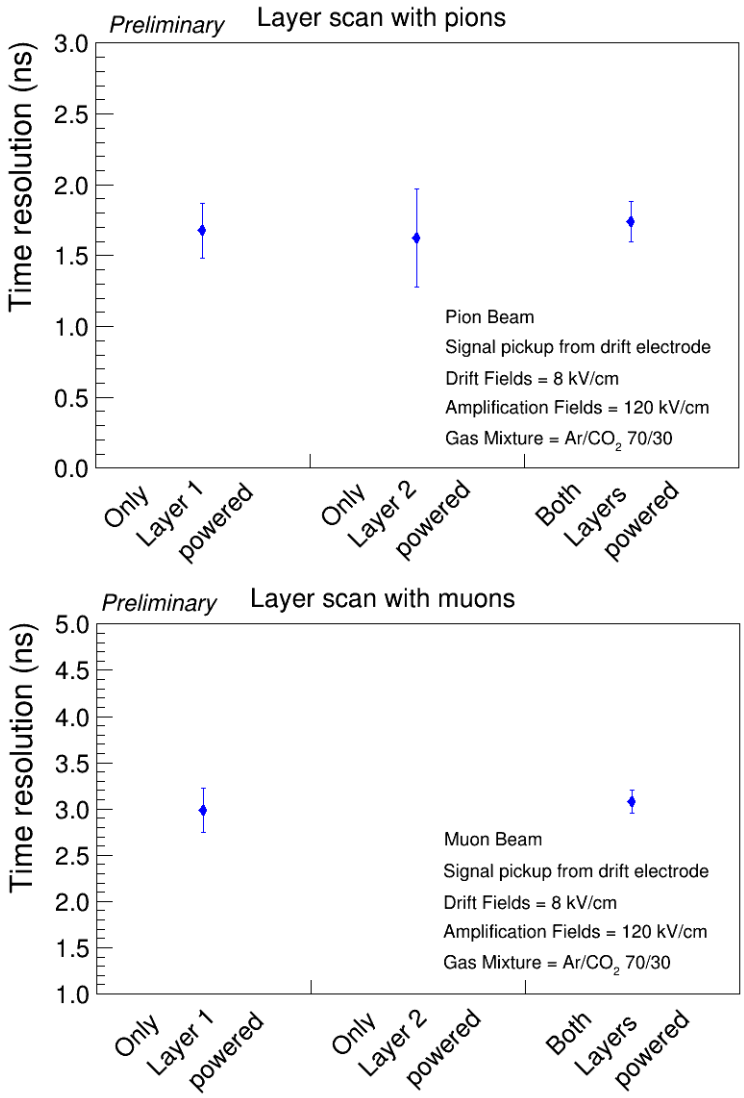

Figure 5.63: Time resolution of the FTM detector as a function of the layer powered. Top: with pion beam; bottom: with muon beam

Fig.5.63 shows the time resolution of the FTM detector as a function of the layer powered, on the left with pion beam, on the right with muons. Two things should be noticed: first of all, the error is bigger in the plot taken with pions for *Layer 2* only with respect to *Layer 1* only; in the muon plot, the *Layer 2* data is not present at all. This is due to the fact that, being equal the applied

fields, the events acquired with only *Layer 2* powered are much less that with only the other layer and the performance of the detector in this configuration are worst. This seems to be a confirmation of the possible problem on *Layer 2* already noticed during the laboratory characterization. On the other side, it seems there is no clear improvement from the measurement with only one layer powered and two layers powered. This could be partially connected to the not perfect functioning of the *Layer 2* underlined above, but also to the fact that, as the detector is not efficient, the two layers are not really in competition between them, so formula 5.3 is not yet completely valid in our prototype.

5.2.2.5 Simulation of the behavior of FTM detector in the CMS background

In order to evaluate the behavior of the FTM detector in the CMS muon system environment, a simulation identical to those performed for the μRWELL detector already described in Section 5.1.2.1 has been developed. The energy ranges and distributions are the same already commented above.

First of all, a simulation of the FTM with the configuration of the first prototype, described and analyzed above, has been performed. The geometry developed in the simulation is the one shown in Fig.5.64

Layer Name	Composition	Depth
Drift Board	FR4Support1 DriftCopper	3.2 mm 35 um
Drift Gap1	GasGap1	250 um
Layer 1	DLC1 Kapton1 RKapton1	2 nm 50 um 25 um
Drift Gap2	**GasGap2**	**250 um**
Layer 2	**DLC2** **Kapton2** **RKapton2**	**2 nm** **50 um** **25 um**
Readout Board	PMMA Coverlay ReadCopper FR4Support2	51 um 76 um 35 um 3.2 mm

Figure 5.64: Geometry of the first FTM prototype simulated with Geant4

The detector is composed by a *Drift board*, made of 3.2 mm of PCB and 35 μm of copper which represent the cathode. The drift gaps are 250 μm thick and

are filled with Ar/CO_2 70%/30%. *Layer#* is instead the amplification region, here composed by a *DLC* deposition, 2 nm thick and simulated as carbon, on a kapton foil, 50 μm-thick. Last element is a layer of resistive kapton, 25 μm-thick. This material in reality is Kapton XC Dupont [109], a custom made material whose composition information were not available. For this reason it was approximated as standard kapton. The detector is finally closed by a *Readout Board*, made of an insulating layer (PMMA+Coverlay) to protect the readout pad from possible discharges, the readout pad itself in copper and a PCB support 3.2 mm thick. The dimension of the detector is 10 x 10 cm^2.

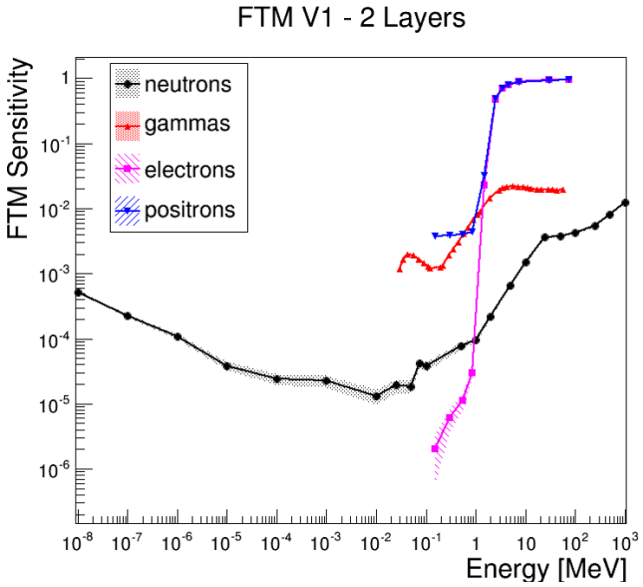

Figure 5.65: Results of the sensitivity simulation of FTM detector performed with Geant4, with kapton 50 μm

Fig.5.65 shows the simulated sensitivity, in black for neutrons, red for gammas, pink for electrons and blue for positrons, as a function of the energy of the incident particle. The behavior is really similar to the one of a Triple-GEM detector, discussed in detail in Section 2.5. Analyzing the processes involved in the interaction of neutrons and gammas, we can find the results shown in Fig.5.66 and 5.67, where the processes are named using the Geant4 convention [116].

Starting from neutrons in Fig.5.66, for the low neutron energies up to 1 keV the dominant interaction is neutron capture on hydrogen and other heavier nuclei, with the emission of gamma rays that in turn undergo Compton scattering and pair production (called *conv*). The intermediate energy range

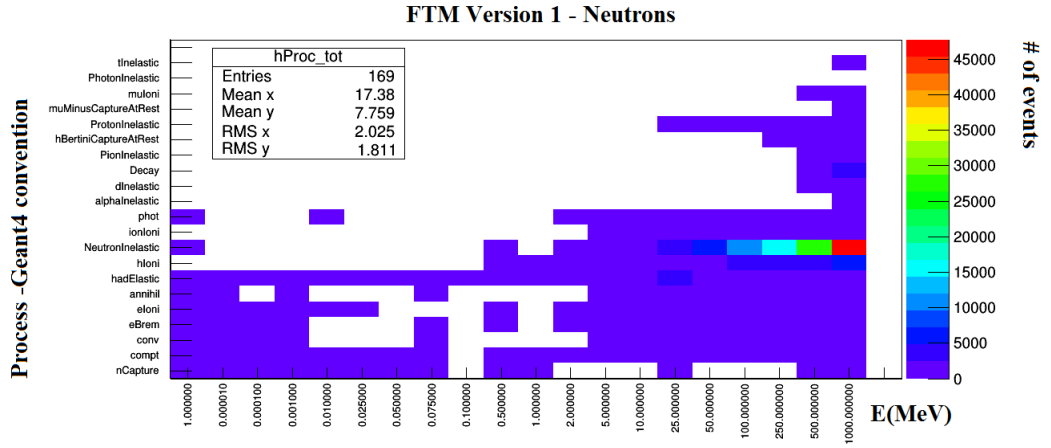

Figure 5.66: Processes induced by neutrons in the FTM detector in the kapton version.

is dominated by neutron elastic scattering on hydrogen nuclei. For neutron energy greater than a few MeV the dominant interaction processes are neutron induced nuclear reactions (*NeutronInelastic*), leading to the fragmentation of the target nucleus and the production of nuclear fragments.

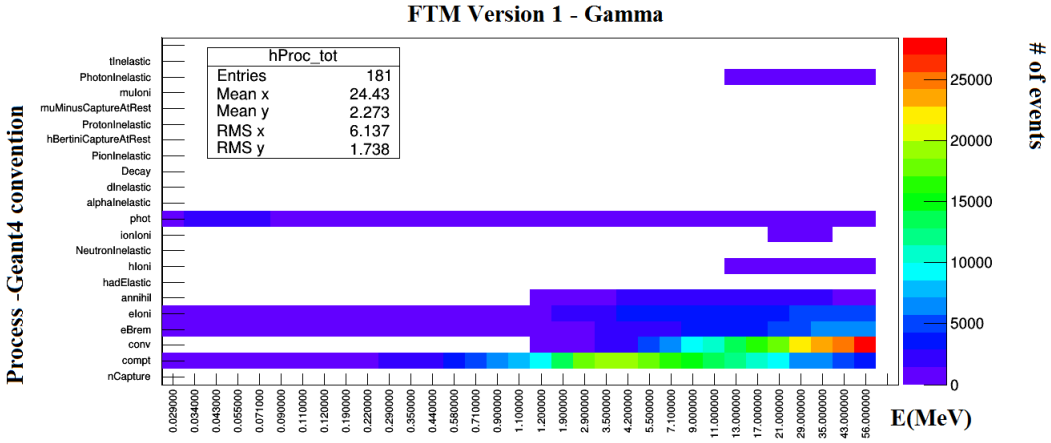

Figure 5.67: Processes induced by neutrons in the FTM detector in the kapton version.

Considering the gamma instead in Fig.5.67, we can see that for energies up to 0.3 MeV the dominant processes are the photoelectric effect (*phot*), the Compton effect (*compt*) as well as the energy loss by ionization and bremsstrahlung by light charged particles released in the interactions. The intermediate energy range is dominated again by Compton scattering, while for photon energy greater than about 13 MeV the dominant interaction pro-

cess is pair production o gamma conversion (*conv*). The processes involved are therefore really similar to those considered for the Triple-GEM technology (see Section 2.5), justifying therefore also the similarity of the sensitivities.

In order to be able to make a comparison also between this FTM structure and those adopted for the new versions, which will be described below, another simulation have been performed using the geometry shown in Fig.5.68.

Layer Name	Composition	Depth
Drift Board	FR4Support1 DriftCopper	3.2 mm 35 um
Drift Gap1	GasGap1	1 mm
Layer 1	DLC1 Kapton1 RKapton1	2 nm 50 um 25 um
Drift Gap2	**GasGap2**	**1 mm**
Layer 2	**DLC2** **Kapton2** **RKapton2**	**2 nm** **50 um** **25 um**
…	…	…
Readout Board	PMMA Coverlay ReadCopper FR4Support2	51 um 76 um 35 um 3.2 mm

Figure 5.68: Geometry of the FTM detector simulated with Geant4, with kapton structure.

The general structure of the detector remains the same, but the gas gaps have been enlarged up to 1 mm. This value was selected as a reference in order to make more straightforward comparison between the technologies. However the thickness of the drift gap is of secondary relevance form the sensitivity point of view, as the majority of the interactions of background particles that produce a valid signal happen in the heavier materials that compose the external layers of the chambers. The amplification regions have the same structure and have been introduced in a modular way, i.e. it is possible to increase the number of stages of the detector simply inserting a new drift gap associated with an amplification layer. The dimension of the chamber are those foreseen for an ME0 chamber, trapezoidal shape 840 mm height, 565 and 268 mm bases.

Fig.5.69 shows the results of the simulation performed with the FTM detector with six stages made of kapton 50 μm. The detector, as did before for

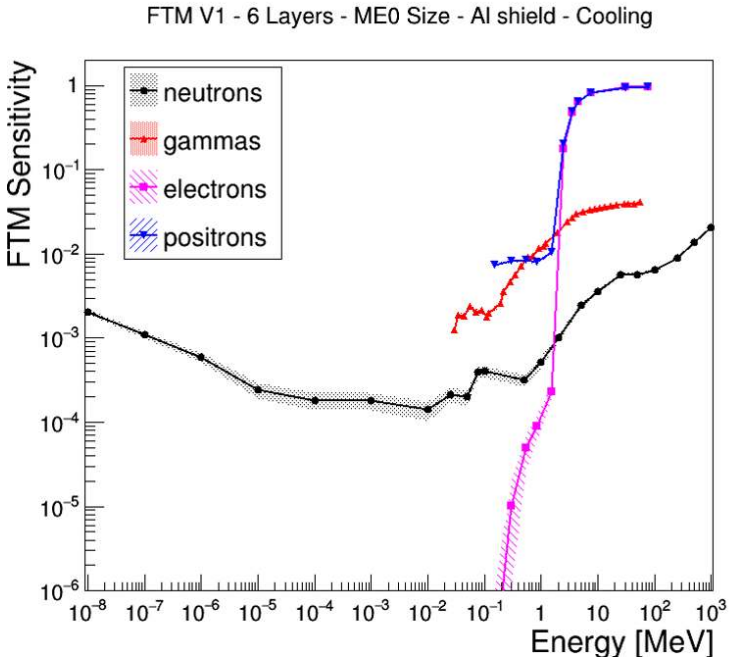

Figure 5.69: Results of the sensitivity simulation of FTM detector performed with Geant4, with kapton 50 μm

the μRWELL simulation, has been simulated also with an aluminum shielding and a cooling system, based on GE1/1 solution.

FTM	Neutrons	Gammas	Electrons	Positrons
2 layers 10 x 10	$(4.00 \pm 1.21) \times 10^{-4}$	$(7.18 \pm 0.17) \times 10^{-3}$	0.222 ± 0.051	0.225 ± 0.050
Nude	$(7.94 \pm 2.04) \times 10^{-4}$	$(1.04 \pm 0.02) \times 10^{-2}$	0.229 ± 0.052	0.237 ± 0.052
With Al shielding	$(9.55 \pm 2.89) \times 10^{-4}$	$(1.11 \pm 0.03) \times 10^{-2}$	0.176 ± 0.044	0.184 ± 0.044
With Al shielding and cooling	$(1.17 \pm 0.35) \times 10^{-3}$	$(1.11 \pm 0.03) \times 10^{-2}$	0.164 ± 0.041	0.172 ± 0.041

Table 5.3: FTM sensitivity results averaged over the particle energy distribution.

Table 5.3 shows the sensitivities averaged over the energy distributions for neutrons, gammas, electrons and positrons. What can be noticed is the increase of sensitivities related to the increase of the dimensions of the detector: the angular distribution of the particles used in the simulation, includes also particles coming with a transversal direction with respect to the detector. For this reason, increasing the dimension of the detector actually increase the probability of the border effect due to these particles. Concerning instead

the variation of sensitivities with the insertion of the aluminum layer and of the cooling, the conclusions that can be drawn are similar to those already explained in detail for μRWELL detector in Section 5.1.2.1.

5.2.2.6 Development of new FTM prototypes

The two main features of the first prototype of FTM detector that should be improved in the following versions are related to the efficiency and the gain, which are fundamental for the possible implementation of the FTM detector into the CMS environment. A higher efficiency could be reached increasing the total drift volume, i.e. increasing the depth of the single drift gap or increasing the number of layers up to reaching a total drift volume of about 3-4 mm. However, increasing the depth of the single drift gap would imply a worsening of the time resolution, because the fluctuation over the position of the first ionization would increase. Then the increase in the number of small gap is the only viable solution for this first point.

A raise of the gain instead can be reached intensifying the field applied to the amplification region, solution not possible with the first version because the higher value of nominal field that could be applied was 120 kV/cm. After that the detector started to discharge, then actually we were operating it already at its limit. The evaluated alternative was to increase the depth of the amplification region.

The natural solution considered was the substitution of the kapton 50 μm with a thicker one: evaluating the possibility offered by the kapton producers, the choice has been the usage of kapton 125 μm.

Fig.5.70 shows gain as a function of the depth of the WELL for different applied fields: comparing for example the gain reached with a field of 10^7 V/m, green line in the top plot and purple line in the bottom plot, it's clear that the fields being equal the gain reached with 125 μm is five orders of magnitude higher. On the contrary, if we want to obtain for instance a gain of 10^4 in 50 μm we have to apply a field of 1.4×10^7 V/m, while in 125 μm only 7×10^6 V/m that correspond to a potential difference of 700 V and 875 V respectively. With the 50μm prototype we couldn't reach such a value, because the detector started to be unstable at 600 V (120 kV/cm). In any case, as already explained above, we were able to go over the Paschen limit of a factor $\sim$ 33%: presuming to be able to observe the same behavior also with the 125 μm, the Paschen limit is at 700 V (from Fig.5.54), so we should reach at least $\sim$ 900 - 930 V,

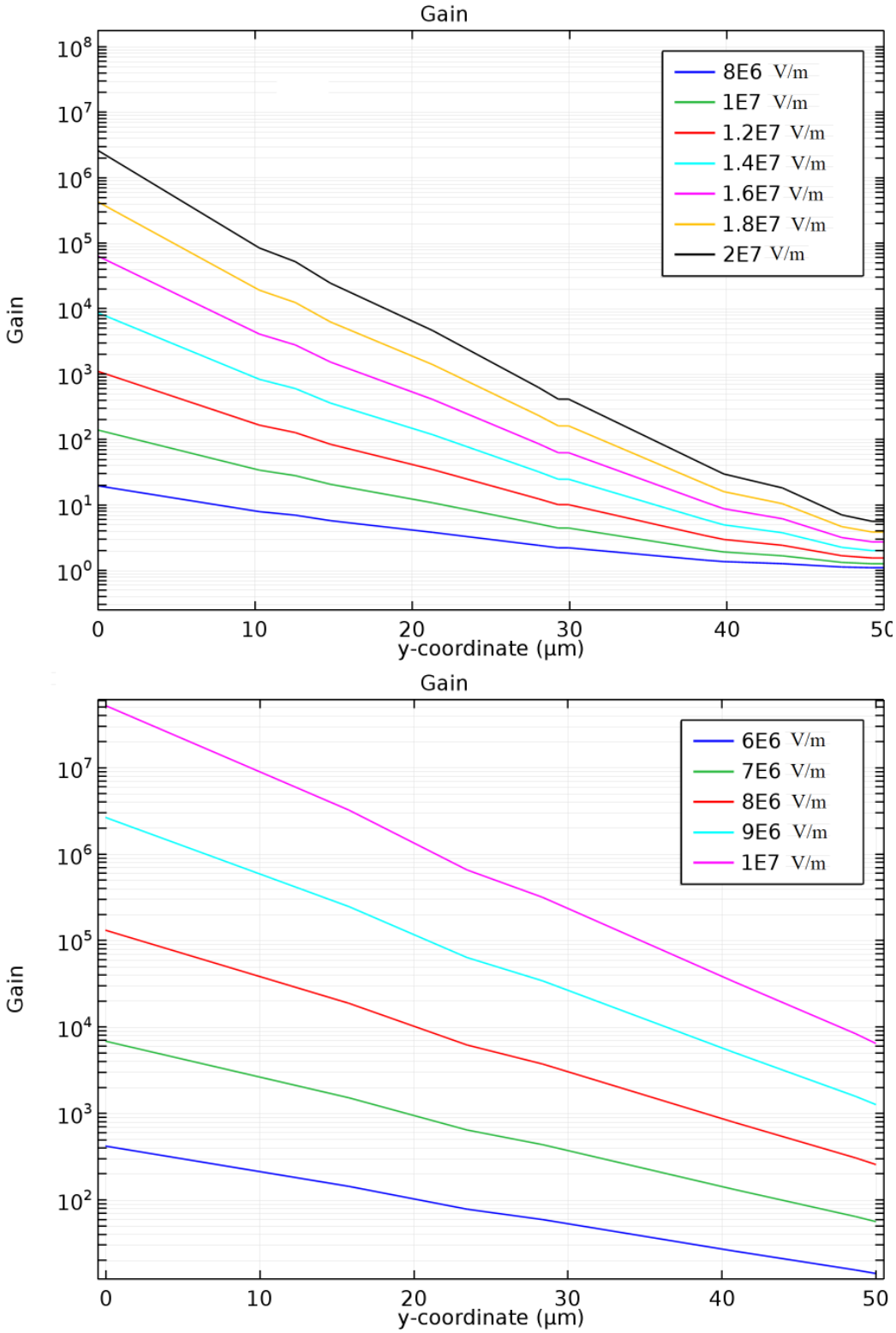

Figure 5.70: Gain vs depth of the WELL (y-coordinate) for Kapton foils of thickness 50 μm (top) and 125 μm (bottom).

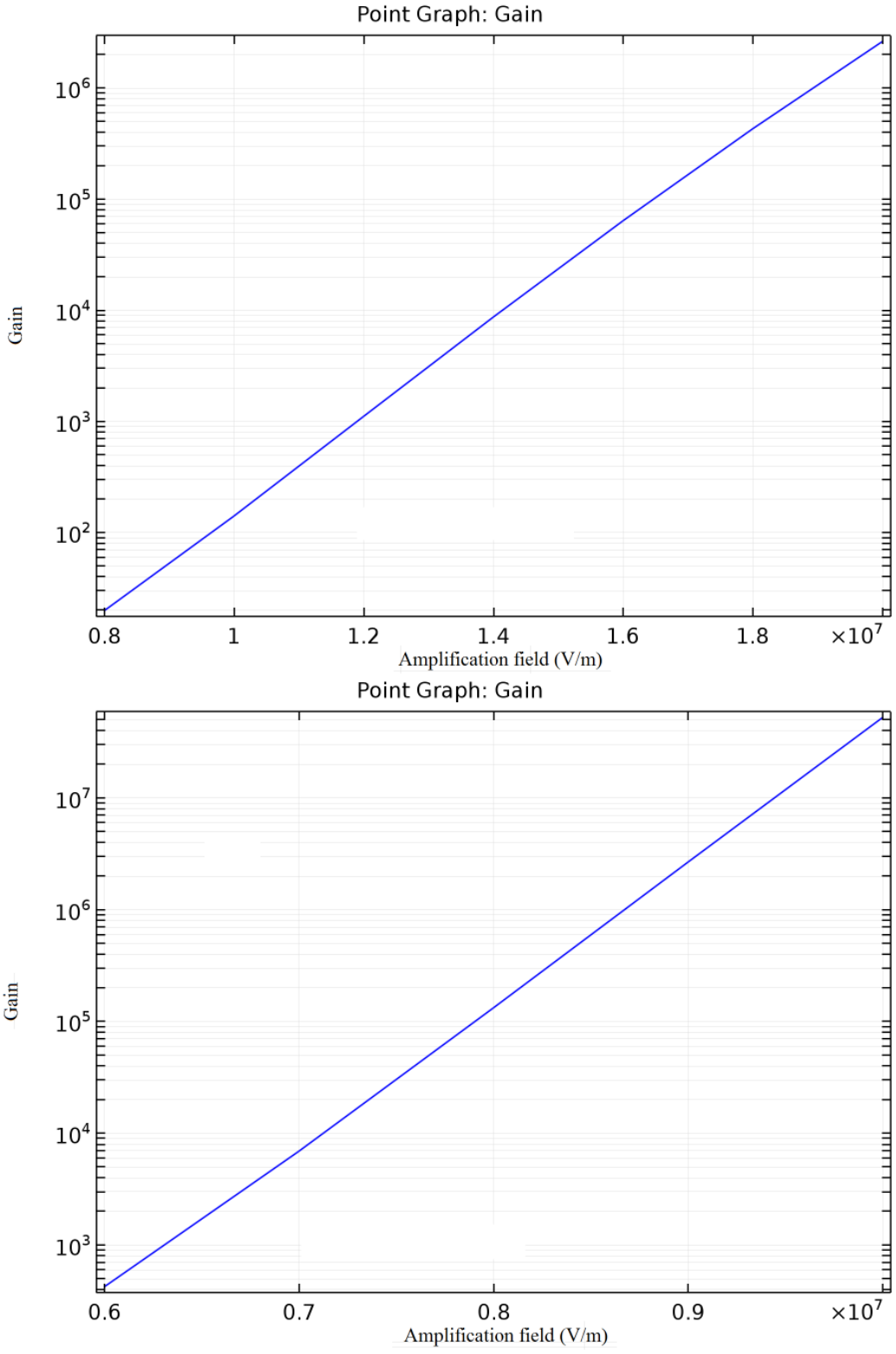

Figure 5.71: Gain vs applied amplification field for prototypes with Kapton 50 μm (left) and 125 μm (right).

enough to produce a gain of 10^4. The detail of the gain reached as a function of the applied amplification field is shown in Fig.5.71.

Considering the response to the CMS background, the 125 μm prototype is expected to react in a way similar to the first version.

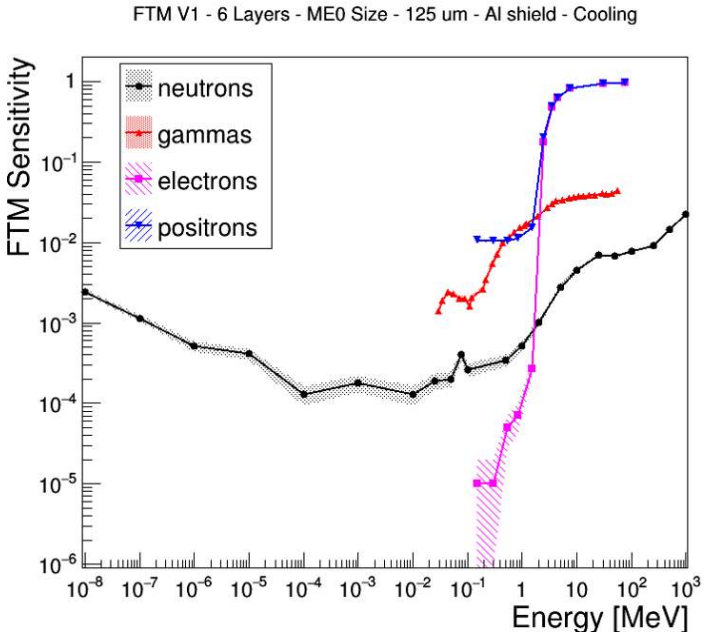

Figure 5.72: Results of the sensitivity simulation of FTM detector performed with Geant4, with kapton 125 μm.

Fig.5.72 shows the sensitivity results for a prototype with six stages, but made with kapton 125 μm, with aluminum shielding and cooling system.

FTM	Neutrons	Gammas	Electrons	Positrons
50 μm	$(1.17 \pm 0.35) \times 10^{-3}$	$(1.11 \pm 0.03) \times 10^{-2}$	0.164 ± 0.041	0.172 ± 0.041
125 μm	$(1.32 \pm 0.40) \times 10^{-3}$	$(1.28 \pm 0.03) \times 10^{-2}$	0.164 ± 0.041	0.172 ± 0.041

Table 5.4: Sensitivity comparison between kapton 50 μm prototype and kapton 125 μm prototype.

Looking at the averaged sensitivity values in Table 5.4, we can notice an increase of the neutrons and gammas sensitivities, due to the increase of the total material budget, as already happened above with the introduction of the aluminum shielding and the cooling. Electrons and positrons sensitivities instead remain constant, because, as already explained above, the absorption of these particles happens prevalently in the external layers of the chamber.

This behavior is also confirmed in Fig.5.73, where the sensitivity of the

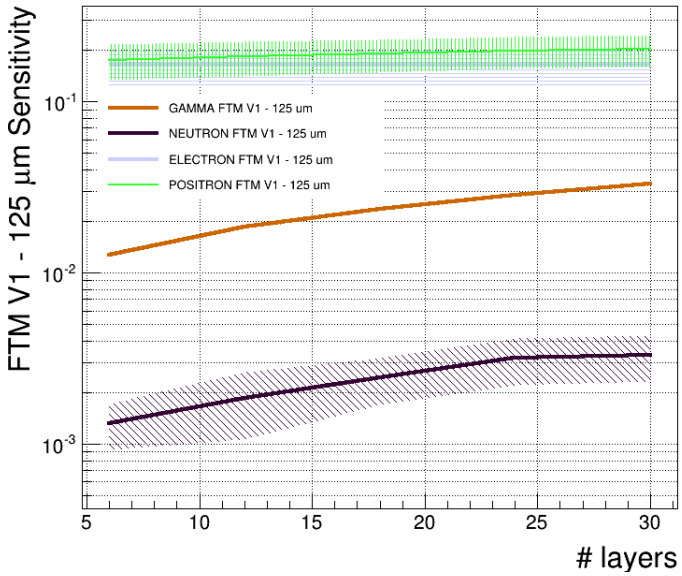

Figure 5.73: Sensitivity of the FTM detector with kapton 125 μm as a function of the number of internal stages.

kapton 125 μm prototype is shown as a function of the number of internal stages.

The development of a prototype based on this material, which seems to be promising in the context of the R&D for the CMS application, is going to start in the next weeks and has not been pursued yet due to a delay in the material procurement.

FTM with PCB 200 μm Due to the unavailability of kapton 125μm, a temporary solution was the substitution of the kapton 50μm with a PCB layer, 200μm thick. The geometry of this new prototype is shown in Fig.5.74

The active area here is made of a PCB 200 μm thick, covered by resistive layer on top initially obtained with standard serigraphy for a surface resistivity of the order of 10 M$\Omega/\square$. The cylindrical holes are obtained with a standard drilling technique, also used for the mesh of Micromegas detectors, and have a diameter of 200 μm and a pitch of 500 μm (limit imposed by the machine that performs the drilling). On the bottom of this first PCB, there is another PCB layer, 200 μm thick, covered with the same resistive layer on top and bottom. It actually closes the active region of one layer and acts as a drift plane for the following one. The two PCB foils as they have been implemented in the prototype are shown in Fig.5.75.

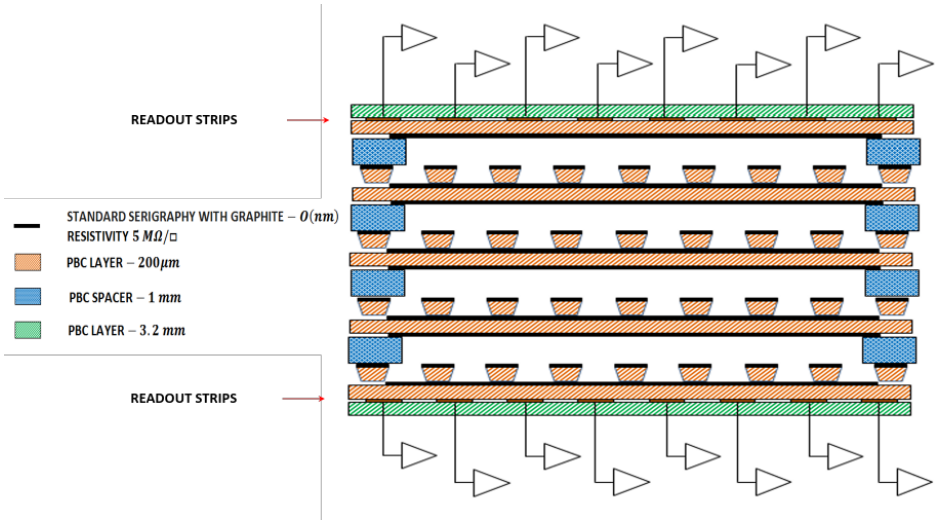

Figure 5.74: Transversal view of the FTM prototype with PCB structure.

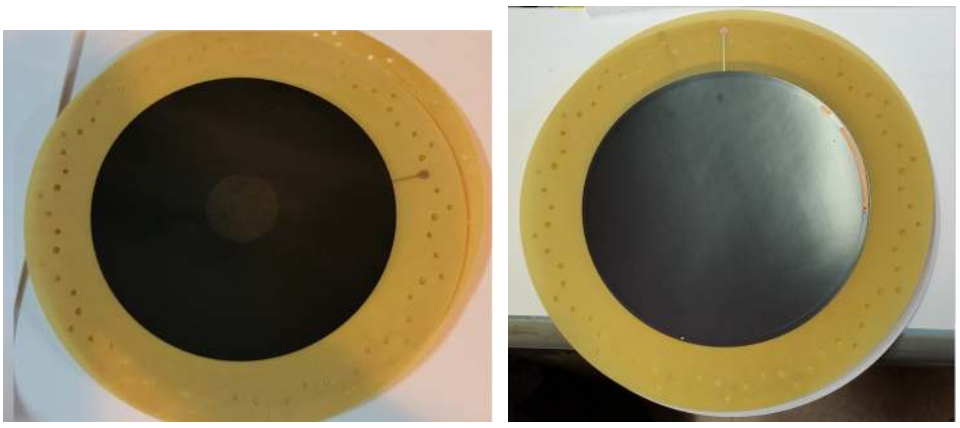

Figure 5.75: Pictures of PCB foils with holes (on the left) and full (on the right) taken during the assembly.

The drift region are initially 1 mm-thick and are obtained with the use of a PCB spacer shown in Fig.5.76: the cross in the middle of the spacer has been added in order to ensure the planarity of the gaps.

The structure is completed by two readout boards, one on the top, the other on the bottom. Each of the board is equipped with 200 strips, in X direction on the top and Y on the bottom, for a total coverage of 10 x 10 cm^2. The active area of the detector however is only $\sim$ 12 cm^2 due to limitation of the machine that makes the drilling.

As shown in Fig.5.77, the structure, initially designed for the 125 μm prototype and then readapted to the new configuration, was developed in order to be modular: the foils are inserted one on top of the other in order to create

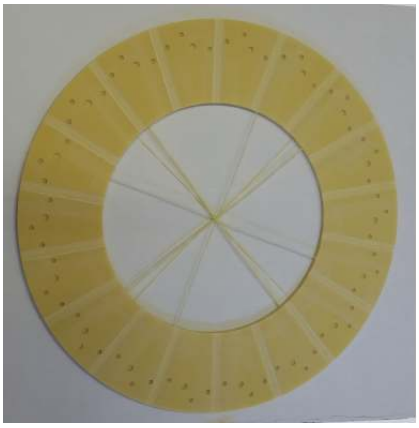

Figure 5.76: Spacer used to create the drift gaps. The planarity is ensured by the cross in the middle of the spacer.

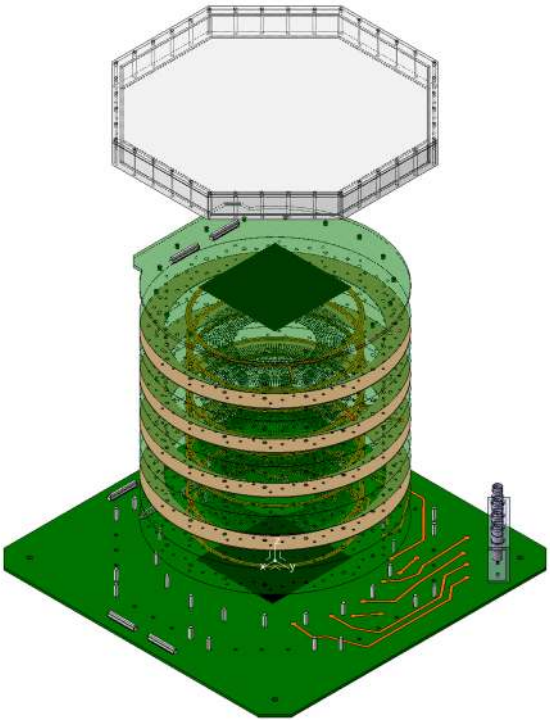

Figure 5.77: Modular structure of the FTM prototype in PCB.

many internal layers. The actual structure is able to host up to twelve layers, with variable drift gap thickness, but the first test were performed with only four.

Once assembled, the prototype was tested in laboratory with different gas mixtures, Ar/CO_2 70%/30%, Ar/CO_2 98%/2%, $Ar/CO_2/CF_4$ 45%/15%/40% and also pure Neon, selected because it can create a huge amount of charge at very low applied field so it could be useful the test the performance of

the detector without stressing it. With all these mixtures we observed two phenomena: first of all, we were not able to reach the expected voltages. Indeed considering for the example the Ar/CO_2 mixture, from the Paschen curve with 200 μm thick foil the breakdown voltage is $\sim$ 1000 V. Assuming to be in the same condition of the kapton prototype, we should be able to reach a potential difference of $\sim$ 1300 V. We observed instead that the maximum voltage we were able to reach was actually slightly lower than 1000 V, exactly in correspondence of the Paschen limit. It seems that the ability to overcome this limit that we had with the kapton prototype here is not valid anymore. Similar considerations can be applied also for the other mixtures tested. Moreover, pushing the detector at its limits, we were able to observe the signals, but not in a continuous way. In fact we were able to see signals from the source for few seconds, then the signals disappeared and we had to wait a long time (up to half an hour) before being able to see them again. Another behavior observed was that the signals were present using a low intensity source, but when we tried to increase the incident flux, the rate of signal detected was decreasing up to disappear completely at the maximum source intensities.

Finally, the operation of the detector was characterized, in all the conditions tried, by the presence of a quite high rate (from tens of Hz to kHz) of huge signals, evident also without the source, that could be connected to the development of discharges inside the detector.

The observations performed drove us to the hypothesis that the problems were related to geometrical imperfection of the prototype, as well as defects in the resistive layers.

First of all, the two PCB foils that make the active area are not glued together, but are only placed one on top of the other. If the stack of foils is not well pushed the consequence is that when the voltage is applied, the two PCB foils are initially stacked together due to the electrostatic force. When a particle interacts and the avalanche is created, the field in the active area is reduced by the presence of charge inside the holes, as well as the attraction between the two foils: they therefore start to separate and then to oscillate between the *stacked* position and the *not-stacked* position. This could be the explanation of the fact that the detector doesn't work in a continuative way and that frequent discharges generate inside it.

Moreover, test on available spare foils demonstrate that the resistivity value in the area in which the holes are drilled is not correct. The production of these

foils follows these steps: the PCB layer is fabricated and coated with graphite, then the holes are drilled. The graphite is deposited before making the drilling in order to be sure that it doesn't fill also the holes. At the end the foil is cleaned with a standard procedure used for PCB in order to remove all the leftover of the drilling. A picture taken during the cleaning procedure of the FTM foils is shown in Fig.5.78.

Figure 5.78: Cleaning of the FTM PCB foils: the foil is washed with water and a industrial soap, scrubbed with a brush and then rinsed.

The standard cleaning procedure used was observed to scratch the graphite deposition, damaging it, with a consequence increase of the resistivity in the holes region of at least one order of magnitude. This effect is shown in Fig.5.79 left, where the clearer region, almost white, highlights the damage of the resistive coating. In addition, once the detector was open to substitute these damaged foils, also defects on the resistive layer of the full-PCB foils were observed: in Fig.5.79 right, a sort of corona drawing the negative of the region with holes on the full foil is pointed out, probably due to discharges developed in the active region.

New foils were produced, both those with holes and the full PCBs, exchanging the graphite coating with resistive kapton DUPONT XC, like the one used for the first FTM version, glued on the PCB foils. The detector has been re-assembled, adding also a further PCB on top of the stack, to push it and reduce as much as possible the oscillation effect described above. Unfortu-

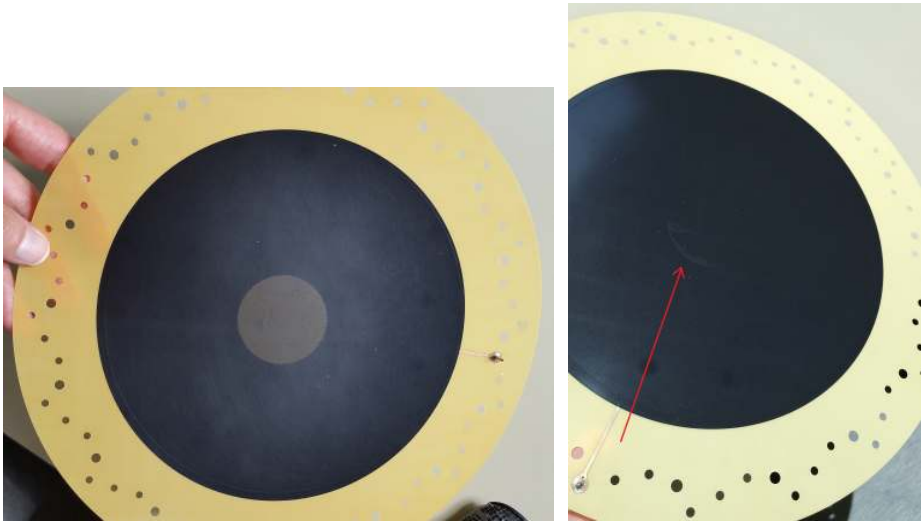

Figure 5.79: Damages of the FTM PCB foil. Left: the clearer region is due to the damaged produced by the cleaning process in the PCB foil with holes. Right: the pointed out corona represents the damage induced on the full PCB foils by discharges in the active region.

nately, these intervention did not lead to a net improvement of the performance of the prototype, that right now still presents unstable behavior and frequent discharge problems.

Due to the differences between this PCB prototype and the first working FTM version, it is difficult to find the real weak point that causes all the problems observed, other than the compactness of the stack and the resistivity of the foils. Between the many hypothesis developed, two have not been completely analyzed so far but are relevant for the discussion:

- ***The diameter and pitch of the holes***: the geometry of the holes was selected on the basis of the availability of the machine that was performing the drilling. It is generally used to make bigger holes in bigger and thicker PCB foils, while here we used it to make holes of 200 μm diameter and 400 μm pitch. This can induce two problems, the first on the detector side, the second on the machine side. On the detector side, the geometry of the holes is not optimized, thing that, as already explained in Section 2.4.2, can deeply influence the gain reachable by the structure. On the machine side, as we are operating it at its extreme limits, imperfections and disuniformity of the drilling can be very likely.
- ***Holes RIMs***: this prototype is actually a THGEM, with a thickness of the active region slightly tinner than the standard used. As discussed

in Section 2.4.3.2, the stable operation of the THGEM is assured only with the presence of RIM made on the borders of the holes, as they allow the application of higher voltages without discharges. In this prototype, there are no RIMs around the holes, because it was supposed that the presence of the resistive layer could be enough to quench possible discharges.

Even if the prototype didn't reach the desired performance, also in this case an evaluation of its sensitivity to the CMS muon system background was performed.

Layer Name	Composition	Depth
Drift Board	FR4Support1 DriftCopper FR4Support2 DLC1	3.2 mm 35 um 200 um 2 nm
Drift Gap1	**GasGap1**	**1 mm**
Layer 1	**DLC2** **FR4Support3** **DLC3** **FR4Support4** **DLC4**	**2 nm** **200 um** **2 nm** **200 um** **2nm**
…	…	…
Drift Gap*N*	GasGap2	1 mm
Layer *N*	DLC5 FR4Support5 DLC6 FR4Support6	2 nm 200 um 2 nm 200 um
Readout Board	ReadCopper FR4Support7	35 um 3.2 mm

Figure 5.80: Geometry of the FTM detector simulated with Geant4, with PCB structure.

The geometry simulated is shown in Fig.5.80. Also here, the structure is modular, and the introduction of a new stage correspond to the introduction of a structure *Drift Gap# + Layer#*, where *Drift Gap#* is again the active gap, 1 mm thick, while *Layer#* here correspond to a PCB (FR4Support) covered on top with a resistive coating that can be DLC or Graphite, but always simulated as carbon, plus another PCB covered on both side by resistive coating.

The results are shown in Fig.5.81 for a prototype ME0 size, covered by a GE1/1-like aluminum shielding and instrumented with a GE1/1-like cooling system.

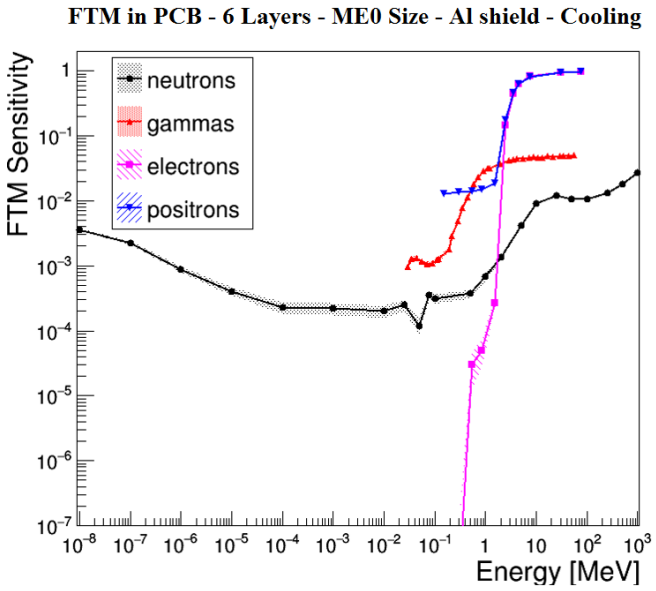

Figure 5.81: Results of the sensitivity simulation of FTM detector performed with Geant4, with PCB 200 μm

FTM	Neutrons	Gammas	Electrons	Positrons
10 x 10	$(9.04 \pm 2.73) \times 10^{-4}$	$(1.38 \pm 0.03) \times 10^{-2}$	0.205 ± 0.048	0.213 ± 0.048
ME0 Nude	$(1.44 \pm 0.43) \times 10^{-3}$	$(1.83 \pm 0.04) \times 10^{-2}$	0.219 ± 0.051	0.233 ± 0.051
With Al shielding	$(1.72 \pm 0.51) \times 10^{-3}$	$(1.89 \pm 0.04) \times 10^{-2}$	0.169 ± 0.042	0.183 ± 0.043
With Al shielding and cooling	$(2.04 \pm 0.61) \times 10^{-3}$	$(1.83 \pm 0.04) \times 10^{-2}$	0.158 ± 0.040	0.172 ± 0.040

Table 5.5: PCB-FTM sensitivity results averaged over the particle energy distribution.

Table 5.5 summarizes the values of the sensitivities, averaged over the energy spectra, for a 10 x 10 cm^2, a nude ME0-size prototype and with the insertion of the aluminum shielding and of the cooling system. The behavior is the same already described above for the other prototypes. Also here we can notice an increase of sensitivities related to the increase of the dimensions of the detector, as observed above for the FTM prototype in kapton.

Moreover, an analysis of the processes involved shows that for neutrons (see Fig.5.82) there is not a remarkable difference between the prototype in kapton and the one in PCB, just a small enhancement of ionization and energy loss by charged hadrons (*hIons*) produced by the neutron inelastic scattering at the higher energy value in the PCB version with respect to the kapton one.

Also in the case of gammas, in Fig.5.83, the behavior in the two geome-

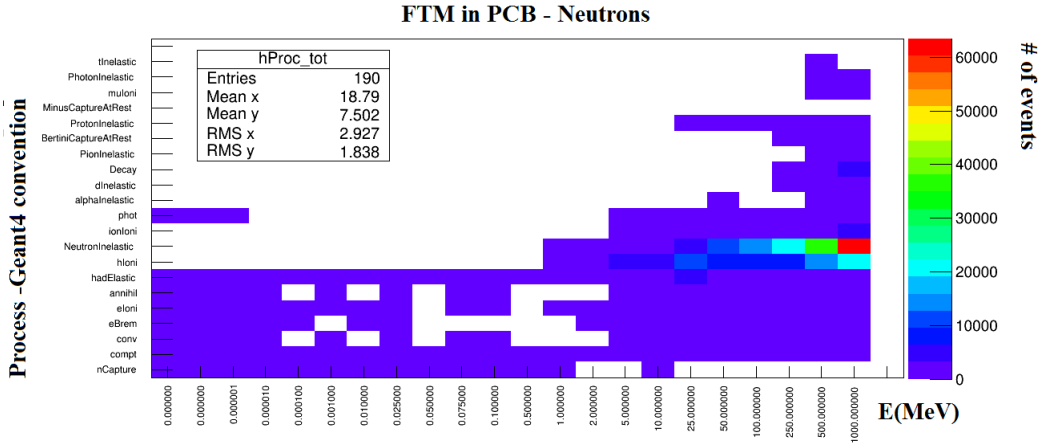

Figure 5.82: Processes induced by neutrons in the FTM detector in the PCB version

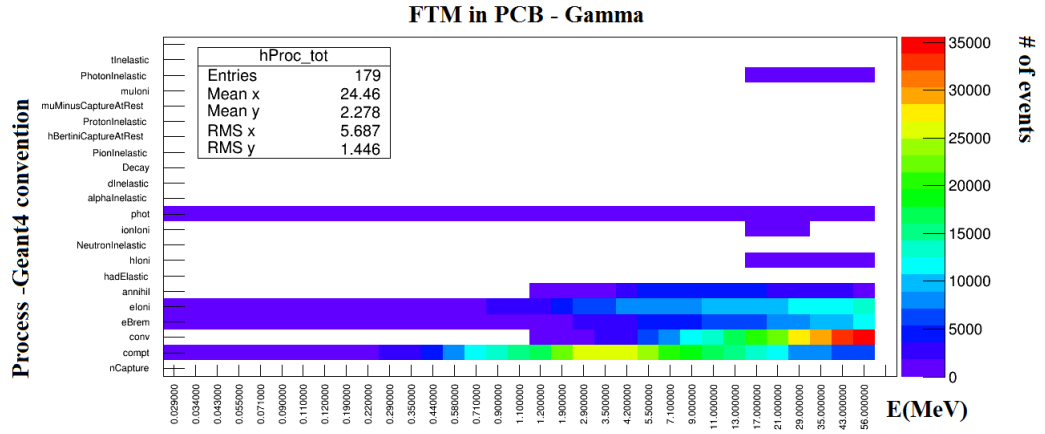

Figure 5.83: Processes induced by neutrons in the FTM detector in the PCB version

tries is similar, the only difference is a small enhancement of ionization and bremsstrahlung by light charged particle in the high energy region of the PCB prototype with respect to the kapton one.

These observations confirm and support also the similarity between the sensitivities obtained with the two geometries.

5.2.2.7 Study of gamma conversion probability and comparison between different technologies

A study of the gamma conversion probability in different thicknesses of kapton and PCB have been performed, in order to better understand the role of these

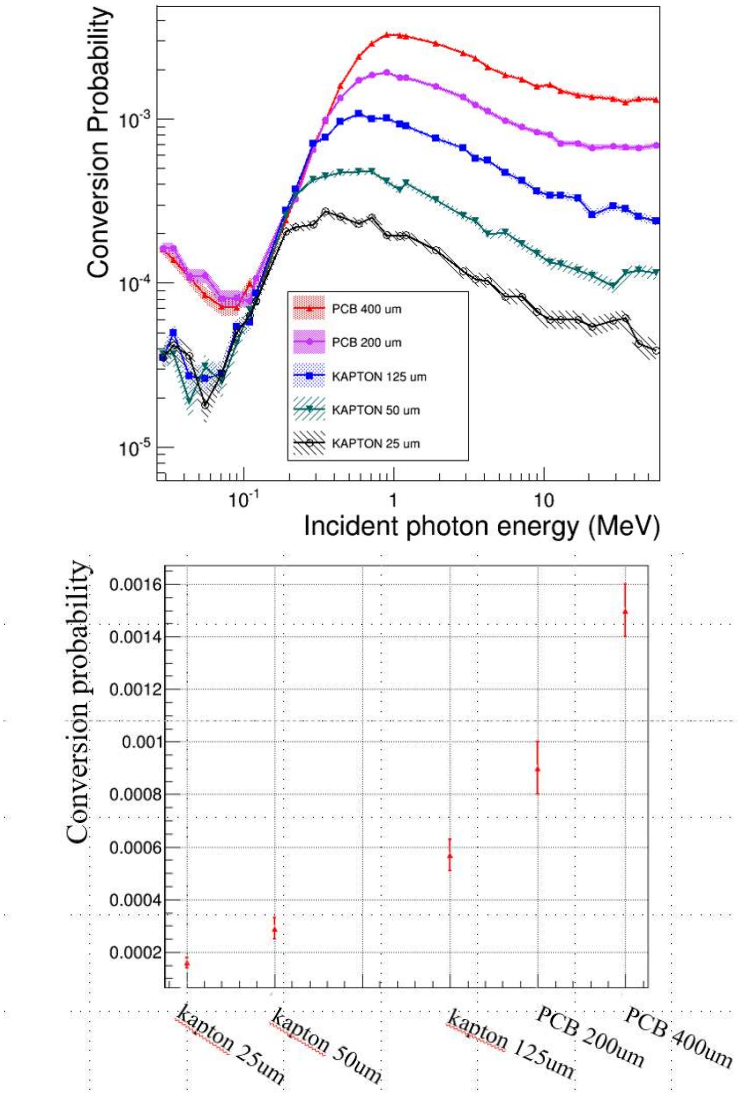

Figure 5.84: Gamma conversion probability in different thicknesses of kapton and PCB. Top: as function of the incident gamma energy. Bottom: convoluted with the GE1/1 spectrum.

materials in the production of charged particles inside the detectors. Fig.5.84 top shows the gamma conversion probability for different thicknesses of the materials as a function of the energy on the incident photon. In the bottom plot instead the conversion probability is averaged over the GE1/1 gamma energy spectrum. As expected, the conversion probability increases with the increase of the thickness of the layer, as in this way we are actually giving more space to the photon to interact. However, up to 400 μm PCB there is no sign of saturation of the probability.

The results obtained with this simulation confirm the hypothesis that the

increase of sensitivity with the insertion of new layers in the detector described above is due to the increase of the total material budget inside of it.

It is worth at this point making a comparison between the sensitivities obtained with the different technologies considered, i.e. Triple GEM, μRWELL and FTM.

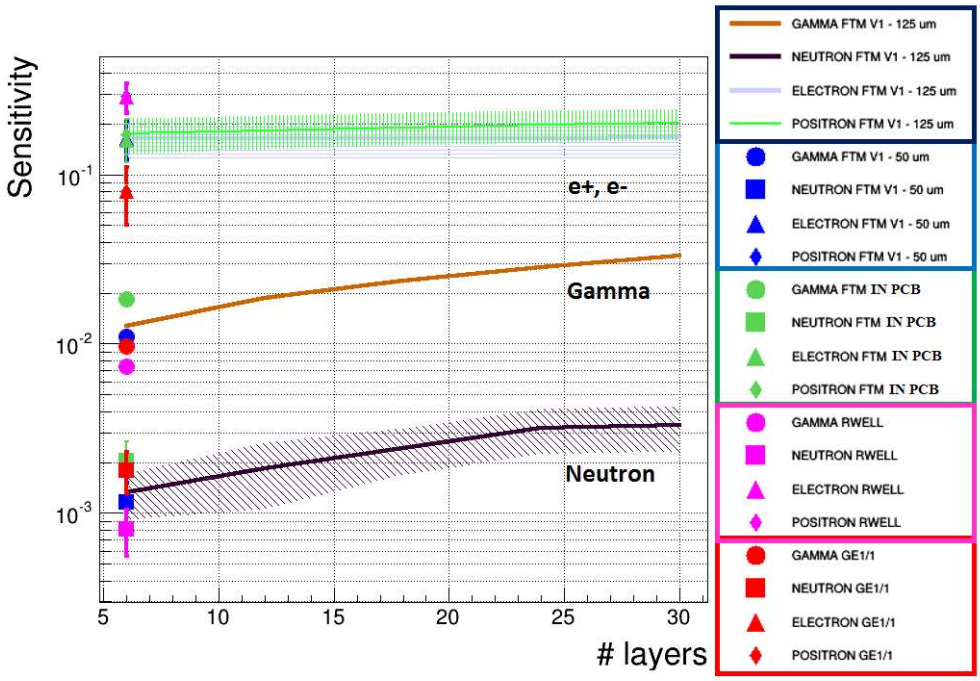

Figure 5.85: Comparison of sensitivities simulated with different technologies.

Fig.5.85 shows the sensitivities as a function of the number of layers for the FTM with kapton 125 μm (continuous lines), for the FTM with kapton 50 μm with six internal stages in blue, for the FTM with PCB with six internal stages in green, the μRWELL in pink and the Triple GEM in red. μRWELL and GEM has been placed in correspondence of the six layers just to facilitate the comparison, but actually they have their own structure described in the related sections.

First of all, it can be noticed that the sensitivities for the different technologies are all comparable, at least at the order of magnitude level: this is due to the fact that the materials and the thicknesses involved are really similar between one prototype and the others.

Slight differences can be found in particular for electrons and positrons sensitivities: the FTM sensitivity to electrons and positrons is almost double

than with Triple GEM: the main difference between a Triple GEM detector and the FTM detector is that in a Triple GEM only the first two gaps are considered as active in this simulation. In fact it is assumed that if a charge particle is produced in the *drift* gap or in the *transfer1* gap of a Triple GEM, then the gain of the detector is able to amplify it and create a visible signal. If the charge particle is produced in the *transfer2* or in the *induction* gaps, it is assumed that the gain of the detector is not anymore enough to produce a visible signal. So actually if in the simulation, the incident particle produces a charged particle in the *transfer2* or in the *induction* gap, this event is not considered as a good event and is not considered in the calculation of the sensitivity. On the contrary, all the gaps of the FTM detector are *drift* gaps, because all the stages are independent, and so they are all active. As for the simulation we are using a angular distribution that foresees particles arriving from every direction, including the back and the front of the chamber, this effect is not negligible at all: in fact an electron arriving at the back of a Triple GEM in order to produce a signal considered valid in our simulation, should create a charged particle that passes through the readout board, the *induction* gap, the third GEM foil, the *transfer2* gap and the second GEM foil without being absorbed, in order to be counted as good event. In the FTM instead it should only pass through the readout board and it would arrive immediately in an active gap in which it would be counted as good event. It is clear that the probability of the two situation is really different and can explain the difference in electrons and positrons sensitivity between the two technologies.

The μRWELL sensitivity to electrons and positrons is higher than FTM and Triple-GEM one: in this case, the consideration done in the previous point is still valid, but in addition we have to consider also the thickness of the materials used. For both Triple-GEM and FTM the drift and readout boards are prevalently composed by PCB, 3.2 mm thick. Also in the μRWELL the base material is PCB, but just 1 mm thick: the consequence is that the probability for electrons and positrons to be absorbed in the external layers of the chamber is lower in the μRWELL detector than in the other technologies and as a consequences, the sensitivity is higher.

5.2.2.8 Dedicated electronics for the new fast timing prototypes

One of the greatest concerns related to the implementation of this new technology is the readout electronics. So far, only analog readout chains were

used: in the first one the preamplification and amplification stages were performed by an ORTEC 142PC preamplifier and an ORTEC 474 amplifier. This configuration provided a very good noise filtering, giving us the possibility to characterize the prototype under the point of view of the uniformity and efficiency. However it is a very slow electronics chain, the signals formed have rising times of the order of 1-10 μs, which of course don't allow the exploitation of the timing performance of the detector. Better results were obtained on this side using a linear electronics chain, composed by a CIVIDEC broadband amplifier followed by a linear amplifier. This chain allowed the measurement of the $\sim$ 1.7 ns time resolution of the first prototype, but it is not adapt for any other test. Indeed, as it is made of two linear elements, it doesn't do any kind of noise filtering, with a consequent drastic reduction of the signal over noise ratio (S/N). The efficiency value for example is deeply affected by this phenomenon, as the low S/N forces the setting of very high thresholds, with the risk of cutting also good events together with the noise. This is actually what happened during the 2015 test beam, when the efficiency measurements were forgone in favor of the analysis of the timing performance.

Moreover, all these electronic chains are actually able to handle only one channel, i.e. with a detector which has just one readout pad or in which is possible to make the OR of the readout strips. This is a configuration which can be accepted for some preliminary test in laboratory, but for example it does not allow the space resolution measurement, as well as the cluster size. If we consider then the installation in CMS, the independent readout of each strip is mandatory for the achievement of the desired performance.

Actually in the framework of the CMS GEM Collaboration, an integrated chip able to reach the time performance expected from the FTM prototypes is not available. Indeed the APV [117], the VFAT_V2 [99] and even the newest VFAT_V3 [29], created on purpose for the GE1/1 station, were developed to be used with classical MPGD, able to reach time resolutions of the order of $\sim$ 4-5 ns. This is what we observe for example with the simulation of VFAT_V3 chip in Fig.5.86, where the time resolution obtained from the detector readout with the VFAT_V3 chip is plotted as a function of the peaking time of the signal.

This results are obtained simulating the signal from the Triple-GEM detector with GARFIELD [119] and then convolving it with the expected transfer function of the front-end amplifier of VFAT_V3 chip. The two curves foresee

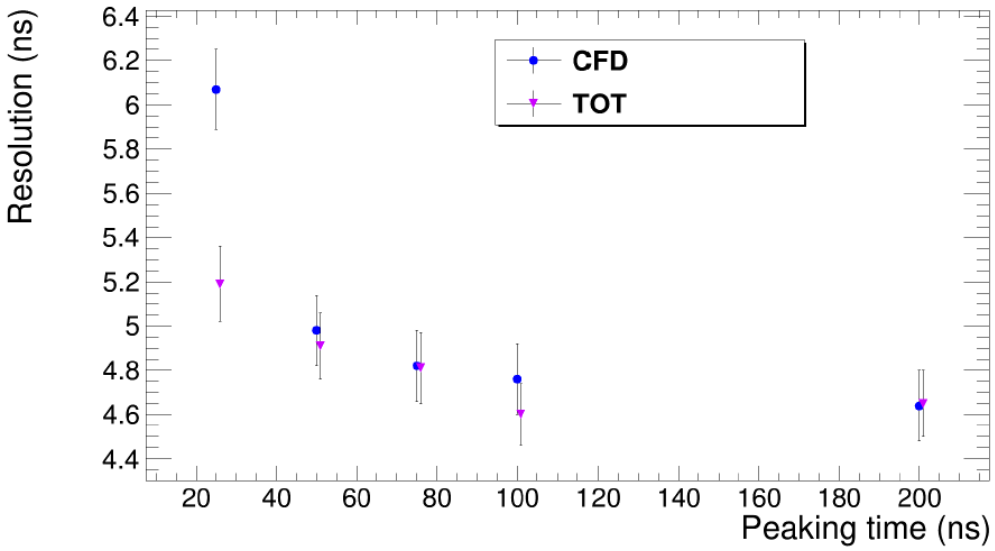

Figure 5.86: Time resolution as a function of the peaking time obtained with a GARFIELD [119] simulation of a GEM read out with the VFAT_V3 chip [118].

the implementation of a constant fraction discriminator (in blue) or of a Time Over Threshold (TOT) discriminator (in purple) in the VFAT design [118].

For this reason the solution has to be found in a chip developed for another group or Collaboration or, if it is not possible, a new chip must be developed on-purpose.

Among the available solutions, the Skiroc chip [120], developed by Omega micro [121], seems to be promising. It is a 64-channel front-end chip, in which each channel is composed by a variable-gain low-noise charge preamplifier followed by a dual shaper, to filter the charge measurement and a trigger chain composed of a high gain fast shaper and a discriminator. The charge can be then read in an analog way or sent into an ADC. The thesholds instead are set with a 10-bit DAC for trigger level and for automatic gain selection level. In total, the gain of the chip is in the range 0.15 mV/fC - 23.4 mV/fC, with an equivalent noise charge (ENC) of 1500 e- with 20pF detector capacitance at mid-gain [120]. The chip can be used for charge or timing measurement, with a reachable time resolution of the order of 500 ps. This value is a great improvement with respect to the solutions considered above. However the chip, which is currently available in two configuration, one in particular developed for CMS HGCal, would have to be re-adapted for the FTM application, for example optimizing the input capacitance to match with the one of the FTM

readout strips or reducing the noise level in order to see the signal from the FTM also when it is working at low gain.

On the other side, also the possibility to develop a new chip, optimized for working with the FTM is being considered too. A first version of a new chip, whose single-channel block diagram is shown in Fig.5.87, is being designed by the INFN-Bari group: the main component, which determines the characteristics of the signal, is a charge sensitive preamplifier. It is developed with the technology TSMC CMOS 130nm and characterized by a charge sensitivity of 54 mV/fC, higher than what can be reached with the Skiroc solution. This property, together with the low ENC value of 187 e- + 16.5 e-/pF, which turns into ENC = 430 e- at the FTM expected capacitance of 15 pF, will allow the detection and amplification of small signals coming from the FTM, element fundamental to reach a higher efficiency with the detector. The minimum time jitter that can be obtained with this preamplifier is of the order of $\sim$ 250 ps.

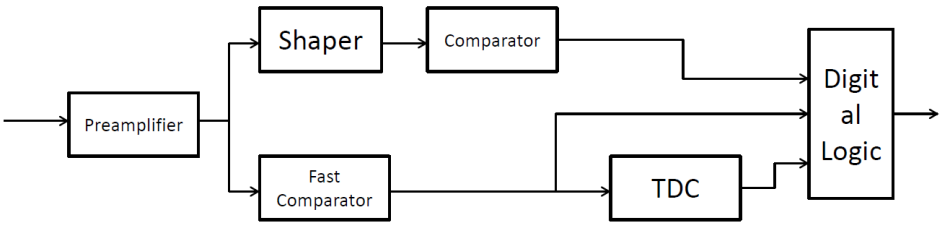

Figure 5.87: Single-channel block diagram of the new chip that is going to be designed for the FTM readout.

After the preamplifier, the diagram foresees two paths: on one side, the signal goes to a shaper and then a comparator and finally is transmitted to the digital logic for the readout. Moreover, the fast timing information, is processed by the other path, where the signal is elaborated by a fast comparator, then goes into a TDC and finally to the digital logic.

The finalization of the schematics for the preamplifier is expected for the end of September 2016, while the shaper and comparators will be completed in October 2016. The final layout of the channels and of the TDC is foreseen for November 2016, in order to start the production of the first prototypes by the end on the year. This would allow a test of the detector with the new electronic chain during the test beams that will be organized in 2017.

5.2.3 Choice of the technology for the ME0 station

The choice of the technology is expected to be for the ME0 station in 2020. The key point of the discussion in this case is represented by the time resolution: if no strict limitations will be posed to the time resolution and only the BX identification will be requested (i.e. time resolution needed is 8 ns), Triple-GEM detectors would be the favored candidate. Indeed, even if so far the first Stacked-GEM prototypes has given results only concerning the time resolution, the Triple-GEM technology is very mature and have proven, during the GE1/1 R&D, to reach all the requested performance. Only an integration of the ageing tests should be planned, in order to fully qualify the behavior of the chamber in the ME0 environment. In this case even the mechanical problem is partially solved, because the ME0 chambers would be smaller than GE1/1, then no stretching problems are expected. The only point that remains open is the possibility to stack six chambers in the space available for ME0, but studies are on-going right now in order to reduce that space occupied by the services and the shielding. However, if the request on the timing will become more stringent, up to 1 ns or lower, the Triple-GEM technology would be discarded immediately, because it is not realistic to reach these time resolutions with this kind of detector. The FTM detector would became the only feasible solution in that case, but before it has to prove to be able to reach almost all the requested performance: the efficiency was not satisfying in the first prototype and must be improved, the space resolution as well as the rate capability have not been measured yet. Moreover, its performance in a radiation environment has not been studied yet and the feasibility of the construction of large size prototypes has not been tested. For the FTM solution, also the necessity of the development of a new dedicated electronics is not negligible. This activity generally demands for a great commitment of manpower and funding, which can play a key role in the development of a project. On this item, Triple-GEM technology would again use the VFAT chip, already developed for GE1/1, which would ask in the worst case for only small improvements.

To conclude, from the technological point of view, Triple-GEM detectors are the favorite choice also for the ME0 station. However the final decision here will strongly depend also on the requests that will come from the neutron background and pile-up rejection. If the detector for the ME0 station will definitively need to have a time resolution better than 1 ns, then the choice

will be necessarily the FTM. Also in this case, however, the implementation of this technology will be possible only if the next prototypes will prove to reach the requested performance in efficiency, space resolution, radiation hardness as well as from the mechanical point of view.

Chapter 6

Conclusions and future perspectives

The upgrade of the CMS muon system foresees the installation of new stations, in the high η region, instrumented with Micropattern Gaseous Detectors.

The first MPGD station, called GE1/1, will be instrumented with Triple-GEM chambers and its installation is approved by the CMS Collaboration for the LS2. In the meantime, few chambers will be installed in the YETS 2016-2017 in order to gain operational experience with the new system. The preparation of GE1/1 chambers for the Slice Test is actually on-going: all the chambers were assembled and they are right now undergoing the sequence of quality control tests aimed at certify their operation. The Collaboration is taking advantage of this opportunity in order to inspect the quality control chain and to train the staff that will be responsible of the assembly and test of all the chambers of the GE1/1 station. The production of the foils for the full station, as well as the other material procurement, is on-going right now, while the assembly of the detectors is planned to start at the beginning of 2017.

The basic structure of the Detector Control System of the GE1/1, which will allow the remote control of all the station once installed in CMS, is finalized, even if it still needs to be fully tested before the integration in the general CMS DCS. In particular, concerning the gas system panel, a discussion is on-going with the CERN gas group [76] in order to prepare a test setup, similar to the one that will be installed in CMS, to be used for a complete qualification of the DCS gas panel. One possibility that is going to be considered is to use directly the final hardware of the station, already installed in CMS and right

now not used.

The operation of the Triple-GEM chambers has been completely qualified in a gamma environment at the GIF and GIF++ facilities. Concerning the neutron background instead, the Louvain-la-Neuve test did not give a final result concerning the sensitivity, but a first estimation of the accumulated charge confirms that it was long enough to qualify the behavior of the detector in neutron field up to an integrated charge of 0.27 mC/cm^2. So far, the Collaboration did not develop a test dedicated to the measurement of neutron-induced discharge probability with a GE1/1 Triple-GEM prototype. Indeed the only discharge probability test was performed with heavily ionizing α particles on a 10×10 cm^2 prototype, from which a discharge probability of 10^{-10} was estimated, at an operational gain of the chamber of 1-2 $\times$ 10^4. In the GE1/1 conditions this value was considered to be not dangerous for the detector operation, as it was not introducing a gain degradation, but only an increase of the dead time up to several millisecond [87]. During the LHCC Comprehensive Review which was held in June 2016, the Collaboration was asked to deepen this aspect, as the effect due to discharges induced by neutrons of the muon system background could deeply affect the performance of the detectors. The importance of this test substantially increases if we consider the possible application of Triple-GEM technology also for the ME0 station: indeed this region is characterized by a more intense flux of neutrons, and as a consequence by a higher expected hit rate, with respect to GE1/1 of a factor $\sim$ 20 in the worst position, from the last FLUKA simulations. Even considering that the surface of the single ME0 chamber is $\sim$ 70% of GE1/1, this implies an increase of the discharge rate of a factor $\sim$ 14 for a given discharge probability of the Triple-GEM technology. As discussed in Section 2.4.2.3, the discharge probability results obtained with different GEM geometries vary also by orders of magnitude, then extrapolating a reliable value for the GE1/1 configuration is not straightforward. For this reason, a first test with a GE1/1 Triple-GEM prototype has been proposed for the end of 2016, at the CHARM facility [122] at CERN, which will allow also to give a reliable estimate of the expected discharge rate in the ME0 station, parameter fundamental to understand if Triple-GEM technology will survive in that region.

In general, we can affirm that the GE1/1 project is at a good stage of its development: the R&D on the detectors is finished with excellent performance obtained, the assembly and quality control procedures have been defined and

are being tested right now with the production of the Slice Test detectors. The production of the Triple-GEMs for the full station will start soon and will lead to the implementation of the GE1/1 station in LS2.

Concerning the other two stations, GE2/1 and ME0, the Collaboration is evaluating two technological solutions for their instrumentation. In both cases the baseline choice is Triple-GEM detector, with a configuration similar to GE1/1. The R&D performed for the GE1/1 station already proved that this technology is able to satisfy the requests for both the stations and the discharge probability study foreseen in the next months will clarify the uncertainties related to the discharge rate in the ME0 environment, as already explained above. A complementary ageing study moreover should be developed for the ME0 case, in order to qualify the Triple-GEM technology up to the expected charge foreseen in that region. The only limit, that could prevent Triple-GEM to be installed in the ME0 station, is the time resolution, that with the first Stacked-GEM ME0 prototype did not go better than 10 ns with the green-house-free Ar/CO_2 70%/30% gas mixture (7 ns with $Ar/CO_2/CF_4$ 45%/15%/40%). Assuming to be able to reach the GE1/1 time resolution, of the order of 7-8 ns with Ar/CO_2 at very high gain, it will be enough for the bunch crossing assignment, but not for the pileup and background rejection with the use of the timing information. If this element will be considered fundamental in the ME0 framework, Triple-GEM technology could not be considered anymore a viable solution for this station. If instead the timing information will not be included, the R&D to be performed with the Triple-GEM technology is just of mechanical nature, making this technology in deep advantage with respect to any other solution for the ME0 station. The problem is already only on the mechanical side for the GE2/1 station, even if here the situation is complicated by the size of the chambers, that would be the largest ever built with this technology.

The optional solutions, μRWELL for GE2/1 and FTM for ME0, are both considered to be right now at a real early stage of their R&D. First of all, both of them still have to prove their performance on large size prototypes, basic element in order to verify the feasibility of their installation in the CMS muon system. μRWELL already demonstrated to reach all the requested performance, except for time resolution which still has to be measured, with small size prototype. Moreover they are advantaged with respect to Triple-GEM prototypes thanks to the ease of their assembly procedure. On the other side,

the fact that the GE2/1 installation has been anticipated to the YETS 2022-2023 force them to rush in the last part of the R&D, i.e. the development of GE1/1-size firstly and then GE2/1-size prototypes.

The time scale for the FTM detector is a bit longer, as the installation of the ME0 station is foreseen for LS3. However, this technology is at a very early stage of its R&D, as the first prototype only gave encouraging results on the time resolution side. Moreover the prototypes developed so far were not able to reach the requested efficiency and gain; the spatial resolution as well as the rate capability, the discharge probability and the resistance to radiation have not been proved yet. Great expectations come from the next prototype, to be build in September 2016 with Kapton 125 μm base material and with resistive layers made in DLC. If this prototype, still small size, will be able to reach higher gains and efficiency, allowing a full characterization both in laboratory and beam, then it will be possible to move to larger size prototype by the end of 2016. Moreover it will be possible to continue the R&D program, which foresees test beams and irradiation tests with neutrons and gamma, as well as the development of a dedicated electronics with enhanced timing properties. If also this prototype will not match the requested performance, it will call into questions the whole FTM project and the feasibility of its inclusion in the CMS R&D program.

The entire Phase II upgrade program is asked to provide concrete results by the first half of 2017, when a Technical Design Report will have to be released by the Collaboration. Moreover, the technological choices, for the GE2/1 and ME0 stations will have to be taken by 2018 and 2020 respectively, in order to allow the planning and implementation of the production of the chambers for each station.

Appendix A

Tensile properties of kapton and GEM foils

During the test performed in Louvain few kapton and GEM foils were irradiated parasitically, with the aim of studying their material properties after the irradiation. Indeed, the GE1/1 assembly technique foresees the possibility to position and re-position the GEM foils multiple times, in order to replace a damaged foil or repair eventual problems. As this of course implies several stretching and loosening cycles, a characterization of tensile properties, like the stress-strain relationship, is fundamental in order to determine the elastic limit which should not be exceeded in order not to produce deformation of the holes. Moreover, the exposure to high radiation fluxes could induce complex phenomena, able to alter the molecular structure of the material and, as a consequence, its elastic properties.

The two quantities measured in the test, and from which the properties of the material were deduced, are indeed the *stress* and the *strain*: let's consider for example a bar, of cross section S, which is subjected to equal and opposite forces F pulling at the ends of the bar. The material is subjected to a *stress*, defined as

$$stress = \frac{F}{S} \tag{A.1}$$

and named also *tensile stress* as every part of the object is subjected to the tension. It is measured in *pascal*, where 1 Pa = 1 N/m^2 [124].

If instead the force is applied tangentially to the object, the ratio between

the force and the cross section S is called *shear stress*. If the object is then twisted on an angle θ, the shear strain is defined as

$$strain = tan\theta \text{ [124]} \tag{A.2}$$

and gives an indication of the deformation of the material. The *elastic modulus* or *Young's modulus* finally measures the resistance of an object to a force which works to deform it elastically. It is defined as the slope of the *stress-strain* curve [124]. Generally, a *stress-strain* curve shows different regions, reflecting different properties of the material: the *elastic region* is the region in which the material returns to its initial undeformed state when the forces are removed; on the opposite the *plastic region* is the region in which the material deforms definitively.

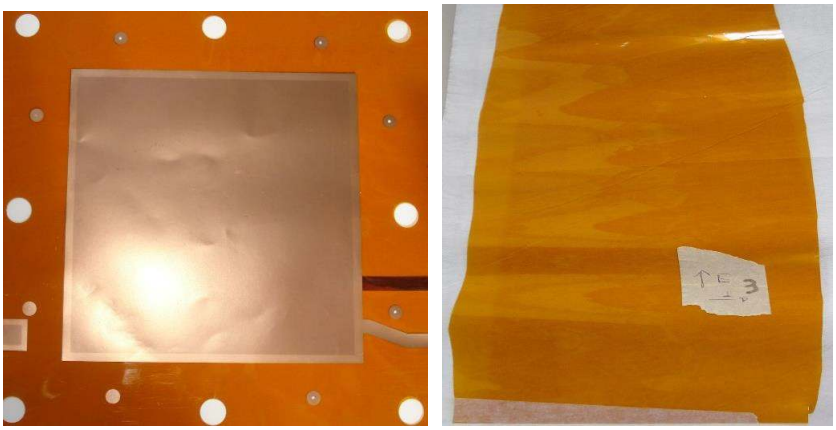

Figure A.1: Pictures of the irradiated samples. Left: 10×10 cm^2 GEM foil; right: Kapton foil.

The study was performed comparing the properties of not-irradiated samples with samples exposed to neutrons and gamma radiations. Neutron-irradiated samples, shown in Fig.A.1, were indeed positioned in the Louvain facility, behind the Triple-GEM detector along the beam line as illustrated in Fig.A.2.

The dose absorbed by kapton and GEM were 0.966 Gy and 4.82 Gy respectively [123].

A third set of samples was irradiated with gamma rays at the CERN Gamma Irradiation Facility (GIF), with a total integrated dose of 0.52 Gy, equivalent to 4 CMS years.

The test was performed in the laboratories of the University of Rome "La Sapienza", where a dedicated setup, described in [123] was developed. The

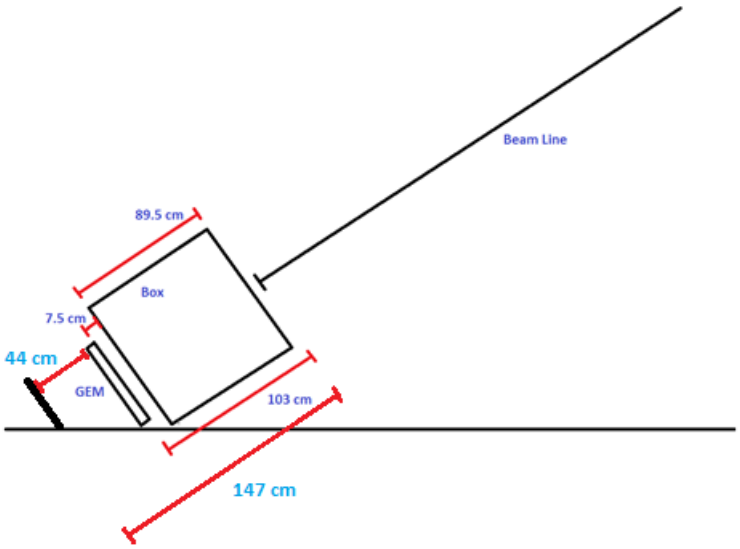

Figure A.2: Position of the irradiated samples in the Louvain facility.

samples were tested with an INSTRON single column vertical testing system [125], while the holes diameter and their changes during stretching were measured with a Keyence VHX-1000 Digital Microscope [126].

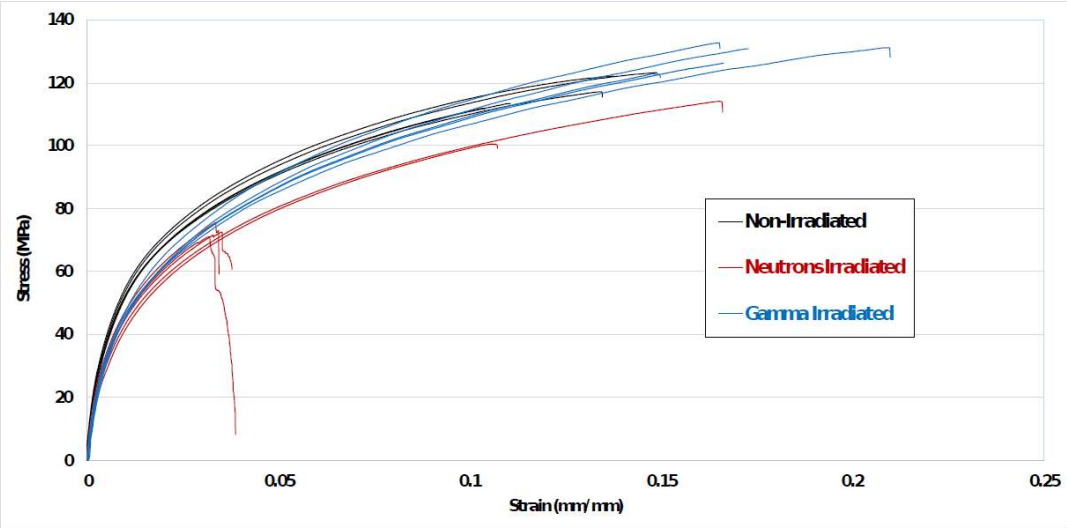

Figure A.3: Tensile test trends comparison of non-irradiated, gamma, and neutrons irradiated samples [123].

The tensile test consists in an elongation under constant rate and increasing force till the rupture point. The results of this test are shown in Fig.A.3, in which the behavior of the three sets, i.e. non-irradiated, gamma and neutrons irradiated, each containing five samples, are compared. All non-irradiated

samples ruptured between 111MPa and 123MPa, while the neutrons irradiated samples have a wide range of rupture points. In general, the rupture mechanism is considered to be related to random cracks propagation due to small imperfections generated during the coating and etching process, likely enhanced by the radiation damage process. The rupture range of the gamma-irradiated samples instead is even higher than the not-irradiated ones.

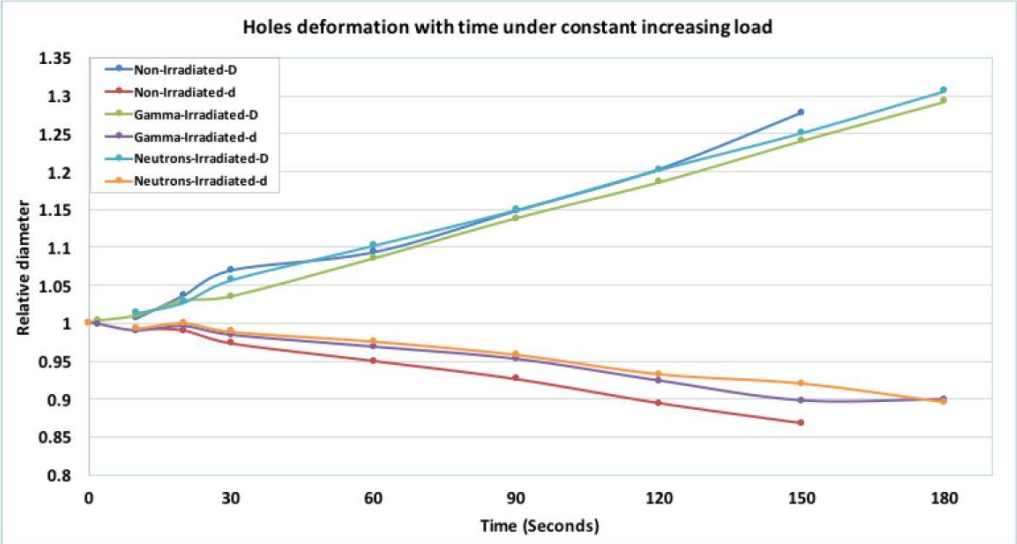

Figure A.4: Relative diameter in short (d) and long (D) diameter of the non-irradiated, gamma and neutrons irradiated samples and their trend lines. The original diameter of the sample at 0 seconds is set to 1. The long diameter (D) is parallel to the direction of stretching and short (d) is perpendicular to it, the specimens are stretched one by one with constant speed 5 mm/minute. [123].

The second test instead is related to the study of the deformation of the holes increasing the load with time. Three sets of samples were used and, in order to analyze the changes of the holes at the microscopic level, a video was recorded by using a digital microscope. In each frame, major and minor diameter of six holes were measured and recorded. Fig.A.4 shows the relative diameters of non-irradiated, gamma and neutrons irradiated samples: the trend of the three sets is similar up to 20 second from the beginning of the test. After that, the short diameter of the non-irradiated samples deformed slightly more than the irradiated.

Finally the Young's modulus of the foils was estimated from the tensile test data: for non-irradiated samples it turned out to be 9.74 GPa, while for gamma and neutrons it was reduced to 8.62 GPa and 8.47 GPa respectively,

suggesting a material degradation also in the elastic region.

A general conclusion is that basically neutrons reduce the strength in the elastic region and also toughness in elastic-plastic and plastic region. On the other hand, the gamma exposure reduced the strength of the material in elastic region, but less than neutrons. Moreover in elastic-plastic and plastic region the material toughness was increased even from the non-irradiated samples [123].

Bibliography

[1] CMS Collaboration, *The CMS experiment at the CERN LHC*, 2008 JINST 3 S08004

[2] ATLAS Collaboration, *The ATLAS experiment at the CERN Large Hadron Collider*, 2008 JINST 3 S08003

[3] O. S. Bruning et al., *LHC Design Report*, Volume 1, CERN-2004-003-V-1

[4] ATLAS Collaboration, *Observation of a new particle in the search for the Standard Model Higgs boson wih the ATLAS detector at the LHC*, Phys. Lett. B 716 (2012) 1

[5] CMS Collaboration, *Observation os a new boson at a mass of 125 GeV with the CMS experiment at the LHC*, Phys. Lett. B 716 (2012) 30

[6] CMS Collaboration, *Technical proposal for the phase II upgrade of the Compact Muon Solenoid*, CERN-LHCC-2015-10, CMS-TDR-15-02

[7] S.Heinemeyer et al., *Electroweak precision observables in the minimal supersymmetric standard model*, Physics Reports 425 (2006) 265-368

[8] S. Meyers, E. Picasso, *The design, construction and commissioning of the CERN large Eelctron-Positron collider*, Contemporary Physics, 31:6, 387-403, DOI: 10.1080/00107519008213789

[9] The Cockcroft Insitute, Postgraduate Lecture Programme, https://www.cockcroft.ac.uk/lectures

[10] A. W. Chao et al., *Handbook of accelerator physics and engineering*, 2^{nd} Edition, 2013, ISBN: 978-981-4415-84-2

[11] CMS Collaboration, *Technical Proposal for the Upgrade of the CMS Detector through 2020*, CERN-LHCC-2011-006, CMS-UG-TP-1, LHCC-P-004, 2011

[12] CMS Collaboration, *Projected performance of an upgraded CMS detector at LHC and HL-LHC: Contribution to the Snowmass Process*, arXiv:1307.7135

[13] A. Holmes.Siedle, L. Adams, *Handbook of radiation effects*, Oxford University Press, 2002, ISBN 0-19-850733-X

[14] CMS Collaboration, *Performance of CMS drift tube chambers with cosmic rays*, 2010 JINST 5 T03015

[15] CMS Collaboration, *Performance of the CMS Cathode Strip Chambers with cosmic rays*, arXiv:0911.4992v2

[16] I. Navarro-Tobar, C. Fernandez-Bedoya on behalf of the CMS Collaboration, CMS CR-2015/298

[17] CMS Collaboration, *The Muon Project, Technical Design Report*, CERN/LHCC 97-32, CMS TDR 3

[18] CMS Collaboration, *CMS Technical Design Report for the Pixel Detector Upgrade*, CERN-LHCC-2012-016, CMS-TDR-11, 2012

[19] CMS Collaboration, *CMS Technical Design Report for the Phase 1 Upgrade of the Hadron Calorimeter*, CERN-LHCC-2012-015, CMS-TDR-010, 2012

[20] CMS Collaboration, *CMS Technical Design Report for the Level-1 Trigger Upgrade*, CERN-LHCC-2013-011, CMS-TDR-12, 2013

[21] M. Tytgat et al., *The upgrade of the CMS RPC system during the first LHC long shutdown*, arXiv:1209.1979v1

[22] M. Abbrescia et al., *R&D for the upgrade of the CMS muon system*, PoS(EPS-HEP2015)224

[23] S. Malik et al., *Interplay and characterization of dark matter searches at colliders and in direct detection experiments*, arXiv:1409.4075

[24] L.Carpenter et al., *Mono-Higgs: a new collider probe of dark matter*, Phys. Rev. D 89 (2014) 075017

[25] I. Azhgirey, V. Talanov, *Proc. of XVIII Workshop on the charged particle accelerators*, Technical Report CMS-NOTE-2005-010, 2000

[26] G. Battistoni et al., *The FLUKA code: description and benchmarking*, AIP Conf. Proc. 896 (2007), no. SLAC-REPRINT-2007-184, 31

[27] A. Colaleo, *Muon Phase-2 Upgrade Overview*, First Muon Comprehensive Review, 28-29 June 2016

[28] F. Palla, *Tracking Triggers for the High Luminosity LHC*, PoS Vertx 2013 (2013) 034

[29] CMS Collaboration, *CMS Technical Design Report for the muon endcap GEM upgrade*, CERN-LHCC-2015-012, CMS-TDR-013

[30] C.-Y. Chen and S. Dawson, *Exploring two Higgs doublet models through Higgs production*, Phys. Rev. D87 (2010) 055016

[31] J.Z.Neil Turok, *Electroweak baryogenesis in the two doublet model*, Nucl. Phys. B358 (1991) 471–473

[32] CMS Collaboration, *The performance of the CMS muon detector in proton-proton collisions at sqrt(s)=7 TeV*, JINST 7(2012)P10002, doi:10.1088/1748-0221/7/10/P10002

[33] A. Safonov, *Trigger studies and plans for optimal presentation in the TDR*, Internal Report at Muon Upgrade Workshop

[34] The ATLAS collaboration, Aad, G., Abbott, B. et al. J. High Energ. Phys. (2014) 2014: 88. doi:10.1007/JHEP11(2014)088

[35] CMS Collaboration, CMS PAS FTR-13-003

[36] Belle Collaboration, *Search for lepton-flavor-violating τ decays into three leptons with 719 million produced $\tau^+\tau^-$ pairs*, Physics Letters B 687 (2010) 139–143

[37] The LHCb collaboration, Aaij, R., Adeva, B. et al. J. High Energ. Phys. (2015) 2015: 121. doi:10.1007/JHEP02(2015)121

[38] F.Lagarde on behalf of the CMS RPC Collaboration, *High rate, fast timing Glass RPC for the high η CMS muon detectors*, arXiv:1606.01398v2

[39] C. Grupen, I. Buvat, *Handbook of particle detection and imaging*, Springer-Verlag, DOI 10.1007/978-3-642-13271-1

[40] W.R. Leo, *Techniques for nuclear and particle physics experiments*, Springer-Verlag, ISBN 978-3-642-57920-2

[41] G.F. Knoll, *Radiation detection and measurement*, Third Edition, John Wiley & Sons, Inc.

[42] F. Sauli, *Gaseous radiation detectors. Fundamental and applications*, Cambridge monographs on particle physics, nuclear physics and cosmology, ISBN 978-1-107-04301-5

[43] A. Syed, *Physics and engineering of radiation detection*, Elsevier, ISBN 978-0-12-045581-2

[44] TH. G. Schut, J. A. Smit, *A direct measurement of the efficiency of the Penning effect*, Physica X, no 6, 1943

[45] H.C. Kim et al., *Qualitative aging study with intense irradiation tests for the CMS forward RPCs*, NIMA 602 (2009) 771-774

[46] Regulation (EU) No 517/2014 of the European Parliament and of the Council on Fluorinated Greenhouse Gases and Repealing Regulation (EC) No 842/2006

[47] L. Benussi et al., *Properties of potential eco-friendly gas replacements for particle detectors in high energy physics*, CERN-OPEN-2015-004

[48] M. Capeans et al., *Strategies for reducing the environmental impact of gaseous detector operation at the CERN LHC experiments*, 10.1016/j.nima.2016.04.067

[49] R. Guida et al., *Characterization of RPC operation with new environmental frindly mixtures for LHC application and beyond*, 2016 JINST 11 C07016

[50] F. Sauli, A. Sharma, *Micropattern gaseous detectors*, Annu.Rev. Nucl. Part. Sci. 1999. 49:341–88

[51] A. Oed, *Position-sensitive detector with microstrip anode for electron multiplication with gases*, NIM A263:351 (1988)

[52] F. Sauli, *Micro-pattern gas detectors*, NIM A 477 (2002) 1-7

[53] L. Shekhtman, *Micro-pattern gaseous detectors*, NIM A 494 (2002) 128-141

[54] E. Nappi, V. Peskov, *Imaging gaseous detectors and their application*, First Edition, 2013 Wiley-VCH Verlag GmbH & Co. KGaA

[55] Y. Giomataris et al., *MICROMEGAS: a high-granularity position-sensitive gaseous detector for high particle-flux environments*, NIM A 376 (1996) 29-35

[56] G. Yakovidis on behalf of the MAMMA Collaboration, *The Micromegas project for the Atlas upgrade*, arXiv:1310.0734v1

[57] S. Bachmann et al., *Charge amplification and transfer process in the Gas Electron Multiplier*, NIM A 438 (1999) 376-408

[58] S. Bachmann et al., *Discharge studies and prevention in the gas electron multiplier (GEM)*, NIM A 479 (2002) 294-308

[59] G. Bencivenni et al., *Advances in triple-GEM detector operation for high-rate particle triggering*, 513 (2003) 264-268

[60] G.Croci et al., *Discharge probability measurement of a Triple GEM detector irradiated with neutrons*, NIM A 712 (2013) 108-112

[61] T. Francke, V. Peskov, *Innovative application and developments of Micro-Pattern Gaseous detectors*, Engineering Science Reference, 2014

[62] R. Bellazzini et al., *The WELL detector*, NIM A 423 (1999) 125-134

[63] A. Breskin et al., *A concise review on THGEM detectors*, Invited Review at INSTR08, Novosibirsk, Feb 28 - March 5 2008

[64] S. Bressler et al., *Recent advances with THGEM detectors*, arXiv:1310.3912

[65] M. Abbrescia et al., *Resistive plate chamber neutron and gamma sensitivity measurement with a ^{252}Cf source*, NIM A 506 (2003) 101–109

[66] A. Magnani et al., CMS DP-2015/001

[67] D. Abbaneo et al., *Test beam results of the GE1/1 prototype for a future upgrade of the CMS high-h muon system*, IEEE Nucl. Sci. Symp. Med. Imag. Conf. Rec. (2011) 1806–1810, doi:10.1109/NSSMIC.2011.6154688, arXiv:1111.4883

[68] D. Abbaneo et al., *Beam Test Results for New Full-scale GEM Prototypes for a Future Upgrade of the CMS High-eta Muon System*, IEEE Nucl. Sci. Symp. Med. Imag. Conf. Rec. (2012) 1172 – 1176, doi:10.1109/NSSMIC.2012.6551293, arXiv:1211.3939.

[69] D. Abbaneo et al., *Performance of a Large-Area GEM Detector Prototype for the Upgrade of the CMS Muon Endcap System*, IEEE Nucl. Sci. Symp. Med. Imag. Conf. Rec. (2014) arXiv:1412.0228.

[70] D. Abbaneo et al., *The status of the GEM project for CMS high-h muon system*, Nucl. Instrum. Meth. A732 (2013) 203–207, doi:10.1016/j.nima.2013.08.015.

[71] A: Abbaneo et al., *A novel application of Fiber Bragg Grating (FBG) sensors in MPGD*, arXiv:1512.08529v1

[72] R. Gomez-Reino et al., *Status of the CMS Detector Control System*, Journal of Physics: Conference Series 396 (2012)012023

[73] C. Gaspar et al., *DIM, a Portable, Light Weight Package for Information Publishing, Data Transfer and Inter-process Communication*, International Conference on Computing in High Energy and Nuclear Physics, Padova (2000)

[74] Etm, http://www.etm.at/index_e.asp

[75] http://www.caen.it/csite/CaenProd.jsp?parent=20&idmod=960

[76] PH - DT - DI Gas project, http://detector-gas-systems.web.cern.ch/detector-gas-systems/HomePage/homePage.htm

[77] S. Agostinelli et al., *GEANT4 - a simulation toolkit*, NIM A 506 (2003) 250-303

[78] O. Militaru, *High flux neutron and proton irradiation facility in Louvain-la-Neuve Cyclotron*, Internal Report

[79] F. Loddo et al., *GASTONE: A new ASIC for the cylindrical GEM inner tracker of KLOE experiment at DAFNE*, NIM A 604 (2009) 23-25

[80] CAEN, http://www.caen.it/csite/CaenProd.jsp?parent=11&idmod=46

[81] Benney, https://aismisc.cern.ch/aismisc/f?p=152:7:211578036263641::NO:RP,7:P7_ITEM:4156

[82] CAEN, http://www.tunl.duke.edu/documents/public/electronics/CAEN/caen_v560.pdf

[83] Keithley, *Model 6487 Picoammeter/Voltage Source, Reference Manual*, 6487-901-01 Rev. B / March 2011

[84] National Instruments, *LabVIEW System Design Software*, http://www.ni.com/labview/i/

[85] KLOE experiment, http://www.lnf.infn.it/kloe2/

[86] Amptek, http://amptek.com/products/mini-x-ray-tube/

[87] J. Merlin, *Study of long-term sustained operation of gaseous detectors for the high rate environment in CMS*, PhD Thesis, CERN-THESIS-2016-041

[88] http://www.nucleide.org/DDEP_WG/Nuclides/Cd-109_tables.pdf

[89] G. Bencivenni et al., *The micro-Resistive WELL detector: a compact spark-protected single amplification-stage MPGD*, Jinst 2015, 10, P02008

[90] J. Robertson, *Diamond-like amorphous carbon*, Materials Science and Engineering: R: Reports, Vol. 37, Issues 4-6, 24 May 2002, Pages 129-281

[91] G.Bencivenni et al., *Advances in micro-Resistive WELL (μ-RWELL) detectors*, Talk at VCI2016 - The 14th Vienna Conference on Instrumentation, 15-19 February 2016

[92] https://edms.cern.ch/ui/file/1106529/LAST_RELEASED/Safety_Guideline_EN_C-2-0-2.pdf

[93] ORTEC, https://www.tau.ac.il/ lab3/MOSSBAUER/Experimental/142 PC-Preamplifier.PDF

[94] ORTEC, www.ortec-online.com/download/474.pdf

[95] LeCroy, http://teledynelecroy.com/lrs/dsheets/428.htm

[96] LeCroy, http://www.fnal.gov/projects/ckm/jlab/623b-spec.htm

[97] Amptek, http://amptek.com/products/mca-8000d-digital-multichannel-analyzer/

[98] http://ab-dep-op-sps.web.cern.ch/ab-dep-op-sps/

[99] P. Aspell et al., *The VFAT Production Test Platform for the TOTEM Experiment*, https://cds.cern.ch/record/1159891/files/p544.pdf

[100] *Turbo: VFAT CTRL/Readout board*, https://indico.cern.ch/event/136793/contributions/1360602/attachments/112026/159286/TURBO-PaulMeeting.pdf

[101] M. Poli Lener, *Triple-GEM detectors for the innermost region of the muon apparatus at the LHCb experiment*, PhD Thesis, , https://cds.cern.ch/record/940631/files/thesis-2006-013.pdf

[102] E. Oliveri, PH-DT-Training Seminar on MPGD detectors, https://indico.cern.ch/event/306552/attachments/583700/803477/PH-DT-TrainingSeminar-MPGD-eoliveri.pdf

[103] LHCb Collaboration, *The LHCb Detector at the LHC*, 2008 JINST 3 S08005

[104] Enea Casaccia: http://www.enea.it/it/centro-ricerche-casaccia/

[105] M. Alfonsi et al., *The LHCb Triple-GEM detector for the inner region of the first station of the muon system: construction and Module-0 performance*, IEEE Transactions on Nuclear Science, VOL. 53, NO. 1, February 2006

[106] R.de Olivera et al., *A novel fast timing micropattern gaseous detector: FTM*, arXiv:1503.05330

[107] D. Abbaneo et al., *R&D on a new type of micropattern gaseous detector: The Fast Timing Micropattern detector*, http://dx.doi.org/10.1016/j.nima.2016.05.067

[108] Kaneka, http://www.kanekatexas.com/apical_technical-data.html

[109] Dupont, http://www.americandurafilm.com/data-sheets/kapton-xc.pdf

[110] COMSOL, https://www.comsol.it/

[111] F. Paschen, Annalen der Physik. 273 (5): 69–75, doi:10.1002/andp.18892730505

[112] M.A. Lieberman, A.J. Lichtenberg, *Principles of plasma discharges and material processing*, 2nd ed., N.J.: Wiley-Interscience, ISBN 978-0471005773

[113] Cividec Instrumentation, *C2 broadband amplifier, 2 GHz, 40 dB*, https://cividec.at/files/15_pdf.pdf

[114] Lecroy, *NIM Model 612AM, 6-Channel Photomultiplier Amplifier*, http://neutron.physics.ucsb.edu/docs/LeCroy%20Manuals/612am-spec.htm

[115] Y. Assran, A. Sharma, *Transport Properties of operational gas mixtures used at LHC*, arXiv:1110.6761

[116] Geant4 processes: naming convention, http://geant4.cern.ch/G4UsersDocuments/UsersGuides/ForApplicationDeveloper/html/TrackingAndPhysics/physicsProcess.html

[117] M. Raymond et al., *The CMS Tracker APV25 0.25 μm CMOS Readout Chip*, https://cds.cern.ch/record/478270/files/raymond.pdf

[118] D. Abbaneo et al., *Design of a constant fraction discriminator for the VFAT3 front-end ASIC of the CMS GEM detector*, 2016 JINST 11 C01023

[119] R. Veenhof, garfield.web.cern.ch/garfield

[120] Skyroc chip: http://omega.in2p3.fr/index.php/products/skiroc.html

[121] Omega micro: http://omega.in2p3.fr/

[122] CHARM facility, http://charm.web.cern.ch/charm/

[123] L. Benussi et al., *Gas Electron Multiplier foil holes: a study of mechanical and deformation effects*, 2016 JINST 11 P08002

[124] http://www.colorado.edu/engineering/CAS/courses.d/Structures.d/IAST.Lect05.d/IAST.Lect05.pdf

[125] http://www.instron.us/en-us/products/testing-systems/universal-testing-systems/electromechanical/3300/3340-single-column

[126] http://www.keyence.com/products/microscope/digital-microscope/index.jsp

Acknowledgements

Now that this journey is finished, there are many people I have to say thanks to...

First of all, I'd like to thank my advisor, Prof.ssa Cristina Riccardi, for having introduced me to this field and for allowing me to grow as a research scientist.

Thanks to all the members of the CMS Pavia Group, Alessandro, Alice, Francesco, Martina, Paola, Paolo M. and Paolo V., who went along with me in these last years and supported me.

Thanks to A. Colaleo, M. Maggi and A. Sharma, for the precious support given to my work.

Thanks to the CMS GEM CERN Group, Anastasia, Andrey, Brian, Jared, Jeremie, Marek, Michele, Mohsin, Sameem, Waqar who welcomed me in the last period spent in the GEM laboratory at CERN.

Thanks to the RD51 people, in particular Eraldo Oliveri, Filippo Resnati and Yorgos Tsipolitis, for their continuos help during the test beams and even beyond. Thanks also to Silvia Franchino for her fundamental support with the FTM and B2B.

Thanks to Beatrice Mandelli, Roberto Guida and all the CERN Gas Group for their precious advices for the development of the GEM DCS. Thanks to Roberto also for having introduced me to the GIF++ activities.

Thanks to Lisa, Rosamaria and Piet for important help while I was writing the first part of this thesis.

I would like also to remember the important contribution that all technicians gave to this work. Without their experience and unvaluable job, many of the tests described in this thesis would have not been possible.

Finally, I wish also to say thanks to Doctors Silvia Maselli and Francesco

Tartarelli who spent time to read this thesis and gave me precious advices.

Di nuovo grazie ai *Disperati*, Alice, Emanuele, Federica, Francesco, Martina e Lisa, per tutti i momenti condivisi nell'ultimo anno. Grazie a Filippo, Samuel e Manrico, per le ottime cene in compagnia, a quando la prossima? Grazie agli amici e colleghi di Pavia, in particolare Aurora, Claudio, Cospi, Nico. Grazie ad Andrea F. e Marta, che hanno condiviso con me e Alice l'ufficio in questi anni..un grazie particolare a Marta per essere stata sempre così disponibile e avermi salvato tutte le volte che mi son svegliata all'ultimo minuto...

Grazie a Giuzz, Marta B., Maura, Nico, Raffaella, Rosma, Archie, Claudio C., Cesare, Palma, Piet e a tutti gli altri amici conosciuti in questi anni che sicuramente mi sto dimenticando di nominare, non vogliatemene a male.

Grazie a chi è rimasto fino alla fine, ma anche a chi invece se n'è andato prima..

Grazie ai miei genitori e ad Andrea, che anche nei momenti più difficili, anche quando sono stata (e so di esserla stata..) insopportabile, mi hanno sopportato e mi hanno appoggiata sempre.

Infine grazie ad Andrea, per essere arrivato ed essere rimasto..per aver accettato i momenti peggiori di questi ultimi anni e averli condivisi con me. Senza di te, forse non sarei arrivata alla fine di questo percorso.